technische universität
dortmund

Quasiparticle decay induced by spin anisotropies in the frustrated spin ladder system $BiCu_2PO_6$

Dissertation
zur Erlangung des akademischen Grades
Dr. rer. nat.
der Fakultät Physik
der Technischen Universität Dortmund

vorgelegt von
Leanna Blanche Müller
geboren in Dortmund als Splinter

Lehrstuhl für Theoretische Physik I
Fakultät Physik
Otto-Hahn-Str. 4
Technische Universität Dortmund

2021

1. Gutachter: Prof. Dr. Götz S. Uhrig, TU Dortmund
2. Gutachter: Prof. Dr. Kai Phillip Schmidt, FAU Erlangen-Nürnberg

Abstract

The inorganic compound $BiCu_2PO_6$ contains tubelike structures, which are described magnetically by weakly coupled frustrated spin ladders with a finite energy gap. The elementary excitations are triplons of which the degeneracy is lifted due to Dzyaloshinskii-Moriya interactions. In certain regions of the Brillouin zone the lifetime of the triplon excitation modes becomes finite due to the hybridization of the single-triplon with the two-triplon states. In addition, the dispersions of these triplon modes show a striking down-bending before ceasing to exist. In experiment, $BiCu_2PO_6$ shows various types of decay processes, which can be caused by different symmetry breaking interactions. In previous studies, we established a minimal model to include all symmetry-allowed interactions, such as the Dzyaloshinskii-Moriya interaction. Based on this minimal model, we show in this thesis that isotropic and anisotropic effects are responsible for noticeable quasiparticle decay and certain down-shifts of the single-triplon energies. The analyses are based on a deepCUT approach for the isotropic case augmented by a perturbative treatment of the anisotropic couplings inducing quasiparticle decay at zero temperature.

Kurzfassung

Die anorganische Verbindung $BiCu_2PO_6$ enthält röhrenartige Strukturen, welche magnetisch durch schwach gekoppelte frustrierte Spinleitern mit einer endlichen Energielücke beschrieben werden. Die elementaren Anregungen sind Triplonen dessen Entartung aufgrund der Dzyaloshinskii-Moriya Wechselwirkungen aufgehoben ist. In bestimmten Bereichen der Brillouin Zone wird die Lebensdauer der Triplonen endlich aufgrund der Hybridisierung der Eintriplon- mit den Zweitriplonenzuständen. Zusätzlich zeigen diese Triplonmoden ein auffälliges Abknicken bevor sie aufhören zu existieren. Im Experiment weist $BiCu_2PO_6$ unterschiedliche Typen von Zerfallsprozessen auf, die durch verschiedene symmetriebrechende Wechselwirkungen verursacht sein könnten. In vorherigen Untersuchungen habe wir ein minimales Model aufgestellt, um alle aufgrund von Symmetrie erlaubten Wechselwirkungen, wie die Dzyaloshinskii-Moriya Wechselwirkung, zu berücksichtigen. Auf Grundlage dieses minimalen Models zeigen wir in dieser Arbeit, dass isotrope und anisotrope Effekte für erkennbaren Quasiteilchenzerfall und bestimmte Absenkungen der Eintriplonenenergien verantwortlich sind. Die Analysen basieren auf einem deepCUT Ansatz für den isotropen Fall, ergänzt durch eine störungstheoretische Behandlung der anisotropen Kopplungen, die Quasiteilchenzerfall bei Temperatur gleich Null induzieren.

Contents

Acronyms

BCPO Bismuth copper phosphate ($BiCu_2PO_6$)

BOT Bond operator theory

CUT Continuous unitary transformation

deepCUT Directly evaluated enhanced perturbative CUT

DM interaction Dzyaloshinskii-Moriya interaction

DSF Dynamic structure factor

HWHM Half-width at half-maximum

INS Inelastic neutron scattering

SOC Spin-orbit coupling

SQPD Spontaneous quasiparticle decay

1 Introduction

The field of condensed matter physics addresses the issues of the physical properties of matter on macroscopic and microscopic level. Its branch concerning matter in the solid phase is the research field of solid state physics. It deals with the question what atomic-scaled properties of a solid material are responsible for its observable characteristics on macroscopic level. The first model to describe the physics of a solid was the DRUDE model in 1900, which characterizes the transport properties of electrons in materials, especially in metals, on a classical level [1, 2]. During the next years the DRUDE model was extended in several ways in order to fill its knowledge gaps [3].
The most important milestone in the field of solid state physics was the introduction of quantum mechanics [4–6]. With this fundamental theory the physics on atomic and subatomic scales can be explained. One of the best known manifestations of quantum mechanics in our everyday life is the phenomenon of magnetism [7, 8]. The first model describing the appearance of magnetism on microscopic level was established by ISING in 1924 [9]. The ISING model characterizes a solid state as a periodic lattice of interacting spins S= ½ [7, 10–13] on microscopic level which results in a net magnetization on macroscopic level. This model was invented to describe phase transitions. In 1930 NÉEL proposed a different form of magnetism called antiferromagnetism [7, 8, 14–16]. In constrast to ferromagnetism, the spins in an antiferromagnet prefer to align antiparallel leading to a zero net magnetization. One interesting phenomenon in the context of antiferromagnetism is the frustrated magnetism [14, 17–19]. It presents a perfect testing ground in which new states and new properties of matter can be discovered [18].

1.1 Frustrated magnetism

In antiferromagnetic materials it is not always possible that all spins, described by classical vectors, align antiparallel to their interacting neighbors. This aspect leads to the field of frustrated magnetism. Frustration occurs when no possible spin configuration of the interacting spins can minimize all individual bond interactions simultaneously [20–22]. In general, frustration can be caused either by competing interactions [21] or

by the underlying lattice structure [14, 17]. The latter case is referred to as geometrical frustration[1]. Figure 1.1 represents examples for each case.

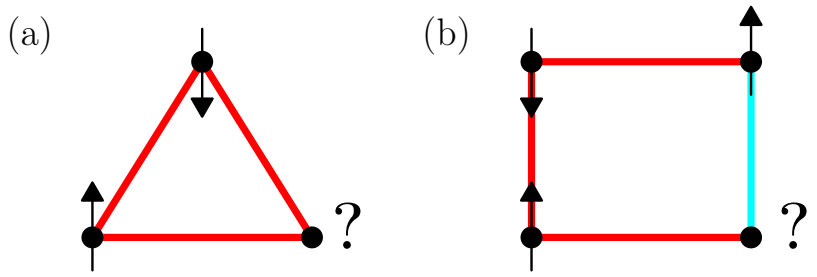

Figure 1.1: Examples of frustrated spin arrangements. At the corner of each plaquette a spin with S=1/2 is located. The red lines visualize antiferromagnetic interactions, whereas the blue line stands for a ferromagnetic interaction.
(a) Geometrical frustration [15,16]. In the triangular lattice two spins align antiparallel. The third spin is frustrated since both its orientations give the same energy and result in one unsatisfied bond. (b) Frustration caused by competing interactions [17]. In the square plaquette three spins arrange antiparallel. The fourth spin is frustrated due to the competing ferro- and antiferromagnetic interactions with its neighbors. Its two possible orientations leave one bond unsatisfied.

Further prominent frustrated lattice structures are for example the kagome lattice in two dimensions [23–25] and in three dimensions the pyrochlore lattice [17, 19][2]. The phenomenon of frustrated magnetism gives rise to a degenerate manifold of possible ground-states leading to magnetic analogies of liquids and ice which are called spin liquids [14] and spin ice [14,30]. Since frustrated materials show new states and new properties of matter, they represent promising candidates for applications in modern technology [31]. Therefore, it is crucial to obtain an in-depth knowledge of the mechanisms which are fundamentally responsible for the characteristics of frustrated systems.

1.2 Experimental analysis of solid state systems

Inelastic neutron scattering (INS) experiments are a paradigm technique for studying the magnetic properties of solid state systems, e.g. spin correlation functions or features of the magnetic excitations [18,32]. In order to characterize the microscopic interactions of a solid state material its underlying structure needs to be specified. For this neutrons with a wavelength in the order of 10^{-10} m and a corresponding energy of a few meV are used standardly[3]. As neutrons hold a magnetic moment, they can interact with

[1] In the context of this thesis, we use the expression frustration as a simplification of geometrical frustration, unless otherwise stated.
[2] Each of these lattice structures holds nearest-neighbors antiferromagnetic interactions. For further interesting frustrated materials we refer to Refs. [14, 26–29].
[3] Neutrons in this energy range are called thermal neutrons.

unpaired electrons in magnetic atoms. Thus, they can reveal information about the magnetic lattice structure of a sample [32]. The basics of INS experiments are shown in figure 1.2.

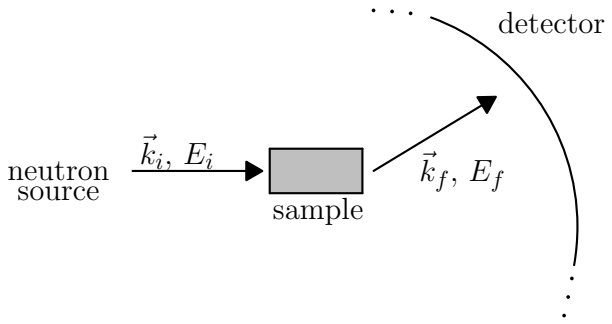

Figure 1.2: Schematic illustration of INS experiments.

A collimated beam of neutrons with initial momentum $\vec{k}_i$ and energy E_i is focused on a sample. The neutrons interact with the sample and a transfer in energy and momentum between the neutrons and the sample takes place. The scattered neutrons hold a different momentum $\vec{k}_f$ and energy E_f providing information about the magnetic properties of the sample. The intensity of the scattered neutrons depends on the momentum transfer $\vec{Q} = \vec{k}_i - \vec{k}_f$ and energy transfer $\hbar\omega = E_i - E_f$. It is proportional to the dynamic structure factor (DSF) $S^{\alpha\beta}(\vec{Q},\omega)$ [33]. The DSF is defined as the FOURIER transform of the time- and momentum-dependent spin-spin correlation function

$$S^{\alpha\beta}(\vec{Q},\omega) = \frac{1}{2\pi}\int_{-\infty}^{\infty} \mathrm{d}t\, \mathrm{e}^{\mathrm{i}\omega t}\langle S^{\alpha}(-\vec{Q},t)S^{\beta}(\vec{Q},0)\rangle \tag{1.2.1}$$

with the spin components $\alpha,\beta \in \{x,y,z\}$ [33–35], see sect. 2.3.1 for more details. As the DSF is an accessible variable in theoretical calculations, it represents an appropriate quantity for comparing theoretical and experimental results. It provides valueable information concerning the magnetic excitations of a material and their mutual interactions.

1.3 The phenomenon of spontaneous quasiparticle decay

Quasiparticles are a fundamental concept in modern condensed matter physics for describing strongly interacting many-body systems [36–38]. Within the quasiparticle picture, complex collective excited states of a many-body system can be described in terms of effective elementary excitations [39]. The quanta of these excitations hold a definite

amount of momentum and energy and are called quasiparticles [39]. They are assumed to have a long or even infinite intrinsic lifetime [38] and to interact weakly with each other [40]. If a system contains interaction terms which couple single-particle and multi-particle states, it is possible that a single particle may decays into the continuum of the multi-particle states spontaneously[4] [37, 40]. With the expression "spontaneously" we mean that the quasiparticle decay takes place at zero temperature (T=0), i.e. its origin are quantum fluctuations and not thermal fluctuations [41, 42].
If spontaneous quasiparticle decay (SQPD) is possible, three different scenarios can occur[5]:

1st The lifetime of the quasiparticle decreases rapidly [41].

2nd The single-particle branch disappears completely [41].

3rd The single-particle dispersion is significantly renormalized in order to avoid an overlap with the multi-particle continuum. It is pushed below the lower boundary of the continuum [39].

Quasiparticle decay was first predicted [43] and then discovered in the excitation spectrum of superfluid ^{4}He [44–46] at temperatures close to zero. In the field of magnetism SQPD was observed by INS experiments in various valence bond type quantum spin systems, for example piperazinium hexachlorodicuprate (PHCC) [37], IPA-$CuCl_3$ [47, 48], $BiCu_2PO_6$ [39] and also in triangular lattice compounds [49, 50].

1.4 The inorganic compound $BiCu_2PO_6$

The quantum antiferromagnet $BiCu_2PO_6$ (BCPO) states a fascinating structure whose manifold magnetic properties have been analyzed in detail in the last decades [39,51–70]. It is also discussed as a candidate for topological insulators [71]. Before discussing its interesting characteristics, observed in INS experiments, and the current research status, our initial focus is on the spin model[6] of BCPO, see figure 1.3.
Although the contained bismuth ions hold a large atomic number ($Z = 83$), they do not host the localized spins S=½. These are localized at the copper ions Cu^{2+} and form the magnetic structure of BCPO. The magnetic model is based on tubelike arranged spin ladders coupled among themselves resulting in a two-dimensional lattice [55, 65].

[4] Note, that momentum and energy have to be conserved [38].
[5] In sect. 2.3 we revive these scenarios and discuss them in more detail.
[6] A detailed description of the crystal structure, which describes the spatial arrangement of all contained ions, was published by Tsirlin *et al.* [60].

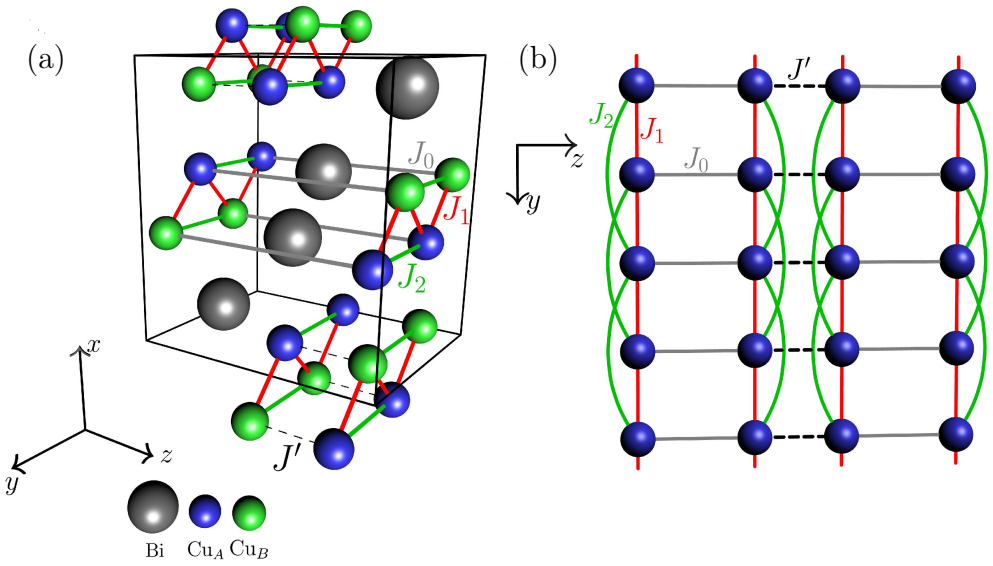

Figure 1.3: Structures of BCPO.
(a) Crystal structure of BCPO. The unit cell is orthorhombic and contains coupled frustrated spin ladders formed by the two inequivalent copper ions Cu_A and Cu_B. We omitted the phosphorus and oxygen ions for a better overview. (b) Effective spin model. The analyzed model is made of frustrated spin ladders, which are coupled by an interladder coupling J'. The inequivalence of the copper ions is neglected.

The tubes represent frustrated spin ladders[7], which are constructed by two crystallographically different types of copper ions Cu_A and Cu_B, see figure 1.3. The elementary excitations are dispersive triplons, i.e. hard-core S=1 quasiparticles [72], which are degenerated for isotropic models. The difference between the copper ions Cu_A and Cu_B arises from the positions of the bismuth ions in the crystal structure. The two types of copper ions alternate along the ladder in y-direction. The coupling between the spins, which belong to different types of copper ions, is the nearest-neighbor (NN) interaction J_1. The couplings J_0 and J' acting perpendicular in z-direction connect different types of copper ions as well. It is an appropriate assumption that a difference in the next-nearest-neighbor (NNN) interaction between the copper ions of the same type exists [60]. These couplings are named J_2 and J_2'. Mostly this aspect is neglected in research. Since noticable dispersion exists in the yz-plane, BCPO has to be considered as a two-dimensional material [60, 69]. Along the x-direction a dispersion is hardly detected, supporting the two-dimensionality [60,69]. The crystal structure of BCPO shows up broken inversion symmetry about the center of the copper bonds [60], see figure 1.3. For this reason anisotropic interactions are possible in BCPO and have to be considered additionally [73, 74]. These anisotropic interactions, referred to as the Dzyaloshinskii-Moriya interaction (DM interaction) arise from the spin-orbit coupling (SOC). They

[7]The ground-state of BCPO is a valence bond solid [71].

lead to the fact that the spectrum of the elementary excitations, i.e. the triplons, is split. As a standard estimate for the relative strength of the DM interactions compared to the isotropic interactions D/J is $|\Delta g|/g$ where g is the gyromagnetic ratio $g \approx 2$ and $\Delta g = g - 2$. For spins in copper ions Δg assumes values from zero to 0.4 so that any value of D/J beyond 0.2 must be considered remarkable. Since the SOC is a relativistic effect, it is of particular importance for elements with a large atomic number implying strong COULOMB potentials and high electronic velocities[8].

After considering the magnetic structure of BCPO in detail, we now discuss interesting characteristics of its excitation spectrum and the current research status. The excitation spectrum of BCPO, received by INS experiments and firstly published by PLUMB *et. al.* [39, 70], shows a wide range of interesting features.

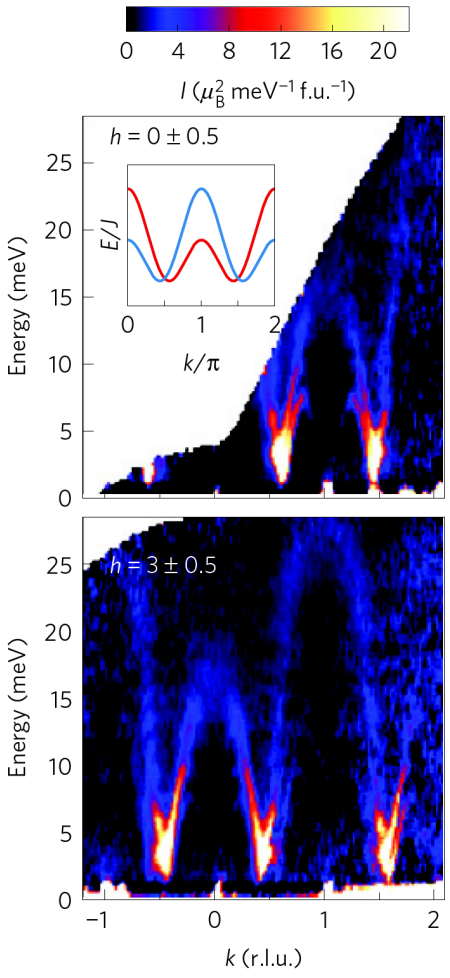

Figure 1.4: Results of the INS experiments on BCPO. The illustrations are taken from Ref. [39].

There are two striking points concerning the excitation spectrum of BCPO, see figures 1.4 and 1.5, which we want to address explicitly.

1st The excitation modes are not degenerated, but split.

2nd Not all excitation modes exist in the complete BRILLOUIN zone, but show up interesting downbendings before ceasing to exist.

The first point emphasizes the assumption that anisotropic interactions are present in BCPO lifting the degeneracy of the excitation modes. The second aspect demonstrates that there are effects in BCPO present which have a significant influence on the lifetime of the excitation modes. In accordance with our previous analysis of the spin model of BCPO, the experimental results confirm the significant influence of the

[8] As BCPO contains bismuth ions holding a large atomic number of $Z = 83$, it is reasonable to expect the presence of anisotropic interactions.

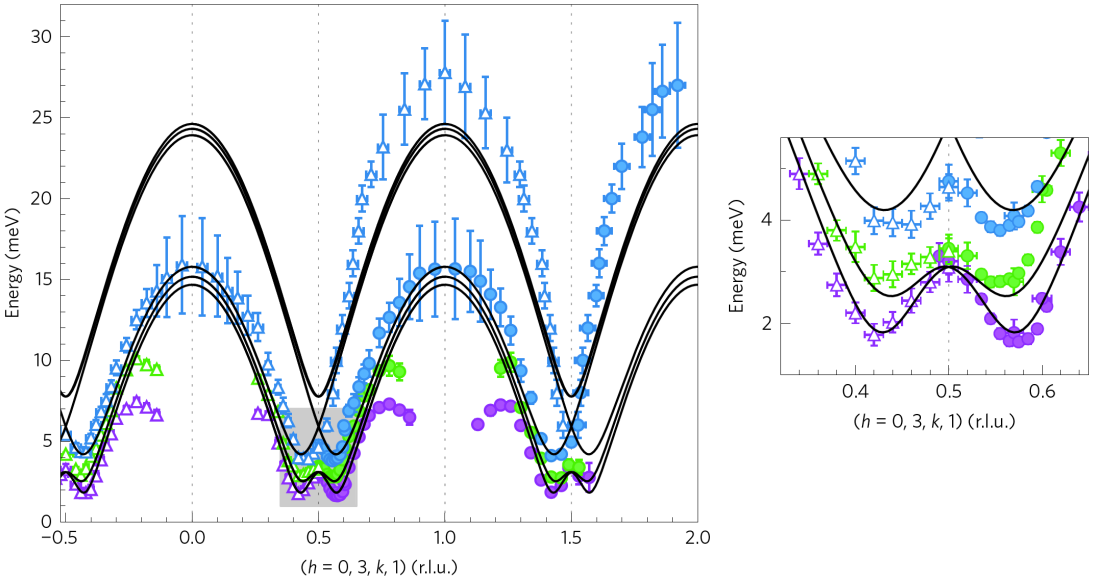

Figure 1.5: Dispersions of the excitation modes in BCPO. The color assigment of the data points indicates the different excitation modes. The grey shaded region around the minimum area is depicted in a more detailed way. The solid lines correspond to theorectical calculations based on a bond operator theory (BOT) on a mean-field level. The illustrations are taken from Ref. [70].

DM interaction on its excitation spectrum. Furthermore the DM interaction is discussed to be also responsible for the observed finite lifetime of the triplons and their absence in specific parts of the BRILLOUIN zone. PLUMB *et. al.* discussed this issue at first [39, 64]. They considered triplon interactions, which are induced by the existing DM interactions, via the bond operator formalism and the GREEN'S function formalism on a one-loop level. These interactions lead to renormalized triplon energies and to the fact that the triplons can decay, i.e. the phenomenon of spontaneous quasiparticle decay (SQPD) arises in BCPO due to DM interactions[9]. The results can explain the decay behavior of the triplons inside the two-triplon continua at a satisfactory level, see figure 1.6 [64]. In contrast, the prominent down-bending behavior cannot be reproduced since the occuring level repulsion effects turn out to be rather small. In addition, only one specific component $\mathbf{D}_1$ out of all existing DM interactions contributes to decay processes and assumes a remarkable value of $\mathbf{D}_1/J_1 = 0.3$. Although two-triplon interactions are taken into account, no bound states occur since these interactions are approximated via a mean-field approach.

[9] Apart from the DM interactions, even isotropic effects in BCPO, for example the previous mentioned difference in the NNN interactions J_2 and J_2', can lead to the phenomenon of SQPD. In chapter 5 we discuss this aspect in detail.

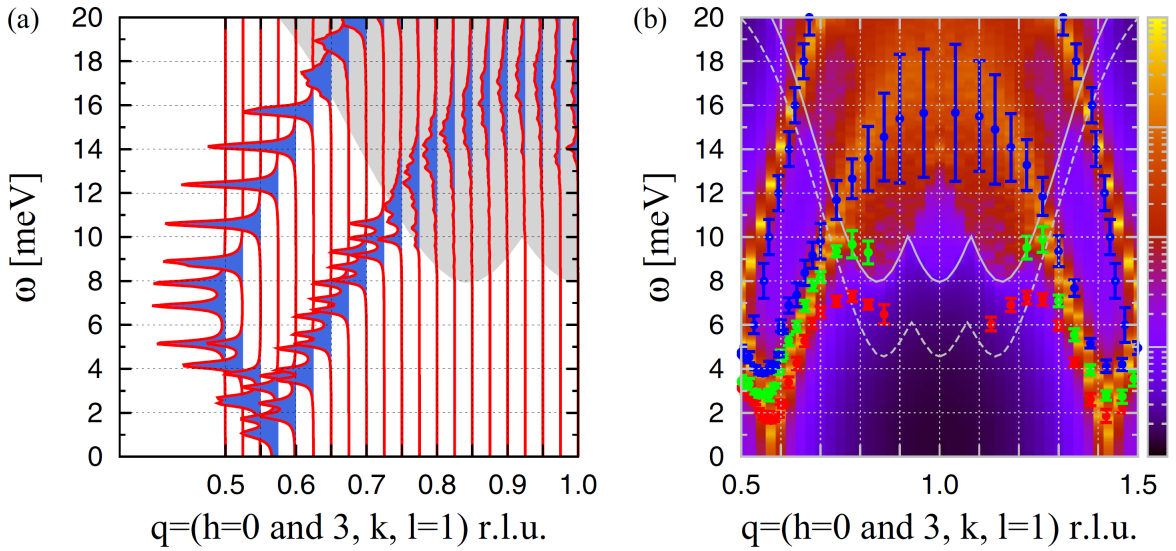

Figure 1.6: Theoretical spectral function of BCPO including interacting triplons.
(a) The spectral function is plotted with lines. They gray shaded region depicts the multitriplon continuum. (b) The spectral function is plotted with a color map. The color dots denote the INS data from Ref. [39]. Note, that the color coding differs compared to figure 1.5. Both illustrations are taken from Ref. [64].

1.5 Goals of this thesis

In this thesis we want to establish a microscopic model for BCPO that explains all its striking features, which have been revealed in INS experiments, by assuming realistic values for the anisotropic interactions. In particular, we want to address the prominent down-bending behavior, which cannot be explained up to now, the finite lifetime of the triplons and their absence in specific parts of the Brillouin zone. We want to point out comprehensibly what exact mechanisms in BCPO are mainly responsible for these features. In order to do so, we use a continuous unitary transformation (CUT) approach for the isotropic case of BCPO augmented by a perturbative treatment of the anisotropic couplings on a mean-field level. We include these corresponding interactions on different operator levels step by step and fit our results to the experimental data. Using this procedure, we can determine the values of the anisotropic couplings and work out what processes are mainly responsible for the dynamics in BCPO.

This thesis is structured as follows. In the next chapter 2, we introduce the basic techniques which have been used in this thesis to set up a comprehensive model for BCPO. In chapter 3 we apply these methods to a toy model and discuss the basic effects of SQPD and two-particle interactions. Then we start in chapter 4 to set up

a model for BCPO by analyzing its effective spin model in detail and including the existing DM interactions on bilinear operator level. In the following chapters 5 and 6 we extend this model of BCPO by taking into account the difference in the NNN interaction ($J_2 \neq J_2'$) and decay processes stemming from the DM interactions. In chapter 7 we consider two-triplon interactions and further enhance our model of BCPO with these. Finally, we conclude in chapter 8.

2 Theoretical foundations

Describing and solving strongly correlated electron systems represents a significant segment in the superordinate research field of theoretical solid state physics. One of its key points is developing methods in order to handle complex systems. These theoretical approaches can be divided into two major groups: analytical and numerical approaches. The analytical approaches can be further divided into mathematically exact solutions and analytical approximations. Prominent candidates for mathematically exact solutions in solid state physics are for example the BETHE ansatz [75] for the one-dimensional HEISENBERG and HUBBARD model [76, 77] and the solution of the ISING model, which can be solved exactly in one dimension [9] and in two dimensions with the restriction to zero magnetic field [78]. Besides these specific problems it is possible to solve every bilinear Hamiltonian in one dimension by a FOURIER transform and/or a BOGOLIUBOV transformation [79, 80]. An example for analytical approximations is the random phase approximation (RPA) [81–83]. However, most of the of strongly correlated electron systems are too complex in order to solve them analytically. Therefore, numerical approaches provide the majority of calculation tools in theoretical solid state physics. Of course, for all numerical methods approximations need to be applied in order to solve these complex systems completely numerically, but their essential properties remain unchanged. To name just a few powerful numerical methods, there are the density matrix renormalization group (DMRG) [84], the Variational Monte-Carlo method [85–87] and the Quantum Monte-Carlo method [88].
In this chapter the used methods of this thesis are discussed. The fundamental theoretical technique of this thesis is given by the method of continuous unitary transformations (CUTs), which constitutes a powerful tool to address complex spin systems. The second important method refers to the problem of diagonalizing quadratic bosonic Hamiltonians. In order to deal with the phenomenon of spontaneous quasiparticle decay, its most essential aspects are outlined subsequently. The chapter concludes with a section about the Dzyaloshinskii-Moriya-interaction, which is responsible for spontaneous quasiparticle decay in BCPO.

Parts of this chapter have been published in Physical Review B [89] and in Physical Review Research as regular articles [71].

2.1 Continuous unitary transformations

Methods which are developed in order to solve Hamiltonians containing complicated interactions have the aim to simplify the Hamiltonian without the loss of its properties. With the method of continuous unitary transformations (CUTs) it is possible to derive an effective tractable Hamiltonian $\mathcal{H}_{\text{eff}}$, which can be solved easily from a complex initial Hamiltonian $\mathcal{H}$ in a controlled manner. Thereby, the starting Hamiltonian $\mathcal{H}$ is simplified step-by-step by applying unitary transformations. It has been proven that it is very useful to derive $\mathcal{H}_{\text{eff}}$ in second quantization in terms of creation and annihilation operators of the elementary excitations seen as quasiparticles [90]. In the case of gapped disordered quantum antiferromagnets, e.g. BCPO, these quasiparticles are often triplons [72]. Terms which change the number of quasiparticles are rotated away [91, 92], or at least some of them depending on the quantity one is interested in [93]. Thus, the ground-state becomes the vacuum of quasiparticles and their dispersion can be taken from the hopping of quasiparticles. In principle, a unitary transformation is a change of basis and can be done in one single step. But it has turned out that it is more appropriate to perform the basis change continuously because this warrants renormalizing properties of the transformation. The processes between states with large energy differences are eliminated first renormalizing the matrix elements of the low-energy states [94].
The basic concept of CUTs was established by Wegner [95] and by Glazek and Wilson [96, 97]. Instead of using a single unitary transformation to simplify the initial Hamiltonian $\mathcal{H}$ we use several continuous unitary transformations

$$\mathcal{H}(l) = U(l)\,\mathcal{H}U^{\dagger}(l)\,, \tag{2.1.1}$$

which are denoted with $U(l)$ and depend on the so-called flow parameter l. For $l = 0$ the relation $U(l=0) = \mathbb{1}$ holds. The flow equation of the Hamiltonian

$$\partial_l \mathcal{H}(l) = [\eta(l), \mathcal{H}(l)] \tag{2.1.2}$$

with the anti-Hermitian generator

$$\eta(l) = (\partial_l U(l))\, U^{\dagger}(l) \tag{2.1.3}$$

outlines the current rate of change of the Hamiltonian $\mathcal{H}(l)$. The flow equation, see eq. (2.1.2), describes a system of coupled differential equations for the prefactors of

the operators, which occur in the Hamiltonian $\mathcal{H}(l)$[1]. In general, an infinite number of differential equations has to be solved which cannot be done completely. Therefore, an appropriate truncation scheme is necessary. With the help of a truncation scheme one can decide whether a term in the Hamiltonian $\mathcal{H}(l)$ has to be considered or neglected so that $\mathcal{H}(l)$ ensures a sufficient good description of the initial Hamiltonian $\mathcal{H}$. There are different types of CUTs existing, which differ in their applied truncation scheme [91, 94, 98, 99]. We make use of the directly evaluated continuous unitary transformation (deepCUT) because it shows strong numerical stability [94]. This method decides whether an operator or a term has to be kept or neglected according to its effect in powers of the expansion parameter x on a chosen target quantity. In our case the target quantity is the dispersion of the triplons [100]. If n describes the order up to which the target quantity should be exact in, all operators and terms, which have an effect on the target quantity in the order $m \leq n$ in x, have to be considered.
Forming the limit $l \to \infty$

$$\mathcal{H}_{\text{eff}} = \lim_{l\to\infty} \mathcal{H}(l) = U(\infty)\,\mathcal{H}U^{\dagger}(\infty) \tag{2.1.4}$$

one receives the effective Hamiltonian, which represents a sufficient good description of the initial Hamiltonian $\mathcal{H}$ and can be analyzed more easily. A CUT denotes a change of basis. This means that observables O have to be transformed into the same basis, which is used to derive the effective Hamiltonian $\mathcal{H}_{\text{eff}}$. The procedure for observables is very similar. One also has to solve the flow equation of the observable

$$\partial_l O(l) = [\eta(l), O(l)] \tag{2.1.5}$$

and receives the effective observable O_{eff} in the limit $l \to \infty$ as well.
The choice of the generator $\eta(l)$ is crucial. It determines the flow of the Hamiltonian $\mathcal{H}(l)$ and has to be chosen with respect to the target quantity. For our target quantity, namely the dispersion, we use the 1n generator [93], which reads

$$\eta_{1\text{n}}(l) = \mathcal{H}_0^+(l) + \mathcal{H}_1^+(l) - \mathcal{H}_0^-(l) - \mathcal{H}_1^-(l). \tag{2.1.6}$$

The operators $\mathcal{H}_0^+(l)$ and $\mathcal{H}_1^+(l)$ consist of all terms of $\mathcal{H}(l)$ which create more quasiparticles than they annihilate out of states with zero or at least one quasiparticle. In contrast, the operators $\mathcal{H}_0^-(l)$ and $\mathcal{H}_1^-(l)$ contain all terms of $\mathcal{H}(l)$ which annihilate more quasiparticles than they create. Clearly, the relation $(\mathcal{H}_m^+(l))^{\dagger} = \mathcal{H}_m^-(l)$ holds. As a consequence, the 1n generator in eq. (2.1.6) is anti-Hermitian. This has to be the case

[1] We choose the prefactors of operators in the Hamiltonian $\mathcal{H}(l)$ to be l-dependent and not the operators themselves, see Ref. [94].

in order to ensure that the CUT is a unitary transformation. With the 1n generator it is possible to decouple the subspaces, which contain zero and one quasiparticle, from all other subspaces. Thus, this generator is suitable for computing the ground-state energy and the dispersion [93].
One specific example for the application of CUTs is the spin ladder model [101–104]. As explained in section 1.4, the magnetic structure of BCPO is not given by a single spin ladder but by multiple spin ladders coupled via a weak interladder coupling, see figure 1.3, resulting in a two-dimensional model. In order to provide a solution for two-dimensional spin ladder models, it is reasonable to solve the single spin ladder with a CUT and to apply a mean-field approach in the elementary excitations [100] to include the interladder interactions. This approach results in a Hamiltonian with quadratic terms which needs to be solved. The next section deals with this issue.

2.2 Diagonalization of quadratic bosonic Hamiltonians

Quadratic Hamiltonians can contain terms which break the conservation of the quasiparticle number, for example in the case of superconductivity [105, 106] where the number of electrons, i.e. fermions, is not conserved. Since the triplons in disordered quantum antiferromagnets, e.g. BCPO, are often treated as free bosons in a mean-field approach, we focus on quadratic bosonic Hamiltonians in the following. These Hamiltonians can be solved by a bosonic Bogoliubov transformation [79, 107–109]. To gain a deeper understanding of this transformation we first discuss a general ansatz with which all kinds of quadratic bosonic Hamiltonians can be solved. Afterwards we discuss a frequently occuring special case which we label as the two-mode case [79, 80].

2.2.1 Bosonic Bogoliubov transformation: general ansatz

In this subsection we introduce a general ansatz to diagonalize Hamiltonians consisting of quadratic bosonic operator terms [110]. Therefore, we study the following Hamiltonian

$$\mathcal{H} = \sum_{i,j=1}^{n} A_{ij} a_i^\dagger a_j + \frac{1}{2} \sum_{i,j=1}^{n} \left(B_{ij} a_i^\dagger a_j^\dagger + B_{ij}^* a_j a_i \right) \tag{2.2.7}$$

with the operators $a_i^\dagger$ and a_j obeying bosonic algebra

$$\left[a_j, a_i^\dagger \right] = \delta_{ij} \tag{2.2.8}$$

and the prefactors $A_{ij}, B_{ij} \in \mathbb{C}$. Since the Hamiltonian $\mathcal{H}$ has to be Hermitian, the matrix A, including the entries A_{ij}, fulfills the condition $A^\dagger = A$. The matrix B, including the entries B_{ij}, fulfills the condition $B^{\mathrm{T}} = B$ because the operators $a_i^\dagger$ and a_j obey bosonic algebra. By defining the column vector

$$\boldsymbol{\alpha} = \left(a_1, ..., a_n, a_1^\dagger, ..., a_n^\dagger\right)^{\mathrm{T}} \tag{2.2.9}$$

with $2n$ entries, containing all bosonic creation and annihilation operators, the commutation relation in eq. (2.2.8) takes the compact form

$$\left[\boldsymbol{\alpha}, \boldsymbol{\alpha}^\dagger\right] = \eta, \tag{2.2.10}$$

where the $2n \times 2n$ matrix

$$\eta = \begin{pmatrix} \mathbb{1}_{n\times n} & 0_{n\times n} \\ 0_{n\times n} & -\mathbb{1}_{n\times n} \end{pmatrix} \tag{2.2.11}$$

is introduced. Using the notation of the column vector $\boldsymbol{\alpha}$ and the corresponding row vector $\boldsymbol{\alpha}^\dagger = \left(a_1^\dagger, ..., a_n^\dagger, a_1, ..., a_n\right)$ the Hamiltonian in eq. (2.2.7) can be rewritten to

$$\mathcal{H} = \frac{1}{2}\boldsymbol{\alpha}^\dagger M \boldsymbol{\alpha} - \frac{1}{2}\mathrm{Tr}\left(A\right). \tag{2.2.12}$$

The matrix M has $2n \times 2n$ entries

$$M = \begin{pmatrix} A & B \\ B^* & A^* \end{pmatrix} \tag{2.2.13}$$

and is Hermitian, i.e. $M^\dagger = M$ holds. Diagonalizing the Hamiltonian $\mathcal{H}$ is equivalent to finding a canonical transformation K defining new quasiparticle operators $b_i^\dagger$ and b_j, which are represented by a linear combination of the bosonic creation and annihilation operators $a_i^\dagger$ and a_j. The mathematical expression

$$\boldsymbol{\beta} = K\boldsymbol{\alpha} \tag{2.2.14}$$

characterizes this relation. As an analogy to the column vector $\boldsymbol{\alpha}$, the new quasiparticle operators describe the entries of the column vector

$$\boldsymbol{\beta} = \left(b_1, ..., b_n, b_1^\dagger, ..., b_n^\dagger\right)^{\mathrm{T}} \tag{2.2.15}$$

and of the row vector $\boldsymbol{\beta}^\dagger = \left(b_1^\dagger, ..., b_n^\dagger, b_1, ..., b_n\right)$. The new quasiparticle operators $b_i^\dagger$ and b_j are expected to obey the bosonic commutation relation as well. A short calculation

$$\left[\boldsymbol{\beta}, \boldsymbol{\beta}^{\dagger}\right] = \left[K\boldsymbol{\alpha}, \boldsymbol{\alpha}^{\dagger}K^{\dagger}\right] \tag{2.2.16a}$$

$$= K\left[\boldsymbol{\alpha}, \boldsymbol{\alpha}^{\dagger}\right]K^{\dagger} \tag{2.2.16b}$$

$$= K\eta K^{\dagger} \tag{2.2.16c}$$

$$\stackrel{!}{=} \eta \tag{2.2.16d}$$

yields the relation

$$\eta = K^{\dagger}\eta K, \tag{2.2.17}$$

which is equivalent to

$$K^{-1} = \eta K^{\dagger}\eta \tag{2.2.18}$$

for the canonical transformation matrix K. Writing the Hamiltonian in terms of the new quasiparticles results in

$$\mathcal{H} = \frac{1}{2}\boldsymbol{\beta}^{\dagger}\eta K\eta M K^{-1}\boldsymbol{\beta} - \frac{1}{2}\mathrm{Tr}\left(A\right). \tag{2.2.19}$$

If K is the matrix, which diagonalizes the matrix ηM into diagonal form[2]

$$K\eta M K^{-1} = \Omega \tag{2.2.20}$$

with the $2n \times 2n$ diagonal matrix Ω, the Hamiltonian shows

$$\mathcal{H} = \frac{1}{2}\boldsymbol{\beta}^{\dagger}\eta\Omega\boldsymbol{\beta} - \frac{1}{2}\mathrm{Tr}\left(A\right). \tag{2.2.21}$$

It can be proven that the matrix Ω has in general the block structure

$$\Omega = \begin{pmatrix} \omega & 0 \\ 0 & -\omega \end{pmatrix} \tag{2.2.22}$$

with the diagonal $n \times n$ matrix $\omega = \mathrm{diag}\left(\omega_1, ..., \omega_n\right)$ containing the eigenvalues $\omega_i \geq 0$ with $i \in \{1, ..., n\}$ of the non-Hermitian matrix ηM [110]. Therefore, the Hamiltonian yields the simple form[3]

$$\mathcal{H} = \mathbf{b}^{\dagger}\omega\mathbf{b} + \frac{1}{2}\mathrm{Tr}\left(\omega\right) - \frac{1}{2}\mathrm{Tr}\left(A\right) \tag{2.2.23}$$

and describes a systems of non-interacting bosonic quasiparticles.
The main point in this calculation is finding the canonical transformation K, which

[2]Therefore the eigenvectors of the matrix ηM are the column vectors of the matrix K^{-1}.

[3]In this notation the relations $\mathbf{b} = \left(b_1, ..., b_n\right)^{\mathrm{T}}$ and $\mathbf{b}^{\dagger} = \left(b_1^{\dagger}, ..., b_n^{\dagger}\right)$ hold.

describes the mapping between the different bosonic operators, see eq. (2.2.14). Thereto, the matrix ηM has to be diagonalized, i.e. the eigenvalue problem

$$\eta M \mathbf{V}^i = \omega_i \mathbf{V}^i, \quad i \in \{1, ..., 2n\} \tag{2.2.24}$$

with the eigenvector $\mathbf{V}^i$ belonging to the eigenvalue ω_i has to be solved. It is important to emphasize that the matrix ηM is non-Hermitian and therefore its eigenvalues do not have to be real in general. At the end of this section we will point out that the matrix ηM is self-adjoint with respect to the "symplectic product". Finally, this fact ensures that the eigenvalues of ηM are truly real. As a consequence, the $2n$ eigenvalues of the non-Hermitian matrix ηM occur in pairs of $(\pm\omega_1, ..., \pm\omega_n)$ with $\omega_i \in \mathbb{R}$, i.e. to every positive eigenvalue the negative counterpart comes up [110].
In contrast to an analytical solution of the eigenvalue problem in eq. (2.2.24), a numerical approach needs more attention when determining the eigenvectors $\mathbf{V}^i$. In numerical computations of eigenvectors the norm of the eigenvectors is set to be equal to 1[4]. Since the entries of the eigenvectors $\mathbf{V}^i$ describe a mapping between two different types of bosonic operators, see eq. (2.2.14), they have to fulfill a specific normalization, which will be re-derived in the following [110].

Therefore, we start by establishing a link between the eigenvectors concerning the eigenvalues $\pm\omega_i$. Derived in Ref. [110] we finde the following statement:
If $\mathbf{V}^i = \begin{pmatrix} \mathbf{X}^i \\ \mathbf{Y}^i \end{pmatrix}$ is an eigenvector of the matrix ηM belonging to the eigenvalue ω_i, then $\mathbf{W}^i = \gamma \left(\mathbf{V}^i\right)^* = \begin{pmatrix} \left(\mathbf{Y}^i\right)^* \\ \left(\mathbf{X}^i\right)^* \end{pmatrix}$ is an eigenvector of the eigenvalue $-\omega_i$.
The vectors $\mathbf{X}^i$ and $\mathbf{Y}^i$ are column vectors with n complex entries each. The matrix γ is a $2n \times 2n$ matrix and given by

$$\gamma = \begin{pmatrix} 0_{n\times n} & \mathbb{1}_{n\times n} \\ \mathbb{1}_{n\times n} & 0_{n\times n} \end{pmatrix}. \tag{2.2.25}$$

To prove this claim we start by multiplying both sides of the original eigenvalue problem, see eq. (2.2.24), with the matrix γ from the left and set up the complexly conjugated expression, which results in

$$\gamma \eta M^* \left(\mathbf{V}^i\right)^* = \omega_i \gamma \left(\mathbf{V}^i\right)^*. \tag{2.2.26}$$

[4]With the expression "norm" the EUCLIDEAN norm is meant.

A short calculation of the expression $\gamma\eta M^*$ shows

$$\gamma\eta M^* = \begin{pmatrix} 0 & \mathbb{1} \\ \mathbb{1} & 0 \end{pmatrix} \begin{pmatrix} \mathbb{1} & 0 \\ 0 & -\mathbb{1} \end{pmatrix} \begin{pmatrix} A^* & B^* \\ B & A \end{pmatrix} \tag{2.2.27a}$$

$$= \begin{pmatrix} -B & -A \\ A^* & B^* \end{pmatrix} \tag{2.2.27b}$$

$$= -\begin{pmatrix} B & A \\ -A^* & -B^* \end{pmatrix} \tag{2.2.27c}$$

$$= -\begin{pmatrix} \mathbb{1} & 0 \\ 0 & -\mathbb{1} \end{pmatrix} \begin{pmatrix} B & A \\ A^* & B^* \end{pmatrix} \tag{2.2.27d}$$

$$= -\begin{pmatrix} \mathbb{1} & 0 \\ 0 & -\mathbb{1} \end{pmatrix} \begin{pmatrix} A & B \\ B^* & A^* \end{pmatrix} \begin{pmatrix} 0 & \mathbb{1} \\ \mathbb{1} & 0 \end{pmatrix} \tag{2.2.27e}$$

$$= -\eta M \gamma. \tag{2.2.27f}$$

Using this relation for eq. (2.2.26) we see that

$$\eta M \gamma \left(\mathbf{V}^i\right)^* = -\omega_i \gamma \left(\mathbf{V}^i\right)^*. \tag{2.2.28}$$

holds. We identify the expression $\gamma \left(\mathbf{V}^i\right)^*$ to be an eigenvector to the eigenvalue $-\omega_i$. Using this relation we can set up the matrix K^{-1} easily, since K^{-1} is specifically chosen to diagonalize the non-Hermitian matrix ηM. As a consequence the matrix K^{-1} consists of the eigenvectors $\mathbf{V}^i$ and $\mathbf{W}^i$,

$$K^{-1} = \left(\mathbf{V}^1, ..., \mathbf{V}^n, \mathbf{W}^1, ..., \mathbf{W}^n\right) = \begin{pmatrix} \mathbf{X}^1, ..., \mathbf{X}^n, \left(\mathbf{Y}^1\right)^*, ..., \left(\mathbf{Y}^n\right)^* \\ \mathbf{Y}^1, ..., \mathbf{Y}^n, \left(\mathbf{X}^1\right)^*, ..., \left(\mathbf{X}^n\right)^* \end{pmatrix}, \tag{2.2.29}$$

which belong to the eigenvalues $\pm\omega_i$ of the matrix ηM.
To calculate the matrix K, which characterizes the mapping between the bosonic operators $a_i^\dagger$ and a_j and the new quasiparticle operators $b_i^\dagger$ and b_j, we use the relation derived in eq. (2.2.18) and get

$$K = \eta \left(K^{-1}\right)^\dagger \eta. \tag{2.2.30}$$

Note that we derived this equation by requiring that the new quasiparticle operators $b_j^\dagger$ and b_i fulfill bosonic algebra, i.e.

$$\left[b_i, b_j^\dagger\right] = \delta_{i,j}, \quad [b_i, b_j] = 0 \quad \text{and} \quad \left[b_i^\dagger, b_j^\dagger\right] = 0. \tag{2.2.31}$$

Starting with eq. (2.2.30) and using the expression for K^{-1} from eq. (2.2.29) yields

$$K = \eta \left(K^{-1}\right)^\dagger \eta \tag{2.2.32a}$$

$$= \begin{pmatrix} \mathbb{1} & 0 \\ 0 & -\mathbb{1} \end{pmatrix} \begin{pmatrix} (\mathbf{X}^1)^\dagger & , & (\mathbf{Y}^1)^\dagger \\ \vdots & , & \vdots \\ (\mathbf{X}^n)^\dagger & , & (\mathbf{Y}^n)^\dagger \\ (\mathbf{Y}^1)^{\mathrm{T}} & , & (\mathbf{X}^1)^{\mathrm{T}} \\ \vdots & , & \vdots \\ (\mathbf{Y}^n)^{\mathrm{T}} & , & (\mathbf{X}^n)^{\mathrm{T}} \end{pmatrix} \begin{pmatrix} \mathbb{1} & 0 \\ 0 & -\mathbb{1} \end{pmatrix} \tag{2.2.32b}$$

$$= \begin{pmatrix} (\mathbf{X}^1)^\dagger & , & -(\mathbf{Y}^1)^\dagger \\ \vdots & , & \vdots \\ (\mathbf{X}^n)^\dagger & , & -(\mathbf{Y}^n)^\dagger \\ -(\mathbf{Y}^1)^{\mathrm{T}} & , & (\mathbf{X}^1)^{\mathrm{T}} \\ \vdots & , & \vdots \\ -(\mathbf{Y}^1)^{\mathrm{T}} & , & (\mathbf{X}^n)^{\mathrm{T}} \end{pmatrix} \tag{2.2.32c}$$

and, thus, an expression for the matrix K. Then, the mapping between the bosonic operators, see eq. (2.2.14), is described by

$$\begin{pmatrix} b_1 \\ \vdots \\ b_n \\ b_1^\dagger \\ \vdots \\ b_n^\dagger \end{pmatrix} = \begin{pmatrix} (\mathbf{X}^1)^\dagger & , & -(\mathbf{Y}^1)^\dagger \\ \vdots & , & \vdots \\ (\mathbf{X}^n)^\dagger & , & -(\mathbf{Y}^n)^\dagger \\ -(\mathbf{Y}^1)^{\mathrm{T}} & , & (\mathbf{X}^1)^{\mathrm{T}} \\ \vdots & , & \vdots \\ -(\mathbf{Y}^1)^{\mathrm{T}} & , & (\mathbf{X}^n)^{\mathrm{T}} \end{pmatrix} \begin{pmatrix} a_1 \\ \vdots \\ a_n \\ a_1^\dagger \\ \vdots \\ a_n^\dagger \end{pmatrix} \tag{2.2.33}$$

resulting in the two important relations

$$b_i = \sum_{j=1}^{n} \left(X_j^i\right)^* a_j - \left(Y_j^i\right)^* a_j^\dagger = \left(\mathbf{V}^i\right)^\dagger \eta \boldsymbol{\alpha} \tag{2.2.34a}$$

$$b_i^\dagger = \sum_{j=1}^{n} X_j^i a_j^\dagger \quad - Y_j^i a_j \quad = \boldsymbol{\alpha}^\dagger \eta \mathbf{V}^i \tag{2.2.34b}$$

with X_j^i $\left(Y_j^i\right)$ being the j-th component of the n-dimensional vector $\mathbf{X}^i$ $(\mathbf{Y}^i)$. Using eqs. (2.2.34) and the bosonic commutator relations, see eq. (2.2.31), sets up the specific normalization of the eigenvectors $\mathbf{V}^i$, which we finally derive in the following.

Utilizing the commutation relation for two annihilation operators yields

$$[b_i, b_j] = b_i b_j - b_j b_i \tag{2.2.35a}$$

$$= \sum_{k=1}^{n} \left(X_k^j\right)^* \left(Y_k^i\right)^* - \left(X_k^i\right)^* \left(Y_k^j\right)^* \tag{2.2.35b}$$

$$\stackrel{!}{=} 0, \tag{2.2.35c}$$

which is equivalent to the condition

$$\left(\mathbf{V}^j\right)^\dagger \eta \mathbf{W}^i = 0, \quad \forall i, j \in \{1, ..., n\}. \tag{2.2.36}$$

Vividly speaking eq. (2.2.36) describes the fact that the eigenvectors $\mathbf{V}^j$ of the positive eigenvalues ω_j are orthogonal to all eigenvectors $\mathbf{W}^i$ belonging to the negative eigenvalues $-\omega_i$ with respect to the matrix η[5]. Taking the commutation relation between bosonic creation and annihilation operators into consideration leads to

$$\left[b_i, b_j^\dagger\right] = b_i b_j^\dagger - b_j^\dagger b_i \tag{2.2.37a}$$

$$= \sum_{k=1}^{n} \left(X_k^i\right)^* X_k^j - \left(Y_k^i\right)^* Y_k^j \tag{2.2.37b}$$

$$\stackrel{!}{=} \delta_{i,j}, \tag{2.2.37c}$$

which is identical to the relation

$$\left(\mathbf{V}^i\right)^\dagger \eta \mathbf{V}^j = \delta_{i,j}. \tag{2.2.38}$$

So the eigenvectors $\mathbf{V}^i$ belonging to the positive eigenvalues ω_i set up an orthonormal basis concerning the product in eq. (2.2.38).
With the help of eq. (2.2.38) it is possible to derive the relation between two eigenvectors $\mathbf{W}^i$ and $\mathbf{W}^j$ belonging to two different negative eigenvalues $-\omega_i$ and $-\omega_j$.

[5]Using the commutation relation $\left[b_i^\dagger, b_j^\dagger\right]$ gives the same result as eq. (2.2.36).

Therefore, we set up the complexly conjugated of eq. (2.2.38) and use $\gamma^2 = \mathbb{1}$

$$\left(\left(\mathbf{V}^i\right)^\dagger\right)^* \eta\gamma\gamma \left(\mathbf{V}^j\right)^* = \left(\left(\mathbf{V}^i\right)^*\right)^\dagger \begin{pmatrix} 0 & 1 \\ -1 & 0 \end{pmatrix} \mathbf{W}^j \tag{2.2.39a}$$

$$= -\left(\left(\mathbf{V}^i\right)^*\right)^\dagger \gamma\eta\mathbf{W}^j \tag{2.2.39b}$$

$$= -\left(\mathbf{W}^i\right)^\dagger \eta\mathbf{W}^j \tag{2.2.39c}$$

$$= \delta_{i,j} \tag{2.2.39d}$$

to obtain the relation

$$\left(\mathbf{W}^i\right)^\dagger \eta\mathbf{W}^j = -\delta_{i,j}. \tag{2.2.40}$$

Summarizing the relations between the different eigenvectors $\mathbf{V}^j$ and $\mathbf{W}^i$, see eqs. (2.2.36), (2.2.38) and (2.2.40), they can be identified as a sort of "generalized scalar product", which has several names such as "quasi-scalar product" or "para-scalar product" in the literature [111–113]. Since eq. (2.2.40) denotes a negative value and a scalar product obeys semi-positivity, we prefer to use the expression "symplectic product" which is the established attribute for a metric with positive and negative values [71].
Furthermore we want to emphasize that the canonical transformation matrix K conserves the symplectic product, see eq. (2.2.17). As previously mentioned in this section, the non-Hermitian matrix ηM is self-adjoint with respect to the symplectic product. To proove this statement we start with the eigenvalue problem, see eq. (2.2.24), and multiply both sides of the equation with $\left(\mathbf{V}^j\right)^\dagger \eta$, which results in

$$\left(\mathbf{V}^j\right)^\dagger M\mathbf{V}^i = \omega_i\delta_{i,j}, \tag{2.2.41}$$

since the eigenvectors $\mathbf{V}^i$ fulfill the algebra of the symplectic product, see eq. (2.2.38), and $\eta^2 = \mathbb{1}$ holds, see eq. (2.2.11). Setting up the hermetically conjugated expression of eq. (2.2.41) and using eq. (2.2.24) yields

$$\left(\mathbf{V}^i\right)^\dagger M^\dagger\mathbf{V}^j = \left(\mathbf{V}^i\right)^\dagger \eta\eta M\mathbf{V}^j \tag{2.2.42a}$$

$$= \left(\mathbf{V}^i\right)^\dagger \eta\mathbf{V}^j\omega_j \tag{2.2.42b}$$

$$= \omega_j\delta_{i,j} \tag{2.2.42c}$$

$$\stackrel{!}{=} \omega_i^*\delta_{i,j}. \tag{2.2.42d}$$

As a consequence, we receive the simple relation

$$\left(\omega_i^* - \omega_j\right)\delta_{i,j} = 0, \tag{2.2.43}$$

which requires the eigenvalues ω_i to be real. Therefore, we conclude this section with the statement that the matrix ηM is self-adjoint with respect to the symplectic product and that its eigenvalues assume real values.

2.2.2 Bosonic BOGOLIUBOV transformation: two-mode case

The previous subsection dealt with Hamiltonians containing terms $a_i^\dagger a_j^\dagger / a_j a_i$, see eq. (2.2.7). A special case of this Hamiltonian is given by

$$\mathcal{H}_{\text{Bogo}} = A\left(a_1^\dagger a_1 + a_2^\dagger a_2\right) + B\left(a_1^\dagger a_2^\dagger + a_2 a_1\right) \tag{2.2.44}$$

with the prefactors $A, B \in \mathbb{R}$, which we label as the two-mode case. This restriction seems like a great simplification, but it turns out that most quadratic bosonic Hamiltonians can be reduced to the appearance of $\mathcal{H}_{\text{Bogo}}$ [79, 80, 100]. To transform this Hamiltonian into a basis with a conserved number of quasiparticles a bosonic BOGOLIUBOV transformation [79, 80]

$$b_1 = \cosh(\vartheta)\, a_1 - \sinh(\vartheta)\, a_2^\dagger \tag{2.2.45a}$$

$$b_2^\dagger = \cosh(\vartheta)\, a_2^\dagger - \sinh(\vartheta)\, a_1 \tag{2.2.45b}$$

can be applied. This transformation superposes the bosonic creation and annihilation operators in order to derive new operators $b_1^{(\dagger)}/b_2^{(\dagger)}$. These new operators fulfill the bosonic algebra as well. Choosing the parameter ϑ to satisfy the condition [22]

$$\tanh(2\vartheta) = -\frac{B}{A} \tag{2.2.46}$$

leads to the particle conserving Hamiltonian

$$\widetilde{\mathcal{H}}_{\text{Bogo}} = \sqrt{A^2 - B^2}\left(b_1^\dagger b_1 + b_2^\dagger b_2 + 1\right) - A. \tag{2.2.47}$$

It is clearly visible that the one-particle dispersion of the new operators is reduced in general. If the relation $B^2 > A^2$ holds, the Hamiltonian $\mathcal{H}_{\text{Bogo}}$, see eq. (2.2.44), does not describe a physical meaningful system since its eigenvalues assume imaginary values. As a consequence, the bosonic BOGOLIUBOV transformation is only valid in the regime $B^2 < A^2$ implying that the quantum fluctuations do not dominate the system. Additionally eq. (2.2.47) shows that a bosonic BOGOLIUBOV transformation decreases the ground-state energy by the amount of $\sqrt{A^2 - B^2} - A < 0$.

2.3 Spontaneous quasiparticle decay

Until now we focused on quadratic bosonic Hamiltonians, which can be solved by a bosonic BOGOLIUBOV transformation. Thereby, bosons are mapped onto new quasiparticles in which basis the bilinear Hamiltonian is diagonalized. So the picture of quasiparticles was preserved, meaning that the new quasiparticles describe the elementary excitations of the system with an infinite lifetime. However, when interaction processes between the HILBERT space of a single particle and the HILBERT space of multiple particles occur, the picture of quasiparticles with an infinite lifetime must be put into proportion [40]. In certain energy regimes it is possible that a single quasiparticle can decay into two or more quasiparticles spontaneously. The expression "spontaneously" means that the quasiparticle decay occurs at zero temperature ($T = 0$) and its origin are quantum fluctuations, not thermal fluctuations [41, 42]. In this section the steps for analyzing spontaneous quasiparticle decay (SQPD) are presented. A concrete model where all steps are applied on follows in chapter 3.

The starting point of our analysis is given by the diagonal Hamiltonian

$$\mathcal{H} = \sum_k \omega_1(k)\, b_k^\dagger b_k, \tag{2.3.48}$$

whereby the bosonic operator $b_k^\dagger$ creates a boson/quasiparticle with momentum k and the operator b_k annihilates one with the same momentum. The Hamiltonian $\mathcal{H}$ conserves momentum and its one-particle dispersion is given by $\omega_1(k)$. The ground-state energy is set to be zero for simplification. Considering states which contain two particles their energy spectrum can be determined by means of the one-particle dispersion. The energies of the two-particle continuum

$$\omega_2(k, q) = \omega_1(q) + \omega_1(k - q) \tag{2.3.49}$$

depend on the total momentum k of the two quasiparticles and the relative momentum q between them [41]. For every fixed total momentum k the relative momentum q can vary from 0 to 2π. For this reason the total momentum fixes only an interval of possible energies instead of a well-defined energy value. Note that eq. (2.3.49) includes no interaction between the two quasiparticles and depends only on the one-particle dispersion. The lower boundary of the two-particle continuum is simply given by

$$\omega_{2,\min}(k) = \min_{q\in[0,2\pi)} \omega_2(k, q) \tag{2.3.50}$$

and the upper boundary of the two-particle continuum can be calculated by

$$\omega_{2,\max}(k) = \max_{q\in[0,2\pi)} \omega_2(k,q)\,. \tag{2.3.51}$$

If the one-particle dispersion and the two-particle continuum overlap, it is possible that a single particle with momentum k and energy $\omega_1(k)$ decays into two particles with momentum q and energy $\omega_1(q)$ and momentum $k-q$ and energy $\omega_1(k-q)$. Note that energy and momentum are conserved if $\omega_2(k,q) = \omega_1(k)$ holds.
There are three different scenarios, which can occur, when SQPD is possible [39]:

1.) As soon as SQPD is plausible the one-particle mode terminates. In this case the elementary excitations cease to exist immediately, when the one-particle dispersion enters the two-particle continuum.

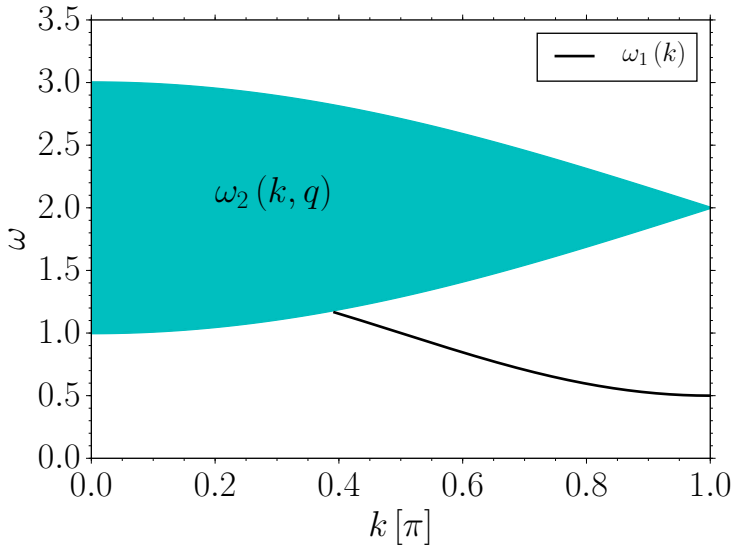

Figure 2.1: Graphic display of the first named SQPD scenario. As soon as the one-particle dispersion $\omega_1(k)$ enters the two-particle continuum $\omega_2(k,q)$, it terminates.

2.) If the one- and two-particle HILBERT space interact with each other, the one-particle dispersion stays inside the two-particle continuum as a resonance, but the lifetime of the elementary excitations becomes finite and the one-particle mode is highly damped.

3.) Another possible scenario, when interactions between the one- and two-particle HILBERT space exist, is that the one-particle dispersion is strongly renormalized in order to avoid an overlap with the two-particle continuum because it is pushed below the lower boundary of the continuum.

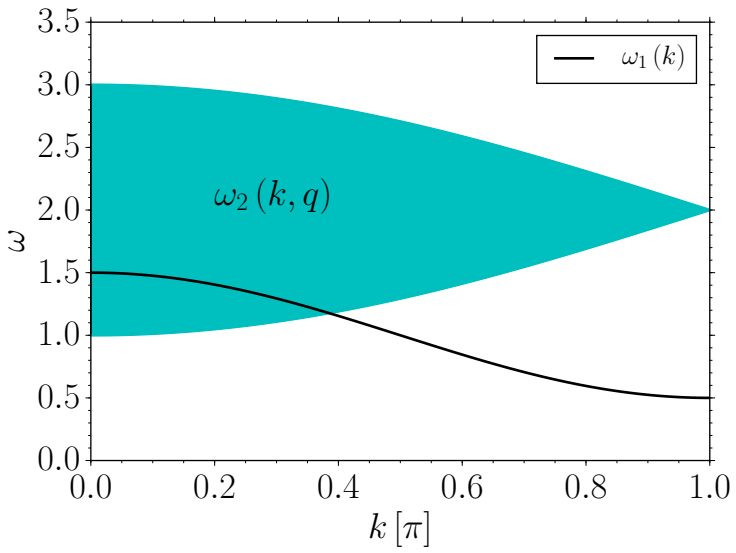

Figure 2.2: Graphic illustration of the second listed SQPD scenario. The one- and two-particle HILBERT space interact with each other and the one-particle dispersion $\omega_1(k)$ stays inside the two-particle continuum $\omega_2(k,q)$ as a resonance.

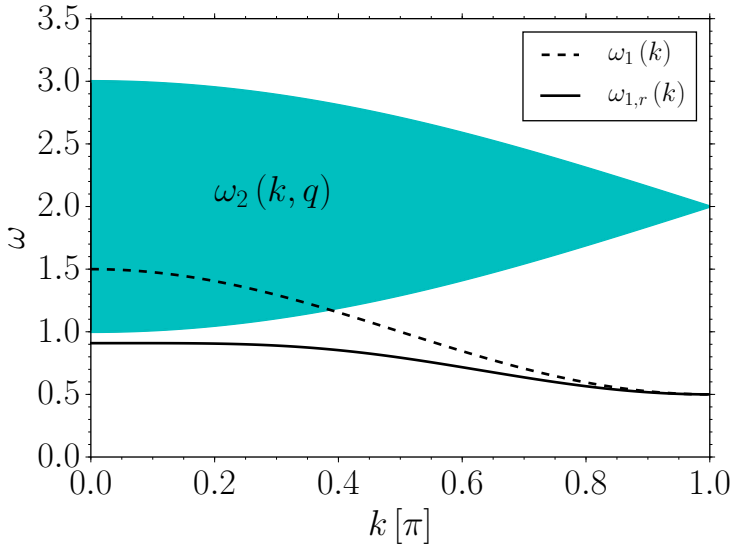

Figure 2.3: Graphic representation of the third mentioned SQPD scenario. The interactions between the one- and two-particle HILBERT space ensure that the one-particle dispersion $\omega_1(k)$ is strongly renormalized. The renormalized one-particle dispersion $\omega_{1,r}(k)$ is pushed below the two-particle continuum $\omega_2(k,q)$ in order to avoid an overlap.

To introduce an interaction between the one- and two-particle HILBERT space we need to take processes into account which describe the transition from a one-particle to a

two-particle state and vice versa. The Hamiltonian

$$\mathcal{H}_{\text{decay}} = \sum_{k,q} \left(\Gamma\left(k,q\right) b_q^\dagger b_{k-q}^\dagger b_k + \text{h.c.} \right) \tag{2.3.52}$$

describes such a process in momentum space. The first part of $\mathcal{H}_{\text{decay}}$ characterizes the decay process of a single particle with momentum k into two particles with momenta q and $k-q$. The amplitude of such a process is given by its prefactor $\Gamma\left(k,q\right)$, which can be a complex number in general. The probability of this process to occur is proportional to $|\Gamma\left(k,q\right)|^2$ according to FERMI's gold rule [114]. The second part of $\mathcal{H}_{\text{decay}}$ describes a fusion process of two particles with momenta q and $k-q$ to a single particle with momentum k. Its probability to happen to also proportional to $|\Gamma\left(k,q\right)|^2$. We see that momentum conservation is fulfilled and that the one-particle dispersion $\omega_1\left(k\right)$ and the two-particle energies $\omega_2\left(k,q\right)$ interact with each other. The resulting Hamiltonian with decay terms reads

$$\mathcal{H}_{\text{full}} = \mathcal{H} + \mathcal{H}_{\text{decay}} = \sum_k \omega_1\left(k\right) b_k^\dagger b_k + \sum_{k,q} \left(\Gamma\left(k,q\right) b_q^\dagger b_{k-q}^\dagger b_k + \text{h.c.} \right) \tag{2.3.53}$$

with the one-particle dispersion $\omega_1\left(k\right)$ and decay/fusion amplitudes $\Gamma\left(k,q\right)$.

2.3.1 Calculation of spectral functions

An appropriate quantity with which SQPD can be demonstrated is the spectral function $A\left(k,\omega\right)$ [36,115]. It depends on the momentum k and energy ω. If normalized to unity, the spectral function can be considered as a probability distribution for finding a single particle with momentum k and energy ω in a system. For a diagonal Hamiltonian in k-space with the one-particle dispersion $\omega_1\left(k\right)$, see eq. (2.3.48), the spectral function is given by a delta-function

$$A_{\text{diag}}\left(k,\omega\right) = \delta\left(\omega - \omega_1\left(k\right)\right), \tag{2.3.54}$$

which is located at the one-particle energy [36,115]. This means concretely that a single particle with momentum k always carries the energy $\omega_1\left(k\right)$. The lifetime of a single particle is given by the inverse of the half-width at half-maximum (HWHM) of peaks in the spectral function. Since a delta-function has zero width per definition the corresponding lifetime of a single particle is infinite in this case. In other words, the single particle cannot decay.

When interaction processes between the one- and two-particle HILBERT space are introduced, see eq. (2.3.53), the situation changes. Now the spectral function is no longer

given by a sharp delta-function but it can be described by a peak with a finite width, e.g. a LORENTZ distribution

$$A_{\text{decay}}(k,\omega) = \frac{\gamma}{\pi\left(\left(\omega - \omega_1(k)\right)^2 + \gamma^2\right)}. \tag{2.3.55}$$

The center of the peak is located at $\omega = \omega_1(k)$ and its HWHM is given by γ[6] [36, 115]. In fact, it is now possible that a single particle with momentum k can have energies which differ from the one-particle energy $\omega_1(k)$. In other words, the picture of a single particle which always carries the momentum k and energy $\omega_1(k)$ loses its significance and the lifetime of a single particle becomes finite

It is important to stress that depending on the context the origin of γ differs. To visualize a single particle with a finite lifetime γ is purely of numerical origin and can be chosen arbitrarily close to zero. If spectral functions are calculated numerically and show up peak structures, these are usually approximated by a LORENTZ distribution. In this case, the fitted value of γ describes real physics, i.e. the inverse finite lifetime of a single particle.

Within INS experiments it is possible to receive information about the magnetic structure of an analyzed sample. Since neutrons carry a magnetic momentum, they interact with the spins of the sample. We label the initial momentum of the neutrons with $\vec{q}$ and their initial energy with E. After interacting with the spins of the sample the momentum and energy of the neutrons change, which we denote with $\vec{q}'$ and E'. The intensity of the scattered neutrons is proportional to the dynamic structure factor (DSF) $S^{\alpha\beta}(\vec{k},\omega)$, which depends on the momentum transfer $\vec{k} = \vec{q} - \vec{q}'$ and energy transfer $\hbar\omega = E - E'$ of the scattered neutrons [33, 34]. In theory the DSF is defined as the FOURIER transform of the time- and momentum-dependent spin-spin correlation function

$$S^{\alpha\beta}(\vec{k},\omega) = \frac{1}{2\pi}\int_{-\infty}^{\infty} \mathrm{d}t\, \mathrm{e}^{\mathrm{i}\omega t}\langle S^{\alpha}(-\vec{k},t) S^{\beta}(\vec{k},0)\rangle \tag{2.3.56}$$

with the spin components $\alpha, \beta \in \{x, y, z\}$ [33–35]. For the simplest case, we neglect the spin flavors and fix the direction of the momentum transfer, i.e. we set $\vec{k} := k$. Since we are interested in single particle spectral functions, the DSF reads

$$S(k,\omega) = \frac{1}{2\pi}\int_{-\infty}^{\infty} \mathrm{d}t\, \mathrm{e}^{\mathrm{i}\omega t}\langle b_k(t)\, b_k^{\dagger}(0)\rangle \tag{2.3.57}$$

[6] In this context $\gamma \in \mathbb{R}^+$ is a simple number and not to be confused with the matrix γ, which we introduced in eq. (2.2.25).

with the operators $b_k(0)/b_k^\dagger(t)$ creating/annihilating an excitation with momentum k at time $t' = 0/t' = t$. The fluctuation-dissipation theorem [116]

$$S(k,\omega) = -\frac{1}{\pi}\frac{1}{1-\mathrm{e}^{-\omega/T}}\,\mathrm{Im}\,G^{\mathrm{ret}}(k,\omega) \tag{2.3.58}$$

describes the connection between the DSF, which is measurable in experiments, and the retarded GREEN'S function $G^{\mathrm{ret}}(k,\omega)$, which is accessible in theory, at temperature T. At zero temperature $T = 0$ we receive the simple relation

$$S(k,\omega) = -\frac{1}{\pi}\,\mathrm{Im}\,G^{\mathrm{ret}}(k,\omega)\,. \tag{2.3.59}$$

In general, the retarded GREEN'S function describes the response of a system to a perturbation [36, 117, 118]. In our case, the perturbation is represented by a neutron which generates an excitation in the analyzed sample using INS experiments. The processes of SQPD can modify the response of the sample to this specific perturbation, i.e. the one-particle dispersion. There are several representations of the retarded GREEN'S function and methods of calculation. In our case, we use the resolvent representation [118]. Its starting point is given by the following expression[7]

$$G^{\mathrm{ret}}(k,\omega) = \langle u_0(k)|\,\frac{1}{\omega-\mathcal{H}_{\mathrm{full}}}\,|u_0(k)\rangle = [\omega\mathbb{1}-\mathcal{H}_{\mathrm{full}}(k)]^{-1}_{00} \tag{2.3.60}$$

which states the 00-element of the inverse matrix $[\omega\mathbb{1}-\mathcal{H}_{\mathrm{full}}(k)]^{-1}$, whereby $\mathcal{H}_{\mathrm{full}}(k)$ is the Hamiltonian $\mathcal{H}_{\mathrm{full}}$ for fixed total momentum k and a ground-state energy shifted to zero, see eq. (2.3.53). The state $|u_0(k)\rangle$ is a one-particle state with fixed momentum k. Using the LANCZOS tridiagonalization [119], see Appendix A, the retarded GREEN'S function from eq. (2.3.60) can be expressed by a continued fraction [118]

$$G^{\mathrm{ret}}(k,\omega) = \cfrac{1}{\omega - a_0(k) - \cfrac{b_1^2(k)}{\omega - a_1(k) - \cfrac{b_2^2(k)}{\omega - a_2(k) - \cdots}}} \tag{2.3.61}$$

consisting of the real, momentum-dependent LANCZOS coefficients $a_i(k)$ and $b_i(k)$.
By introducing the self-energy [115]

$$\Sigma(k,\omega) = \cfrac{b_1^2(k)}{\omega - a_1(k) - \cfrac{b_2^2(k)}{\omega - a_2(k) - \cdots}} \tag{2.3.62}$$

[7] Note that this expression of the retarded GREEN'S function implies zero temperature $T = 0$.

the retarded GREEN'S function can be rewritten as

$$G^{\mathrm{ret}}(k,\omega) = \frac{1}{\omega - \omega_1(k) - \Sigma(k,\omega)}, \tag{2.3.63}$$

whereby the one-particle dispersion $\omega_1(k)$ is identical to the expression for $a_0(k)$, see eq. (A.4a) in Appendix A. The relation between the retarded GREEN'S function and the spectral function is rather simple[8]

$$A(k,\omega) = -\frac{1}{\pi}\,\mathrm{Im}\,G^{\mathrm{ret}}(k,\omega) \tag{2.3.64}$$

whereby the spectral function fulfills the relation

$$\int_{-\infty}^{\infty} A(k,\omega)\,\mathrm{d}\omega = 1, \tag{2.3.65}$$

which is known as the sum rule [36]. Considering the spectral function as a probability distribution as explained before the sum rule becomes clear quickly.

2.3.2 Calculating spectral functions outside the two-particle continuum

Inside the two-particle continuum, where SQPD is possible, the self-energy $\Sigma(k,\omega)$ holds a real and an imaginary part, see Appendix A. Therefore the spectral function assumes non-zero values only inside the two-particle continuum. Outside of the continuum its value is zero per definition. This statement has to be put into concrete terms and needs further explanation. In general, a pole in the real part of the retarded GREEN'S function corresponds to a peak in its imaginary part. Outside of the two-particle continuum these poles are equivalent to delta-functions in the imaginary part of the retarded GREEN'S function, i.e. the spectral function, see eq. (2.3.64). These delta-functions describe so-called quasiparticle peaks. To determine the position of possible quasiparticle peaks one has to identify the values of ω, which fulfill the DYSON equation [120]

$$\left(G^{\mathrm{ret}}(k,\omega)\right)^{-1} = f(\omega) = \omega - \omega_1(k) - \mathrm{Re}\,\Sigma(k,\omega) = 0. \tag{2.3.66}$$

[8] Compared with eq. (2.3.59) we see that the DSF and the spectral function are identical within our applied approximations.

As already mentioned, one has to find the poles of the retarded GREEN'S function outside of the two-particle continuum, which we call $\omega_{1,r}(k)$[9]. The values of $\omega_{1,r}(k)$ define the renormalized one-particle dispersion due to the influence of decay processes[10].
To gain the spectral weight of the quasiparticle peaks a TAYLOR expansion [121] up to the first order in ω around its roots $\omega_{1,r}(k)$

$$\begin{aligned} f(\omega;\omega_{1,r}(k)) &= \underbrace{f(\omega_{1,r}(k))}_{=0} + \underbrace{f'(\omega_{1,r}(k))}_{=:s}(\omega-\omega_{1,r}(k)) + \mathcal{O}\left((\omega-\omega_{1,r}(k))^2\right) \\ &= s(\omega-\omega_{1,r}(k)) + \mathcal{O}\left((\omega-\omega_{1,r}(k))^2\right) \end{aligned} \tag{2.3.67a}$$

has to be performed[11]. To receive the spectral function outside of the two-particle continuum near $\omega_{1,r}(k)$ we use a standard proceeding in calculating retarded GREEN'S functions by shifting the energy ω into the complex plane by a small real parameter δ reading

$$G^{\mathrm{ret}}(k,\omega)|_{\omega\approx\omega_{1,r}(k)} = \lim_{\delta\to 0^+} G^{\mathrm{ret}}(k,\omega+\mathrm{i}\delta)|_{\omega\approx\omega_{1,r}(k)} \tag{2.3.68a}$$

$$= \lim_{\delta\to 0^+} \frac{1}{s(\omega+\mathrm{i}\delta-\omega_{1,r}(k)) + \underbrace{\mathcal{O}\left((\omega-\omega_{1,r}(k))^2\right)}_{\approx 0 \text{ for } \omega\approx\omega_{1,r}(k)}} \tag{2.3.68b}$$

$$= \frac{1}{s}\lim_{\delta\to 0^+} \frac{1}{(\omega-\omega_{1,r}(k))+\mathrm{i}\delta} \tag{2.3.68c}$$

$$= \frac{1}{s}\mathcal{P}\left(\frac{1}{\omega-\omega_{1,r}(k)}\right) - \frac{\mathrm{i}\pi}{s}\delta(\omega-\omega_{1,r}(k)) \tag{2.3.68d}$$

with the CAUCHY principal value $\mathcal{P}$ [122]. Applying eq. (2.3.64) gives us

$$A(k,\omega) = \frac{1}{s}\delta(\omega-\omega_{1,r}(k)) \tag{2.3.69}$$

[9] Therefore we need an algorithm to determine the poles of a function numerically, which is equivalent to calculating the roots of the denominator of a function. In this thesis we used BRENT'S method, see Appendix C.

[10] Inside of the two-particle continuum one uses the DYSON equation as well to calculate the renormalized one-particle dispersion $\omega_{1,r}(k)$.

[11] To determine derivatives we use the central difference quotient, which is given by $f'(x) = (f(x+h)+f(x-h))/2h$ for a one-dimensional function $f(x)$ depending on a parameter $x\in\mathbb{R}$. If the analyzed function is three-times differentiable, the error of the central difference quotient is smaller than the error of other difference quotients. If this is not the case, then the error is of the same order. We used a step size of $h = 10^{-8}$ for the calculations.

for the spectral function outside of the two-particle continuum. The quantity $1/s$ is called the spectral weight of a quasiparticle. By this the sum rule has to be modified[12]

$$\int_{-\infty}^{\infty} A(k,\omega)\,\mathrm{d}\omega = \frac{1}{s} + \int_{\omega_{2,\min}(k)}^{\omega_{2,\max}(k)} A(k,\omega)\,\mathrm{d}\omega = 1. \tag{2.3.70}$$

2.3.3 Calculating renormalized dispersions and lifetimes

As discussed in sect. 2.3.1 the one-particle dispersion is affected by interactions between the one- and two-particle HILBERT spaces. The so-called renormalized one-particle dispersion $\omega_{1,r}(k)$ corresponds to the solutions of the DYSON equation, see eq. (2.3.66). This relation holds inside and outside of the two-particle continuum. Inside the two-particle continuum the lifetime of the quasiparticles, whose energies are described by the renormalized one-particle dispersion, becomes finite. To determine its value we compare the general expression of the spectral function

$$A(k,\omega) = \frac{-\operatorname{Im}\Sigma(k,\omega)}{\pi\left(\left(\omega-\omega_1(k)-\operatorname{Re}\Sigma(k,\omega)\right)^2+\left(\operatorname{Im}\Sigma(k,\omega)\right)^2\right)} \tag{2.3.71}$$

from eqs. (2.3.64) and (2.3.63) with the LORENTZ distribution from eq. (2.3.55). Note that the imaginary part of the self-energy is negative per definition, see Appendix A, and that this comparison implies the assumption that the self-energy does not depend on the energy ω explicitly, i.e. $\Sigma(k,\omega) = \Sigma(k)$ holds [123]. Therefore, the HWHM of the quasiparticle peaks at the renormalized one-particle dispersion is given by [123]

$$\gamma(k) = -\operatorname{Im}\Sigma\left(k,\omega_{1,r}(k)\right). \tag{2.3.72}$$

The lifetime of the quasiparticles is the inverse of the HWHM $\gamma(k)$ and reads

$$\tau(k) = \frac{1}{\gamma(k)} = \frac{1}{-\operatorname{Im}\Sigma\left(k,\omega_{1,r}(k)\right)}. \tag{2.3.73}$$

Vividly speaking this means that the broader the quasiparticle peak, the shorter the lifetime of the quasiparticle is. To visualize the lifetime of quasiparticles in figures it is a standard practice to plot the renormalized one-particle dispersion $\omega_{1,r}(k)$ with error bars, whose half length is equal to the corresponding HWHM. As discussed in sect. 2.3.2 outside of the two-particle continuum quasiparticle peaks are given by delta-functions.

[12] If there is more than one value of ω fulfilling eq. (2.3.66), one has to perform these explained steps for all roots separately. Therefore one adds up all spectral weights $\frac{1}{s_i}$ in eq. (2.3.70).

Since the width of delta-functions is zero, the lifetime of the corresponding quasiparticles is infinite, which means that these quasiparticles are stable and do not decay.

2.4 Dzyaloshinskii-Moriya-interaction

Up to now only the effects of SQPD on the one-particle dispersion have been discussed. In this section the origin of SQPD in BCPO, which is given by the Dzyaloshinskii-Moriya-interaction, is outlined. This interaction has anisotropic character[13]. Theoretical models of materials often neglect the existence of anistropic interactions since their consideration is complicated and they are expected to have only a small influence compared to isotropic interactions [70]. If the symmetry of the crystal structure of the considered material is high enough, anisotropic interactions do not exist. This is the case for crystal structures with only one magnetic ion per unit cell. Therefore, point symmetry exists. In general crystal structures which contain two magnetic ions per unit cell break point symmetry with respect to the middle of both ions and anisotropic interactions assume a finite value[14], see figure 2.4. The main effect of anisotropic interactions is lifting the spin degeneracy of the magnetic excitation modes.

[13] With the expression anisotropic we mean spin anisotropic, i.e. the couplings between the spin flavors x, y and z are not identical.

[14] It is also possible that the two magnetic ions per unit cell are located in such a way that point symmetry concerning the middle of both ions is not broken. In this case no anisotropic interactions exist.

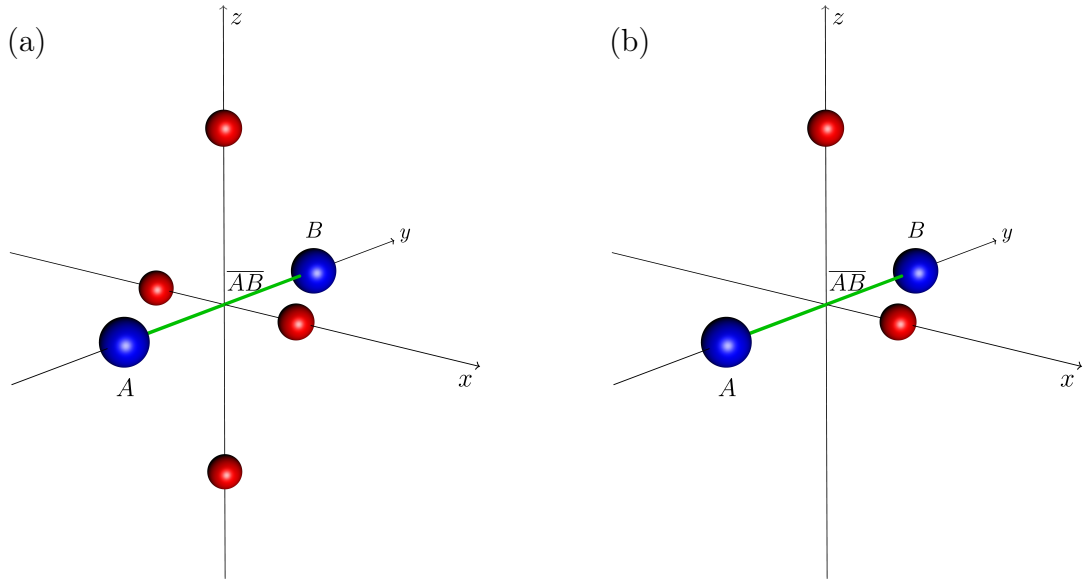

Figure 2.4: (a) Schematic representation of an arrangement of interacting spins, illustrated by blue spheres and labeled with A and B. The connecting line $\overline{AB}$ is highlighted in green. The red spheres depicting other ions in the crystal structure are arranged in such a way that point symmetry with respect to the middle of the connecting line $\overline{AB}$ exists. Therefore, no anisotropic interactions occur.
(b) Similiar arrangement of interacting spins to panel (a). Due to the two missing red spheres compared to panel (a) point symmetry with respect to the middle of the connecting line $\overline{AB}$ is broken. As a consequence, anisotropic interactions can assume a finite value.

2.4.1 Anisotropic interactions

The first who proposed anisotropic interactions was Dzyaloshinskii in 1958 [124]. With the antisymmetric anisotropic interaction

$$\mathcal{H}_{\mathrm{D}} = \mathbf{D} \cdot (\mathbf{S}_1 \times \mathbf{S}_2) \tag{2.4.74}$$

between two spins $\mathbf{S}_1$ and $\mathbf{S}_2$ it was possible to explain the existing weak ferromagnetic momentum of the antiferromagnetic quantum magnet hematite α-Fe_2O_3 on a phenomenological level based on a symmetry analysis [8]. The vector $\mathbf{D}$ in eq. (2.4.74) contains real coefficients. This antisymmetric anisotropic interaction ensures that the two spin $\mathbf{S}_1$ and $\mathbf{S}_2$ in a quantum antiferromagnet tilt instead of arranging antiparallel. Beyond the level of a symmetry analysis, Moriya was able to deduce this interaction by extending the Anderson theory of superexchange [125] by including the spin-orbit coupling [73, 74]. The spin-orbit coupling (SOC) describes a relativistic effect [5] and

becomes important for materials containing ions with a large atomic number[15].
With the help of second order perturbation theory MORIYA received the expression

$$E^{(2)}_{R,R'} = J_{R,R'}\left(\mathbf{S}\left(R\right)\cdot\mathbf{S}\left(R'\right)\right) + \mathbf{D}^{(2)}_{R,R'}\cdot\left(\mathbf{S}\left(R\right)\times\mathbf{S}\left(R'\right)\right) + \mathbf{S}\left(R\right)\cdot\Gamma^{(2)}_{R,R'}\cdot\mathbf{S}\left(R'\right) \quad (2.4.75)$$

for the energy between two spins at the positions R and R'. The first term in eq. (2.4.75) stands for the isotropic HEISENBERG interaction [76] between the two spins with the coupling constant $J_{R,R'}$. The second term describes the antisymmetric anisotropic interaction, see eq. (2.4.74), and the third term characterizes the symmetric anisotropic interaction between the two spins via the tensor $\Gamma^{(2)}_{R,R'}$. The expressions antisymmetric and symmetric refer to the behavior of the terms under exchange the two interacting spins. The antisymmetric anisotropic interaction is called Dzyaloshinskii-Moriya-interaction (DM interaction) and arises in linear order of the SOC. The symmetric anisotropic interaction is of second order in the SOC. In spite of this, it is essential to consider both anisotropic interactions because the symmetric anisotropic interaction is not negligible compared to the DM interaction [126].

2.4.2 Symmetric anisotropic interactions

The components $\Gamma^{\alpha\beta}_{ij}$ of the tensor Γ_{ij} describe the symmetric anisotropic interaction between the two spin components S^{α}_{i} and S^{β}_{j}. We choose the tensor Γ_{ij} to be traceless since any finite trace can be incorporated into the isotropic HEISENBERG interaction $J_{ij}\mathbf{S}_i\mathbf{S}_j$. Additionally the tensor has to be symmetric. The single components $\Gamma^{\alpha\beta}_{ij}$ depend on the corresponding $\mathbf{D}_{ij}$ vectors and HEISENBERG couplings J_{ij}. The relation between these couplings is outlined in this section.
According to SHEKHTMAN *et al.* [126] it is possible to map a Hamiltonian of the type

$$\mathcal{H} = J\mathbf{S}_1\mathbf{S}_2 + \mathbf{D}\cdot\left(\mathbf{S}_1\times\mathbf{S}_2\right) + \mathbf{S}_1\Gamma\mathbf{S}_2 \quad (2.4.76)$$

containing isotropic (J) and anisotropic interactions ($\mathbf{D},\Gamma$), interacting between two spins on site 1 and 2, onto an isotropic system

$$\mathcal{H} = J'\mathbf{S}_1\mathbf{S}'_2 \quad (2.4.77)$$

in a rotated basis. The reason for this is that the anisotropic interactions arise from the SOC, which results in a rotation of the spin hopping from site 1 to site 2. The spin $\mathbf{S}'_2$ represents the spin $\mathbf{S}_2$ in the rotated basis with the corresponding isotropic coupling J'. Without loss of generality, we choose the z-axis as the rotation axis for $\mathbf{S}'_2$. At the end of this calculation we will generalize the direction of the rotation axis. Thus, the relation

[15] In BCPO the bismuth ions with an atomic number of $Z = 83$ are likely to be responsible for the influence of the SOC.

between the spins $\mathbf{S}_2$ and $\mathbf{S}_2'$ is given by

$$\mathbf{S}_2' = \begin{pmatrix} \cos(\varphi) & \sin(\varphi) & 0 \\ -\sin(\varphi) & \cos(\varphi) & 0 \\ 0 & 0 & 1 \end{pmatrix} \mathbf{S}_2 \tag{2.4.78}$$

with φ being the angle of the rotation. Applying the transformation from eq. (2.4.78) on eq. (2.4.77) yields

$$\mathcal{H} = J\mathbf{S}_1\mathbf{S}_2 + J\left(\sqrt{1+\frac{\mathbf{D}^2}{J^2}} - 1\right) S_1^z S_2^z + \mathbf{D}\cdot(\mathbf{S}_1 \times \mathbf{S}_2) \tag{2.4.79}$$

with the abbreviations $J = J'\cos(\varphi)$ and $\mathbf{D} = J'\sin(\varphi)\,\mathbf{e}_z$. It is reasonable to expand the expression $\sqrt{1+\frac{\mathbf{D}^2}{J^2}} = 1 + \frac{\mathbf{D}^2}{2J^2}$ in leading order since it is expected that the absolute value of the vector $\mathbf{D}$ is small compared to the isotropic coupling J. Now we generalize the calculation, i.e. $\mathbf{D}$ does not point into the z-direction anymore but into an arbitrary direction. With this the Hamiltonian yields

$$\mathcal{H} = J\mathbf{S}_1\mathbf{S}_2 + \frac{\mathbf{D}^2}{2J} S_1^{\mathbf{D}} S_2^{\mathbf{D}} + \mathbf{D}\cdot(\mathbf{S}_1 \times \mathbf{S}_2)\,, \tag{2.4.80}$$

whereby the components $S_i^{\mathbf{D}}$ stand for the component of the spin $\mathbf{S}_i$ pointing into the same direction as the vector $\mathbf{D}$ and are given by the projection $S_i^{\mathbf{D}} = \frac{\mathbf{D}\mathbf{S}_i}{\sqrt{\mathbf{D}^2}}$. The anti-symmetric anisotropic term in eq. (2.4.80) has already the correct form, cf. eq. (2.4.76). Splitting the first two terms of eq. (2.4.80) into their components results in

$$\mathcal{H} = \sum_{\alpha,\beta} S_1^\alpha \left(J\delta^{\alpha\beta} + \frac{D^\alpha D^\beta}{2J}\right) S_2^\beta + \mathbf{D}\cdot(\mathbf{S}_1 \times \mathbf{S}_2)\,. \tag{2.4.81}$$

Bearing in mind that the trace of the tensor Γ has to be zero we rewrite eq. (2.4.81) to become

$$\mathcal{H} = \sum_{\alpha,\beta} S_1^\alpha \left(\tilde{J}\delta^{\alpha\beta} + \Gamma^{\alpha\beta}\right) S_2^\beta + \mathbf{D}\cdot(\mathbf{S}_1 \times \mathbf{S}_2) \tag{2.4.82}$$

using the substitutions

$$\tilde{J} = J + \frac{\mathbf{D}^2}{6J}, \tag{2.4.83a}$$

$$\Gamma^{\alpha\beta} = \frac{D^\alpha D^\beta}{2J} - \frac{\delta^{\alpha\beta}\mathbf{D}^2}{6J}. \tag{2.4.83b}$$

Note that the isotropic coupling is now given by $\tilde{J}$ instead of J. Once again we take into account that the absolute value of the vector $\mathbf{D}$ is expected to be small compared to J.

Thus, the approximation $\tilde{J} \approx J$ is valid. Therefore we receive the general expression

$$\Gamma_{ij}^{\alpha\beta} = \frac{D_{ij}^{\alpha} D_{ij}^{\beta}}{2J_{ij}} - \frac{\delta^{\alpha\beta}\mathbf{D}_{ij}^2}{6J_{ij}} \tag{2.4.84}$$

for the components of the tensor Γ_{ij}, which contains only anisotropic interactions, i.e. it has a trace of zero[16].

2.4.3 Selection rules of Moriya

The direction of the vectors $\mathbf{D}_{ij}$ is defined by the present symmetries of the analyzed crystal structure. The five selection rules of Moriya [74] relate the different couplings based on point group symmetries of the crystal structure and provide information concerning the direction of the $\mathbf{D}$ vectors.
Moriya formulated them by considering two interacting ions with spins whose positions are label with A and B. The center of the connecting line $\overline{AB}$ is named C.

1st If C is a center of inversion, then $\mathbf{D} = 0$ holds.

2nd If there is a mirror plane perpendicular to $\overline{AB}$ and passing through C, then $\mathbf{D} \perp \overline{AB}$ is valid.

3rd If a mirror plane including the positions A and B exists, the vector $\mathbf{D}$ is perpendicular to this mirror plane.

4th In the case of a two-fold rotation axis perpendicular to the line $\overline{AB}$ and passing through C, then $\mathbf{D}$ is perpendicular to this two-fold rotation axis.

5th If there is an n-fold axis ($n \geq 2$) passing along $\overline{AB}$, the relation $\mathbf{D} \parallel \overline{AB}$ holds.

If several rules hold true and provide competing statements, then only $\mathbf{D} = 0$ is the correct solution.

[16] There are also other representations of Γ_{ij} in the literature without vanishing trace [39, 70].

3 A toy model for spontaneous quasiparticle decay

Quasiparticles are the concept of choice for describing excitations in quantum magnets with a finite spin gap [36]. These quasiparticles are treated as stable excitations with an infinite lifetime. As discussed in section 2.3 this picture of quasiparticles/elementary excitations has to be reconsidered when interaction processes between the HILBERT space of a single quasiparticle and the HILBERT space of multiple quasiparticles come into play [40]. In this case the possibility of a single quasiparticle decaying into two or more quasiparticles spontaneously is given. As a reminder, the word "spontaneously" implies the fact that the quasiparticle decay takes place at zero temperature ($T = 0$). For this reason quantum fluctuations and not thermal fluctuations are responsible for spontaneous quasiparticle decay (SQPD).
In this chapter a toy model is discussed, for which the individual steps to analyze SQPD, see section 2.3, are performed. As an appropriate toy model we use a simple one-dimensional bosonic model with hopping elements. In spite of this simplicity a realistic spin S=½ HEISENBERG ladder with a finite spin gap Δ can be mapped onto such a one-dimensional model [93, 123].

In the limit of decoupled dimers the ground-state of a spin S=½ HEISENBERG ladder [101–104] with antiferromagnetic couplings is given by the product state of spin S=0 singlets on each rung. The elementary excitation of a single S=0 singlet is a S=1 quasiparticle, which is called triplon [72]. In the absence of external magnetic fields or any intrinsic anisotropies the triplons are threefold degenerate with the polarizations x, y and z, which are referred to as flavors. Triplons on different rungs act like bosons but they also obey the Pauli exclusion principle. As an approximation we treat the triplons as free bosons in a mean-field approach with only one flavor to analyze the fundamental aspects of SQPD in our toy model.

3.1 Influence of bilinear terms

Our one-dimensional toy model with arbitrary hopping terms is given by the Hamiltonian[1]

$$\mathcal{H}_0 = \sum_{i=0}^{N-1} \left(t_0 b_i^\dagger b_i \right) + \sum_{i=0}^{N-1} \sum_{\substack{d=-n, \\ d\neq 0}}^{n} \left(t_d b_i^\dagger b_{i+d} + \text{h.c.} \right), \tag{3.1.1}$$

whereby the bosonic operator $b_i^\dagger$ creates a quasiparticle at site i and b_i annihilates one at the same site. In total there are N sites, which we label by the site index i. The parameter d holds the maximum distance n over which hopping processes are possible. The prefactor t_d describes the hopping amplitude of a boson from site $i+d$ to site i[2]. The probability of a boson hopping from site $i+d$ to site i is proportional to $|t_d|^2$. Additionally we assume periodic boundary conditions, i.e. $b_N = b_0$ holds. This type of translationally invariant Hamiltonians can be solved by a FOURIER transform

$$b_i^\dagger = \frac{1}{\sqrt{N}} \sum_k \mathrm{e}^{-\mathrm{i}kr_i} b_k^\dagger \tag{3.1.2a}$$

$$b_i = \frac{1}{\sqrt{N}} \sum_k \mathrm{e}^{\mathrm{i}kr_i} b_k \tag{3.1.2b}$$

with the bosonic operator $b_k^\dagger$ creating a boson with momentum k and b_k annihilating a boson with momentum k. The momenta are discretized $k = \frac{2\pi m}{N}$ with $m = 0, ..., N-1$. After this transformation the Hamiltonian reads

$$\mathcal{H}_0 = \sum_k \omega_1(k)\, b_k^\dagger b_k \tag{3.1.3}$$

with the one-particle dispersion

$$\omega_1(k) = t_0 + 2\sum_{d=1}^{n} t_d \cos(kd). \tag{3.1.4}$$

The Hamiltonian is momentum conserving due to the translational invariance in real space. In more realistic models pair creation terms such as $b^\dagger b^\dagger$ can occur and break

[1] Note, that we introduce our toy model without any dimensions or global energy scale for reasons of simplicity.

[2] To use realistic values for the parameters t_d we choose values calculated from a deepCUT, which are listed in Appendix B. These values fulfill the condition $t_d = t_{-d}$ because the S=1/2 HEISENBERG ladder is symmetric around its rungs.

particle conservation[3]. We also add this effect to our toy model via the expression

$$\mathcal{H}_{\text{Bogo}} = \sum_{i=0}^{N-1} \sum_{d'=-n'}^{n'} \left(\epsilon_{d'} b_i^\dagger b_{i+d'}^\dagger + \text{h.c.} \right) \tag{3.1.5}$$

with the parameter $\epsilon_{d'}$, whose square value is proportional to the probability that two bosons are created/annihilated at site i and $i + d'$. The index d' characterizes the maximum distance n' between two created/annihilated bosons. To treat $\mathcal{H}_{\text{Bogo}}$ in the same basis as $\mathcal{H}_0$ we also apply a FOURIER transform for the former and receive

$$\mathcal{H}_{\text{Bogo}} = \sum_k \left(\epsilon(k)\, b_k^\dagger b_{-k}^\dagger + \text{h.c.} \right) \tag{3.1.6}$$

with

$$\epsilon(k) = \sum_{d'=-n}^{n} \epsilon_{d'} \cos(k d') \tag{3.1.7}$$

as a result. The operator $\mathcal{H}_{\text{Bogo}}$ is momentum conserving such as $\mathcal{H}_0$. Adding both Hamiltonians shows that the resulting Hamiltonian is not diagonal in momentum space. This problem can be solved by applying a bosonic BOGOLIUBOV transformation [79, 80]

$$\widetilde{b}_k^\dagger = \cosh(\vartheta_k)\, b_k^\dagger - \sinh(\vartheta_k)\, b_{-k} \tag{3.1.8a}$$

$$\widetilde{b}_{-k} = \cosh(\vartheta_k)\, b_{-k} - \sinh(\vartheta_k)\, b_k^\dagger, \tag{3.1.8b}$$

which superposes the bosonic creation and annihilation operators to derive new operators $\widetilde{b}_k^\dagger / \widetilde{b}_k$, which fulfill bosonic algebra as well, see section 2.2.2. Choosing the parameter ϑ_k to satisfy the condition [22]

$$\tanh(2\vartheta_k) = -\frac{2\epsilon(k)}{\omega_1(k)} \tag{3.1.9}$$

the diagonalized Hamiltonian is given by

$$\widetilde{\mathcal{H}} = \sum_k \widetilde{\omega}_1(k)\, \widetilde{b}_k^\dagger \widetilde{b}_k + \Delta E \tag{3.1.10}$$

with the modified one-particle dispersion[4]

$$\widetilde{\omega}_1(k) = \sqrt{(\omega_1(k))^2 - 4(\epsilon(k))^2} \tag{3.1.11}$$

[3] For instance, this scenario becomes real by coupling many single S=1/2 HEISENBERG ladders to gain a two-dimensional model [100].

[4] If $\epsilon(k)$ is complex, the modified one-particle dispersion reads $\sqrt{(\omega_1(k))^2 - 4|\epsilon(k)|^2}$.

and the ground-state energy

$$\Delta E = \frac{1}{2} \sum_{k} \left(\widetilde{\omega}_1 (k) - \omega_1 (k) \right). \tag{3.1.12}$$

As previously mentioned in section 2.2.2, we see clearly that the modified one-particle dispersion $\widetilde{\omega}_1 (k)$ assumes complex values for $4 \left(\epsilon (k) \right)^2 > \left(\omega_1 (k) \right)^2$. This scenario describes a system which is not physically meaningful. Therefore, we confine our toy model to the physically meaningful regime $4 \left(\epsilon (k) \right)^2 < \left(\omega_1 (k) \right)^2$. The BOGOLIUBOV transformation lowers the one-particle dispersion in the whole BRILLOUIN zone and ensures a decrease of the ground-state energy by the amount of ΔE.
To simplify our future calculations we set the prefactors $\epsilon_{d'}$ to be zero except for $d' = 0$, so that the relation

$$\epsilon (k) = \epsilon_0 =: \epsilon \tag{3.1.13}$$

holds.
Considering the existence of two quasiparticles in the system the corresponding two-particle continuum $\widetilde{\omega}_2 (k, q)$, see eq. (2.3.49), is given by[5]

$$\widetilde{\omega}_2 (k, q) = \widetilde{\omega}_1 (q) + \widetilde{\omega}_1 (k - q). \tag{3.1.14}$$

[5]Note, that this expression of the two-particle continuum does not consider interactions between the two particles.

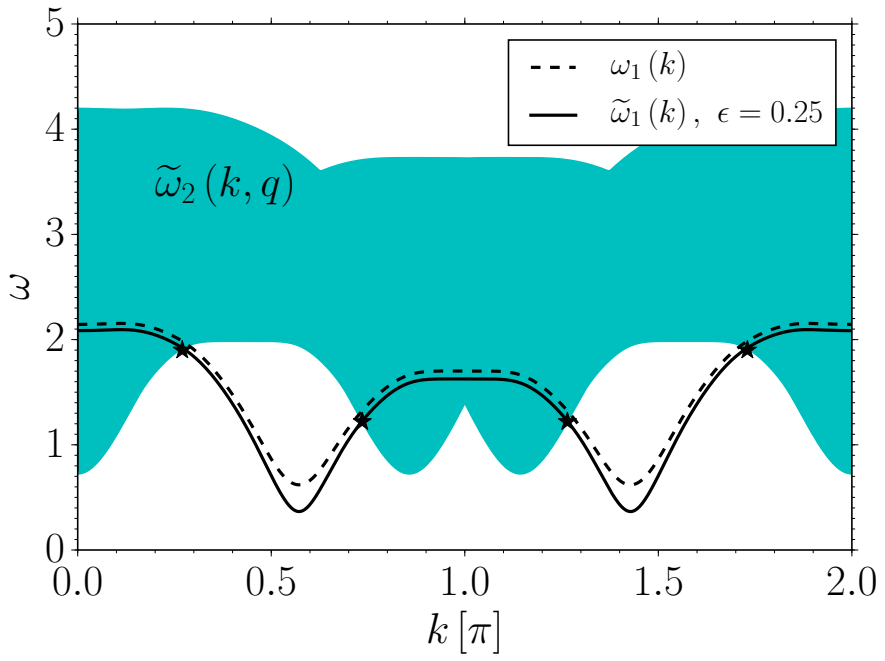

Figure 3.1: Graphic display of the one-particle dispersion $\omega_1(k)$ (eq. (3.1.4)), the modified one-particle dispersion $\widetilde{\omega}_1(k)$ with $\epsilon = 0.25$ (eq. (3.1.11)) and the corresponding two-particle continuum $\widetilde{\omega}_2(k,q)$ (eq. (3.1.14)). The $\star$-symbols mark the points of intersection between $\widetilde{\omega}_1(k)$ and the lower boundary of $\widetilde{\omega}_2(k,q)$. In the intervalls, where the lower boundary of $\widetilde{\omega}_2(k,q)$ is below $\widetilde{\omega}_1(k)$, SQPD is possible.

3.2 Influence of decay terms

To introduce an interaction between the one- and two-particle HILBERT space we need to take processes into account, which describe the decay of one particle into two particles. The expression[6]

$$\mathcal{H}_{\text{decay}} = v \sum_{i=0}^{N-1} \sum_{\delta=-\delta n}^{\delta n} \left(v_\delta b_i^\dagger b_{i+\delta}^\dagger b_{i+\delta} + \text{h.c.} \right) \tag{3.2.15}$$

in real space visualizes such a process[7]. The first summand of $\mathcal{H}_{\text{decay}}$ characterizes the decay of a single particle at site $i+\delta$ into two particles at sites $i+\delta$ and i. The probability of this process is given by $|v \cdot v_\delta|^2$. By contrast, the second summand describes the confluence of two particles on sites i and $i+\delta$ to a single particle on site $i+\delta$. This process happens with the complex conjugated amplitude and same probability.

[6]Note, that eq. (3.2.15) states a specific choice. In general the indices of the operators are given by $(i,j,l) = (i, i+\delta, i+\delta')$. To keep our toy model still simple we use $(i,j,l) = (i, i+\delta, i+\delta)$.

[7]It is important to mention that the distance between the two new created particles δ varies from $-\delta n$ to δn, which can be different from the maximum hopping distance $\pm n$, see eq. (3.1.1). The values of the prefactors v_δ are listed in Appendix B and fulfill the relation $v_\delta = v_{-\delta}$. The variable $v \in \mathbb{R}$ is for tuning the decay terms.

Due to the translation invariance of $\mathcal{H}_{\text{decay}}$ we perform a FOURIER transform yielding

$$\mathcal{H}_{\text{decay}} = \frac{1}{\sqrt{N}} \sum_{k,q} \left(v\left(k,q\right) b_q^\dagger b_{k-q}^\dagger b_k + \text{h.c.} \right) \tag{3.2.16}$$

with

$$v\left(k,q\right) = \frac{v}{2} \left(\sum_{\delta=-\delta n}^{\delta n} v_\delta \cos\left(q\delta\right) + \sum_{\delta=-\delta n}^{\delta n} v_\delta \cos\left(\left(k-q\right)\delta\right) \right). \tag{3.2.17}$$

The first part of the Hamiltonian $\mathcal{H}_{\text{decay}}$ in momentum space characterizes the decay process of a single particle with momentum k into two particles with momenta q and $k-q$ in order to conserve momentum.
We treat the decay processes as a perturbation regarding the solved problem in section 3.1, i.e. we transform $\mathcal{H}_{\text{decay}}$ into the same basis as $\widetilde{\mathcal{H}}$, see eq. (3.1.10), and add both Hamiltonians for further studies. Therefore, we have to apply a BOGOLIUBOV transformation, see eqs. (3.1.8), on the decay/fusion terms of $\mathcal{H}_{\text{decay}}$. As a result, we receive trilinear terms of the form $\widetilde{b}^\dagger\widetilde{b}^\dagger\widetilde{b}^\dagger/\widetilde{b}\widetilde{b}\widetilde{b}$ and $\widetilde{b}^\dagger\widetilde{b}^\dagger b/\widetilde{b}^\dagger\widetilde{b}\widetilde{b}$ and additionally due to normal-ordering linear terms of the form $\widetilde{b}_0^\dagger/\widetilde{b}_0$ at fixed momentum $k=0$. The prefactors of these terms are given by

$$\begin{aligned}
\widetilde{b}_q^\dagger\widetilde{b}_{k-q}^\dagger\widetilde{b}_k \quad : \quad & v\left(k,q\right)\cosh\left(\vartheta_q\right)\cosh\left(\vartheta_{k-q}\right)\cosh\left(\vartheta_k\right) \\
& + v\left(-k+q,q\right)\cosh\left(\vartheta_q\right)\sinh\left(\vartheta_k\right)\sinh\left(\vartheta_{k-q}\right) \\
& + v\left(q,k\right)\sinh\left(\vartheta_k\right)\cosh\left(\vartheta_{k-q}\right)\sinh\left(\vartheta_q\right) \\
& + v\left(q,k\right)\cosh\left(\vartheta_k\right)\sinh\left(\vartheta_{k-q}\right)\cosh\left(\vartheta_q\right) \\
& + v\left(k-q,-q\right)\sinh\left(\vartheta_q\right)\cosh\left(\vartheta_k\right)\cosh\left(\vartheta_{k-q}\right) \\
& + v\left(k,q\right)\sinh\left(\vartheta_q\right)\sinh\left(\vartheta_{k-q}\right)\sinh\left(\vartheta_k\right)
\end{aligned} \tag{3.2.18a}$$

$$\begin{aligned}
\widetilde{b}_q^\dagger\widetilde{b}_{-k-q}^\dagger\widetilde{b}_k^\dagger : \quad & v\left(-k,q\right)\cosh\left(\vartheta_q\right)\cosh\left(\vartheta_{k+q}\right)\sinh\left(\vartheta_k\right) \\
& + v\left(k,-q\right)\sinh\left(\vartheta_q\right)\sinh\left(\vartheta_{k+q}\right)\cosh\left(\vartheta_k\right)
\end{aligned} \tag{3.2.18b}$$

$$\widetilde{b}_0^\dagger \quad : \quad \sum_q \left(2v\left(q,0\right)\sinh^2\left(\vartheta_q\right) + v\left(0,q\right)\sinh\left(\vartheta_q\right)\cosh\left(\vartheta_q\right)\right)\left(\cosh\left(\vartheta_0\right)+\sinh\left(\vartheta_0\right)\right), \tag{3.2.18c}$$

whereby one has to keep in mind the overall scaling factor $\frac{1}{\sqrt{N}}$, see eq. (3.2.16).
By way of reminder, we want to analyze the influence of decay terms which describe an interaction between the one- and two-particle HILBERT space on the one-particle dispersion. Since we are dealing with bosons, the considered HILBERT space has infinite dimension. To perform further studies we restrict ourselves to the one- and two-particle HILBERT space and the interaction between both. We expect the decay/fusion terms

$\widetilde{b}^\dagger\widetilde{b}^\dagger\widetilde{b}/\widetilde{b}^\dagger\widetilde{b}\widetilde{b}$ to have the biggest influence by far since we are considering quasiparticle decay at zero temperature. As a consequence, we only keep terms of the type $\widetilde{b}^\dagger\widetilde{b}^\dagger\widetilde{b}/\widetilde{b}^\dagger\widetilde{b}\widetilde{b}$ in our ongoing discussion and neglect the other terms from eqs. (3.2.18b) and (3.2.18c), which describe quantum fluctuations creating/annihilating one and three particles. The resulting Hamiltonian with decay terms reads

$$\widetilde{\mathcal{H}}_{\text{decay}} = \sum_k \widetilde{\omega}_1(k)\,\widetilde{b}_k^\dagger\widetilde{b}_k + \frac{1}{\sqrt{N}}\sum_{k,q}\left(\widetilde{\Gamma}(k,q)\,\widetilde{b}_q^\dagger\widetilde{b}_{k-q}^\dagger\widetilde{b}_k + \text{h.c.}\right) \tag{3.2.19}$$

with the modified one-particle dispersion $\widetilde{\omega}_1(k)$ from eq. (3.1.11) and $\widetilde{\Gamma}(k,q)$ representing the expression from eq. (3.2.18a).

3.3 Influence of interaction terms

Besides transitions between the one- and two-particle HILBERT space, which we introduced in sect. 3.2, we also discuss two-particle interactions and their effects on the one-particle dispersion $\widetilde{\omega}_1(k)$, see eq. (3.1.11). An attractive two-particle interaction enables the existence of bound states [4,6] and lowers two-particle states energetically. This energy reduction combined with transitions between the one- and two-particle HILBERT space, see sect. 3.2, ensures an increased level repulsion. Finally, this results in a further lowering of the one-particle dispersion $\widetilde{\omega}_1(k)$.

The expression

$$\mathcal{H}_{\text{inter}} = -w\sum_{i=0}^{N-1} n_{i+1}n_i = -w\sum_{i=0}^{N-1} b_{i+1}^\dagger b_i^\dagger b_i b_{i+1} \tag{3.3.20}$$

with $w \in \mathbb{R}^+$ describes such an attractive two-particle interaction process in real space between next-neighbors. The operator $\mathcal{H}_{\text{inter}}$ annihilates two particles at adjacent sites i and $i+1$ and creates two particles at the same sites. The interaction strength is constant and given by $-w < 0$. As $\mathcal{H}_{\text{inter}}$ is translationally invariant, we can perform a FOURIER transform yielding

$$\mathcal{H}_{\text{inter}} = \frac{1}{N}\sum_{k,q,p} w(k,q,p)\,b_p^\dagger b_{k-p}^\dagger b_q b_{k-q} \tag{3.3.21}$$

with

$$w(k,q,p) = -\frac{w}{2}\left(\cos(p-q) + \cos(k-p-q)\right). \tag{3.3.22}$$

In momentum space the Hamiltonian $\mathcal{H}_{\text{inter}}$ characterizes interactions between two-particle states which hold a total momentum k and a relative momentum q and different two-particle states with a total momentum k and relative momentum p. As the relative momenta q and p are independent, $\mathcal{H}_{\text{inter}}$ describes couplings between all possible two-

particle states with a fixed momentum k[8].
Just like in sect. 3.2, the next step would be to transform $\mathcal{H}_{\text{inter}}$ into the same basis as $\widetilde{\mathcal{H}}$, see eq. (3.1.10), and to add it to the Hamiltonian $\widetilde{\mathcal{H}}_{\text{decay}}$, see eq. (3.2.19). To keep the model simple we omit this step and add the interaction Hamiltonian $\mathcal{H}_{\text{inter}}$ to the bilinear and trilinear terms in $\widetilde{\mathcal{H}}_{\text{decay}}$ directly[9]. Therefore we do a direct mapping

$$b_k^\dagger \to \widetilde{b}_k^\dagger \quad b_k \to \widetilde{b}_k \tag{3.3.23}$$

so that we can add the two particle interactions to our toy model right away. Finally, the Hamiltonian of our toy model including decay and two-particle interaction terms is given by

$$\widetilde{\mathcal{H}}_{\text{full}} = \sum_k \widetilde{\omega}_1(k)\, \widetilde{b}_k^\dagger \widetilde{b}_k + \frac{1}{\sqrt{N}} \sum_{k,q} \left(\widetilde{\Gamma}(k,q)\, \widetilde{b}_q^\dagger \widetilde{b}_{k-q}^\dagger \widetilde{b}_k + \text{h.c.} \right) + \frac{1}{N} \sum_{k,q,p} w(k,q,p)\, \widetilde{b}_p^\dagger \widetilde{b}_{k-p}^\dagger \widetilde{b}_q \widetilde{b}_{k-q} \tag{3.3.24}$$

with the modified one-particle dispersion $\widetilde{\omega}_1(k)$ from eq. (3.1.11), $\widetilde{\Gamma}(k,q)$ representing the expression from eq. (3.2.18a) and the term $w(k,q,p)$ describing the interaction between two particles, see eq. (3.3.22).

3.4 Results of the toy model

3.4.1 Analysis of decay terms, $v \neq 0$ and $w = 0$

In this subsection we focus on the effects of SQPD in our toy model neglecting two-particle interactions, see sect. 3.3, i.e. we refer to the Hamiltonian $\widetilde{\mathcal{H}}_{\text{decay}}$, see eq. (3.2.19). The first step to analyze the effects of SQPD in our toy model is the Lanczos tridiagonalization of the Hamiltonian $\widetilde{\mathcal{H}}_{\text{decay}}$, see eq. (3.2.19). The initial state is a single particle state with fixed momentum k, which we name $|k\rangle$. Due to the conservation of the total momentum k a single particle can only decay into two particles with momenta q and $k-q$. We describe these two-particle states via $|q, k-q\rangle$ [127]. So the Hamiltonian $\widetilde{\mathcal{H}}_{\text{decay}}$ can be expressed in the basis constructed by the single particle state $|k\rangle$ and the two-particle states $|q, k-q\rangle$. In figure 3.2 the convergence behavior of the Lanczos coefficients, which is explained in Appendix A, is demonstrated.

[8] In the case $p = q$ the Hamiltonian $\mathcal{H}_{\text{inter}}$ outlines a self-interaction of the corresponding two-particle state.

[9] A stringent application of the Bogoliubov transformation, see eqs. (3.1.8), would lead to additional bilinear terms of the form $\widetilde{b}^\dagger \widetilde{b}^\dagger / \widetilde{b}\widetilde{b}$ and $\widetilde{b}^\dagger \widetilde{b}$, which we would have to include into our model as well.

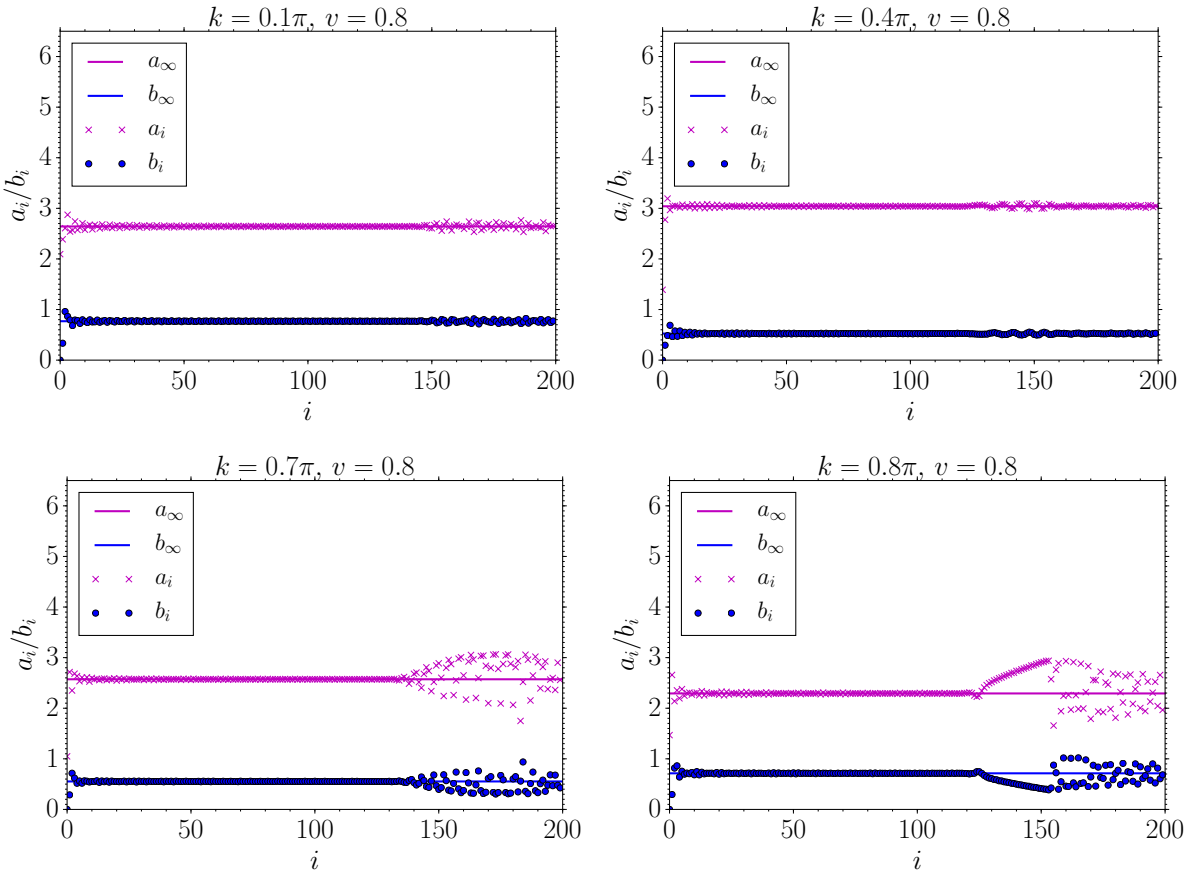

Figure 3.2: Convergence behavior of the LANCZOS coefficients for different k-values of the toy model with parameters $\epsilon = 0.25$, $v = 0.8$ and a discretization of $N = 1000$ in k-space. The index i represents the number of the LANCZOS coefficients. In total 200 LANCZOS steps have been performed.

It is easy to see that the calculated LANCZOS coefficients $a_i(k)$ and $b_i(k)$ show the correct convergence behavior, which is determined by the lower and upper edge of the two-particle continuum $\widetilde{\omega}_2(k, q)$ [128]. The exact expressions of the limiting values $a_\infty(k)$ and $b_\infty(k)$ are listed in Appendix A. Due to the fact that in numeric calculations the discretization N of the k-space is a finite number the LANCZOS coefficients show deviations after they converged towards $a_\infty(k)$ and $b_\infty(k)$. These deviations describe finite size effects [129] and do not have any physical meaning. Therefore, it is necessary to identify the number of LANCZOS steps $n_{\text{Lanczos,max}}$ at which the coefficients reached their limiting values appropriately. The continued fraction describing the resolvent, see eq. (2.3.61), is then performed up to $n_{\text{Lanczos,max}}$ coefficients and then terminated with a suitable terminator [118, 130], see Appendix A. For our toy model we find the index $n_{\text{Lanczos,max}} = 70$ to be an appropriate choice for further calculations[10].

[10]Note, that the concrete value of $n_{\text{Lanczos,max}} = 70$ belongs to the parameters $\epsilon = 0.25$ and $v = 0.8$. If the latter parameters change, it is possible that $n_{\text{Lanczos,max}}$ has be chosen differently.

The next interesting quantity to consider is the spectral function, whose calculation is described in sects. 2.3.1 and 2.3.2.

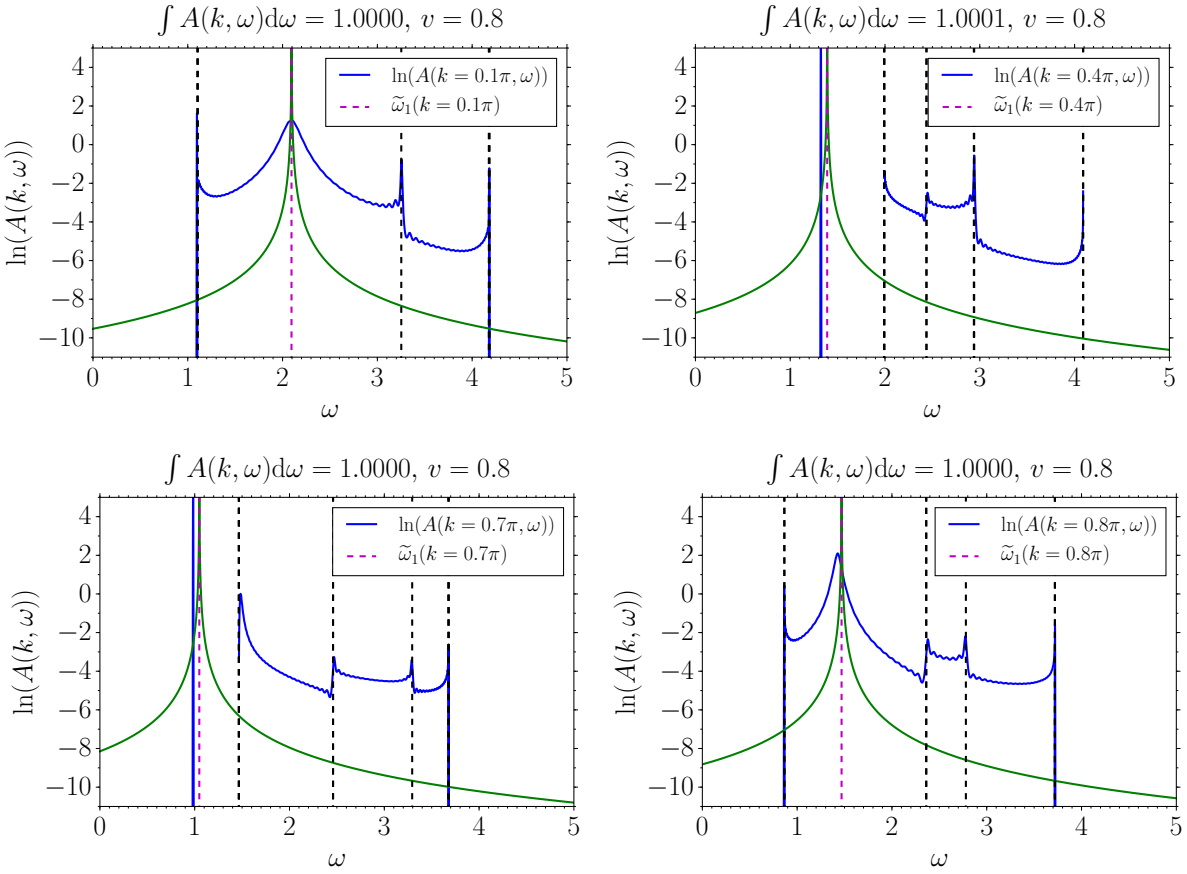

Figure 3.3: Spectral functions $A\,(k,\omega)$ for different k-values of the toy model for the parameters $\epsilon = 0.25$ and $v = 0.8$, which belong to the results in figure 3.2. Note, that the y-axis has a logarithmic scale. The black dashed lines show the positions of the local and global extrema in the two-particle continuum $\widetilde{\omega}_2\,(k,q)$. The green lines illustrate a LORENTZ distribution, see eq. (2.3.55), centered at the one-particle dispersion $\widetilde{\omega}_1\,(k)$ and a HWHM $\gamma = 0.001$. The energy ω is discretized in steps of 0.001.

The presented spectral functions in figure 3.3 illustrate a number of features, which we discuss in the following.

Shape inside the two-particle continuum

It is cleary visible that inside the two-particle continuum the spectral function has a finite value. All its contained peaks hold an intrinsic width, see eq. (2.3.72). At $k = 0.1\pi$ and $k = 0.8\pi$ the one-particle dispersion is located inside the two-particle continuum. At these k-values we notice that the peak at the position of the one-particle dispersion becomes broader compared to the general LORENTZ distribution holding a

HWHM which is identical to the discretization of the energy[11]. This demonstrates that the lifetime of the quasiparticles becomes finite due to the existing decay processes. At $k = 0.8\pi$ a slight shift of the quasiparticle peak to smaller energies can be observed. This effect stems from the level repulsion induced by the hybridization of the one-particle and two-particle HILBERT spaces, see eq. (3.2.19).
Another notable characteristic is the occurence of VAN HOVE singularities [131]. These are visualized by kinks in the spectral function located at the energy values, at which the two-particle continuum holds local extrema. Close to its local extrema the two-particle continuum goes flat, which means that there are many two-particle states with roughly the same energy. This fact becomes visible in the spectral function with spikes at the corresponding energies. All illustrations in figure 3.3 show the existence of VAN HOVE singularities located at the expected energy values.

Limiting behavior of the spectral function

The band edges of a two-particle continuum are determined by their global extrema. The limiting behavior of the spectral function at the band edges and at the already mentioned local extrema of the two-particle continuum depends on the dimension d of the system, namely according to

$$A(k,\omega) \propto |\omega - \omega_c|^{\frac{d}{2}-1}, \tag{3.4.25}$$

whereby ω_c stands for the band edges of the two-particle continuum $\widetilde{\omega}_{2,\max}(k)$ and $\widetilde{\omega}_{2,\min}(k)$ and its local extrema in each case[12] [132]. Since our toy model is one-dimensional, we expect the limiting behavior of the spectral function to be like $\frac{1}{\sqrt{|\omega-\omega_c|}}$. All presented spectral functions in figure 3.3 show this limiting behavior clearly.

Quasiparticle peaks outside the two-particle continuum

As explained in sect. 2.3.2, quasiparticle peaks can occur outside of the two-particle continuum. All displayed k-values in figure 3.3 contain quasiparticle peaks. They are visualized by sharp lines [36]. In the cases where the one-particle dispersion is located outside the two-particle continuum the appearing quasiparticle peaks are slightly shifted to lower energies and hold a large spectral weight of $1/s = 0.95$ for $k = 0.4\pi$ and $1/s = 0.93$ for $k = 0.7\pi$. In addition, further quasiparticle peaks occur like the one at $k = 0.7\pi$, which is located close the upper band edge and has only a small spectral weight of $1/s = 0.0002$. In the cases $k = 0.1\pi$ and $k = 0.8\pi$ quasiparticle peaks with small spectral weight $1/s$ in the order of magnitude of $0.001 - 0.0001$ occur closely to the

[11] In our case we set the HWHM for the general LORENTZ distribution to be $\gamma = 0.001$, see figure 3.3.
[12] For $d = 2$ the exponent in eq. (3.4.25) is zero. This implies a finite jump or a logarithmic singularity.

band edges as well. They are spurious and appear only because of numerical reasons due to the discretization of the energy ω. Thus, they can be neglected for physical interpretation[13].

Fulfilling the sum rule

All illustrations in figure 3.3 show the integral of the spectral function, which has to be equal to one due to the sum rule, see eq. (2.3.70). We can see clearly that the sum rule is fulfilled for all analyzed k-values. For numerical calculations the sum rule is an important issue in order to determine an appropriate discretization of the energy ω. If the energy discretization is chosen too large, this becomes visible in a not fulfilled sum rule, which is notably smaller or larger than one.

To complete the analysis of the toy model we discuss the renormalized dispersion. Its computation is outlined in section 2.3.3.
The results of the renormalized dispersion in figure 3.4 seem questionable and not intuitive. At nearly every momentum k various values of the renormalized dispersion $\omega_{1,r}(k)$ exist. It is also astonishing to find data points with huge errorbars, see the prominent examples at momenta $k \approx 0.5\pi$ and $k \approx 0.6\pi$, which are located near the upper boundary of the two-particle continuum $\widetilde{\omega}_2(k,q)$.

These examples represent the point where theoretically correct formulae and calculations clash with numerics. It is necessary to distinguish whether a numerically correct solution of the DYSON equation, see eq. (2.3.66), represents a solution with a physical meaning or not. In other words: Not every solution stands for the energy of a quasiparticle.
It is a challenge to decide whether a numerically correct value of $\omega_{1,r}(k)$ represents real physics or not. To approach this task one has to introduce additional decision criteria. These criteria classify the calculated solutions of $\omega_{1,r}(k)$ to values with a physical meaning and values which stem from discretization effects. More concretely, we need to introduce specific criteria, which make sure that the values $\omega_{1,r}(k)$ describe a quasiparticle peak in the corresponding spectral function $A(k,\omega)$. Since it is not possible to analyze all spectral functions $A(k,\omega)$ for each momentum k separately, it is necessary to think of a criterion or multiple criteria, which can be applied on the numerical data of the renormalized dispersion.

[13] The structure of the spectral function consists of peaks and kinks, as mentioned before in this subsection. If the discretization of the energy ω is chosen too large, it is possible that the peak structure is not highly resolved, especially close to the quasiparticle peaks. As a consequence, a non-negligible amount of the spectral weight is missing and the sum rule is not fulfilled.

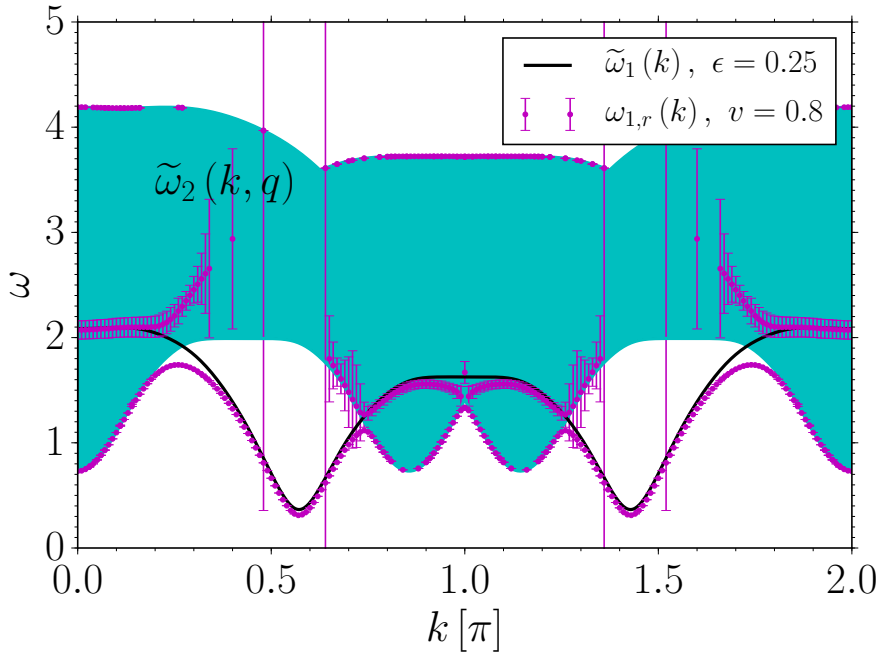

Figure 3.4: Renormalized dispersion $\omega_{1,r}(k)$ of the toy model for the parameters $\epsilon = 0.25$ and $v = 0.8$, which belongs to the results in figures 3.2 and 3.3. In addition, the dispersion $\widetilde{\omega}_1(k)$ is displayed to visualize the effects of SQPD. The graphic shows all solutions of the DYSON equation, see eq. (2.3.66). The size of the errorbars of the renormalized dispersion inside the two-particle continuum $\widetilde{\omega}_2(k,q)$ corresponds to the related HWHM $\gamma(k)$, see eq. (2.3.72).

Similiar to the calculation and representation of the spectral function $A(k,\omega)$ we consider whether the calculated solution of $\omega_{1,r}(k)$ is located inside or outside the two-particle continuum $\widetilde{\omega}_2(k,q)$.

Solutions of the DYSON equation inside the two-particle continuum

Inside the two-particle continuum the spectral function shows peaks with an intrinsic finite width[14], see sect. 2.3.1. The positions of the peaks represent the energies of a quasiparticle or a resonant mode. An associated quantity of these energies is the HWHM γ, see eq. (2.3.72). It is related to the lifetime of the quasiparticles or resonant modes, see sect. 2.3.3. A large HWHM indicates a peak in the spectral function, which is smeared out, and therefore a quasiparticle or resonance with a short lifetime. Since a quasiparticle or resonance has to hold a sufficient long lifetime to be identified as a quasiparticle or resonance, the HWHM is a candidate for an appropriate quantity to differentiate between solutions of the DYSON equation with a purely numerical origin and the solutions which describe real physics. These solutions characterize the energy

[14]In general, sharp peaks inside the two-particle continuum can also derive from binding phenomena.

of a quasiparticle or a resonance. As the width of the two-particle continuum

$$\Delta\widetilde{\omega}_2(k) = \widetilde{\omega}_{2,\max}(k) - \widetilde{\omega}_{2,\min}(k) \tag{3.4.26}$$

varies for each momentum k, considering only the HWHM is not significant enough as a criterion to determine peaks within the spectral function. The key issue is that the HWHM of a peak has to be small compared to the width of the corresponding two-particle continuum. A peak with a large HWHM can still be identified as a peak within an ever boarder two-particle continuum. Therefore, the relative HWHM $\gamma(k)/\Delta\widetilde{\omega}_2(k)$, with $\gamma(k)/\Delta\widetilde{\omega}_2(k) \ll 1$, serves as an appropriate quantity to identify the solutions of the DYSON equation, which characterize the energy of a quasiparticle or resonance.
To explain this issue more closely we compare the results of the spectral function $A(k,\omega)$, see figure 3.3, with the results of the renormalized dispersion $\omega_{1,r}(k)$, see figure 3.4, at the momenta $k = 0.1\pi$ and $k = 0.4\pi$. The spectral function $A(k = 0.1\pi, \omega)$ displays a clear peak near the corresponding one-particle dispersion $\widetilde{\omega}_1(k = 0.1\pi)$. The width of the peak is finite, but small enough compared to the width of the two-particle continuum to identify the peak as a peak. In contrast, the spectral function $A(k = 0.4\pi, \omega)$ does not show a visible peak inside the two-particle continuum. Despite this, figure 3.4 shows at $k = 0.4\pi$ two solutions, one at $\omega \approx 3$ and one near the one-particle dispersion $\widetilde{\omega}_1(k = 0.4\pi)$. The solution inside the two-particle continuum $\widetilde{\omega}_2(k = 0.4\pi, q)$ at $\omega \approx 3$ holds a HWHM of $\gamma \approx 0.86$. This means that the spectral function $A(k = 0.4\pi, \omega)$ has a resonance at $\omega \approx 3$. But no peak can be identified in figure 3.3 since the relative HWHM $\gamma/\Delta\widetilde{\omega}_2 \approx 0.41$ is large. Thus, this corresponding solution of the DYSON equation does not describe the energy of a quasiparticle or another well-defined mode but is of pure numerical nature. At the momentum $k = 0.7\pi$ we obtain similar results, since the DYSON equation holds solutions at $\omega \approx 1$, $\omega \approx 1.5$ and $\omega \approx 3.7$, see figure 3.4. The solution inside the two-particle continuum at $\omega \approx 1.5$ does not display a clear peak in the spectral function $A(k = 0.7\pi, \omega)$, see figure 3.3[15].
To conclude these observations, the relative HWHM states an appropriate quantity to distinguish inside the two-particle continuum whether a solution of the DYSON equation describes the energy of a quasiparticle or a well-defined resonance, which can be identified in the corresponding spectral function with a clear peak or not. Therefore, it is reasonable to display only the solutions with a relative HWHM below a certain threshold $\left(\gamma(k)/\Delta\widetilde{\omega}_2(k)\right)_{\max} \ll 1$. This threshold can be determined by testing different values and analyzing the shape of spectral function in detail.

[15]The other solutions at $\omega \approx 1$ and $\omega \approx 3.7$ are located outside of the two-particle continuum and are discussed in the following.

Solutions of the DYSON equation outside the two-particle continuum

As pointed out in sect. 2.3.2, it is possible that the spectral function holds delta-functions, which are located outside of the two-particle continuum. These delta-functions describe so-called quasiparticle peaks with a certain spectral weight $1/s$ [72]. Since a quasiparticle or a bound state has to possess a sufficient large value of $1/s$ to be identified as a quasiparticle or a bound state, the spectral weight is an appropriate quantity to differentiate between spurious solutions of the DYSON equation resulting from numerical artefacts and true physical solutions, i.e. a quasiparticle or (anti-) bound states.

To outline this issue more precisely we compare the results of the spectral function $A(k,\omega)$, see figure 3.3, and the results of the renormalized dispersion $\omega_{1,r}(k)$, see figure 3.4, once again. The spectral functions $A(k=0.4\pi,\omega)$ and $A(k=0.7\pi,\omega)$ display peaks near the corresponding one-particle dispersion $\widetilde{\omega}_1(k)$. These peaks are located cleary outside of the two-particle continuum. As mentioned before, the spectral weight of these peaks is $1/s = 0.95$ for $k = 0.4\pi$ and $1/s = 0.93$ for $k = 0.7$. For the latter momentum the spectral function shows an additional peak very close to the upper boundary of the two-particle continuum at $\omega \approx 3.7$ with a spectral weight of $1/s = 0.0002$. The calculation of the spectral function $A(k,\omega)$ and thereby the calculation of the renormalized dispersion $\omega_{1,r}(k)$ are sensitive to the discretization of the energy ω. It is a reasonable approach to choose the energy discretization fine enough so that the calculated spectral function $A(k,\omega)$ fulfills the sum rule, see eq. (2.3.70), for every momentum k.

In the case of no SQPD the spectral function is given by a single delta-function. Its spectral weight is $1/s = 1$. This is the maximum value, since in this scenario there is no interaction between the one- and two-particle Hilbert space and the corresponding self-energy $\Sigma(k,\omega)$, see eq. (2.3.62), is zero. For this reason, it is obvious to choose the spectral weight $1/s$ as an additional criterion to distinguish between the spurious peaks outside the two-particle continuum and the physical ones, which describe quasiparticles or (anti-) bound states. Therefore, it is immediately apparent to display only the solutions with a spectral weight $1/s$ greater than a certain threshold $(1/s)_{\min}$. In order to set this threshold we follow the results of the literature [72, 133–135] and also test different values within a simultaneous analysis of the shape of the spectral function.

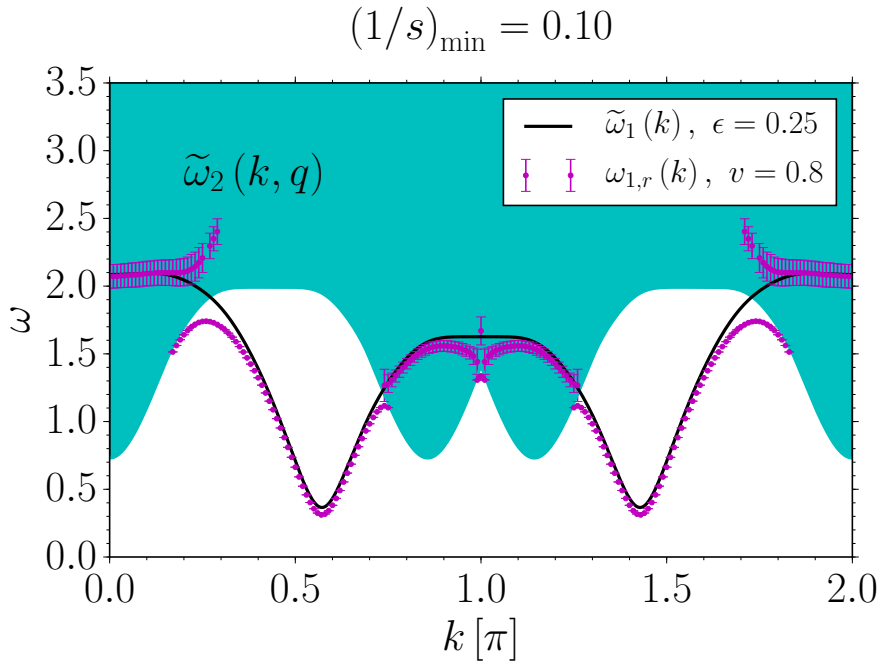

Figure 3.5: Renormalized dispersion $\omega_{1,r}(k)$ of the toy model for the parameters $\epsilon = 0.25$, $v = 0.8$ and the threshold $(\gamma(k)/\Delta\widetilde{\omega}_2(k))_{\max} = 0.05$. Outside the two-particle continuum only the solutions of the DYSON equation holding a spectral weight $1/s \geq (1/s)_{\min} = 0.1$ are displayed since these describe quasiparticle peaks in the corresponding spectral function $A(k,\omega)$, see figure 3.3.

Since the two introduced criteria act on different areas of the energy scale, i.e. the maximum relative HWHM $(\gamma(k)/\Delta\widetilde{\omega}_2(k))_{\max}$ acts inside the two-particle continuum and the minimum spectral function $1/s_{\min}$ outside the two-particle continuum, it is possible that more than one solution of the DYSON equation can remain as a possible quasiparticle, resonance or (anti-) bound state energy at a specific momentum k. Inside the two-particle continuum the remaining solutions describe quasiparticles or resonances holding a finite lifetime, which is sufficient long in order to be identified. Outside of the two-particle continuum they represent the energies of a quasiparticle or (anti-) bound state with infinite lifetime holding a sufficient large amount of spectral weight.
In addition to the renormalized one-particle dispersion $\omega_{1,r}(k)$, see figure 3.5, we also present a color plot of the corresponding spectral function $A(k,\omega)$, see figure 3.6. This color plot stresses our results according to the introduction of the relative HWHM as a criterion to detect quasiparticle peaks in the spectral function. Inside the two-particle continuum we clearly see a large amount of weight near the energies we identified as the renormalized one-particle dispersion $\omega_{1,r}(k)$, see figure 3.5. We can also notice the structure of the VAN HOVE singularities inside the continuum and that their weight is less compared to the weight of the corresponding quasiparticle peaks.

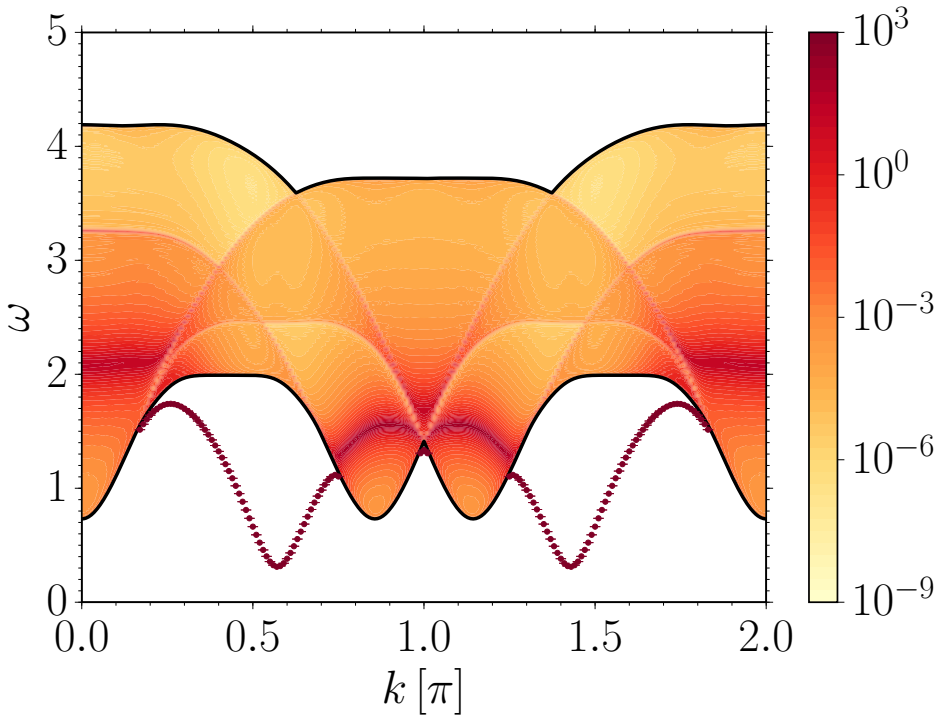

Figure 3.6: Logarithmic color map of the spectral function $A(k,\omega)$ for the toy model with the previously analyzed parameters $\epsilon = 0.25$ and $v = 0.8$. The black solid lines represent the lower and the upper boundary of of the two-particle continuum $\widetilde{\omega}_2(k,q)$ for a fixed total momentum k. Outside of the continuum only peaks in the spectral function $A(k,\omega)$ with a minimal spectral weight of $(1/s)_{\text{min}} = 0.1$ are depicted with zero error bars implying that the corresponding excitations have an infinite lifetime.

Finally, we compare the renormalized dispersion $\omega_{1,\text{r}}(k)$ for different hybridization strengths v between the one- and two-particle HILBERT space, see figure 3.7.

An increasing value of the variable v describes a stronger hybridization between the one- and two-particle HILBERT space. This results in a stronger renormalization, e.g. a stronger downshift, of the one-particle dispersion outside the two-particle continuum and a larger HWHM of the quasiparticle peaks inside the two-particle continuum, respectively. For further increasing values of v it is even possible that the one-particle dispersion is reduced so significantly that it assumes negative values, see also eq. (3.1.11) for the bosonic BOGOLIUBOV transformation. In this context the hybridization between the one- and two-particle HILBERT space is so strong that the whole system is no longer physically stable.
Another interesting aspect to discuss is the down-bending of the renormalized dispersion $\omega_{1,\text{r}}(k)$ near the two-particle continuum $\widetilde{\omega}_2(k,q)$. As expected, figure 3.7 shows clearly that with increasing v the down-bending of the renormalized dispersion becomes more and more pronounced.

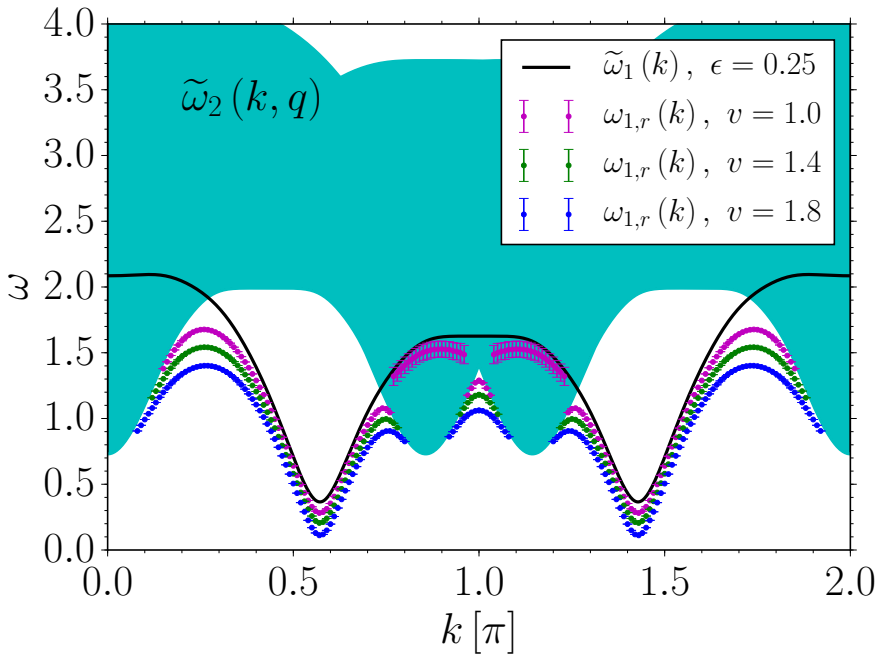

Figure 3.7: Renormalized dispersion $\omega_{1,r}(k)$ of the toy model for different hybridization strengths, tuned by the parameter v, see eq. (3.2.17). The criteria for identifying the quasiparticle peaks in the corresponding spectral functions are set to $(\gamma(k)/\Delta\widetilde{\omega}_2(k))_{\max} = 0.03$ and $(1/s)_{\min} = 0.1$.

3.4.2 Analysis of two-particle interaction terms, $v = 0$ and $w \neq 0$

In this subsection we study only the effects of two-particle interaction terms in our toy model and do not take decay/fusion terms into account, i.e. we refer to the Hamiltonian $\widetilde{\mathcal{H}}_{\text{full}}$, see eq. (3.3.24), with $v = 0$. Finite attractive two-particle interaction terms can lead to the phenomenon that two particles form a so-called bound state [4, 6]. A bound state is characterized by the fact that its energy is less than the sum of the energies of each particle. Therefore, it is not possible to separate these particles without expending energy. To receive the dispersion of the two-particle bound state $\omega_{\text{bound}}(k)$ of our toy model we can proceed similar to the steps described in sect. 3.4.1. The only difference to the steps in sect. 3.4.1 is the choice of the initial state for the Lanczos tridiagonalization because we consider only two-particle interactions in this subsection and cannot start from a single particle state. Therefore, we choose the two-particle state

$$|k,1\rangle = \frac{1}{\sqrt{N}} \sum_{i=0}^{N-1} \mathrm{e}^{\mathrm{i}k\left(r_i+\frac{1}{2}\right)} \widetilde{b}_i^\dagger \widetilde{b}_{i+1}^\dagger |0\rangle \tag{3.4.27}$$

as the intial two-particle state for the Lanczos algorithm [123]. This state characterizes a two-particle state in real space with a total momentum k where two bosons are created

out of the vaccum state $|0\rangle$ on adjacent sites i and $i+1$. As we perform all our calculations in momentum space, we apply a FOURIER transform yielding

$$|k,1\rangle = \frac{1}{\sqrt{N}} \sum_q \cos\left(\frac{k}{2} - q\right) \widetilde{b}_q^\dagger \widetilde{b}_{k-q}^\dagger |0\rangle \,. \tag{3.4.28}$$

This state is a superposition of all possible two-particle states $|q, k-q\rangle$, which hold a fixed total momentum k and a variable relative momentum q. In figure 3.8 the dispersion of the two-particle bound state is depicted for different two-particle interaction strengths w.

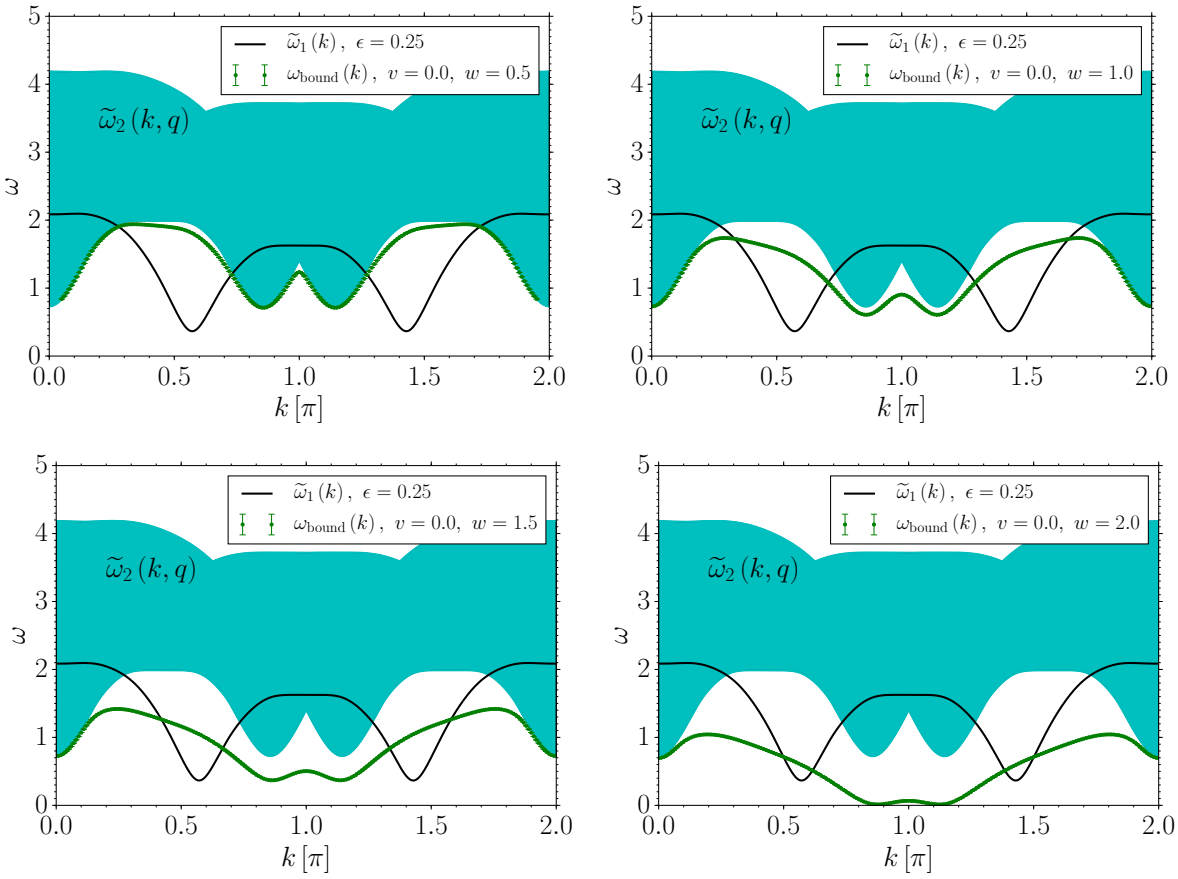

Figure 3.8: Dispersion of the two-particle bound state $\omega_{\text{bound}}(k)$ for different two-particle interaction strengths w. For the calculations a discretization of $N = 1000$ in k-space was chosen and 200 LANCZOS steps have been performed. In order to solve the corresponding DYSON equation, see eq. (2.3.66), the energy ω is discretized in steps of 0.001 and up to $n_{\text{Lanczos,max}} = \{50, 30, 20, 20\}$ LANCZOS coefficients for $w = \{0.5, 1.0, 1.5, 2.0\}$ were used. Due to the definition of a two-particle bound state only solutions of the DYSON equation below the two-particle continuum $\widetilde{\omega}_2(k,q)$ can be identified with the dispersion $\omega_{\text{bound}}(k)$. The lifetime of the two-particle bound state is infinite per definition, see sect. 2.3.3.

As expected, the introduction of an attractive two-particle interaction in our toy model

gives rise to a two-particle bound state. With increasing interaction strength, i.e. a larger amount of energy is required to separate the two bosons, the dispersion of the two-particle bound state $\omega_{\text{bound}}(k)$ is reduced further. Note, that within our ansatz for calculating $\omega_{\text{bound}}(k)$, see sects. 2.3.2 and 2.3.3, it is possible to receive negative values for $\omega_{\text{bound}}(k)$ for sufficient large values of w. Since negative energies describe unstable systems, we discard these solutions.

As already mentioned, it is necessary to expend energy to separate the two particles forming a bound state. This amount of energy is known as the binding energy ΔE_{bound}. It is defined as the energy difference

$$\Delta E_{\text{bound}}(k) = \widetilde{\omega}_{2,\text{min}}(k) - \omega_{\text{bound}}(k) \tag{3.4.29}$$

between the lower boundary[16] of the two-particle continuum $\widetilde{\omega}_2(k,q)$, see eq. (3.1.14), and the energy of the two-particle bound state $\omega_{\text{bound}}(k)$. In figure 3.9 the binding energy for different two-particle interaction strengths w is depicted.

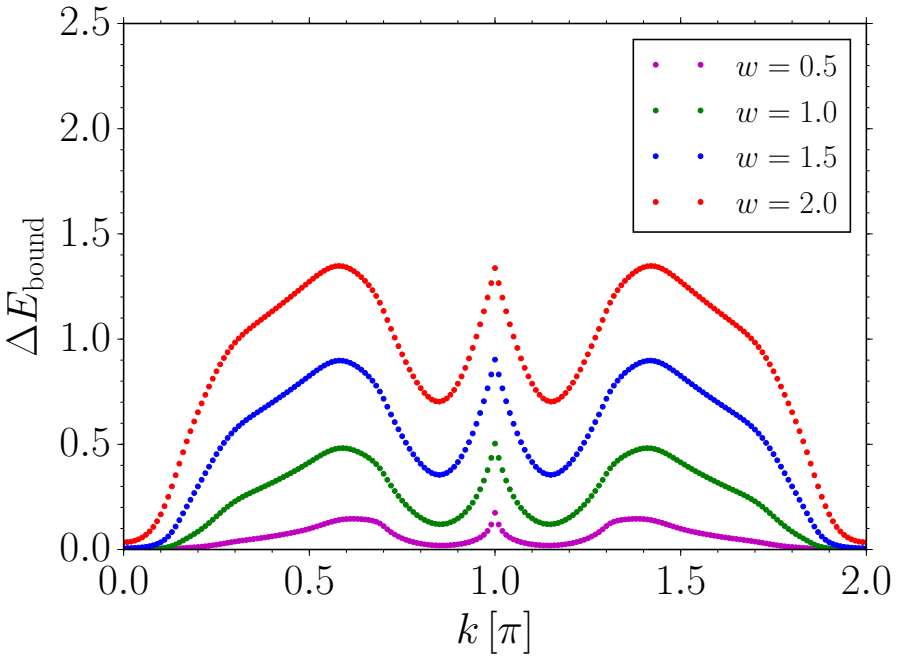

Figure 3.9: Binding energy $\Delta E_{\text{bound}}(k)$ for different interaction strengths w. The results belong to the two-particle bound states which are shown in figure 3.8.

The results are consistent with our expectation that a stronger attractive two-particle interaction strength w leads to a larger binding energy $\Delta E_{\text{bound}}(k)$, i.e. a larger amount of energy needs to be expended in order to separate the two particles which form the two-particle bound state.

[16]The lower boundary of the two-particle continuum is given by $\widetilde{\omega}_{2,\text{min}}(k) = \min_{q\in[0,2\pi)}\widetilde{\omega}_2(k,q)$.

3.4.3 Analysis of decay and two-particle interaction terms, $v \neq 0$ and $w \neq 0$

In this subsection we investigate the effects of SQPD and an attractive two-particle interaction on the one-particle dispersion $\widetilde{\omega}_1(k)$, see eq. (3.1.11), and the two-particle bound state $\omega_{\text{bound}}(k)$, i.e. we consider the Hamiltonian $\widetilde{\mathcal{H}}_{\text{full}}$ from eq. (3.3.24) with finite values of v and w. In order to receive the corresponding renormalized one-particle dispersion $\omega_{1,r}(k)$ and renormalized two-particle bound state $\omega_{\text{bound},r}(k)$ we apply the same steps as outlined in the previous sects. 3.4.1 and 3.4.2. Figure 3.10 shows the results for a fixed value of $v = 0.8$ for the decay/fusion processes and variable values of w for the attractive two-particle interaction.

Comparing the results shown in figure 3.10 with the renormalized one-particle dispersion $\omega_{1,r}(k)$ without two-particle interactions, see figure 3.5[17] and with the dispersion of the two-particle bound state $\omega_{\text{bound}}(k)$, see figure 3.8, noticeable renormalization effects can be identified. A clear assignment for the renormalized one-particle dispersion $\omega_{1,r}(k)$ and the renormalized two-particle bound state $\omega_{\text{bound},r}(k)$ for $v \neq 0$ and $w \neq 0$ is not possible within our calculation path. The points where the dispersion of the two-particle bound state $\omega_{\text{bound}}(k)$, see figure 3.8, and the undisturbed one-particle dispersion $\widetilde{\omega}_1(k)$ intersect describe typical anti-crossing situations. Due to the finite values of v for decay/fusion processes and finite values of w for two-particle interactions the one-particle dispersion and the two-particle bound state are interacting with each other. As a consequence, their dispersions are separated at the anti-crossing points in the BRILLOUIN zone and the gap between them grows with increasing two-particle interactions strength w for a fixed value of v and vice versa. To distinguish which quasiparticle energies belong to the one-particle and which to the two-particle HILBERT space we use different colors in figure 3.10. We sort the quasiparticle energies by comparing the solutions with the results for the renormalized one-particle dispersion $\omega_{1,r}(k)$ for $w = 0$ and with the results for the dispersion of the two-particle bound state $\omega_{\text{bound}}(k)$ for $v = 0$, see figure 3.8[18], in order to reproduce the previously mentioned anti-crossing situations.

[17] Note, that the thresholds used in figures 3.5 and 3.10 differ.

[18] As explained in sect. 3.4.2 our applied ansatz for calculating the quasiparticle energies gives rise to negative values for large values of w or v. As these solutions describe unstable systems, we discard them.

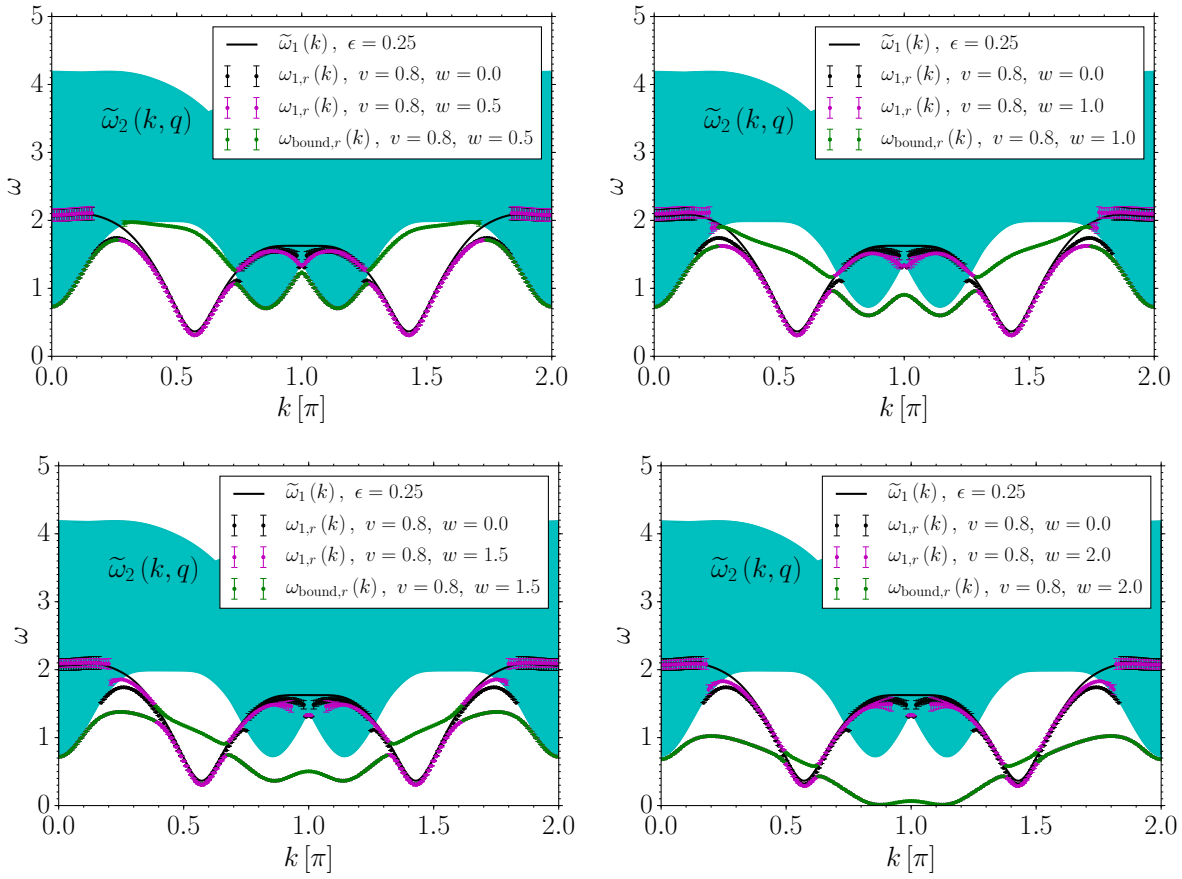

Figure 3.10: Renormalized one-particle dispersion $\omega_{1,r}(k)$ and renormalized dispersion of the two-particle bound state $\omega_{\text{bound},r}(k)$ for a fixed value of $v = 0.8$ and different two-particle interaction strengths w. As a discretization in k-space $N = 1000$ was chosen and 200 LANCZOS steps have been performed. The energy ω is discretized in steps of 0.001 and up to $n_{\text{Lanczos,max}} = \{40, 30, 20, 20\}$ LANCZOS coefficients for $w = \{0.5, 1.0, 1.5, 2.0\}$ were used. The reason for the different values of $n_{\text{Lanczos,max}}$ is that with an increasing value of the two-particle interaction strength w the LANCZOS coefficients show deviations from their limiting values at earlier iteration steps. Peaks in the corresponding spectral function inside the two-particle continuum $\widetilde{\omega}_2(k,q)$ with a relative HWHM of $(\gamma(k)/\Delta\widetilde{\omega}_2(k)) = 0.04$ are identified as quasiparticle peaks. Outside the two-particle continuum all shown data hold a minimal spectral weight of $(1/s)_{\text{min}}$=0.001.

As a final point on our toy model we point out another particular feature. Our calculations reveal that it is not possible the receive the energy of the renormalized two-particle bound state $\omega_{\text{bound},r}(k)$ at $k = \pi$ if the one-particle state $|k\rangle$ is chosen as a start state for the LANCZOS tridiagonalization. However, choosing the two-particle state $|k, 1\rangle$, see eq. (3.4.28), as a start state yields the renormalized energy of the two-particle bound state at $k = \pi$. Further investigations reveal that the transition probability

$$p(k) = |\langle k|\,\widetilde{\mathcal{H}}_{\text{full}}\,|k, 1\rangle\,|^2 \tag{3.4.30}$$

is equal to zero at $k = \pi$. This means that at this specific k-value the Hamiltonian $\widetilde{\mathcal{H}}_{\text{full}}$ generates no overlap between the two-particle start state $|k, 1\rangle$ and the one-particle state $|k\rangle$. As a consequence, the two-particle HILBERT space will not be left in the LANCZOS tridiagonalization and the renormalized energy of the two-particle bound state $\omega_{\text{bound},r}(k)$ can be detected at $k = \pi$. The solution for this specific feature of our toy model can be found by a detailed analysis of the prefactor $\widetilde{\Gamma}(k, q)$, see eq. (3.2.19), which describes the amplitude of the decay/fusion processes. Since our toy model is invariant under a reflection at a single site the coefficients v_δ obey the relation $v_{-\delta} = v_\delta$, see sect. 3.2. As a consequence, the prefactor $\widetilde{\Gamma}(k, q)$ is symmetric around $k = \pi$ in the relative momentum q, i.e. $\widetilde{\Gamma}(k = \pi, -q) = \widetilde{\Gamma}(k = \pi, q)$ holds. As the two-particle start state $|k, 1\rangle$, see eq. (3.4.28), is antisymmetric in the relative momentum q for $k = \pi$, the transition probability $p(k)$, see eq. (3.4.30), has to vanish for $k = \pi$. Therefore, it is crucial to combine all quasiparticle energies from calculations using the one-particle state $|k\rangle$ and the two-particle state $|k, 1\rangle$ in order to receive the renormalized dispersions in the whole BRILLOUIN zone.

3.5 Chapter summary

At the end of this chapter we sum up the key aspects. At first a simple toy model to demonstrate the effects of SQPD was introduced. We were able to observe the three different characteristics of SQPD, namely the termination of the one-particle dispersion, its resonance behavior with a finite HWHM within the two-particle continuum and its strong renormalization to avoid an overlap with the corresponding two-particle continuum. In the course of the analysis of the toy model we came to the conclusion that it is necessary to apply specific criteria to the numerically calculated solutions of the DYSON equation. It is essential to introduce these criteria to distinguish between solutions of the DYSON equation, which describe the energy of a well-defined quasiparticle, resonance or (anti-) bound state, and the solutions, which are only numerical artefacts without a physical meaning. Therefore, we established two criteria to handle this issue. Focusing only on solutions inside the two-particle continuum the ratio between the HWHM of a peak and the width of the two-particle continuum represents a resonable criterion to use. Considering the energy range outside the two-particle continuum the value of the spectral weight is a suitable quantity to identify the energies of a quasiparticle or (anti-) bound state. Combining these two criteria results in receiving a renormalized dispersion with a plausible meaning. In addition to transitions between the one- and two-particle HILBERT space, we also introduced an attractive two-particle interaction in our toy model. This interaction leads to a two-particle bound state and shows also renormalization effects in combination with decay/fusion processes on the one-particle dispersion and on the two-particle bound state.

4 Description of the quantum antiferromagnet $BiCu_2PO_6$ on bilinear operator level

To describe and understand the magnetic properties of a material it is essential to have an in-depth knowledge of its crystallographic structure. Based on this information a model characterizing the magnetic structure of the material can be set up. In this chapter the magnetic structure of the quantum antiferromagnet $BiCu_2PO_6$ (BCPO) is analyzed. Furthermore, we set up a model, based on deepCUT results for a single frustrated spin ladder, to describe the properties of its elementary excitations, i.e. the one-particle dispersions, taking only bilinear operator terms into account, which stem from anisotropic couplings, in a mean-field approach. This bilinear anisotropic model of BCPO serves as a suitable starting point in order to study its effects of SQPD in the following chapters.

Parts of this chapter have been published in Physical Review B as a regular article [89]. The manuscript and the interpreation of the data contain contributions from Götz S. Uhrig and myself. Furthermore, I received data using calculations from Holger Krull and Nils A. Drescher for the isotropic model and created all figures.
In addition, parts of this chapter have been published in Physical Review Research as a regular article [71]. This manuscript and the interpretation contain contributions from Maik Malki, Götz S. Uhrig and myself. I contributed the CUT results, parts of the symmetry analysis and the calculation of the generalized ket states $|\mathbf{k}, n\rangle\rangle$. Maik Malki implemented the topological calculations.

4.1 Isotropic analysis of BCPO

To provide a comprehensive description for the split one-particle dispersions of BCPO it is essential to consider anisotropic couplings, see sect. 1.4. Since these are expected to be small compared to the isotropic couplings, it is reasonable to discuss the magnetic structure of BCPO neglecting anisotropies in the first place by using a deepCUT, see sect. 2.1. The aim of this analysis is to determine the values of the isotropic couplings

J_1, J_2 and J', see figure 1.3. Thereby, we gain an effective isotropic model of BCPO to which we add anisotropic couplings at a later stage.

4.1.1 Results for the isotropic spin ladder

To study the spectrum of a single frustrated spin ladder it is necessary to set up its Hamiltonian

$$\mathcal{H}_{\text{ladder}} = J_0\mathcal{H}_0 + J_1\mathcal{H}_1 + J_2\mathcal{H}_2, \tag{4.1.1a}$$

$$\mathcal{H}_0 = \sum_i \mathbf{S}_i^{\text{L}}\mathbf{S}_i^{\text{R}}, \tag{4.1.1b}$$

$$\mathcal{H}_1 = \sum_{i,\tau} \mathbf{S}_i^{\tau}\mathbf{S}_{i+1}^{\tau}, \tag{4.1.1c}$$

$$\mathcal{H}_2 = \sum_{i,\tau} \mathbf{S}_i^{\tau}\mathbf{S}_{i+2}^{\tau}, \tag{4.1.1d}$$

in the first place. The variable i denotes the rung index and τ assumes the values L for the left leg of the spin ladder and R for the right leg. We determine the rung coupling J_0 to be the global energy scale and therefore define the ratios $x = J_1/J_0$ and $y = J_2/J_1$. The parameter x states the expansion around the limit of decoupled dimers. This means that for $x \to 0$ at constant y no interaction between the dimers exists. Therefore, the parameter x is chosen as the expansion parameter in the deepCUT calculations and determines the truncation scheme. With the parameter y the relative strength of the NN and NNN coupling along the legs of the spin ladder can be tuned. The deepCUT provides the effective Hamiltonian

$$\mathcal{H}_{\text{ladder}}^{\text{eff}} = \sum_{k,\alpha} \omega_0(k)\, t_k^{\alpha,\dagger} t_k^{\alpha}, \tag{4.1.2}$$

which describes the dispersive triplons[1]. The operator $t_k^{\alpha,\dagger}$ (t_k^{α}) creates (annihilates) a triplon [72, 136] holding momentum k and flavor $\alpha \in \{x, y, z\}$. Since only isotropic couplings are analyzed up to this point the dispersion $\omega_0(k)$ is the same for all flavors. As pointed out in sect. 2.1 observables have to be transformed into the same basis as the Hamiltonian.

4.1.2 Results for coupled isotropic spin ladders

Since the structure of BCPO contains multiple frustrated spin ladders coupled by an interladder coupling J', it is necessary to include this effect as well. In order to do so,

[1] The deepCUT also determines the ground-state energy E_0. As we are interested in the dynamics of the triplons, we neglect the value of the ground-state energy.

we transform a single spin operator

$$S^{\alpha,\mathrm{L}}_{i,\mathrm{eff}} = \sum_{\delta=-n}^{n} a_\delta \left(t^{\alpha,\dagger}_{i+\delta} + t^{\alpha}_{i+\delta} \right) + ... \tag{4.1.3}$$

into the same basis as the effective Hamiltonian $\mathcal{H}^{\mathrm{eff}}_{\mathrm{ladder}}$. The dots stand for terms containing normal-ordered bilinear or a larger number of triplon operators. These terms are neglected similar to previous applications, which showed matching results to corresponding experiments [100]. The index δ assumes values from $-n$ to n in integer steps. The effective spin operator, see eq. (4.1.3), is not local anymore but a superposition of triplon operators from rung $i-\delta$ to $i+\delta$. The coefficients a_δ represent the probability amplitude of the triplon operator on rung $i+\delta$. Vividly spoken this means that the triplon, which is completely local in the limit of decoupled dimers, becomes smeared out when the NN interaction J_1 and the NNN interaction J_2 assume finite values. Considering only linear contributions to the effective spin operator, see eq. (4.1.3), the relation

$$S^{\alpha,\mathrm{L}}_{i,\mathrm{eff}} = -S^{\alpha,\mathrm{R}}_{i,\mathrm{eff}} \tag{4.1.4}$$

holds. This follows from the fact that triplon excitations have odd parity relative to the ground-state with respect to a reflection on the center line of a spin ladder [101, 136]. From now on the triplons are treated as free bosons in a mean-field approach. This approach constitues an approximation of course, but it is reasonable, since the interladder coupling J' is small compared to the rung coupling, i.e. $|J'/J_0| \ll 1$ holds[2]. A Fourier transform of the effective spin operator yields

$$S^{\alpha,\mathrm{L}}_{\mathrm{eff}}(k) = a(k) \left(t^{\alpha,\dagger}_{k} + t^{\alpha}_{-k} \right) \tag{4.1.5}$$

with

$$a(k) = \sum_{\delta} a_\delta e^{\mathrm{i}k\delta} = \sum_{\delta} a_\delta \cos(k\delta) . \tag{4.1.6}$$

The absolute value squared of $a(k)$ describes the weight of the dominant single-particle mode in the dynamic structure factor at zero temperature with respect to the assumptions made. In the single-mode approximation [137] this weight equals the momentum-resolved static structure factor. Note, that the prefactors a_δ satisfy the relation $a_\delta = a_{-\delta}$ due to the mirror symmetry about a rung, see figure 1.3.

[2]Note, that the hard-core properties of the triplons within a single spin ladder are taken into account exactly by the deepCUT, see sect. 4.1.1.

To include the interladder coupling J' the Hamiltonian

$$\mathcal{H}' = J' \sum_{i,j} \mathbf{S}^{\mathrm{R}}_{i,j} \mathbf{S}^{\mathrm{L}}_{i,j+1} \tag{4.1.7}$$

coupling two adjacent spin ladders, which are indicated by the index j, has to be taken into account. Mapping the spin operators onto the effective spin operators, see eq. (4.1.3), and performing a FOURIER transform leads to the effective Hamiltonian

$$\mathcal{H}'^{,\mathrm{eff}} = -J' \sum_{k,l,\alpha} d_{k,l} \left(t^{\alpha,\dagger}_{k,l} + t^{\alpha}_{-k,-l} \right) \left(t^{\alpha}_{k,l} + t^{\alpha,\dagger}_{-k,-l} \right) \tag{4.1.8}$$

in momentum space with the expression

$$d_{k,l} = \cos(l)\, a^2(k)\,. \tag{4.1.9}$$

The variable l represents the wave vector perpendicular to the spin ladder in z-direction, see figure 1.3, in reciprocal lattice units (r.l.u.). Adding the Hamiltonians $\mathcal{H}^{\mathrm{eff}}_{\mathrm{ladder}}$ for all ladders, see eq. (4.1.2), and the interladder part $\mathcal{H}'^{,\mathrm{eff}}$, see eq. (4.1.8), leads to the complete isotropic Hamiltonian. We can solve this easily with a BOGOLIUBOV transformation, see eqs. (3.1.8), and receive the two-dimensional dispersion

$$\omega(k,l) = \omega(k) = \sqrt{(\omega_0(k))^2 - 4J' d_{k,l} \omega_0(k)} \tag{4.1.10}$$

of the complete isotropic system[3].

To gain a comprehensive description of the spectrum of BCPO it is crucial to consider anisotropic couplings, which lift the spin isotropy, since the experimental data demonstrate different modes. Thus, the already discussed isotropic model is not sufficient to describe BCPO. But with the help of the two-dimensional isotropic model, we determine the best matching values concerning the coupling ratios $x = J_1/J_0$ and $y = J_2/J_1$ for the measured data. For this purpose we focus on two essential features of the measured dispersions.

As the first criterion, we choose the momentum at which the gap Δ occurs. This momentum value is referred to as k^*_Δ. As a second criterion, we use the ratio between the lower maximum $\omega(\pi)$ and the gap Δ. Therefore, we use the first published results of the dispersion [39, 70], see figure 4.1. Since there are three occuring modes in the data, we have to choose one mode to determine the value of k^*_Δ. For this we use the data of mode

[3] The measured data of BCPO were collected for a fixed momentum $l = 1\,\mathrm{r.l.u.}$ and vary in the momentum k, which corresponds to the rung index i along a single spin ladder. Therefore, we often neglect the second momentum l since we fix it to be $l = 2\pi$ and write $\omega(k)$ instead of $\omega(k,l)$.

1 because it is the lowest-lying mode. We read off the value $k^*_\Delta = (0.575 \pm 0.005)\,(\text{r.l.u.})$. Defining the ratio $(\omega(\pi)/\Delta)^*$ is challenging as well, since there are different gap values present. Therefore, we use mode 3 as it is the only mode which was experimentally observed in the whole BRILLOUIN zone[4]. Due to the large error bars of the dispersion around $k = \pi$ we average these values from $k_{\text{start}} = 0.8\,(\text{r.l.u.})$ to $k_{\text{end}} = 1.2\,(\text{r.l.u.})$ and get $\omega(\pi)^* = 14\,\text{meV}$ as a final value. The gap value of mode 3 can be read off and is $\Delta^* = 3.8\,\text{meV}$. Thus, we end up with $(\omega(\pi)/\Delta)^* = 3.7$ as a reference value. Due to the already mentioned large error bars we assume a deviation from this value of up to 0.5 to be acceptable.

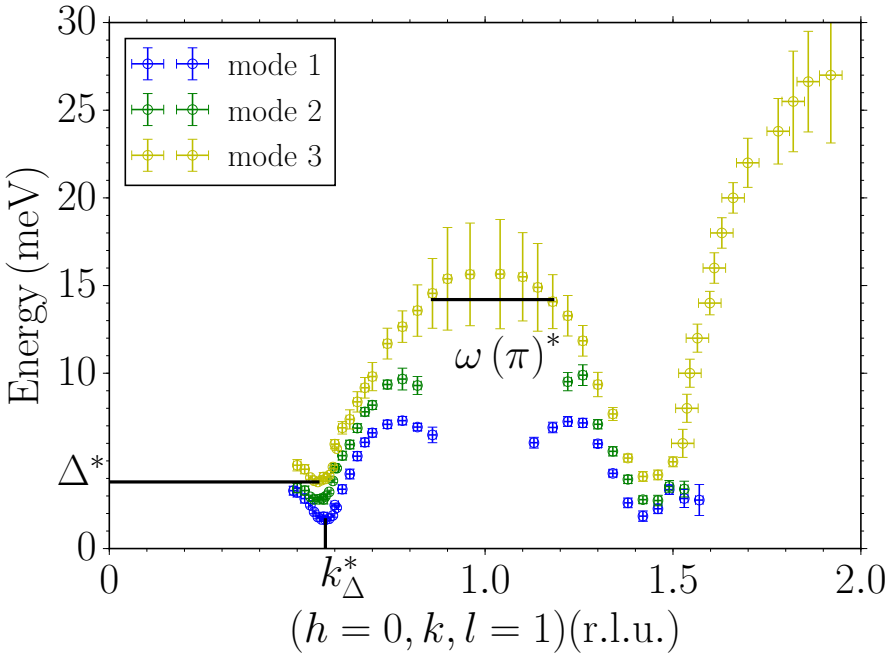

Figure 4.1: Experimental data, measured by inelastic neutron scattering [39, 70]. The determined value $k^*_\Delta = 0.575\,(\text{r.l.u.})$ stands for the position of the gap of mode 1. The average value of mode 3 at $k = \pi$ is given by $\omega(\pi)^* = 14\,\text{meV}$ and the corresponding gap value is $\Delta^* = 3.8\,\text{meV}$.

In figure 4.2 the curves defined by $k_\Delta = k^*_\Delta$ and $\omega(\pi)/\Delta = (\omega(\pi)/\Delta)^*$ for different ratios of x and y are presented. Here we fix the relative value of the interladder coupling to be $J'/J_0 = 0.16$ as it has been done in previous studies [39, 70]. Figure 4.2 shows an overlap of the two criteria at $x \approx 1.2$ and $y \approx 0.9$. Within the tolerated error range even larger values than 1.2 for x show an overlap of both criteria. Isotropic dispersions with values of $x = 1.3$ to 1.7 and $y = 0.9$ were also analyzed but did not lead to an improvement. A variation of the parameter y does not help fitting the theoretical

[4]At a later stage of this thesis this association becomes even more reasonable since the anisotropic couplings are responsible for lowering the dispersion, especially in the low-energy regime.

calculations to the experimental data either. Thus, with the analysis of the magnetic structure of BCPO concerning only isotropic couplings we receive the best matching parameter values to be $x = 1.2$, $y = 0.9$ and $J'/J_0 = 0.16$.

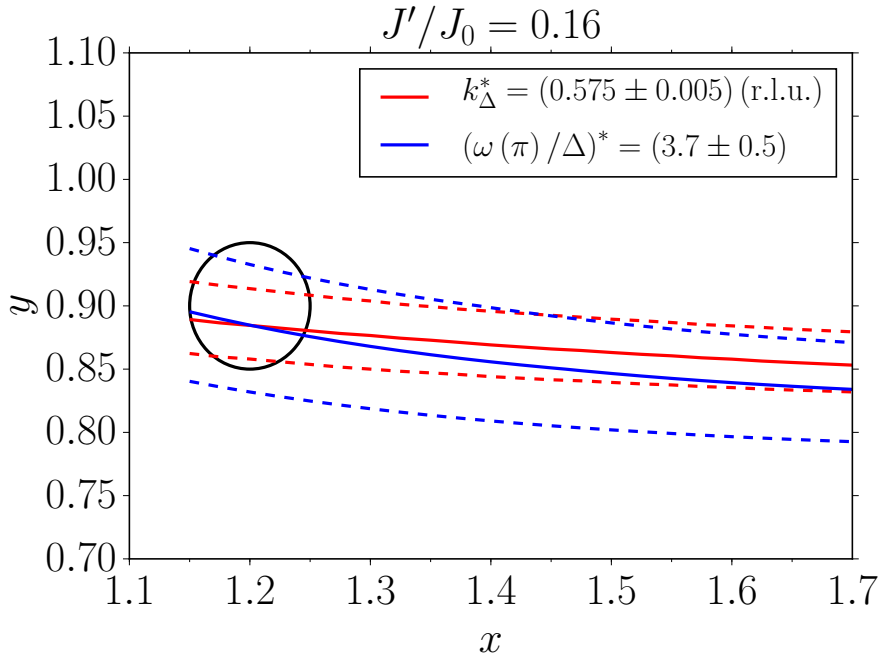

Figure 4.2: Correspondence of the chosen criteria with two-dimensional isotropic dispersions, see eq. (4.1.10), for different values of x and y. The interladder coupling $J'/J_0 = 0.16$ is fixed. The red solid line shows $k_\Delta = k^*_\Delta = 0.575$ (r.l.u.) and the corresponding dashed lines represent the deviations by ± 0.005, i.e. $k_\Delta = (0.575 \pm 0.005)$ (r.l.u.). The blue solid line depicts the ratio $\omega(\pi)/\Delta = (\omega(\pi)/\Delta)^* = 3.7$ and the corresponding dashed line indicate the accepted deviations by ± 0.5, i.e. $\omega(\pi)/\Delta = (3.7 \pm 0.5)$. Both criteria are fulfilled for $x \approx 1.2$ and $y \approx 0.9$, marked by a circle.

4.2 Anisotropic analysis of BCPO

Starting from the isotropic model, which has been discussed in the previous section, anisotropic couplings need to be included in order to provide a reasonable model for BCPO. Its crystal structure, see figure 1.3, demonstrates that the inversion symmetry about the center of each Cu-Cu bond is broken due to the positions of the Bismuth ions. Therefore, it is necessary to consider anisotropic couplings, i.e. the Hamiltonian

$$\mathcal{H} = \mathcal{H}_{\text{ladder}} + \sum_{i,j} \mathbf{D}_{ij} \left(\mathbf{S}_i \times \mathbf{S}_j \right) + \sum_{i,j} \sum_{\alpha,\beta} \Gamma_{ij}^{\alpha\beta} S_i^\alpha S_j^\beta , \tag{4.2.11}$$

which consists of the isotropic spin ladder $\mathcal{H}_{\text{ladder}}$, see eqs. (4.1.1), the DM interaction $\mathbf{D}_{ij} \left(\mathbf{S}_i \times \mathbf{S}_j \right)$ and the symmetric anisotropic exchange $\Gamma_{ij}^{\alpha\beta} S_i^\alpha S_j^\beta$, see sect. 2.4. The sums with the indices i and j count each pair of spins once. The couplings concerning the

rungs of the spin ladder are denoted with the index 0, i.e. J_0, $\mathbf{D}_0$ and $\Gamma_0^{\alpha\beta}$. The couplings related to the NN interactions are marked with the index 1, thus J_1, $\mathbf{D}_1$ and $\Gamma_1^{\alpha\beta}$. The components considering the NNN interactions carry the index 2, thus J_2, $\mathbf{D}_2$ and $\Gamma_2^{\alpha\beta}$, see also figure 1.3. The components of the $\mathbf{D}$ vectors are real and constant coefficients.

4.2.1 Symmetry analysis of BCPO

To decide whether a component D_{ij}^{α} has to vanish or not, one has to apply the rules of Moriya [74] to the crystal structure of BCPO, see figures 1.3 and 4.3.

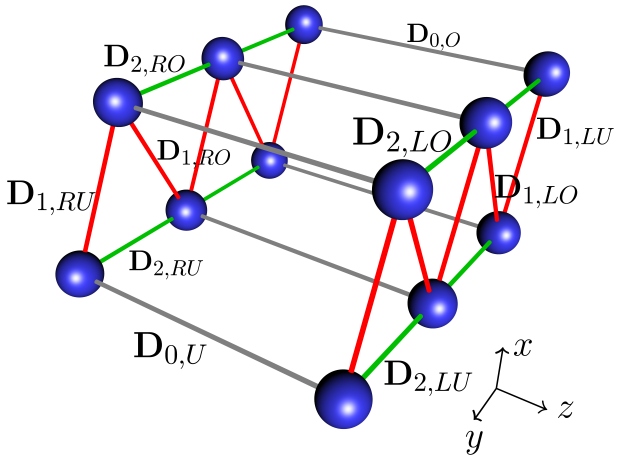

Figure 4.3: Schematic representation of the spin ladder structure of BCPO. The blue spheres represent the copper ions Cu_A and Cu_B, see figure 1.3, which act like a spin S=1/2. The different bonds are marked with the corresponding $\mathbf{D}$ vectors. The unit cell of the spin ladder contains an upper and a lower rung.

Besides the rules of Moriya it is possible to obtain more information about the $\mathbf{D}$ vectors concerning the signs of the components along the ladder direction by considering translations and glide reflections.

Each bond holds one $\mathbf{D}$ vector, see figure 4.3. For the NN and NNN bonds the spin operators in the outer product $\mathbf{D}_{ij}\,(\mathbf{S}_i \times \mathbf{S}_j)$ are arranged according to ascending y coordinate. For the rung coupling the spin operators are ordered according to ascending z coordinate. Neglecting the difference between the copper sites Cu_A and Cu_B, see figure 1.3, i.e. treating all sites as equal, the crystal structure of BCPO fulfills the following symmetries:

(1) RS_y: Rotation by π about $\vec{y}$ located in the middle of the ladder tube and a shift by half a unit cell.

(2) R_x: Rotation by π about $\vec{x}$ located in the middle of a rung.

(3) S_{xy}: Reflection at the xy plane located in the middle of the ladder.

(4) S_{xz}: Reflection at the xz plane located on a rung.

(5) SS_{yz}: Reflection at the yz plane located in the middle of the ladder and a shift by half a unit cell.

By applying these five symmetries to each bond, see figure 4.3, one obtains relations between the different bonds and so relations between the components of the **D** vectors. For an exemplary demonstration of this symmetry analysis we refer to the literature [71, 89] and Appendix D. At this point we present only the results, see table 4.1.

D_{ij}^{α}	along the legs	parity
D_0^y	alternating	odd
D_1^x	uniform	odd
D_1^y	alternating	odd
D_2^x	uniform	odd
D_2^z	alternating	even

Table 4.1: Behavior of the sign along the legs of the spin ladder and the parity with respect to the symmetry SS_{xy} of the **D** vectors. Components not listed vanish due to symmetry arguments. The parity of D_0^y does not refer to the component itself, but to the corresponding term in the Hamiltonian.

As Shekhtman *et al.* [126] pointed out, it is crucial to consider also the symmetric anisotropic interactions $\Gamma_{ij}^{\alpha\beta}$, see sect. 2.4.2, although they are of second order in the SOC compared to the antisymmetric anisotropic interactions $\mathbf{D}_{ij}$, see sect. 2.4.1. Since the components of the symmetric tensor Γ_{ij} are determined by the corresponding $\mathbf{D}_{ij}$ vector and Heisenberg coupling J_{ij}, see eq. (2.4.84), we can translate the properties of the $\mathbf{D}_{ij}$ vectors, see table 4.1, to the properties of each matrix element $\Gamma_{ij}^{\alpha\beta}$. The results are listed in table 4.2.

$\Gamma_{ij}^{\alpha\beta}$	along the legs	parity
Γ_0^{xx}	uniform	even
Γ_0^{yy}	uniform	even
Γ_0^{zz}	uniform	even
Γ_1^{xx}	uniform	even
Γ_1^{xy}	alternating	even
Γ_1^{yy}	uniform	even
Γ_1^{zz}	uniform	even
Γ_2^{xx}	uniform	even
Γ_2^{xz}	alternating	odd
Γ_2^{yy}	uniform	even
Γ_2^{zz}	uniform	even

Table 4.2: Behavior of the sign along the legs of the spin ladder and the parity with respect to the symmetry SS_{xy} of the components $\Gamma_{ij}^{\alpha\beta}$. Components not listed vanish according to eq. (2.4.84) or they are given by their equivalent expression $\Gamma_{ij}^{\beta\alpha}$.

4.2.2 Derivation and solution of the bilinear anisotropic Hamiltonian of BCPO

In this section we present the derivation of the bilinear anisotropic Hamiltonian of BCPO, which includes all existing DM interactions, and its solution.
The following analysis takes the results for coupled isotropic spin ladders, see sect. 4.1.2, as a starting point, i.e. the values $x = 1.2$, $y = 0.9$ and $J'/J_0 = 0.16$ are set and will not be varied. Their calculation is performed by a deepCUT using the 1n generator up to order 13 in x, see Appendix E for the numerical results.
At this point we focus on bilinear terms stemming from the anisotropic couplings because only they influence the one-particle dispersion on the mean-field level. Therefore, we treate the DM interactions by a mean-field approach like we did before with the interladder coupling J', see sect. 4.1.2. This approximation is justified with the expected smallness of the DM interactions compared to the corresponding isotropic Heisenberg couplings.

To derive a Hamiltonian for BCPO containing anisotropic interactions on bilinear operator level, we perform the following steps:

1st Write down the anisotropic interaction terms in the basis of the spin operators $S_i^{\alpha,\mathrm{L/R}}$.

2nd Map the spin operators $S_i^{\alpha,\mathrm{L/R}}$ onto the effective spin operators $S_{i,\mathrm{eff}}^{\alpha,\mathrm{L/R}}$, see eqs. (4.1.3) and (4.1.4), using the results of the deepCUT.

3rd We treate the triplon operators as standard bosonic operators in a mean-field approach and apply a FOURIER transform, see eqs. (3.1.2). At this point we neglect the hard-core constraint of the triplon operators. This approximation is motivated by the assumption that the main influence of the hard-core constraint is reflected in the dynamics of the single frustrated isotropic spin ladder. Since its solution is calculated by a deepCUT, which respects the hard-core constraint, the main influence of the hard-core constraint is encoded in the coefficients a_δ for the effective spin operators $S^{\alpha,\mathrm{L/R}}_{i,\mathrm{eff}}$, see eq. (4.1.3).

As a result, we receive the effective anisotropic interaction terms which contribute to the Hamiltonian in momentum space k. Of course, we have to perform these steps for all existing components D^α_{ij} and $\Gamma^{\alpha\beta}_{ij}$, see tables 4.1 and 4.2, separately. To illustrate this procedure in detail we choose the component D^z_2. It is the only **D** component with even parity, see table 4.1, which implies that no other **D** component can give a contribution to the Hamiltonian on bilinear operator level since a single triplon operator is odd by construction[5].
First, we write down the corresponding anisotropic interaction term which reads

$$\mathcal{H}^{\mathrm{D}}_{\mathrm{NNN},z} = \sum_i \sum_{\tau\in\{\mathrm{L,R}\}} D^{z,\tau}_{2,i} \left(\mathbf{S}^\tau_i \times \mathbf{S}^\tau_{i+2}\right)_z . \tag{4.2.12}$$

The index i stands for the rungs and the index τ describes the left (L) and right (R) leg of the spin ladder. The component D^z_2 has even parity and an alternating sign, see table 4.1, which means that $D^{z,\mathrm{L}}_{2,i} = D^{z,\mathrm{R}}_{2,i} = (-1)^i D^z_2$ holds. Replacing the spin operators $S^{\alpha,\mathrm{L/R}}_i$ with the effective spin operators $S^{\alpha,\mathrm{L/R}}_{i,\mathrm{eff}}$, see eq. (4.1.3), yields the effective anisotropic interaction

$$\mathcal{H}^{\mathrm{D,eff}}_{\mathrm{NNN},z} = 2D^z_2 \sum_i (-1)^i S^{x,\mathrm{L}}_{i,\mathrm{eff}} \left(S^{y,\mathrm{L}}_{i+2,\mathrm{eff}} - S^{y,\mathrm{L}}_{i-2,\mathrm{eff}}\right). \tag{4.2.13}$$

The last step is to express the effective spin operators in eq. (4.2.13) in terms of triplon operators, see eq. (4.1.3), treat them as free bosons and perform a FOURIER transform, which results in

$$\mathcal{H}^{\mathrm{D,eff}}_{\mathrm{NNN},z} = 4D^z_2 \mathrm{i} \sum_k a(k)\, a(k+\pi) \sin(2k) \left(t^{x,\dagger}_k \left(t^{y,\dagger}_{-k-\pi} + t^y_{k+\pi}\right) - \mathrm{h.c.}\right). \tag{4.2.14}$$

We see that the component D^z_2 is responsible for a coupling between the x mode at momentum k and the y mode at momentum $k+\pi$. As a consequence, it is already

[5] This means that **D** components with odd parity can only generate operator terms which consist of an odd number of single triplon operators, for example linear or trilinear contributions. In the course of this thesis, we pick up on this point when we include processes of SQPD in BCPO.

assured that the dispersions of the different modes will be split since the effective anisotropic Hamiltonian does not treat all spin flavors equally as expected.

For the next step we have to calculate the dispersions of the effective anisotropic Hamiltonian containing the influence of all $\mathbf{D}_{ij}$ components and Γ_{ij} entries with even parity since only they can give a contribution within our approach. As the effective anisotropic Hamiltonian consists of triplon operator terms of the types

$$t^{\alpha,\dagger}_{k,l}t^{\alpha}_{k,l}, \quad t^{\alpha,\dagger}_{k,l}t^{\alpha,\dagger}_{-k,-l}, t^{\alpha}_{k,l}t^{\alpha}_{-k,-l}, \quad t^{x,\dagger}_{k,l}t^{y,\dagger}_{-k-\pi,-l}, t^{x}_{k,l}t^{y}_{-k-\pi,-l}, \quad t^{x,\dagger}_{k,l}t^{y}_{k+\pi,l}, t^{y,\dagger}_{k+\pi,l}t^{x}_{k,l} \tag{4.2.15}$$

with flavors $\alpha \in \{x, y, z\}$, we can apply the general ansatz, presented in sect. 2.2.1, to diagonalize it.
Considering the z mode it turns out that it does not couple to the x and y mode. Only the symmetric anisotropic interactions Γ^{zz}_0, Γ^{zz}_1 and Γ^{zz}_2 have an effect on the z mode, see table 4.2 and eq. (4.2.11). Therefore, the effective anisotropic Hamiltonian for the z mode is given by

$$\mathcal{H}^{\text{eff}}_{\text{BCPO},z} = \sum_{k,l} \epsilon_z(k,l)\, t^{z,\dagger}_{k,l}t^{z}_{k,l} + \mu_z(k,l)\left(t^{z,\dagger}_{k,l}t^{z,\dagger}_{-k,-l} + t^{z}_{k,l}t^{z}_{-k,-l}\right) \tag{4.2.16}$$

with the definitions

$$\epsilon_z(k,l) = \omega_0(k) - 2J'\cos(l)\,a^2(k) - 2\Gamma^{zz}_0 a^2(k) + 4\Gamma^{zz}_1 a^2(k)\cos(k) + 4\Gamma^{zz}_2 a^2(k)\cos(2k) \tag{4.2.17a}$$

$$\mu_z(k,l) = -J'\cos(l)\,a^2(k) - \Gamma^{zz}_0 a^2(k) + 2\Gamma^{zz}_1 a^2(k)\cos(k) + 2\Gamma^{zz}_2 a^2(k)\cos(2k)\,. \tag{4.2.17b}$$

Comparing the Hamiltonian $\mathcal{H}^{\text{eff}}_{\text{BCPO},z}$ with the Hamiltonian $\mathcal{H}_{\text{Bogo}}$, see eq. (2.2.44) in sect. 2.2.2, leads to the conclusion that $\mathcal{H}^{\text{eff}}_{\text{BCPO},z}$ can be solved with a bosonic BOGOLIUBOV transformation. Following the results from sect. 2.2.2 it becomes clear that the mapping on bosonic operators $\tilde{t}^{z,\dagger}_{k,l}/\tilde{t}^{z}_{k,l}$ via the transformation

$$t^{z,\dagger}_{k,l} = \cosh\left(\vartheta^z_{k,l}\right)\tilde{t}^{z,\dagger}_{k,l} + \sinh\left(\vartheta^z_{k,l}\right)\tilde{t}^{z}_{-k,-l} \tag{4.2.18a}$$

$$t^{z}_{-k,-l} = \cosh\left(\vartheta^z_{k,l}\right)\tilde{t}^{z}_{-k,-l} + \sinh\left(\vartheta^z_{k,l}\right)\tilde{t}^{z,\dagger}_{k,l} \tag{4.2.18b}$$

with the parameter $\vartheta^z_{-k,-l} = \vartheta^z_{k,l}$ fulfilling the condition

$$\tanh\left(2\vartheta^z_{k,l}\right) = -\frac{2\mu_z(k,l)}{\epsilon_z(k,l)} \tag{4.2.19}$$

diagonalizes the Hamiltonian $\mathcal{H}^{\text{eff}}_{\text{BCPO},z}$. The solved Hamiltonian

$$\widetilde{\mathcal{H}}^{\text{eff}}_{\text{BCPO},z} = \sum_{k,l} \widetilde{\omega}_z\left(k,l\right) \tilde{t}^{z,\dagger}_{k,l} \tilde{t}^{z}_{k,l} \tag{4.2.20}$$

describes non-interacting bosonic quasiparticles with the one-particle dispersion[6]

$$\widetilde{\omega}_z\left(k,l\right) = \widetilde{\omega}_z\left(k\right) = \sqrt{\left(\epsilon_z\left(k,l\right)\right)^2 - 4\left(\mu_z\left(k,l\right)\right)^2}. \tag{4.2.21}$$

The remaining part of the effective anisotropic Hamiltonian is more complicated to solve because it contains operator terms, which affect the x and y mode separately and couples the x and y mode at different momenta k and $k+\pi$, see eq. (4.2.15). This type of Hamiltonian, i.e. the effective anisotropic Hamiltonian including only the operator terms of the x and y mode, can be solved by the general ansatz, explained in sect. 2.2.1, as the issue is a quadratic bosonic Hamiltonian.
Therefore, it is necessary to rewrite the remaining effective anisotropic Hamiltonian in a generalized Nambu notation[7], see eq. (2.2.12),

$$\mathcal{H}^{\text{eff}}_{\text{BCPO},xy} = \frac{1}{2} \sum_{k,l} \boldsymbol{\alpha}^{\dagger}_{k,l} \mathcal{M}_{k,l} \boldsymbol{\alpha}_{k,l}, \tag{4.2.22}$$

whereas the column vector $\boldsymbol{\alpha}_{k,l}$ contains the bosonic triplon operators

$$\boldsymbol{\alpha}_{k,l} = \left(t^{x,\dagger}_{k,l}, t^{y,\dagger}_{k+\pi,l}, t^{x}_{-k,-l}, t^{y}_{-k-\pi,-l}\right)^{\mathrm{T}}. \tag{4.2.23}$$

Note, that the sum in eq. (4.2.22) runs over all values of $l \in [0, 2\pi)$ (lattice constant set to unity) in the BRILLOUIN zone while it runs only over the values $k \in [0, \pi)$, i.e. over half the BRILLOUIN zone. The reason is that the above column vector in eq. (4.2.23) addresses the momenta k and $k+\pi$ simultaneously. Note also, that this ansatz is not completely equivalent to the ansatz explained in sect. 2.2.1 because we exploit the fact that the analyzed Hamiltonian conserves momentum up to a factor of π. Therefore, the

[6] As mentioned before in sect. 4.1.2, the measured data of BCPO were obtained for a fixed momentum $l = 1\,\text{r.l.u.}$ and vary in the momentum k. Therefore, we neglect the second momentum l and write $\widetilde{\omega}_z\left(k\right)$ instead of $\widetilde{\omega}_z\left(k,l\right)$.
[7] As we are only interested in the dynamics of the triplons, we neglect unimportant constants.

matrix $\mathcal{M}_{k,l}$ is a Hermitian 4×4 matrix

$$\mathcal{M}_{k,l} = \begin{pmatrix} \omega_0(k) + A(k,l) & \mathrm{i}B(k) & A(k,l) & \mathrm{i}B(k) \\ -\mathrm{i}B(k) & \omega_0(k+\pi) + C(k,l) & -\mathrm{i}B(k) & C(k,l) \\ A(k,l) & \mathrm{i}B(k) & \omega_0(k) + A(k,l) & \mathrm{i}B(k) \\ -\mathrm{i}B(k) & C(k,l) & -\mathrm{i}B(k) & \omega_0(k+\pi) + C(k,l) \end{pmatrix} \tag{4.2.24}$$

with the shorthand notations

$$A(k,l) = d_1(k,l) + \Gamma_0^{xx}(k) + \Gamma_1^{xx}(k) + \Gamma_2^{xx}(k) \tag{4.2.25a}$$

$$B(k) = \Gamma_1^{xy}(k) - D_2^z(k) \tag{4.2.25b}$$

$$C(k,l) = d_2(k,l) + \Gamma_0^{yy}(k) + \Gamma_1^{yy}(k) + \Gamma_2^{yy}(k). \tag{4.2.25c}$$

The abbreviations in eqs. (4.2.25) stand for

$$d_1(k,l) = -2J' \cos(l)\, a^2(k) \tag{4.2.26a}$$

$$d_2(k,l) = -2J' \cos(l)\, a^2(k+\pi) \tag{4.2.26b}$$

$$\Gamma_0^{xx}(k) = -2\Gamma_0^{xx} a^2(k) \tag{4.2.26c}$$

$$\Gamma_1^{xx}(k) = 4\Gamma_1^{xx} a^2(k) \cos(k) \tag{4.2.26d}$$

$$\Gamma_2^{xx}(k) = 4\Gamma_2^{xx} a^2(k) \cos(2k) \tag{4.2.26e}$$

$$\Gamma_0^{yy}(k) = -2\Gamma_0^{yy} a^2(k+\pi) \tag{4.2.26f}$$

$$\Gamma_1^{yy}(k) = -4\Gamma_1^{yy} a^2(k+\pi) \cos(k) \tag{4.2.26g}$$

$$\Gamma_2^{yy}(k) = 4\Gamma_2^{yy} a^2(k+\pi) \cos(2k) \tag{4.2.26h}$$

$$\Gamma_1^{xy}(k) = 4\Gamma_1^{xy} a(k)\, a(k+\pi) \sin(k) \tag{4.2.26i}$$

$$D_2^z(k) = 4D_2^z a(k)\, a(k+\pi) \sin(2k). \tag{4.2.26j}$$

As described in sect. 2.2.1 solving the effective anisotropic Hamiltonian $\mathcal{H}^{\mathrm{eff}}_{\mathrm{BCPO},xy}$ is equivalent to mapping the bosonic triplon operators, included in the vector $\boldsymbol{\alpha}_{k,l}$, onto new bosonic quasiparticle operators which we denote with the flavors b and u. This mapping can be expressed by the relation

$$\boldsymbol{\beta}_{k,l} = K_{k,l} \boldsymbol{\alpha}_{k,l}, \tag{4.2.27}$$

see also eq. (2.2.14), with the column vector

$$\boldsymbol{\beta}_{k,l} = \left(\tilde{t}^{b,\dagger}_{k,l}, \tilde{t}^{u,\dagger}_{k,l}, \tilde{t}^{b}_{-k,-l}, \tilde{t}^{u}_{-k,-l} \right)^{\mathrm{T}} \tag{4.2.28}$$

containing the new bosonic quasiparticle operators with the flavors b and u. The matrix $K_{k,l}$ characterizes the connection between the different bosonic operators for each momentum pair (k,l), i.e. it states the corresponding canonical transformation. Following the steps described in sect. 2.2.1 we choose the matrix $K_{k,l}$ to diagonalize the matrix

$$\eta\mathcal{M}_{k,l} = \begin{pmatrix} \omega_0(k) + A(k,l) & \mathrm{i}B(k) & A(k,l) & \mathrm{i}B(k) \\ -\mathrm{i}B(k) & \omega_0(k+\pi) + C(k,l) & -\mathrm{i}B(k) & C(k,l) \\ -A(k,l) & -\mathrm{i}B(k) & -\omega_0(k) - A(k,l) & -\mathrm{i}B(k) \\ \mathrm{i}B(k) & -C(k,l) & \mathrm{i}B(k) & -\omega_0(k+\pi) - C(k,l) \end{pmatrix} \tag{4.2.29}$$

in order to solve the Hamiltonian $\mathcal{H}^{\mathrm{eff}}_{\mathrm{BCPO},xy}$. Note that the matrix $\eta\mathcal{M}_{k,l}$ fulfills the relation $\eta\mathcal{M}_{k,l} = \mathcal{M}^{\mathrm{T}}_{\mathrm{all}}$, see Ref. [89]. The matrix $\mathcal{M}_{\mathrm{all}}$ describes the same issue and was derived with a different ansatz. For further details we refer to Ref. [89]. Since transposing an $n \times n$ matrix does not change its eigenvalues, we can take over the analytic expression for the eigenvalues of $\eta\mathcal{M}_{k,l}$, which yields

$$\widetilde{\omega}_{b,u}(k,l) = \widetilde{\omega}_{b,u}(k) = \pm\sqrt{\frac{1}{2}\Omega_1^2(k,l) \pm \frac{1}{2}\sqrt{\Omega_2^2(k,l) + 16\omega_0(k)\,\omega_0(k+\pi)\,B^2(k)}} \tag{4.2.30}$$

with[8]

$$\Omega_1(k,l) = (\omega_0(k))^2 + 2\omega_0(k)\,A(k,l) + (\omega_0(k+\pi))^2 + 2\omega_0(k+\pi)\,C(k,l) \tag{4.2.31a}$$

$$\Omega_2(k,l) = (\omega_0(k))^2 + 2\omega_0(k)\,A(k,l) - (\omega_0(k+\pi))^2 - 2\omega_0(k+\pi)\,C(k,l)\,. \tag{4.2.31b}$$

As a consequence, the solution of the effective anisotropic Hamiltonian $\mathcal{H}^{\mathrm{eff}}_{\mathrm{BCPO},xy}$ is given by

$$\widetilde{\mathcal{H}}^{\mathrm{eff}}_{\mathrm{BCPO},bu} = \sum_k \left(\widetilde{\omega}_b(k)\,\tilde{t}^{b,\dagger}_k \tilde{t}^b_k + \widetilde{\omega}_u(k)\,\tilde{t}^{u,\dagger}_k \tilde{t}^u_k\right) \tag{4.2.32}$$

with the dispersion $\widetilde{\omega}_b(k)$ corresponding to the positive lower value of eq. (4.2.30), and the dispersion $\widetilde{\omega}_u(k)$ belonging to the positive upper value of eq. (4.2.30). The solved Hamiltonian $\widetilde{\mathcal{H}}^{\mathrm{eff}}_{\mathrm{BCPO},bu}$ is diagonal in momentum space k and consists of two new bosonic quasiparticles with the flavors b and u.

Note, that the dispersions $\widetilde{\omega}_b(k)$ and $\widetilde{\omega}_u(k)$ contain contributions of the original x mode at momentum k and of the original y mode at momentum $k+\pi$, see the entries of the column vector $\boldsymbol{\alpha}_{k,l}$ in eq. (4.2.23). As the x mode at momentum k and the y mode at momentum $k+\pi$ couple, no clear mapping of the original x and y modes onto the new bosonic quasiparticles with flavors b and u can be made. Since the sum in eq.

[8]Note, that within our applied ansatz in order to solve the Hamiltonian $\mathcal{H}^{\mathrm{eff}}_{\mathrm{BCPO},xy}$ its eigenvalues occur in pairs $(\pm\widetilde{\omega}_b(k), \pm\widetilde{\omega}_u(k))$, see eq. (4.2.30) and sect. 2.2.1.

(4.2.32) runs over the values $k \in [0, \pi)$, and to ensure that no mode is counted twice, we associate the dispersions $\widetilde{\omega}_b(k)$ and $\widetilde{\omega}_u(k)$ within the intervall $k \in [0, \pi)$ with the original x mode at momentum k. As a consequence, the original y mode at momentum k corresponds to the shifted dispersions $\widetilde{\omega}_b(k+\pi)$ and $\widetilde{\omega}_u(k+\pi)$ within the same intervall $k \in [0, \pi)$. Since the experimental data address all modes simultaneously, we depict our solutions for $\widetilde{\omega}_b(k)$ and $\widetilde{\omega}_b(k+\pi)$ in results[9].

Since the aim of this thesis is to analyze the effects of SQPD in BCPO we need to address the full diagonalizing transformation of the matrix $\eta\mathcal{M}_{k,l}$, i.e. we have to calculate the eigenvalues and the corresponding eigenvectors. As explained in sect. 2.2.1, the inverse matrix $K_{k,l}^{-1}$ for each momentum pair (k,l) consists of the eigenvectors of the non-Hermitian matrix $\eta\mathcal{M}_{k,l}$. We decide to assign the positive lower eigenvalue of eq. (4.2.30) to the b mode and the other positive eigenvalue to the u mode. As a consequence, the first column vector of the inverse matrix $K_{k,l}^{-1}$ yields the eigenvector belonging to the positive lower eigenvalue $\widetilde{\omega}_b(k)$, which we denote with $\mathbf{K}^{(0)}(k,l)$. Therefore, the second column of the inverse matrix $K_{k,l}^{-1}$ is given by the eigenvector $\mathbf{K}^{(1)}(k,l)$ which belongs to the eigenvalue $\widetilde{\omega}_u(k)$.
Following the results derived in sect. 2.2.1 and due to the fact that the eigenvalues fulfill the relation

$$\widetilde{\omega}_{b,u}(-k,-l) = \widetilde{\omega}_{b,u}(k,l) \tag{4.2.33}$$

we can determine the components of the eigenvectors $\mathbf{K}^{(2)}(k,l)$ and $\mathbf{K}^{(3)}(k,l)$, which belong to the negative eigenvalues $-\widetilde{\omega}_b(k,l)$ and $-\widetilde{\omega}_u(k,l)$, without calculating them explicitly. With the explicit representation of the eigenvectors

$$\mathbf{K}^{(0)}(k,l) = \left(K_{00}^{-1}(k,l), K_{10}^{-1}(k,l), K_{20}^{-1}(k,l), K_{30}^{-1}(k,l)\right)^{\mathrm{T}} \tag{4.2.34a}$$

$$\mathbf{K}^{(1)}(k,l) = \left(K_{01}^{-1}(k,l), K_{11}^{-1}(k,l), K_{21}^{-1}(k,l), K_{31}^{-1}(k,l)\right)^{\mathrm{T}} \tag{4.2.34b}$$

the components of the eigenvectors $\mathbf{K}^{2}(k,l)$ and $\mathbf{K}^{3}(k,l)$ read

$$\mathbf{K}^{(2)}(k,l) = \left(K_{20}^{-1}(k,l), K_{30}^{-1}(k,l), K_{00}^{-1}(k,l), K_{10}^{-1}(k,l)\right)^{\mathrm{T}} \tag{4.2.35a}$$

$$\mathbf{K}^{(3)}(k,l) = \left(K_{21}^{-1}(k,l), K_{31}^{-1}(k,l), K_{01}^{-1}(k,l), K_{11}^{-1}(k,l)\right)^{\mathrm{T}}, \tag{4.2.35b}$$

see also eq. (2.2.28). As a result, only the explicit calculation of the eigenvectors $\mathbf{K}^{(0)}(k,l)$ and $\mathbf{K}^{(1)}(k,l)$, which belong to the positive eigenvalues $\widetilde{\omega}_{b,u}(k)$, is necessary.

[9] During our analysis it turned out that we can only describe the low-energy regime of BCPO using our present model, which means that the anisotropic effects on the dispersion $\widetilde{\omega}_u(k)$ are not relevant at this point, see also sect. 4.2.3.

Another issue one has to take into account when computing the eigenvectors $\mathbf{K}^{(0)}(k,l)$ and $\mathbf{K}^{(1)}(k,l)$ is their normalization. Numerical tools provide eigenvectors which have an EUCLIDEAN norm equal to one. As outlined in sect. 2.2.1 the eigenvectors of the non-Hermitian matrix $\eta\mathcal{M}_{k,l}$ have to obey the "symplectic" norm for each momentum pair (k,l) reading

$$\left(\mathbf{K}^{(i)}(k,l)\right)^{\dagger}\eta\mathbf{K}^{(j)}(k,l)=\delta_{i,j} \tag{4.2.36}$$

with the indices $i,j\in\{0,1\}$ so that the new quasiparticle modes b and u fulfill bosonic algebra. This means that it is crucial to rescale the eigenvectors $\mathbf{K}^{(0)}(k,l)$ and $\mathbf{K}^{(1)}(k,l)$ after determining them by an appropriate programming routine[10].
The second important point is the phase of the eigenvectors of $\eta\mathcal{M}_{k,l}$ which can be chosen arbitrarily up to this point. Therefore, it is necessary to set up an additional criterion which solves this issue. For k-values which are multiples of π the effective anisotropic Hamiltonian $\mathcal{H}^{\text{eff}}_{\text{BCPO},xy}$, see eq. (4.2.22) does not couple the x and y mode. For this specific k-values the x and y have to be treated separately like it is the case for the z mode using a bosonic BOGOLIUBOV transformation. As a consequence, the components of the eigenvectors simply read

$$\mathbf{K}^{(0)}(k,l)=\left(\cosh\left(\vartheta^{x}_{k,l}\right),0,\sinh\left(\vartheta^{x}_{k,l}\right),0\right)^{\mathrm{T}} \tag{4.2.37a}$$

$$\mathbf{K}^{(1)}(k,l)=\left(0,\cosh\left(\vartheta^{y}_{k+\pi,l}\right),0,\sinh\left(\vartheta^{y}_{k+\pi,l}\right)\right)^{\mathrm{T}} \tag{4.2.37b}$$

in order to provide the solutions of separate bosonic BOGOLIUBOV transformations for the x and y mode. By analogy with the isolated z mode the parameters $\vartheta^{x}_{k,l}$ and $\vartheta^{y}_{k+\pi,l}$ have to fulfill the conditions

$$\tanh\left(2\vartheta^{x}_{k,l}\right)=-\frac{2\mu_x(k,l)}{\epsilon_x(k,l)} \tag{4.2.38a}$$

$$\tanh\left(2\vartheta^{y}_{k+\pi,l}\right)=-\frac{2\mu_y(k+\pi,l)}{\epsilon_y(k+\pi,l)} \tag{4.2.38b}$$

[10] In this thesis we use the programming routines of EIGEN in C++.

using the abbreviations

$$\frac{\epsilon_x(k,l)}{2} = \frac{\omega_0(k)}{2} - J'\cos(l)\,a^2(k) - \Gamma_0^{xx}a^2(k) + 2\Gamma_1^{xx}a^2(k)\cos(k) + 2\Gamma_2^{xx}a^2(k)\cos(2k) \tag{4.2.39a}$$

$$\frac{\mu_x(k,l)}{2} = -\frac{J'\cos(l)\,a^2(k)}{2} - \frac{\Gamma_0^{xx}a^2(k)}{2} + \Gamma_1^{xx}a^2(k)\cos(k) + \Gamma_2^{xx}a^2(k)\cos(2k) \tag{4.2.39b}$$

$$\frac{\epsilon_y(k,l)}{2} = \frac{\omega_0(k)}{2} - J'\cos(l)\,a^2(k) - \Gamma_0^{yy}a^2(k) + 2\Gamma_1^{yy}a^2(k)\cos(k) + 2\Gamma_2^{yy}a^2(k)\cos(2k) \tag{4.2.39c}$$

$$\frac{\mu_y(k,l)}{2} = -\frac{J'\cos(l)\,a^2(k)}{2} - \frac{\Gamma_0^{yy}a^2(k)}{2} + \Gamma_1^{yy}a^2(k)\cos(k) + \Gamma_2^{yy}a^2(k)\cos(2k)\,. \tag{4.2.39d}$$

As a reminder, we want to introduce a criterion to fix the phase of the eigenvectors of $\eta\mathcal{M}_{k,l}$. In order to reproduce the special cases for the decoupled x and y mode, as already discussed, we choose the phase in such a way that the entry with the largest modulus is a positive real number. To explain this idea in detail we consider the general numerical solution of the eigenvector

$$\mathbf{K}^{(0)}(k,l) = \left(K_{00}^{-1}(k,l), 0, K_{20}^{-1}(k,l), 0\right)^{\mathrm{T}} \tag{4.2.40}$$

in the case of the decoupled x and y mode with the possible complex entries

$$K_{00}^{-1}(k,l) = a_{00}(k,l) + \mathrm{i}b_{00}(k,l) \tag{4.2.41a}$$

$$K_{20}^{-1}(k,l) = a_{20}(k,l) + \mathrm{i}b_{20}(k,l) \tag{4.2.41b}$$

using the real coefficients $a_{00}(k,l)$, $b_{00}(k,l)$, $a_{20}(k,l)$ and $b_{20}(k,l)$. Out of these four real coefficients we have to identify the one whose absolute value is the largest. Then the phase of the eigenvector is chosen such that the eigenvector entry with this outlined coefficient is real and positive.
For our example this means that if we found the coefficient $b_{00}(k,l) < 0$ to have the largest absolute value, we have to multiply the whole eigenvector $\mathbf{K}^{(0)}(k,l)$ with the imaginary unit i. The complex entries then read

$$K_{00}^{-1}(k,l) = -b_{00}(k,l) + \mathrm{i}a_{00}(k,l) \tag{4.2.42a}$$

$$K_{20}^{-1}(k,l) = -b_{20}(k,l) + \mathrm{i}a_{20}(k,l) \tag{4.2.42b}$$

with the realpart $-b_{00}(k,l)$ being a positive number and having the largest absolute

value compared to the other coefficients $a_{00}(k,l)$, $a_{20}(k,l)$ and $b_{20}(k,l)$. After that, we have to ensure that the imaginary part of the component $K_{00}^{-1}(k,l)$ vanishes. We achieve this by multiplying the whole eigenvector with the complex phase $e^{i\frac{a_{00}(k,l)}{b_{00}(k,l)}}$. This criterion concerning the complex phase of the eigenvectors $\mathbf{K}^{(0)}(k,l)$ and $\mathbf{K}^{(1)}(k,l)$ is reasonable since it reproduces the solutions for the case of the decoupled x and y modes, see eqs. (4.2.37a).

With these two criteria concerning the length and the phase of the eigenvectors $\mathbf{K}^{(0)}(k,l)$ and $\mathbf{K}^{(1)}(k,l)$ it is numerically ensured that the inverse matrix $K_{k,l}^{-1}$ describes a canonical transformation between the original x and y modes and the new bosonic quasiparticles with the flavors b and u.

4.2.3 Results for the bilinear anisotropic Hamiltonian of BCPO

The main goal of the bilinear anisotropic description of BCPO is to determine the values of the allowed $\mathbf{D}$ components, see table 4.1, which provide the best fit to the experimentally measured data of the dispersions. We received the experimental data for the one-particle dispersions, initially published in Ref. [70], by private communication from the corresponding author. These data have been received by performing inelastic neutron scattering (INS), which represents a well-established method to study the properties of magnetic excitations in solid states [32–34].

To create a basis for fitting the experimental dispersion data by adjusting the anisotropic couplings we study the effects of each component on the calculated dispersion $\widetilde{\omega}_b(k)$[11], see eq. (4.2.30). The results are listed in table 4.3.
We forego a detailed analysis concerning the effects of each $\mathbf{D}$ component on the dispersion $\widetilde{\omega}_b(k)$ as the main issue of this thesis is the influence of SQPD in BCPO. The effects on bilinear operator level constitute a starting point for this task.
With the knowledge of the effects of each $\mathbf{D}$ component we can search for the values of the $\mathbf{D}$ components which provide the best match between our calculated dispersions and the experimentally received data in a systematic manner. We undertake the results of the isotropic approach, see sect. 4.1, i.e. the parameters $x = 1.2$, $y = 0.9$ and $J'/J_0 = 0.16$ are kept fixed. With this starting point we search for appropriate values of the $\mathbf{D}$ components and the energy scale J_0. We indicate the $\mathbf{D}$ components in units of the associated isotropic coupling, i.e. $\widetilde{D}_i^\alpha = D_i^\alpha / J_i$ with $i \in \{0,1,2\}$ holds.

[11] We present only the effects of the anisotropic couplings on $\widetilde{\omega}_b(k)$ because during our analysis it turned out that the dispersion $\widetilde{\omega}_z(k)$ cannot be fitted in a satisfying way. We address this aspect in the following. So far, the effects on the dispersion $\widetilde{\omega}_u(k)$, see eq. (4.2.30), are not relevant for our analysis since we want to describe the low-energy regime.

D_{ij}^{α}	lin.	effect on $\widetilde{\omega}_b(k)$
D_0^y	✗	increase in the complete BRILLOUIN zone
D_1^x	✗	asymmetric shift about $k = \frac{\pi}{2}$
		$\rightarrow$ lowering at $k > \frac{\pi}{2}$
D_1^y	✗	asymmetric shift about $k = \frac{\pi}{2}$
		$\rightarrow$ lowering at $k < \frac{\pi}{2}$
D_2^x	✗	lowering around the minimum
D_2^z	✓	linear effect: shift minimum to higher k-values
		quadratic effect: increase around the minimum

Table 4.3: Effects of an increase of the various **D**-components on the dispersion $\widetilde{\omega}_b(k)$, see eq. (4.2.30). If the component induces an effect in linear order it is marked by ✓, otherwise we put ✗. All components contribute in quadratic order, i.e. via the symmetric Γ-components.

In the following we discuss several issues concerning our best fit, which is shown in figure 4.4.

(i) It is possible to achieve a good description in the minimum area of mode 1 and mode 2 with the calculated dispersions $\widetilde{\omega}_b(k)$ and $\widetilde{\omega}_b(k+\pi)$, which stem from the x and y mode. The fitted values of the components $\widetilde{D}_1^x$ and $\widetilde{D}_1^y$ are large stating an unsatisfying feature. We expected the relative anisotropic couplings to assume values in the order of $0.1 - 0.2$ as they come from the SOC, see sect. 2.4.1. But we have to choose the components $\widetilde{D}_1^x$ and $\widetilde{D}_1^y$ so large in order to obtain a sufficient large value of Γ_1^{xy}, see eq. (2.4.84). This term leads to a lowering of the dispersions $\widetilde{\omega}_b(k)$ and $\widetilde{\omega}_b(k+\pi)$ around the point $k = 0.5\,\text{r.l.u.}$ and to a flattening of the W-shape of the dispersions. At $k = 0.5\,\text{r.l.u.}$ the dispersion without anisotropic couplings, see the black dashed line in figure 4.4, takes a value of 7.00 meV but the experimental data of mode 1 and mode 2 reveal values of 3.20 meV and 3.55 meV. This means that the anisotropic couplings have to reduce the dispersion at this point by 3 to 4 meV. To obtain this large energy difference the component Γ_1^{xy}, which has the main influence on the dispersion at $k = 0.5\,\text{r.l.u.}$, has to assume a large value. Therefore, the components $\widetilde{D}_1^x$ and $\widetilde{D}_1^y$ need to be chosen large. We set $\widetilde{D}_1^y$ to be slightly larger than $\widetilde{D}_1^x$ to create a small asymmetric behavior of the dispersions about $k = 0.5\,\text{r.l.u.}$, which is apparent in the experimental data. Note that it is possible to swap the course of the two lower modes stemming from the x and y mode by simply swapping the values of $\widetilde{D}_1^x$ and $\widetilde{D}_1^y$.

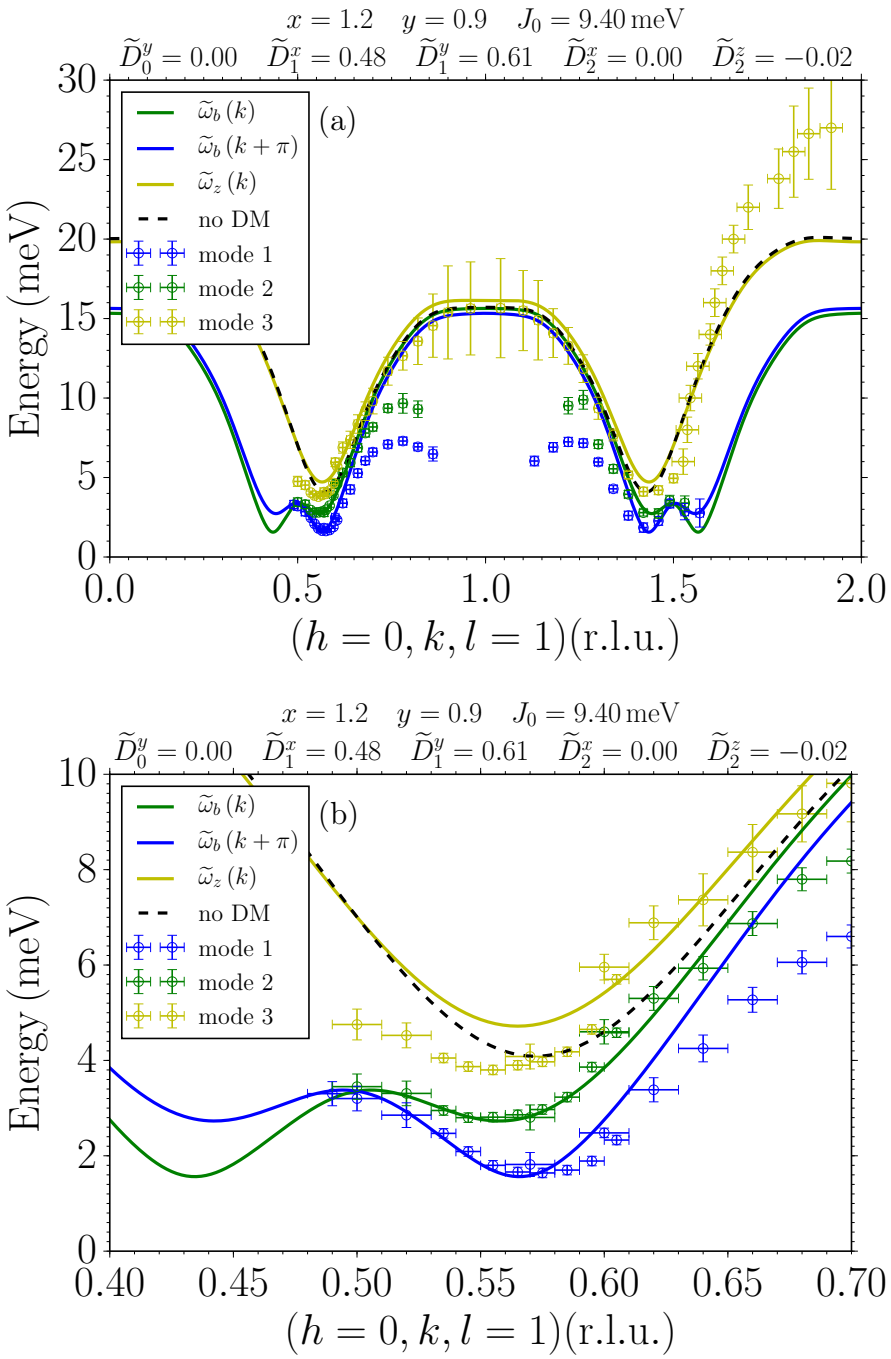

Figure 4.4: (a) Fitted theoretical dispersions $\widetilde{\omega}_z(k)$, $\widetilde{\omega}_b(k)$ and $\widetilde{\omega}_b(k+\pi)$, which stem from the z, x and y mode for the fixed parameters $x = 1.2$, $y = 0.9$ and $J'/J_0 = 0.16$. The fitted parameters are J_0, $\widetilde{D}_0^y$, $\widetilde{D}_1^x$, $\widetilde{D}_1^y$, $\widetilde{D}_2^x$ and $\widetilde{D}_2^z$. Their values are listed in the panel itself. (b) Zoom of panel (a) into the vicinity of the left minimum.

(ii) We choose the value of $\widetilde{D}_2^z$ to be negative and small, compared to the parameters $\widetilde{D}_1^x$ and $\widetilde{D}_1^y$. At first, this does not seem intuitive since the component $\widetilde{D}_2^z$ is the only one directly affecting the dispersions in linear order due to its even parity, see tables 4.1

and 4.3. But it turned out that the linear effect of $\widetilde{D}_2^z$ is rather small and its quadratic effect via the matrix entries Γ_2^{xx} and Γ_2^{yy} is not conducive for fitting the dispersion $\widetilde{\omega}_b(k)$ around the minimum, see table 4.3. The negative sign of $\widetilde{D}_2^z$ can be explained by analyzing eq. (4.2.30) in detail. Only a negative sign for $\widetilde{D}_2^z$ can provide a positive combination of the effects of Γ_1^{xy} and $\widetilde{D}_2^z$, i.e. the asymmetric shift about $k = 0.5\,\text{r.l.u.}$ and the shift of the minimum to higher k-values, so that the minimum is approximated in a satisfying way.

(iii) Figure 4.4 reveals major discrepancies between the shape of the calculated z mode $\widetilde{\omega}_z(k)$ and the measured mode 3. These cannot be eliminated without the loss of the satisfying description of mode 1 and mode 2 around the minimum. The overall shape of the calculated dispersion $\widetilde{\omega}_z(k)$, see eq. (4.2.21), is similiar to the dispersion without any anisotropic couplings. However, this appearance is logical since the z mode is isolated from the x and y mode and solved by an own bosonic Bogoliubov transformation, see eq. (4.2.16). The finite values of the components Γ_1^{zz} and Γ_2^{zz} act on the z mode and increase the dispersion $\widetilde{\omega}_z(k)$, see eq. (4.2.21), around the minimum.

(iv) One dominant characteristic of the two lower measured modes 1 and 2 is the down-bending towards lower energies around $k = 0.75\,\text{r.l.u.}$ and the complete vanishing at around $k = 1\,\text{r.l.u.}$. Our theoretical results for the two lowest modes do not reproduce these effects at all. To explain these features of the measured data we have the strong presumption that at these parts of the Brillouin zone the two-triplon continuum and the one-triplon states hybridize so that the one-triplon dispersions show level repulsion [40, 41]. This will result in the prominent shown down-bending of the two lowest modes. The importance of the discussion of two-triplon continua has already been pointed out qualitatively by Plumb *et al.* [39] and Hwang and Kim [64]. In their approach hybridization effects between the one- and two-particle Hilbert space and two-triplon interactions were taken into account using a quadratic bond operator theory in combination with the Green's function formalism including one-loop self-energy corrections. The main advantage of this ansatz is that the decay behavior of the triplons inside the two-triplon continuum can be reproduced, see figure 1.6. However, one point of criticism is that only a contribution of $\mathbf{D}_1$ to the hybridization effects can be identified and that its level repulsion effects are rather small on the one-loop level. The down-bending behavior of the two lowest modes in BCPO remains inexplainable. So far no quantitative theoretical description of this dominant down-bending behavior exists to our knowledge. We address this issue in the following chapters 5 and 6 of this thesis when the effects of SQPD in BCPO are taken into account and discussed in detail.

(v) The maximum value reached by the calculated z mode is ≈19 meV, whereas the measured maximum value is ≈27 meV. With our derived formular of the z mode it is not possible to achieve a better match between experiment and theory without losing the good fit in the low-energy regime. No parameter in the dispersion $\widetilde{\omega}_z(k)$, see eq. (4.2.21), helps concerning this issue including the isotropic parameters, i.e. x, y and J'. The large error bars of the measured data points at high energies stem from peaks holding a large width in the corresponding DSF, see sect. 2.3.1. This means that these data points represent resonances, see sect. 3.4.1. As a consequence, it is reasonable to presume that states of a higher triplon number and the hybridization with the one-triplon states need to be considered in order to achieve a better fit, especially concerning these resonances. We address this point in the course of this thesis when we discuss the hybridization of two-triplon and one-triplon states, see chapters 5 and 6.

4.2.4 Topological properties of BCPO

Besides the main goal of this thesis to fit the experimentally observed dispersions of BCPO, a project concerning its topological properties was realized and yielded interesting results [71]. In this project the bilinear anisotropic description of BCPO is used in order to calculate different topological quantities such as the Zak phase [138], which is a qualified topological invariant for one-dimensional systems, or the Berry curvature [138, 139]. The two key points of this work are the following statements:

1st The triplon excitations in BCPO hold a non-trivial Zak phase.

2nd Despite the existing non-trivial Zak phase in BCPO, no localized edge modes could be found.

On the first point, we found out that the mode stemming from the z mode with the one-particle dispersion $\widetilde{\omega}_z(k)$, see eq. (4.2.21), is topologically trivial, i.e. it has a vanishing Zak phase in k- and l-direction. In comparison, the modes described by the dispersions $\widetilde{\omega}_b(k)$ and $\widetilde{\omega}_b(k+\pi)$, see eq. (4.2.30), which originate from the x and y mode, hold a non-trivial Zak phase of π in k-direction corresponding to the direction along the spin ladder, see figure 1.3. In perpendicular direction, i.e. in l-direction, their Zak phase is also trivial, i.e. equal to zero. The required difference $\widetilde{D}_1^x \neq \widetilde{D}_1^y$ in order to fit the experimental data, see sect. 4.2.3, is the fundamental reason for this non-trivial Zak phase in k-direction. In the case $\widetilde{D}_1^x = \widetilde{D}_1^y$ the Zak phase vanishes or cannot be defined. With regard to the second key point, it has emerged that the bulk-boundary correspondence has to be refined in its general statement [140–142]. The bulk-boundary correspondence presents a theorem which makes a statement about topological non-trivial invariants implying the existence of in-gap states which are often localized [143–146]. During our analysis it turned out that the bulk-boundary correspondence has to be specified in its statement by respecting the distinction between a *direct* and an *indirect*

gap. We found out that the localization of edge modes requires the existence of an *indirect* gap, i.e. a finite energy difference independent of momentum. In contrast, the existence of a non-trivial topology in particular modes only requires the modes to be separated, i.e. the existence of a *direct* gap at each momentum is sufficient.
Thus, this project has the final result that BCPO is a gapful, disordered quantum antiferromagnet with a non-trivial finite Zak phase and provides a deeper understanding of the bulk-boundary correspondence.

4.3 Chapter summary

The aim of this analysis was to describe its experimentally measured dispersion data by including anisotropic couplings up to bilinear operator level in a mean-field approach. A comprehensive symmetry analysis of the spin ladder structure of BCPO revealed that only one out of five allowed DM interactions has an effect on the Hamiltonian in linear order. The other components contribute in second order. We expected these anisotropic couplings to accept values between 10 % and 20 % of the isotropic couplings. With our present model we could not meet these expectations. We needed to choose large values of $\mathbf{D}_1 \approx 0.6 J_1$ in order to achieve an agreement between experiment and theory in the low-energy regime. Additionally, we could not describe the broad resonances at high energies at $\approx 25\,\mathrm{meV}$. The prominent down-bending behavior is another striking property of the experimental data, which we could not reproduce with our theoretical model until now. However, we have the strong presumption that the hybridization between one-particle states and states of a higher number of triplons is crucial to improve the match. We address this issue in the following chapters 5 and 6.
Our results are consistent with the results of Plumb *et al.*, see Ref. [70]. This group faced the same issue by using the bond operator theory (BOT) on mean-field level. They received the following results for their best fitting parameters: $x = y = 1$, $J_0 = 8\,\mathrm{meV}$, $J' = 1.6\,\mathrm{meV}$, $\widetilde{D}_1^x = 0.6$ and $\widetilde{D}_1^y = 0.45$. Our fitted parameters go roughly with the parameters of Plumb *et al.*, i.e. they only differ up to 20 %. This means that our CUT based approach confirms the BOT results and refines them. As the CUT takes the hard-core constraint of the triplons into account exactly compared to the mean-field approach in the BOT [147], we consider our CUT based results to be more suitable in order to describe the magnetic structure of BCPO. Despite this, the large values of the DM interactions did not fulfill our expectations concerning the anisotropy in the exchange of the copper spins as discussed previously. Finally, we pointed out that BCPO shows also interesting topological features, such as a non-trivial Zak phase and no localized edge modes.

5 Description of the quantum antiferromagnet $BiCu_2PO_6$ on trilinear operator level with spin isotropic effects

In the previous chapter we established a model for the quantum magnet BCPO including anisotropic couplings on bilinear operator level. As a result, we received a satisfying description of the experimentally measured data in the low-energy regime. Thereby, it is necessary to choose DM couplings which assume values up to 60 % compared to the isotropic couplings. The prominent down-bending and vanishing behavior of the two lower modes at around $k = 1\,\mathrm{r.l.u.}$ cannot be described at all with our present model. In contrast, the third measured mode remains stable in this range but shows significant larger error bars implying the existence of resonances. So far no theoretical description of the down-bending exists to our knowledge. Numerous groups in the community of solid state physics agree on the reasonable assumption that the hybridization between one-triplon and multiple-triplon states is responsible for the observed down-bending behavior [39, 64, 70, 89]. To take these effects into account for the quantum antiferromagnet BCPO we need to consider couplings in its magnetic structure which induce operator terms arbitrating between HILBERT spaces of different numbers of triplons.

One existing effect in BCPO which can solve this issue is a variation in the next-nearest-neighbor coupling originating from the two inequivalent copper ions Cu_A and Cu_B, see sect. 1.4. This effect has odd parity and therefore gives rise to transition processes between the one- and two-particle HILBERT space. To the best of our knowledge, no theoretical description of this effect exists in the literature. In this chapter we explore the consequences of this effect in regards to SQPD. With this extension of our model of BCPO we expect to obtain an improved fit between the experimental data and theory choosing smaller DM couplings as in the bilinear anisotropic model, see chapter 4.

5.1 Analysis of the alternating NNN coupling J_2

The simplest processes which describe SQPD are given by trilinear terms reading $t^\dagger t^\dagger t / t^\dagger t t$, see sect. 2.3. These terms characterize the decay of a single triplon into two triplons/the fusion of two triplons into one triplon and induce transitions between the one- and two-particle HILBERT space directly. As already mentioned in sect. 4.2.2, only effects with odd parity with respect to a reflection at the center line of the spin ladder structure, see also sect. 4.2.1 and figure 4.3, can generate operator terms which contain an odd number of single triplon operators, e.g. trilinear operator terms. The key idea of this issue is that a single triplon operator has odd parity, see sect. 4.1.2, and that the parity of an observable represents a conserved quantity.

One effect, which has odd parity in the crystal structure of BCPO, is a variation of the NNN coupling J_2. As mentioned in sect. 1.4, there are two crystallographically different types of copper ions Cu_A and Cu_B existing in BCPO due to the positions of the bismuth ions, see figure 1.3. Thus, it is reasonable to assume that the NNN interaction among the Cu_A and the NNN interaction among the Cu_B differ [60]. We label the NNN interaction concerning the copper ions Cu_A as J_2 and for the copper ions Cu_B as J_2'.

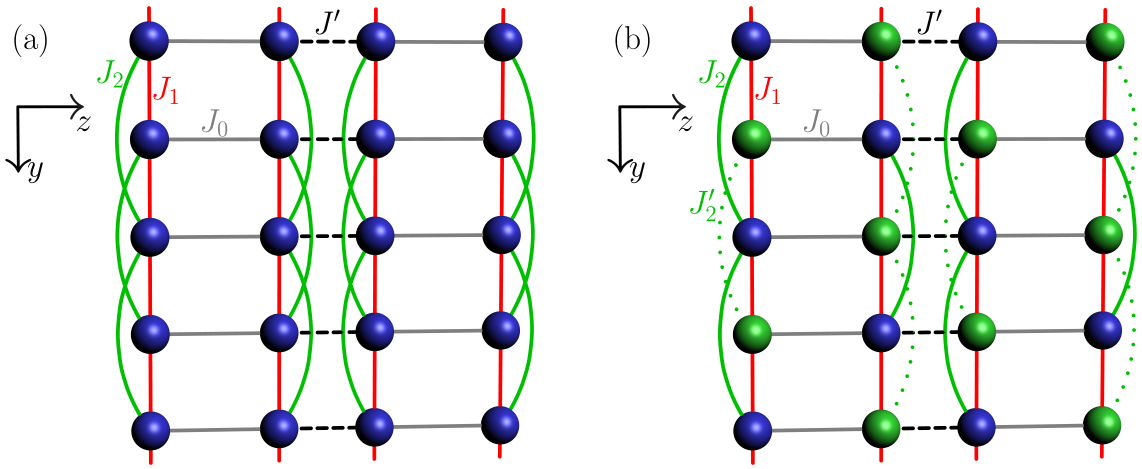

Figure 5.1: (a) Effective spin model without distinguishing between the inequivalent copper sites. All copper sites are treated equally, i.e. the NNN interaction J_2 does not vary. (b) Effective spin model in consideration of the two inequivalent copper ions Cu_A (blue spheres) and Cu_B (green spheres). This effective spin model was proposed by TSIRLIN *et al.* [60]. The NNN interactions between the different copper ions Cu_A and Cu_B are considered differently by J_2 and J_2'. This alternation of the NNN coupling has odd parity with respect to a reflection at the center line of the spin ladder structure.

We can express the difference between the two NNN interactions by

$$J_2 = \begin{cases} J_2 = \overline{J}_2 \left(1 + \delta\right) \\ J_2' = \overline{J}_2 \left(1 - \delta\right) \end{cases} \tag{5.1.1}$$

with an averaged coupling strength $\overline{J}_2$ and a variation parameter $\delta \in [0, 1]$ indicating how large the two NNN interactions differ. In the previous model, see chapter 4, no difference between the NNN couplings was considered, i.e. the case $\delta = 0$ was discussed. The other extreme case is $\delta = 1$ implying that only an interaction between the copper ions of the type Cu_A exists assuming a value of $J_2 = 2\overline{J}_2$.
The couplings J_2 and J_2', see eq. (5.1.1), can be divided into an even part $\left(\overline{J}_2\right)$, which is the same for both NNN couplings, and an odd part $\left(\pm\overline{J}_2\delta\right)$, which changes sign. The even component $\overline{J}_2$ is the part considered in the model of the single frustrated spin ladder discussed before in sect. 4.1.1. This means that the even component $\overline{J}_2$ is identical to the NNN coupling J_2 in chapter 4. To take the effects of the odd part $\pm\overline{J}_2\delta$ into account we treat this component as an observable in the context of perturbation theory. Note, that this is the same ansatz we applied to the anisotropic couplings in sect. 4.2.2. Therefore, we write down the actual observable characterizing the variation of the NNN interaction

$$\overline{J}_2\delta \sum_i \left(-1\right)^i \left(\mathbf{S}_i^{\mathrm{L}}\mathbf{S}_{i+2}^{\mathrm{L}} - \mathbf{S}_i^{\mathrm{R}}\mathbf{S}_{i+2}^{\mathrm{R}}\right), \tag{5.1.2}$$

see eq. (4.1.1). It is easy to realize that this expression has odd parity and alternates along the ladder in y-direction, see figure 5.1 b). Applying a deepCUT transforms the operator part of eq. (5.1.2) into operator terms including an odd number of single triplon operators, e.g. trilinear terms giving rise to the phenomenon of SQPD[1]. Focusing on linear and trilinear operator level leads to the emerging operator terms[2]

$$t_{i+\delta_1}^{y,\dagger} t_{i+\delta_2}^{z,\dagger} t_{i+\delta_3}^{x}, \quad t_{i+\delta_1}^{x,\dagger} t_{i+\delta_2}^{z,\dagger} t_{i+\delta_3}^{y}, \quad t_{i+\delta_1}^{x,\dagger} t_{i+\delta_2}^{y,\dagger} t_{i+\delta_3}^{z}, \quad t_{i+\delta_1}^{x,\dagger} t_{i+\delta_2}^{y,\dagger} t_{i+\delta_3}^{z,\dagger} \tag{5.1.3}$$

with the relative distances δ_1, δ_2 and δ_3 in real space including the Hermitian conjugated part of each operator term. Note, that we only concentrate on terms up to trilinear operator level since we expect these to have the main influence on the effects of SQPD as mentioned before in sect. 3.2.

[1] The applied deepCUT was performed up to order 11 in the Hamiltonian, i.e. up to order 10 for observables [94]. Since the spin ladder structure is invariant under the reflection symmetry S_{xy}, see figure 4.3 and sect. 4.2.1, this means that for observables processes with a maximum distance of 2×10 rungs in real space are taken into account.

[2] In fact, we are only interested in trilinear terms. Despite this, we extract all operator terms up to trilinear operator level, i.e. also linear operator terms if existing.

Performing a deepCUT it turns out that the spin observable in eq. (5.1.2) does not generate linear terms, i.e. a single triplon creation/annihilation operator, although its odd parity can give rise to them. The reason for the absent linear operator terms is that the transformed spin observable in eq. (5.1.2) is spin isotropic, i.e. it stays invariant under shifting the flavors x, y and z. This is equivalent to the statement that the spin observable has a total spin of S=0, i.e. it is spin conserving. In contrast, a single triplon operator always has a concrete spin orientation, i.e. it has a total spin of S=1. So it is obvious that a spin isotropic observable cannot generate linear triplon operator terms in general. Following the steps described in sect. 4.2.2 we treat the triplon operators as bosonic operators in the framework of a mean-field approach and apply a FOURIER transform, see eqs. (3.1.2). This leads to the expression

$$\overline{J}_2\delta \sum_{k,q} \sum_{\delta_1,\delta_2,\delta_3} \frac{\alpha^{\alpha',\beta',\gamma'}_{\delta_1,\delta_2,\delta_3}}{\sqrt{N_k}} \mathrm{e}^{\mathrm{i}(\delta_2-\delta_1)q} \mathrm{e}^{\mathrm{i}(\delta_3-\delta_2)k} \mathrm{e}^{-\mathrm{i}\pi\delta_2} t_q^{\alpha',\dagger} t_{k-q+\pi}^{\beta',\dagger} t_k^{\gamma'} \tag{5.1.4}$$

for the terms of the type $t_{i+\delta_1}^{\alpha',\dagger} t_{i+\delta_2}^{\beta',\dagger} t_{i+\delta_3}^{\gamma'}$ with the flavor combinations $(\alpha',\beta',\gamma') \in \{(y,z,x),(x,z,y),(x,y,z)\}$, see eq. (5.1.3). The variable $\alpha^{\alpha',\beta',\gamma'}_{\delta_1,\delta_2,\delta_3} \in \mathbb{C}$ is the prefactor of the triplon operator terms in real space determined by the applied deepCUT. The quantity N_k describes the discretization of the momentum k. Note, that a relative momentum q corresponding to the total momentum k appears. The alternating sign in the transformed spin observable, see eq. (5.1.2), results in the shift of π concerning the momentum of the second creation operator $t_{k-q+\pi}^{\beta',\dagger}$. The FOURIER transform of the remaining operator term in eq. (5.1.3) reads

$$\overline{J}_2\delta \sum_{k,q} \sum_{\delta_1,\delta_2,\delta_3} \frac{\beta^{x,y,z}_{\delta_1,\delta_2,\delta_3}}{\sqrt{N_k}} \mathrm{e}^{\mathrm{i}(\delta_2-\delta_1)q} \mathrm{e}^{\mathrm{i}(\delta_2-\delta_3)k} \mathrm{e}^{-\mathrm{i}\pi\delta_2} t_q^{x,\dagger} t_{-k-q+\pi}^{y,\dagger} t_k^{z,\dagger} \tag{5.1.5}$$

with the variable $\beta^{x,y,z}_{\delta_1,\delta_2,\delta_3} \in \mathbb{C}$ characterizing the prefactor of the corresponding triplon operator term in real space, which is calculated by the deepCUT applied.
At this point we classify two different approaches in order to include the effects of SQPD stemming from the variation of the NNN coupling J_2.

(i) We take the effects of the decay and fusion terms in eq. (5.1.4) into account directly by adding these terms to the solution of a single frustrated spin ladder as discussed in sect. 4.1.1. This means that the decay and fusion terms are treated as a perturbation to the effective Hamiltonian $\mathcal{H}^{\mathrm{eff}}_{\mathrm{ladder}}$, see eq. (4.1.2) with the one-particle dispersion $\omega_0(k)$. We determine how the dispersion $\omega_0(k)$ is renormalized due to the effects of SQPD. After calculating the renormalized dispersion $\omega_{0,r}(k)$ we add the effects of the interladder coupling J', see sect. 4.1.2, and the effects

of the anisotropic couplings as described in sect. 4.2.2. Note, that this is an inaccurate ansatz since its starting point is the isotropic single frustrated spin ladder, not the bilinear anisotropic model of BCPO, and the effects of SQPD treat all excitation modes as equals. We refer to this approach as the **direct approach**.

(ii) We consider the Hamiltonians $\widetilde{\mathcal{H}}^{\text{eff}}_{\text{BCPO},z}$ and $\widetilde{\mathcal{H}}^{\text{eff}}_{\text{BCPO},bu}$, see eqs. (4.2.20) and (4.2.32), as our starting point and then add the effects of SQPD to the solution of the bilinear anisotropic Hamiltonian of BCPO. In order to do so the trilinear terms resulting from the variation of J_2 have to be transformed by applying the same BOGOLIUBOV transformations derived in sect. 4.2.2, which solve the issue on bilinear anisotropic operator level. Afterwards, we proceed as described in the direct approach and analyze how the dispersions $\widetilde{\omega}_z(k)$ and $\widetilde{\omega}_b(k)$, see eqs. (4.2.21) and (4.2.30), are renormalized. With this accurate ansatz the effects of SQPD treat all excitation modes individually. We name this approach the **complete approach**.

5.2 Results for the direct approach

By applying the direct approach our starting point is the solved single frustrated spin ladder, see sect. 4.1.1, with the one-triplon dispersion $\omega_0(k)$, see eq. (4.1.2). The decay/fusion terms stemming from the J_2 variation, see eq. (5.1.4), can simply be added since they are in the same basis as the Hamiltonian $\mathcal{H}^{\text{eff}}_{\text{ladder}}$, see eq. (4.1.2). The resulting Hamiltonian reads

$$\mathcal{H}_{J_2,\text{direct}} = \sum_{k,\alpha} \omega_0(k)\, t_k^{\alpha,\dagger} t_k^{\alpha} + \overline{J}_2 \delta \sum_{k,q} \sum_{\alpha',\beta',\gamma'} \left(\Gamma^{\alpha'\beta'\gamma'}(k,q)\, t_q^{\alpha',\dagger} t_{k-q+\pi}^{\beta',\dagger} t_k^{\gamma'} + \text{h.c.} \right), \quad (5.2.6)$$

with $\alpha \in \{x,y,z\}$ and the prefactor

$$\Gamma^{\alpha'\beta'\gamma'}(k,q) = \sum_{\delta_1,\delta_2,\delta_3} \frac{\alpha^{\alpha',\beta',\gamma'}_{\delta_1,\delta_2,\delta_3}}{\sqrt{N_k}} \mathrm{e}^{\mathrm{i}(\delta_2-\delta_1)q} \mathrm{e}^{\mathrm{i}(\delta_3-\delta_2)k} \mathrm{e}^{-\mathrm{i}\pi\delta_2} \quad (5.2.7)$$

for the different flavor combinations $(\alpha',\beta',\gamma') \in \{(y,z,x),(x,z,y),(x,y,z)\}$. In the direct approach we only take the influence of operator terms of the type $t^\dagger t^\dagger t / t^\dagger t t$ into account since these describe a hybridization of the one- and two-triplon HILBERT space. As explained in sect. 3.2, we expect these operator terms to have the strongest impact on the phenomenon of quasiparticle decay at zero temperature. Operator terms of the type $t^\dagger t^\dagger t^\dagger / t t t$ in eq. (5.1.5) describe quantum fluctuations creating/annhilating three triplons and are completely neglected in the direct approach. In order to determine the renormalized dispersion $\omega_{0,r}(k)$ of the one-triplon dispersion $\omega_0(k)$ we restrict ourselves to the one- and two-triplon HILBERT spaces and transitions between them, equally to the toy model in sect. 3.2.

The Hamiltonian $\mathcal{H}_{J_2,\text{direct}}$ in eq. (5.2.6) points out a hybridization of the one-triplon states with momentum k and two-triplon states with total momentum $k+\pi$. This shift by π derives from the alternating behavior of the odd J_2 part, see the factor of $(-1)^i$ in eq. (5.1.2) and the effect of the alternating component D_2^z in eqs. (4.2.13) and (4.2.14). As a consequence, the limiting values for the LANCZOS coefficients $a_\infty(k)$ and $b_\infty(k)$, see Appendix A, are given by the lower and upper boundary of the two-particle continuum

$$\omega_2(k+\pi,q) = \omega_0(q) + \omega_0(k-q+\pi) \tag{5.2.8}$$

at total momentum $k+\pi$. Performing a LANCZOS tridiagonalization for the Hamiltonian $\mathcal{H}_{J_2,\text{direct}}$ in eq. (5.2.6) and applying the steps described in sects. 2.3.1, 2.3.2 and 2.3.3 result in the renormalized dispersion $\omega_{0,r}(k)$. Note, that the renormalized dispersion $\omega_{0,r}(k)$ is spin isotropic as well as the one-triplon dispersion $\omega_0(k)$ because the decay/fusion terms in $\mathcal{H}_{J_2,\text{direct}}$ stem from a spin isotropic observable, see sect. 5.1. Due to the fact that the structure of BCPO contains multiple frustrated spin ladders, which are coupled by an interladder coupling J', see sect. 4.1.2, we include this effect in the direct approach as well in order to receive the two-dimensional dispersion

$$\omega_r(k,l) = \omega_r(k) = \sqrt{(\omega_{0,r}(k))^2 - 4J'd_{k,l}\omega_{0,r}(k)}. \tag{5.2.9}$$

This expression is identical to eq. (4.1.10) with the simple substitution $\omega_0(k) = \omega_{0,r}(k)$[3]. With the help of eq. (5.2.9) we determine the best matching values for the coupling ratios $x = J_1/J_0$ and $y = J_2/J_1$ for the measured data of BCPO as we did previously in sect. 4.1.2. For the deviation of the J_2 coupling we use the fixed ratio $J_2'/J_2 = 0.5$, which is equivalent to $\delta = 1/3$, see eq. (5.1.1), proposed by TSIRLIN [60]. As outlined in sect. 4.1.2, we focus on the two criteria $k_\Delta^* = (0.575 \pm 0.005)$ (r.l.u.) and $(\omega(\pi)/\Delta)^* = (3.7 \pm 0.5)$ which we want to describe as well as possible with the two-dimensional trilinear isotropic model, see eq. (5.2.9).

In figure 5.2 the curves defined by $k_\Delta = k_\Delta^*$ and $\omega(\pi)/\Delta = (\omega(\pi)/\Delta)^*$ for different ratios of x and y are presented. The relative value of the interladder coupling is fixed $J'/J_0 = 0.16$ by analogy with the case $\delta = 0$ in sect. 4.1.2. Compared to the two-dimensional isotropic model without the effects of the J_2 variation, see figure 4.2, no area in figure 5.2 is visible where both criteria are fulfilled. This fact can be explained by considering two aspects concerning the effects of a finite value of δ on the one-triplon dispersion $\omega_0(k)$.

[3] As already mentioned in sect. 4.1.2, the measured data of BCPO were collected for a fixed momentum $l = 1$ r.l.u. and varying momentum k. Therefore, we neglect the second momentum l and write $\omega_r(k)$ instead of $\omega_r(k,l)$.

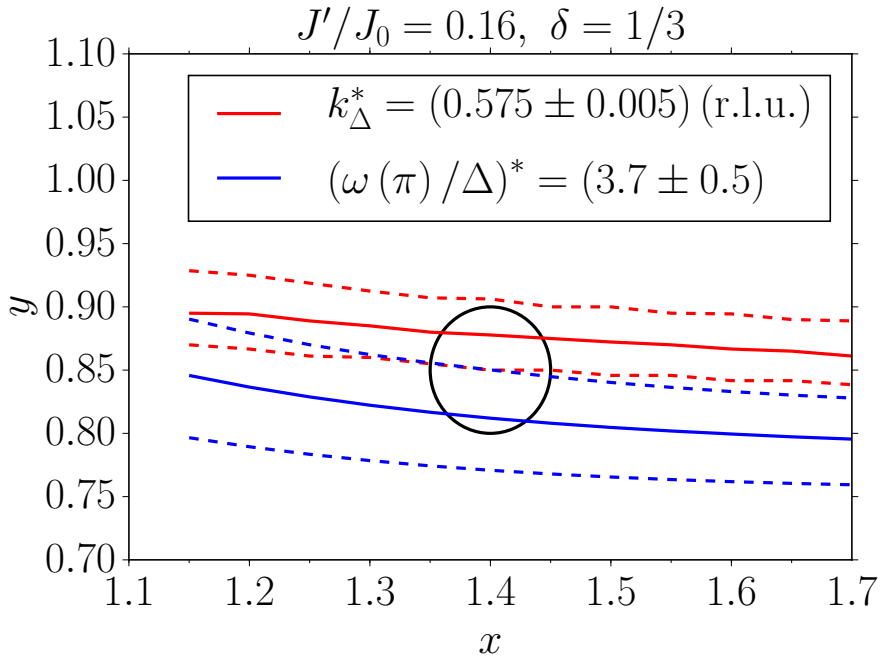

Figure 5.2: Correspondence of the chosen criteria with the renormalized dispersions $\omega_r(k)$ for different values of x and y. The variation of the J_2 coupling $\delta = 1/3$ is fixed as well as the interladder coupling $J'/J_0 = 0.16$. The red solid line shows $k_\Delta = k^*_\Delta = 0.575$ (r.l.u.) and the corresponding dashed lines represent the deviations by ± 0.005, i.e. $k^*_\Delta = (0.575 \pm 0.005)$ (r.l.u.). The blue solid line depicts the ratio $\omega(\pi)/\Delta = (\omega(\pi)/\Delta)^* = 3.7$ and the corresponding dashed lines indicate the accepted deviations by ± 0.5, i.e. $(\omega(\pi)/\Delta)^* = (3.7 \pm 0.5)$. The circle marks the area where both criteria are fulfilled within the range of the accepted deviations at $x \approx 1.4$ and $y \approx 0.85$.

(i) The main effect of the decay/fusion terms in the Hamiltonian $\mathcal{H}_{J_2,\text{direct}}$, see eq. (5.2.6), on the one-triplon dispersion is a shift to lower energies since the one-triplon dispersion tries to avoid an overlap with the corresponding two-triplon continuum due to level repulsion, see also the third scenario of SQPD in sect. 2.3. This energy shift does not show a strong modulation in the Brillouin zone and is rather constant for all values of k. Therefore, the position of the energy gap does not change significantly. The curve of the gap positions, see the red solid lines in figures 4.2 and 5.2, reflects this issue by not displaying large differences.

(ii) Understanding the curve of the ratio $\omega(\pi)/\Delta$ needs a deeper insight. A finite value of δ ensures an overall lowering of the one-triplon dispersion. Thus, the value of the energy gap Δ is reduced. But at $k = \pi$ no hybridization between the one- and two-particle Hilbert space exists, i.e. the prefactor of the decay/fusion terms,

see eq. (5.2.7), fulfills the relation

$$\Gamma^{\alpha'\beta'\gamma'}\left(k=\pi,q\right)=0 \tag{5.2.10}$$

for all relative momenta q. This is due to the fact that the decay/fusion terms in real space, see eq. (5.1.3), with their prefactors obey the same rotational symmetries in spin space as the original spin observable, see eq. (5.1.2). More specifically, the rotational invariance by a rotation of $\pi/2$ of these decay/fusion terms in real space is responsible for the missing hybridization of the one- and two-particle HILBERT space at $k=\pi$. As a consequence, the value of the one-triplon dispersion at $k=\pi$ does not change, i.e. the relation $\omega_{0,r}\left(k=\pi\right)=\omega_0\left(k=\pi\right)$ holds. Due to the reduced energy gap Δ the ratio $\omega\left(\pi\right)/\Delta$ changes. Therefore, the blue solid lines in figures 4.2 and 5.2 display differences.

These two aspects explain the missing overlap of both criteria at $x\approx 1.2$ and $y\approx 0.9$ in figure 5.2 compared to figure 4.2. Considering the tolerated error ranges for each criterion an overlap at $x\approx 1.4$ and $y\approx 0.85$ can be identified. In constrast to the two-dimensional isotropic model without the SQPD effects of the J_2 variation, other ratios of x and y do not show an overlap within the tolerated error ranges. Thus, we expect the values $x=1.4$, $y=0.85$, $J'/J_0=0.16$ and $\delta=1/3$ to present the best matching parameters for the magnetic structure of BCPO.

On the basis of the trilinear isotropic model we include the effects of anisotropic couplings in order to describe the three different experimentally observed modes of BCPO. Using the direct approach we can determine the best fitting DM couplings by simply substituting the isotropic dispersion $\omega_0\left(k\right)$ in the results of the anisotropic analysis of BCPO on bilinear operator level, see eqs. (4.2.21) and (4.2.30), by the renormalized isotropic dispersion $\omega_{0,r}\left(k\right)$. Note, that the direct approach is only an approximation in order to obtain a first impression on the reduction of the $\mathbf{D}$ values compared to the anisotropic bilinear model, see sect. 4.2.3. No new analysis of the $\mathbf{D}$ components is necessary since their effects do not depend on the isotropic dispersion. Undertaking the results of the trilinear isotropic model, i.e. the parameters $x=1.4$, $y=0.85$, $J'/J_0=0.16$ and $\delta=1/3$, we vary the $\mathbf{D}$ components and the energy scale J_0 to receive the best description of the experimental data. In the following, we address several issues concerning our best fit, see figure 5.3, and compare these with the results of the bilinear anisotropic model, see figure 4.4 and sect. 4.2.3.

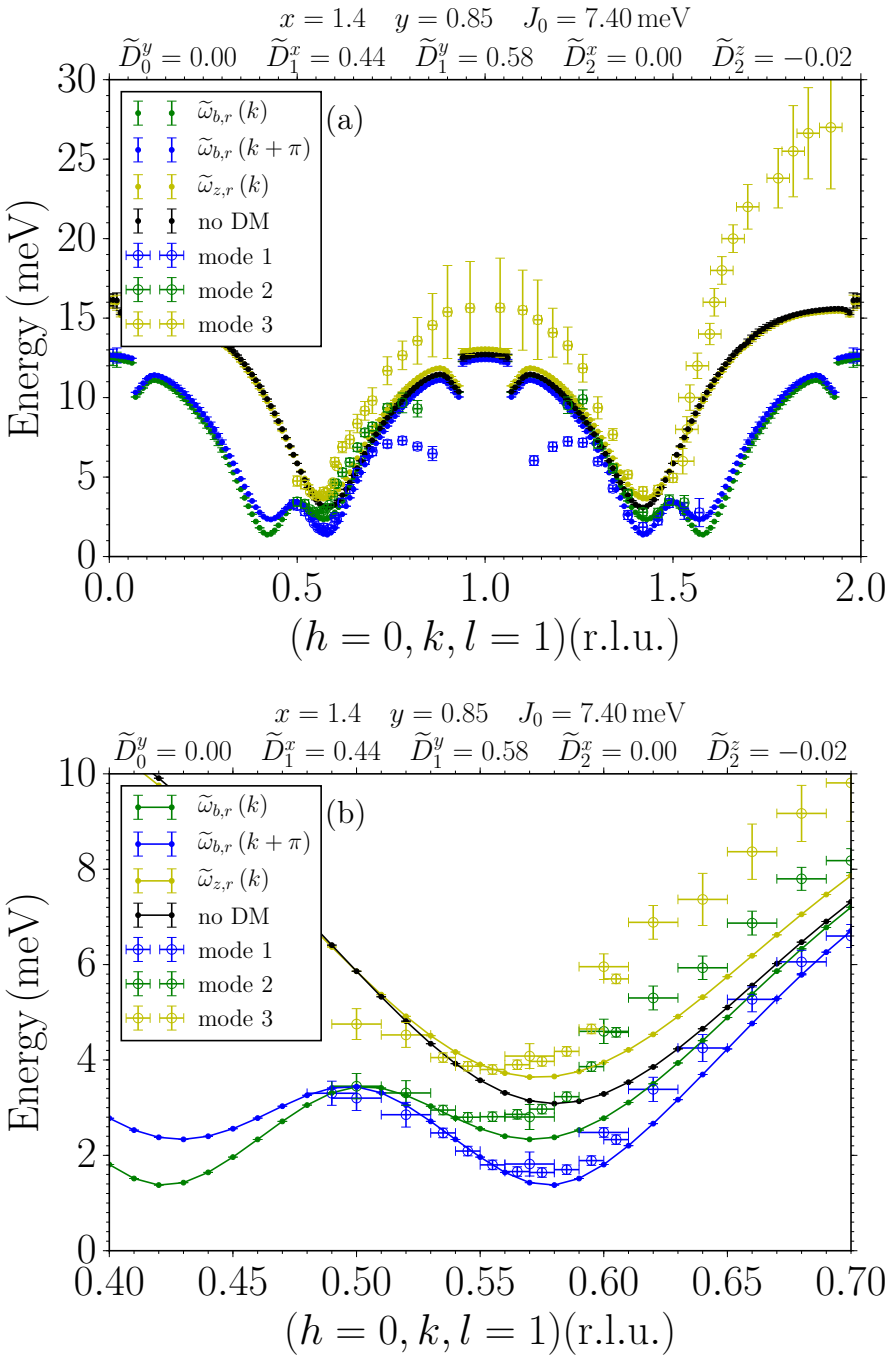

Figure 5.3: (a) Fitted theoretical dispersions $\widetilde{\omega}_{b,r}(k)$, $\widetilde{\omega}_{b,r}(k+\pi)$ and $\widetilde{\omega}_{z,r}(k)$, which stem from the x, y and z mode for the fixed parameters $x = 1.4$, $y = 0.85$, $J'/J_0 = 0.16$ and $\delta = 1/3$. Their displayed error bars depict the corresponding HWHM, see eq. (2.3.72). For the calculation of the isotropic renormalized dispersion $\omega_{0,r}(k)$ a maximum relative HWHM of $(\gamma(k)/\Delta\omega_2(k+\pi))_{\max} = 0.1$ and a minimal spectral weight of $(1/s)_{\min} = 0.001$ are set as thresholds to identify quasiparticle peaks in the corresponding spectral functions, see sect. 3.4.1. The fitted parameters are J_0, $\widetilde{D}_0^y$, $\widetilde{D}_1^x$, $\widetilde{D}_1^y$, $\widetilde{D}_2^x$ and $\widetilde{D}_2^z$. Their values are listed in the panel itself. (b) Zoom of panel (a) into the vicinity of the left minimum.

(i) The good description in the minimum area of mode 1 and mode 2 with the calculated dispersions $\widetilde{\omega}_{b,r}(k)$ and $\widetilde{\omega}_{b,r}(k+\pi)$ could not be reproduced, i.e. the fit between theory and experiment becomes worse, when we include the effects of a finite variation of the NNN coupling J_2. Although this issue does not state a satisfying aspect, it can be explained. Comparing the results for the trilinear isotropic model in figure 5.2 with the corresponding results of the bilinear isotropic model in figure 4.2 the consideration of trilinear isotropic operator terms makes it more difficult to find appropriate ratios of $x = J_1/J_0$ and $y = J_2/J_1$, which provide a satisfying description of the position of the gap k_Δ and the energy ratio $\omega(\pi)/\Delta$. As discussed before, in contrast to the bilinear isotropic model the trilinear isotropic model does not lead to well matching values for the parameters x and y, see figure 5.2. Therefore, it is not surprising that the effects of SQPD stemming from the variation of J_2 do not improve the agreement between theory and experiment since the effects of the anisotropic couplings do not change. The fitted values of the parameters $\widetilde{D}_1^x = 0.44$ and $\widetilde{D}_1^y = 0.58$ remain large but could be reduced slightly compared to the bilinear anisotropic model with $\widetilde{D}_1^x = 0.48$ and $\widetilde{D}_1^y = 0.61$. This fact can also be explained by the finite value of $\delta = 1/3$ which provides a lowering of the renormalized dispersion $\omega_{0,r}(k)$ compared to $\omega_0(k)$. It is remarkable that the effects of SQPD stemming from the finite value of $\delta = 1/3$, which describes a large J_2 variation of $J_2'/J_2 = 0.5$, provide only a small improvement concerning a reduction of the $\mathbf{D}$ components in general. At $k = 0.5\,\mathrm{r.l.u.}$ the renormalized dispersion $\omega_r(k)$ including the interladder coupling J', see eq. (5.2.9), assumes a value of $6.56\,\mathrm{meV}$. Compared with the results of the bilinear isotropic model, see figure 4.4, this represents a reduction of only $7\,\%$. This means that the anisotropic couplings still need to lower the dispersion by $\approx 3\,\mathrm{meV}$. As outlined in sect. 4.2.3, the parameter Γ_1^{xy} has the main influence on the dispersions at $k = 0.5\,\mathrm{r.l.u.}$. As a consequence, the components $\widetilde{D}_1^x$ and $\widetilde{D}_1^y$ still need to assume large values in order to yield a large value of Γ_1^{xy}. As well as in the bilinear anisotropic model we chose the value of $\widetilde{D}_1^y$ to be slightly larger than $\widetilde{D}_1^x$ in order to create the visible slight asymmetric shift about $k = 0.5\,\mathrm{r.l.u.}$. Note, that even with a finite value of δ the two lower modes stemming from the x and y modes can be converted into each other by simply swapping the values of $\widetilde{D}_1^x$ and $\widetilde{D}_1^y$.

(ii) Including a finite value of δ the parameter $\widetilde{D}_2^z = -0.02$ remains. As explained in sect. 4.2.3, this component cannot improve the match between theory and experiment since its linear effect is rather small and its quadratic effects even deteriorate a good description of the experimental data. As mentioned in aspect (i), the starting point of the trilinear isotropic model is not as good as in the bilinear isotropic model. As a consequence, the effects of the parameter $\widetilde{D}_2^z$ cannot improve the results significantly.

(iii) As well as in figure 4.4 major discrepancies between the shape of the calculated z mode $\widetilde{\omega}_{z,r}(k)$ and the measured mode 3 can be observed in figure 5.3. This appearance is not unexpected since the shape of the isotropic dispersion $\omega_0(k)$ presenting the starting point in the bilinear anisotropic analysis is not significantly changed by a finite value of $\delta = 1/3$ as discussed before. So the shape of the renormalized dispersion $\omega_{0,r}(k)$ is similar to the shape of $\omega_0(k)$. Since the anisotropic couplings have the identical effects on $\omega_{0,r}(k)$ as on $\omega_0(k)$ within the direct approach, we cannot expect the variation of the NNN coupling J_2 to provide an improvement concerning this issue.

(iv) Considering the characteristic down-bending behavior of mode 1 and mode 2 the influence of a finite value of δ using the direct approach does not improve the fit, either. However, since we take effects of SQPD into account, we can identify a clear down-bending behavior for all calculated modes in figure 5.3. In constrast to the experimental data, all calculated modes show this down-bending behavior. This follows from the fact that the analyzed effects of SQPD are spin isotropic and therefore all modes are treated equally. The hybridization between the one-triplon states and the two-triplon states occurs around $k \approx 1$ r.l.u. but shows only remarkably small effects. Inside the two-triplon continuum the peaks in the corresponding spectral functions are just slightly smeared out and hold a small HWHM. This means that the included effects of SQPD do not have a strong influence on the lifetime of the triplons and that they can still be identified and labeled as quasiparticles in the entire Brillouin zone.

(v) Figure 5.3 reveals that the maximum value reached by the calculated z mode is $\approx$16 meV, whereas in the case of no SQPD effects in figure 4.4 the value is $\approx$19 meV. The measured data show up a value of $\approx$27 meV. This observation is a direct consequence of the finite value of $\delta = 1/3$ causing a lowering of the dispersion in the complete Brillouin zone. As discussed before the effects of the hybridization between the one-triplon states and the two-triplons states are rather small and cannot explain the observed resonances at high energies.

At the end of this section we sum up our results for the variation of the NNN coupling J_2 using the direct approach for the quantum antiferromagnet BCPO. The aim of this analysis was to improve the description of the experimental dispersion data of BCPO compared to the previous analysis concerning the bilinear anisotropic issue. Our expectation was that a finite variation of the J_2 coupling leads to a better agreement between theory and experiment. Additionally, we assumed that this goal can be reached with smaller values for the $\mathbf{D}$ components compared to the large values of $\mathbf{D}_1 \approx 0.6 J_1$ within the bilinear anisotropic model of BCPO. Unfortunately, using the direct approach does

not meet these expectations. However, the results show up several promising features, i.e. a slight reduction of $\mathbf{D}_1 \approx 0.58 J_1$ and first indications of a down-bending behavior, which the experimental data display clearly. Again we stress that the direct approach is an easier ansatz compared to the complete approach, which considers the solved bilinear anisotropic model of BCPO as a starting point. In the following section the complete approach and its results are discussed in detail. We strongly expect this ansatz to provide an improvement concerning the agreement between the dispersions in theory and experiment with reduced $\mathbf{D}$ components.

5.3 Results for the complete approach

In this section we present the complete approach in order to include the effects of SQPD stemming from the J_2 variation in BCPO and its results. Compared to the direct approach the complete approach represents a more comprehensive concept because its starting point is set by the solved bilinear anisotropic Hamiltonians $\widetilde{\mathcal{H}}^{\text{eff}}_{\text{BCPO},z}$ and $\widetilde{\mathcal{H}}^{\text{eff}}_{\text{BCPO},bu}$, see eqs. (4.2.20) and (4.2.32), instead of the Hamiltonian $\mathcal{H}^{\text{eff}}_{\text{ladder}}$, see eq. (4.1.2). This is the important difference between these two approaches. Several steps for the complete approach have already been realized in sect. 5.1. We explain it in detail at this point since we discuss further couplings, which induce SQPD and which we analyze within the complete approach as well, in chapter 6.

To study the effects of SQPD stemming from spin couplings with odd parity on the solved bilinear anisotropic issue of BCPO, derived in sect. 4.2.2, we perform the following steps:

1st Express the odd spin coupling term in the basis of the spin operators $S_i^{\alpha,\text{L/R}}$.

2nd Transform the odd spin coupling term from the first step with the help of a deepCUT in order to receive linear $t^{\alpha,\dagger}_{i+\delta}/t^{\alpha}_{i+\delta}$ and trilinear operator terms $t^{\alpha',\dagger}_{i+\delta_1} t^{\beta',\dagger}_{i+\delta_2} t^{\gamma'}_{i+\delta_3} / t^{\alpha',\dagger}_{i+\delta_1} t^{\beta',\dagger}_{i+\delta_2} t^{\gamma',\dagger}_{i+\delta_3}$ + h.c. with the flavors $\alpha, \alpha', \beta', \gamma' \in \{x, y, z\}$ and the relative distances δ_1, δ_2 and δ_3 in real space.

3rd By analogy with the bilinear anisotropic analysis of BCPO, see sect. 4.2.2, we treat the triplon operators as standard bosonic operators in a mean-field approach and apply a FOURIER transform. At this point the hard-core constraint of the triplon operators is neglected. This approximation is reasonable because we assume that the main influence of the hard-core constraint is considered in the dynamics of the single frustrated spin ladder. As its solution is received by a deepCUT, which takes the hard-core constraint into account, the main influence of the hard-core constraint is encoded in the prefactors of the linear and trilinear operators terms from the second step.

4^{th} Transform the trilinear operator terms into the basis of the Hamiltonians $\widetilde{\mathcal{H}}^{\text{eff}}_{\text{BCPO},z}$ and $\widetilde{\mathcal{H}}^{\text{eff}}_{\text{BCPO},bu}$, see eqs. (4.2.20) and (4.2.32). To this end, we map the triplon operators of the flavor z onto the operators $\tilde{t}^{z,(\dagger)}$ using the bosonic BOGOLIUBOV transformation, see eqs. (4.2.18). Triplon operators with the flavors x and y are mapped onto a linear combination of the bosonic operators $\tilde{t}^{b,(\dagger)}$ and $\tilde{t}^{u,(\dagger)}$ using the canonical transformation matrix $K^{-1}_{k,l}$, see eq. (4.2.27).

5^{th} Order all trilinear operator terms according to normal-ordering and neglect terms of the type $t^\dagger t^\dagger t^\dagger / ttt$ and $t^\dagger / t$. This approximation is motivated by the assumption that the main influence on the effects of quasiparticle decay at zero temperature stems from decay/fusion terms of the type $t^\dagger t^\dagger t / t^\dagger tt$. Furthermore, we are only interested in the one- and two-particle HILBERT space and the transitions between them. As linear and trilinear operator terms of the type $t^\dagger t^\dagger t^\dagger / ttt$ do not link the one- and two-particle HILBERT space, we can neglect them.

6^{th} Since the decay/fusion terms are now in the same basis as the Hamiltonians $\widetilde{\mathcal{H}}^{\text{eff}}_{\text{BCPO},z}$ and $\widetilde{\mathcal{H}}^{\text{eff}}_{\text{BCPO},bu}$, we can simply add them. Considering a maximum number of two quasiparticles we perform a LANCZOS tridiagonalization and calculate the renormalized dispersions $\widetilde{\omega}_{z,r}(k)$ and $\widetilde{\omega}_{b,r}(k)$ as explained in sects. 2.3.1, 2.3.2 and 2.3.3.

For the J_2 variation the first two steps of the complete approach have already been carried out in sect. 5.1. The next step is a FOURIER transform. Since the bilinear anisotropic description of BCPO is a two-dimensional issue, we have to add an index j to all trilinear operator terms in eq. (5.1.3) indicating different frustrated spin ladders, see figure 5.1. Applying a two-dimensional FOURIER transform changes the results of eqs. (5.1.4) and (5.1.5) to

$$\mathcal{H}_{J_2,\text{decay,2D}} = \overline{J}_2 \delta \sum_{k,q} \sum_{l,p} \sum_{\delta_1,\delta_2,\delta_3} \frac{\alpha^{\alpha',\beta',\gamma'}_{\delta_1,\delta_2,\delta_3}}{\sqrt{N_k N_l}} \mathrm{e}^{\mathrm{i}(\delta_2-\delta_1)q} \mathrm{e}^{\mathrm{i}(\delta_3-\delta_2)k} \mathrm{e}^{-\mathrm{i}\pi\delta_2} t^{\alpha',\dagger}_{q,p} t^{\beta',\dagger}_{k-q-\pi,l-p} t^{\gamma'}_{k,l} \quad (5.3.11)$$

and

$$\mathcal{H}_{J_2,\text{fluc,2D}} = \overline{J}_2 \delta \sum_{k,q} \sum_{l,p} \sum_{\delta_1,\delta_2,\delta_3} \frac{\beta^{x,y,z}_{\delta_1,\delta_2,\delta_3}}{\sqrt{N_k N_l}} \mathrm{e}^{\mathrm{i}(\delta_2-\delta_1)q} \mathrm{e}^{\mathrm{i}(\delta_2-\delta_3)k} \mathrm{e}^{-\mathrm{i}\pi\delta_2} t^{x,\dagger}_{q,p} t^{y,\dagger}_{-k-q-\pi,-l-p} t^{z,\dagger}_{k,l}. \quad (5.3.12)$$

The additional momentum l corresponds to the index j labeling the spin ladders in z-direction, see figure 5.1. Its relative momentum is denoted with p. The variable N_l describes the discretization of the momentum l. We identified the relation $N_l = N_k/5$

as reasonable since the bandwidths[4]

$$\Delta_{l=1} = \max_k \omega\left(k, l=1\right) - \min_k \omega\left(k, l=1\right) \tag{5.3.13}$$

of the two-dimensional dispersion $\omega\left(k,l\right)$, see eq. (4.1.10), and

$$\Delta = \max_{k,l} \omega\left(k,l\right) - \min_{k,l} \omega\left(k,l\right) \tag{5.3.14}$$

fulfill the relation $\Delta_{l=1}/\Delta \approx 5$ using the parameter values $x = 1.2$, $y = 0.9$ and $J'/J_0 = 0.16$, see sect. 4.1.2. Note, that except of the normalization factor $1/\sqrt{N_l}$ the FOURIER transforms of the trilinear terms in one and two dimensions do not differ[5]. This follows from the fact that the J_2 variation affects only the coupled frustrated spin ladders separately and not the connection between them, see figure 5.1.
The next step in the complete approach is to transform the trilinear operator terms in momentum space, see eqs. (5.3.11) and (5.3.12), into the same basis as the Hamiltonians $\widetilde{\mathcal{H}}^{\text{eff}}_{\text{BCPO},z}$ and $\widetilde{\mathcal{H}}^{\text{eff}}_{\text{BCPO},bu}$. After normal-ordering these we obtain the following triplon operator terms with prefactors

$$\begin{array}{llll}
\tilde{t}^{z,\dagger}_{q,p}\tilde{t}^{b,\dagger}_{k-q,l-p}\tilde{t}^{b}_{k,l}, & \tilde{t}^{z,\dagger}_{q,p}\tilde{t}^{u,\dagger}_{k-q,l-p}\tilde{t}^{b}_{k,l}, & \tilde{t}^{z,\dagger}_{q,p}\tilde{t}^{b,\dagger}_{k-q,l-p}\tilde{t}^{u}_{k,l}, & \tilde{t}^{z,\dagger}_{q,p}\tilde{t}^{u,\dagger}_{k-q,l-p}\tilde{t}^{u}_{k,l}, \\
\tilde{t}^{b,\dagger}_{q,p}\tilde{t}^{b,\dagger}_{k-q,l-p}\tilde{t}^{z}_{k,l}, & \tilde{t}^{b,\dagger}_{q,p}\tilde{t}^{u,\dagger}_{k-q,l-p}\tilde{t}^{z}_{k,l}, & \tilde{t}^{u,\dagger}_{q,p}\tilde{t}^{u,\dagger}_{k-q,l-p}\tilde{t}^{z}_{k,l}, & \tilde{t}^{z,\dagger}_{0,0}, \\
\tilde{t}^{z,\dagger}_{q,p}\tilde{t}^{b,\dagger}_{-k-q,-l-p}\tilde{t}^{b,\dagger}_{k,l}, & \tilde{t}^{z,\dagger}_{q,p}\tilde{t}^{b,\dagger}_{-k-q,-l-p}\tilde{t}^{u,\dagger}_{k,l}, & \tilde{t}^{z,\dagger}_{q,p}\tilde{t}^{u,\dagger}_{-k-q,-l-p}\tilde{t}^{u,\dagger}_{k,l}, &
\end{array} \tag{5.3.15}$$

including trilinear and linear operator terms and the Hermitian conjugated part of each operator term. Note, that the shift of π, see eqs. (5.3.11) and (5.3.12), in the second operator of trilinear terms has vanished. The reason for this is that this shift by π is already respected in the canonical transformation matrix $K^{-1}_{k,l}$, see eq. (4.2.27). Hence, the trilinear operator terms in eq. (5.3.15) describe a coupling between one-particle modes at a fixed momentum pair (k,l) and different two-particle continua with the same total momentum pair. It is noticeable that after normal-ordering a linear contribution $\tilde{t}^{z,\dagger}_{0,0}/\tilde{t}^{z}_{0,0}$ at fixed momenta $(k=0, l=0)$ shows up since the original spin observable, see eq. (5.1.2), is spin isotropic. But this disagreement is explained by the fact that the prefactor of the linear terms $\tilde{t}^{z,\dagger}_{0,0}/\tilde{t}^{z}_{0,0}$ is equal to zero. This has to be the case because the spin observable describing the J_2 variation, see eq. (5.1.2), has no outstanding spin orientation and the applied mapping on the operators $\tilde{t}^{z,(\dagger)}$, $\tilde{t}^{b,(\dagger)}$ and $\tilde{t}^{u,(\dagger)}$ is a canonical transformation, which conserves this fact. Following the steps of the complete approach

[4]For the bandwidth $\Delta_{l=1}$ we fix the momentum $l = 1$ since the experimental data of BCPO have been obtained for this specific value.

[5]Note, that in the direct approach, see sect. 5.2, a one-dimensional FOURIER transform for the trilinear operator terms was performed because the starting point is the solved frustrated spin ladder, which is a one-dimensional model.

we discard all trilinear operator terms, which do not describe a transition between the one-particle and two-particle HILBERT space, i.e. trilinear operator terms with three creation or three annihilation operators are neglected. The remaining triplon operator terms from eq. (5.3.15) are then given by

$$\begin{aligned} &\tilde{t}^{z,\dagger}_{q,p}\tilde{t}^{b,\dagger}_{k-q,l-p}\tilde{t}^{b}_{k,l}, \quad \tilde{t}^{z,\dagger}_{q,p}\tilde{t}^{u,\dagger}_{k-q,l-p}\tilde{t}^{b}_{k,l}, \quad \tilde{t}^{z,\dagger}_{q,p}\tilde{t}^{b,\dagger}_{k-q,l-p}\tilde{t}^{u}_{k,l}, \quad \tilde{t}^{z,\dagger}_{q,p}\tilde{t}^{u,\dagger}_{k-q,l-p}\tilde{t}^{u}_{k,l}, \\ &\tilde{t}^{b,\dagger}_{q,p}\tilde{t}^{b,\dagger}_{k-q,l-p}\tilde{t}^{z}_{k,l}, \quad \tilde{t}^{b,\dagger}_{q,p}\tilde{t}^{u,\dagger}_{k-q,l-p}\tilde{t}^{z}_{k,l}, \quad \tilde{t}^{u,\dagger}_{q,p}\tilde{t}^{u,\dagger}_{k-q,l-p}\tilde{t}^{z}_{k,l}. \end{aligned} \tag{5.3.16}$$

Since we are only interested in the z and b mode in order to describe the low-energy regime, we analyze the effects of the trilinear terms on these modes. Eq. (5.3.16) reveals that the b mode can decay in two different ways, i.e. a single triplon with flavor b and momenta (k,l) can decay into two particles with flavors z and b and momenta (q,p) and $(k-q,l-p)$ and it can decay into two particles with flavors z and u and momenta (q,p) and $(k-q,l-p)$. This means that the one-particle dispersion $\widetilde{\omega}_b(k,l)$ couples to the two-particle continua

$$\widetilde{\omega}_{2,zb}(k,l,q,p) = \widetilde{\omega}_z(q,p) + \widetilde{\omega}_b(k-q,l-p) \tag{5.3.17a}$$

$$\widetilde{\omega}_{2,zu}(k,l,q,p) = \widetilde{\omega}_z(q,p) + \widetilde{\omega}_u(k-q,l-p) \tag{5.3.17b}$$

with the total momenta (k,l) and the corresponding relative momenta (q,p) using the one-particle dispersions $\widetilde{\omega}_z(k,l)$ and $\widetilde{\omega}_{b,u}(k,l)$ derived in eqs. (4.2.21) and (4.2.30).
Considering the decay channels of a single particle with flavor z and fixed momenta (k,l) eq. (5.3.16) reveals that it can decay in three different ways. Thus, the one-particle dispersion $\widetilde{\omega}_z(k,l)$ couples to the three different two-particle continua

$$\widetilde{\omega}_{2,bb}(k,l,q,p) = \widetilde{\omega}_b(q,p) + \widetilde{\omega}_b(k-q,l-p) \tag{5.3.18a}$$

$$\widetilde{\omega}_{2,bu}(k,l,q,p) = \widetilde{\omega}_b(q,p) + \widetilde{\omega}_u(k-q,l-p) \tag{5.3.18b}$$

$$\widetilde{\omega}_{2,uu}(k,l,q,p) = \widetilde{\omega}_u(q,p) + \widetilde{\omega}_u(k-q,l-p). \tag{5.3.18c}$$

As a consequence, the limiting values for the LANCZOS coefficients $a_\infty(k,l)$ and $b_\infty(k,l)$, see Appendix A, are given by the lower and upper boundary of all the corresponding continua, see eqs. (5.3.17) and (5.3.18).
The next and last step of the complete approach is to add the trilinear terms in eq. (5.3.16) to the Hamiltonians $\widetilde{\mathcal{H}}^{\text{eff}}_{\text{BCPO},z}$ and $\widetilde{\mathcal{H}}^{\text{eff}}_{\text{BCPO},bu}$, see eqs. (4.2.20) and (4.2.32). We forego the explicit expression for this Hamiltonian including the solved bilinear anisotropic part and the trilinear operator terms from eq. (5.3.16) since the prefactors of the trilinear terms have to be evaluated numerically anyway. For this Hamiltonian we perform a LANCZOS tridiagonalization and apply the steps described in sects. 2.3.1,

2.3.2 and 2.3.3 in order to receive the renormalized dispersions $\widetilde{\omega}_{z,r}(k)$ and $\widetilde{\omega}_{b,r}(k)$. On this basis we search for the values of the **D** components which provide the best match between our calculated renormalized dispersions $\widetilde{\omega}_{z,r}(k)$ and $\widetilde{\omega}_{b,r}(k)$ and the experimentally received data in a systematic manner. Actually, it would be necessary to analyze the effects of every single **D** component on the renormalized dispersions in detail, see table 4.3. The prefactors of the decay/fusion terms in eq. (5.3.16) do not depend on the **D** components explicitly. They are only influenced by the **D** components via the transformation matrix $K^{-1}_{k,l}$ and the parameter $\vartheta^z_{k,l}$, see eqs. (4.2.27) and (4.2.19). So it is reasonable to start our fitting process by using the results of the bilinear anisotropic issue, see figure 4.4. Then, we vary the **D** components and the energy scale J_0 in a systematic manner step by step to receive the best match between theory and the experimental data of BCPO[6]. Since we have the information about the effects of all anisotropic couplings on the bilinear anisotropic model of BCPO, see table 4.3, we can use these as a first orientation for the complete approach. The parameters $x = 1.2$, $y = 0.9$, $J'/J_0 = 0.16$ are fixed such as the results of the bilinear anisotropic description of BCPO, see sect. 4.2.3. We choose these fixed parameters since in the complete approach the bilinear anisotropic model of BCPO serves as our starting point. Concerning the J_2 variation we stick to the value $\delta = 1/3$ as discussed previously in sect. 5.2.
In the following, we focus on several aspects concerning our best fit, see figures 5.4, 5.5 and 5.6, and compare these with the results of the bilinear anisotropic model, see figure 4.4, and the results of the direct approach, see figure 5.3.

[6]In the following chapter 6 the decay/fusion terms depend explicitly on the **D** components. In that context, an analysis of the effects of each **D** component on the renormalized dispersion $\widetilde{\omega}_{b,r}(k)$ is performed by analogy with the bilinear anisotropic model.

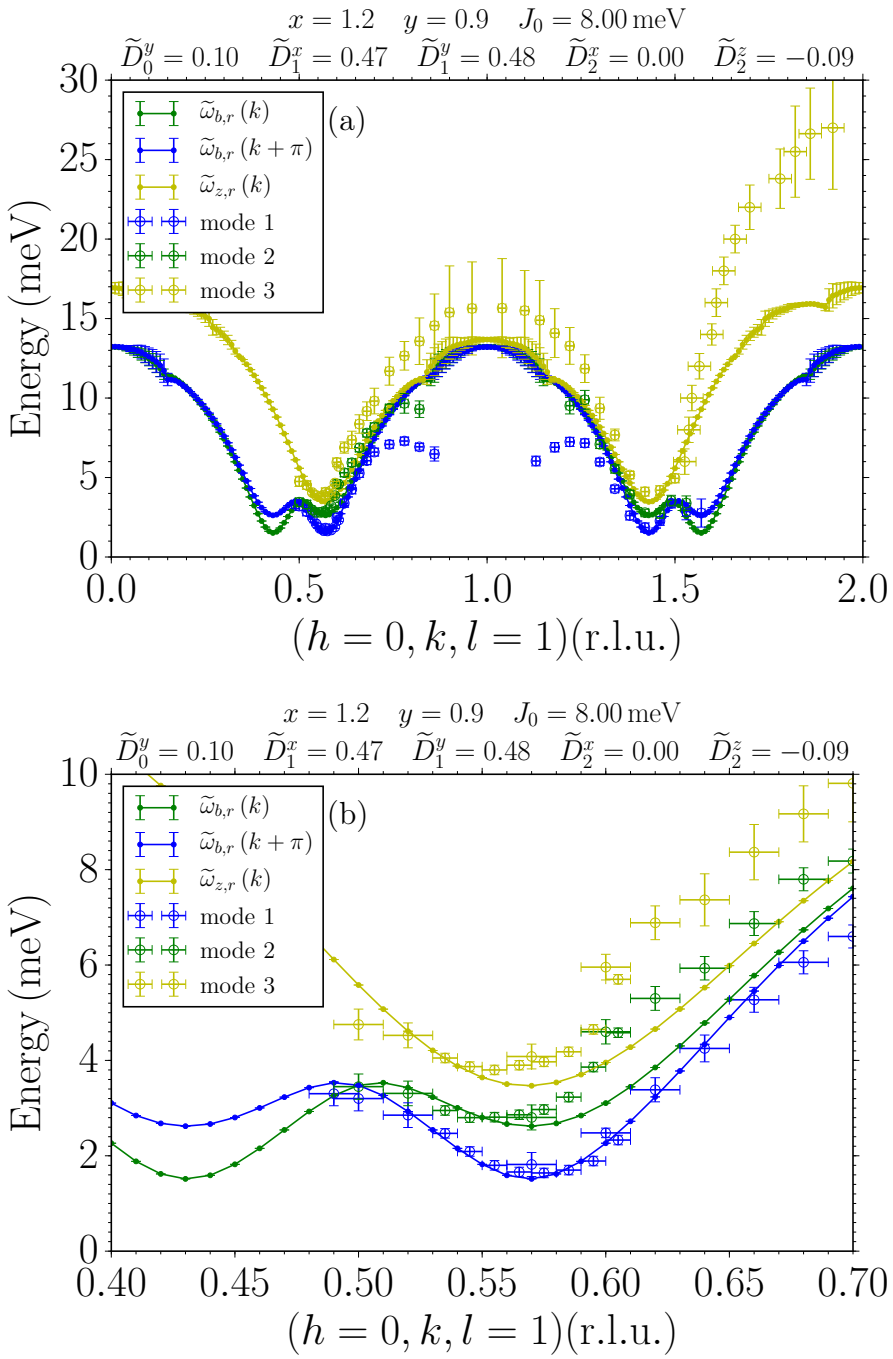

Figure 5.4: (a) Fitted theoretical dispersions, which stem from the x, y and z mode for the fixed parameters $x = 1.2$, $y = 0.9$, $J'/J_0 = 0.16$ and $\delta = 1/3$. Their displayed error bars depict the corresponding HWHM, see eq. (2.3.72). As thresholds to identify quasiparticle peaks in the corresponding spectral functions, see sect. 3.4.1, we set a maximum relative HWHM of $(\gamma(k)/\Delta\widetilde{\omega}_2(k))_{\max} = 0.1$ and a minimal spectral weight of $(1/s)_{\min} = 0.005$. The fitted parameters are J_0, $\widetilde{D}_0^y$, $\widetilde{D}_1^x$, $\widetilde{D}_1^y$, $\widetilde{D}_2^x$ and $\widetilde{D}_2^z$. Their values are listed in the panel itself. (b) Zoom of panel (a) into the vicinity of the left minimum.

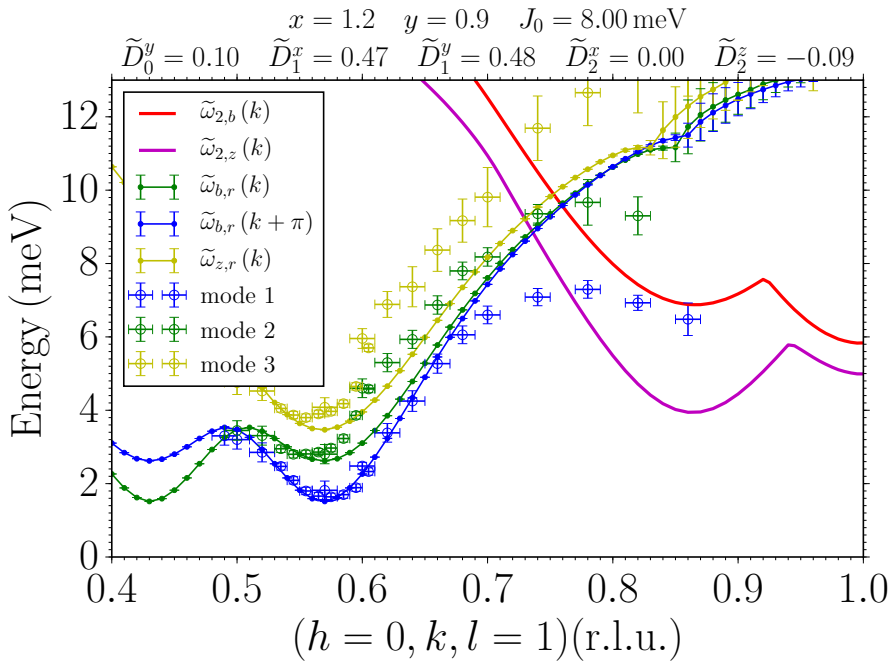

Figure 5.5: Zoom of panel (a) of figure 5.4 into the range where mode 1 and 2 show the prominent down-bending behavior. Additionally, the lower boundaries of the two-particle continua $\widetilde{\omega}_{2,b}(k)$ and $\widetilde{\omega}_{2,z}(k)$ belonging to the one-particle dispersions $\widetilde{\omega}_{b,r}(k)$ and $\widetilde{\omega}_{z,r}(k)$ are depicted by solid lines.

(i) The match between the two lowest-lying modes 1 and 2 and the calculated dispersions $\widetilde{\omega}_{b,r}(k)$ and $\widetilde{\omega}_{b,r}(k+\pi)$ has improved compared to the results of the direct approach. Out of the results from the bilinear anisotropic model, the direct approach and the complete approach the latter shows the best fit around the minimum area of mode 1 and 2. By this we mean that mode 1 is well described from $k \approx 0.5\,\mathrm{r.l.u.}$ to $k \approx 0.7\,\mathrm{r.l.u.}$. Another positive aspect concerning the results of the complete approach is the larger reduction of the component $\widetilde{D}_1^y$ starting with $\widetilde{D}_1^y = 0.61$ for the bilinear anisotropic model, $\widetilde{D}_1^y = 0.58$ for the direct approach and $\widetilde{D}_1^y = 0.48$ for the complete approach. This states an achieved reduction up to 20 %. This is possible since the finite variation of the NNN coupling J_2 already ensures a lowering of the one-particle dispersions so that not only the anisotropic couplings are responsible for decreasing the dispersions. This means that the values of the anisotropic couplings can be chosen smaller while still achieving an equivalently satisfying description of the low-energy regime. As a reminder, we expect the anisotropic couplings to assume values of the order of $0.1 - 0.2$ as their origin is the SOC, see sect. 2.4.1. Still, we do not reach the range of values consistent with this assumption completely. But the continuous reduction of the components $\widetilde{D}_1^x$ and $\widetilde{D}_1^x$ by taking into account the effects of SQPD demonstrates clearly that these effects can lead to values of the anisotropic couplings

which are reasonable. However, the values of $\widetilde{D}_1^x = 0.47$ and $\widetilde{D}_1^y = 0.48$ are crucial in order to create the apparent W-shape of the measured modes 1 and 2 and they are still large. In contrast, for the first time during our analysis of BCPO the component $\widetilde{D}_0^y$ assumes a finite value of $\widetilde{D}_0^y = 0.1$, which is in agreement with our expectations. As mentioned in table 4.3, the component $\widetilde{D}_0^y$ increases the dispersions $\widetilde{\omega}_{b,r}(k)$ and $\widetilde{\omega}_{b,r}(k+\pi)$ in the complete BRILLOUIN zone, which turned out to be a negative effect in the bilinear anisotropic model and in the direct approach. But in the complete approach this effect becomes important since it compensates the dominant effects of the component Γ_1^{xy} via $\widetilde{D}_1^x$ and $\widetilde{D}_1^y$. Since the finite value of $\delta = 1/3$ already reduces the one-particle dispersions, we need a component which regulates the strong reduction effects of $\widetilde{D}_1^x$ and $\widetilde{D}_1^y$ in the minimum area. By setting $\widetilde{D}_0^y = 0.1$ we can solve this issue. Note, that also in the complete approach it is possible to swap the two lower modes stemming from the x and y mode by simply exchanging the values of $\widetilde{D}_1^x$ and $\widetilde{D}_1^y$.

(ib) In the previous part (i) we focused mainly on the satisfying match between mode 1 and the theoretical dispersion relation $\widetilde{\omega}_{b,r}(k+\pi)$. Considering the agreement between mode 2 and our calculated solution $\widetilde{\omega}_{b,r}(k)$ we notice that the complete approach provides a better match in the minimum area than the direct approach but not than the bilinear anisotropic model. One aspect which explains this issue is the fact that mode 2 was not taken into account in the isotropic analysis, see sect. 4.1.2, and in the direct approach, see sect. 5.2. Only the data of mode 1 and 3 were utilized. Therefore, it is reasonable not to expect a satisfying description of mode 2 from the beginning[7]. Since our calculated two lowest-lying modes depend on each other, i.e. they are identical up to a shift of π, an improvement concerning the agreement between $\widetilde{\omega}_{b,r}(k+\pi)$ and mode 1 implies a deterioration in the match between $\widetilde{\omega}_{b,r}(k)$ and mode 2.

(ii) The absolute value of the component $\widetilde{D}_2^z$ increases from -0.02 for the bilinear anisotropic model of BCPO and the direct approach up to -0.09 for the complete approach. This value is still small compared to the large values of $\widetilde{D}_1^x$ and $\widetilde{D}_1^y$ but more realistic concerning our assumption that the anisotropic couplings assume values of the order of $0.1 - 0.2$ in units of the corresponding isotropic couplings. The linear effect of $\widetilde{D}_2^z$ becomes more important in the complete approach since it is mainly responsible for the good match of the position of the gap of mode 1. Additionally, it ensures the satisfying description of the slope of mode 1 in the intervall $k = 0.6\,\text{r.l.u.} - 0.7\,\text{r.l.u.}$, see panel (b) in figure 5.4, which improved strongly compared to the previous results,

[7] In the bilinear anisotropic model of BCPO it turned out that mode 1 and 2 could both be described in the minimum area in a satisfying way although mode 2 was not included in the isotropic analysis, see sect. 4.1.2. So it is a further characteristic of the bilinear anisotropic model that it can describe mode 1 and 2 in the low-energy regime simultaneously.

see figures 4.4 and 5.3. In contrast to the results of the bilinear anisotropic model and the direct approach, the quadratic effect of $\widetilde{D}_2^z$ via the matrix entries Γ_2^{xx} and Γ_2^{yy} is considered positively in the complete approach in order to achieve a good agreement between theory and experiment. As well as the component $\widetilde{D}_0^y$ the quadratic contributions of $\widetilde{D}_2^z$ increase the dispersions $\widetilde{\omega}_b(k)$ and $\widetilde{\omega}_b(k+\pi)$ around the minimum and therefore compensate the effects of the components $\widetilde{D}_1^x$ and $\widetilde{D}_1^y$, see also the previous aspect (ib). The negative sign of $\widetilde{D}_2^z$ does not influence the behavior of the matrix entries Γ_2^{xx} and Γ_2^{yy}, see eq. (2.4.84). Despite this, it is important to choose a negative value for $\widetilde{D}_2^z$ so that it can damp the effects of the component Γ_1^{xy} as described in the bilinear anisotropic model and in the direct approach. Thus, only a negative value for the component $\widetilde{D}_2^z$ can improve the fit between our calculated results and the experimentally measured data in the low-energy regime.

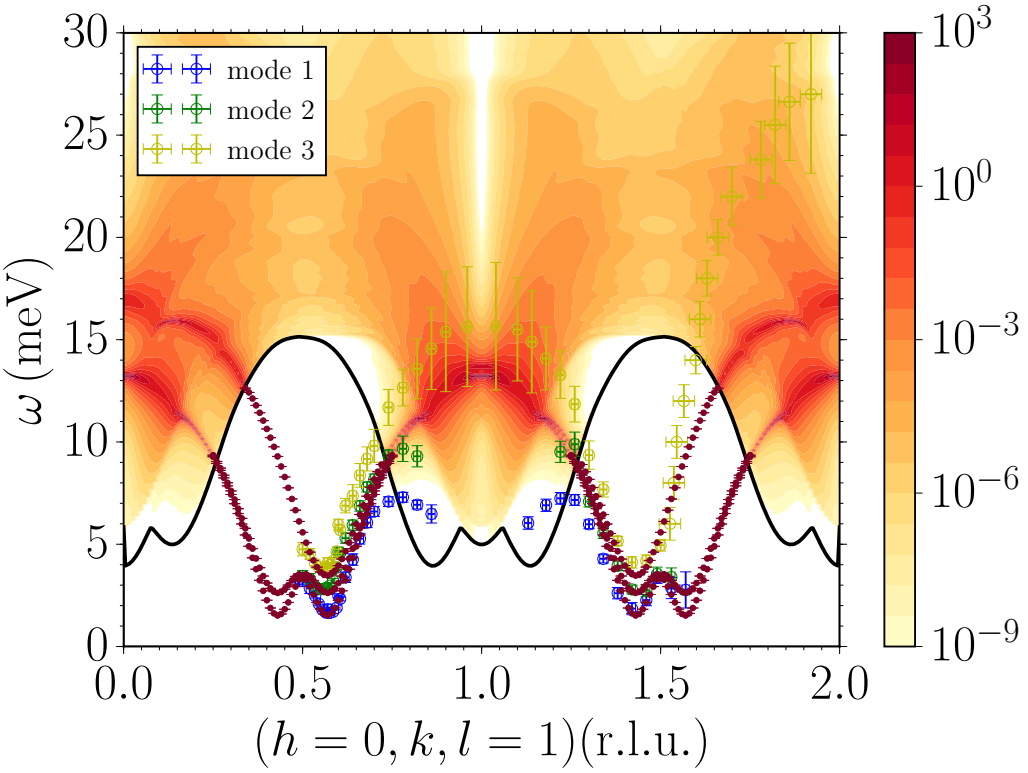

Figure 5.6: Logarithmic color map of the computed spectral function $A(k,\omega)$ for the fitted renormalized one-particle dispersions $\widetilde{\omega}_{b,r}(k)$, $\widetilde{\omega}_{b,r}(k+\pi)$ and $\widetilde{\omega}_{z,r}(k)$ with the parameters shown in figure 5.4. The black solid line represents the lowest boundary of the two-particle continua $\widetilde{\omega}_{2,b}(k)$, $\widetilde{\omega}_{2,b}(k+\pi)$ and $\widetilde{\omega}_{2,z}(k)$. Outside the corresponding two-particle continua the one-particle dispersions are depicted with error bars equal to zero, which imply triplon excitations with infinite lifetime.

(iii) Considering the shape of the dispersion $\widetilde{\omega}_{z,r}(k)$ determined by the complete approach the major discrepancies observed in the bilinear anisotropic model and the direct approach remain, i.e. the missing match between $\widetilde{\omega}_{z,r}(k)$ and the measured mode 3. Compared to the bilinear anisotropic ansatz, see figure 4.4, the z mode is shifted to lower energies in the entire BRILLOUIN zone. In contrast to the results of the direct approach, see figure 5.3, the complete approach provides a better fit around $k = 1\,\text{r.l.u.}$ but it is still impossible to reproduce the resonances in this range. As explained before the finite values of the components Γ_0^{zz}, Γ_1^{zz} and Γ_2^{zz} acting on the z mode in the complete approach increase the one-particle dispersion around the minimum. At this point, it is crucial to recall the effect of the variation of J_2, which already ensures a lowering of all modes. So the anisotropic couplings compensate this effect in such a way that the results in the complete approach concerning the z mode produce the best description of mode 3 up to this point. Adjusting the values of the anisotropic couplings to achieve a better fit for mode 3 would result in a declined fit of the two lowest modes 1 and 2.

(iv) The down-bending behavior of mode 1 and 2 towards lower energies around $k = 0.75\,\text{r.l.u.}$ represents an important property of the experimentally received data. As a reminder, our expectation is that this prominent down-bending behavior stems from the hybridization between one-triplon and two-triplon states. Using the complete approach for the variation of J_2 we take these effects into account but unfortunately the level repulsion turns out to be too weak in order to reproduce the characteristic down-bending behavior of the two lowest modes, see also figure 5.6. In contrast to the direct approach, where the decay behavior of all modes is identical, each mode decays differently in the complete approach. Only a slight down-bending behavior around $k = 0.8\,\text{r.l.u.}$ can be identified, see figure 5.4 and 5.5, but it is not sufficient enough to provide a satisfying description of the experimental data. Note, that only the parameter $\delta = 1/3$ of the J_2 variation is responsible for SQPD in this issue and no other effects in BCPO. The close-up of the area where the renormalized one-particle dispersions and the corresponding two-particle continua overlap, see figure 5.5, illustrates no significant shifts of the one-particle dispersions to lower energies or energies outside the two-particle continuum. A detailed look into the performed numerical calculations reveals the unexpected fact that the hybridization of the one-triplon and two-triplon states, i.e. the absolute values of the prefactors of the decay terms, see eq. (5.3.16), are noticeable smaller at momenta where the one-particle dispersions and the corresponding two-particle continua overlap compared to other areas of the BRILLOUIN zone. As a consequence, the peaks of the corresponding spectralfunctions near $k = 0.8\,\text{r.l.u.}$ are sharp and their positions are near the undisturbed one-particle dispersions, see figure

5.7. Considering the color map of the spectral function $A(k,\omega)$ in figure 5.6 displays that it is possible to identify clear quasiparticle peaks in the spectral function for all k values in the complete BRILLOUIN zone. Around $k = 0.8\,\text{r.l.u.}$ it is also clearly visible that no strong SQPD processes exist, i.e. the peaks in the spectral function are just slightly smeared out and show negligibly small weight near the lower boundary of the two-particle continuum. As in the direct approach, the effects of SQPD do not have a strong influence on the lifetime of the triplons so that they can still be identified and labeled as quasiparticles in the whole BRILLOUIN zone.

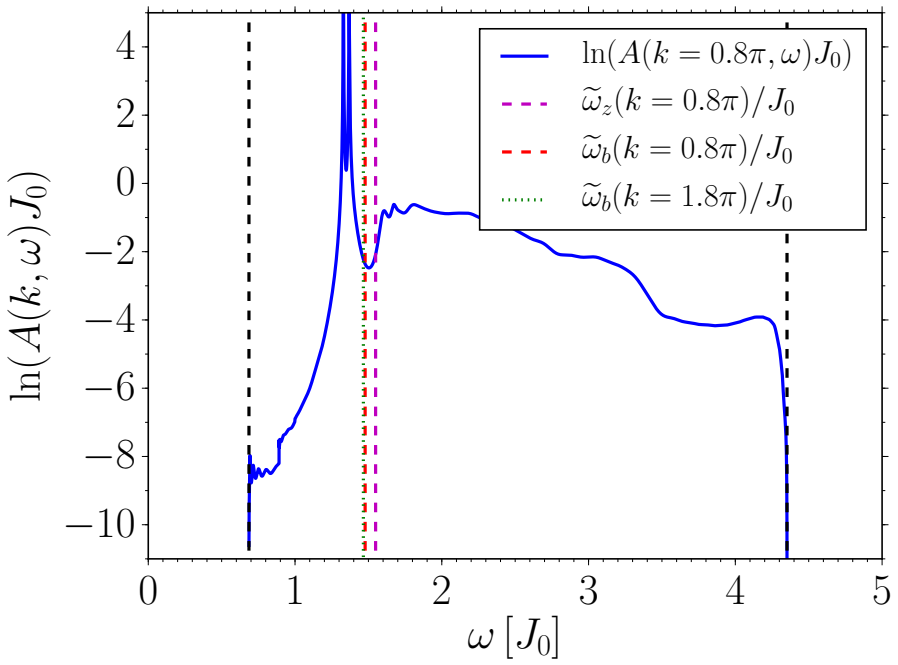

Figure 5.7: Spectral function $A(k,\omega)$ for fixed momentum $k = 0.8\pi$ containing the contributions of the low-energy modes $\widetilde{\omega}_z(k)$, $\widetilde{\omega}_b(k)$ and $\widetilde{\omega}_b(k+\pi)$. Note, that the y-axis has a logarithmic scale. The black dashed lines represent the lower and upper boundary of all corresponding two-particle continua $\widetilde{\omega}_{2,z}(k)$, $\widetilde{\omega}_{2,b}(k)$ and $\widetilde{\omega}_{2,b}(k+\pi)$. The colored dashed lines mark the positions of the dispersions $\widetilde{\omega}_z(k)$, $\widetilde{\omega}_b(k)$ and $\widetilde{\omega}_b(k+\pi)$, see eqs. (4.2.21) and (4.2.30), for fixed momentum $k = 0.8\pi$. The energy ω is discretized in steps of $0.0001 J_0$.

(v) The maximum value reached is ≈17 meV for the z mode, which is 1 meV larger compared to the results of the direct approach. However, the large difference to the measured values of ≈27 meV remains. Comparing the size of the displayed error bars of the z mode, i.e. the HWHM of the quasiparticle peaks in the spectral function, around $k = 2\,\text{r.l.u.}$ in figures 5.3 and 5.4, it is noticeable that they are larger for the complete approach than for the direct approach. But still it is not possible to explain the high energy regime with the assumed effects of SQPD in BCPO. Even with the complete approach

for the variation of the J_2 coupling we cannot determine an appropriate set of parameters in order to improve the match between theory and experiment at high energies.

At the end of this section we sum up our results for the variation of the NNN coupling J_2 using the complete approach for the quantum antiferromagnet BCPO. The aim of this analysis was to provide an enhanced description of the experimental dispersion data of BCPO compared to the previous studies in sects. 4.2.3 and 5.2. The important aspect of the complete approach is that the decay behavior of each mode stemming from anisotropic couplings in BCPO is treated individually. With this more detailed analysis of a finite variation in the J_2 coupling we expected to achieve an improved agreement between theory and experiment using smaller values for the **D** components compared to the direct approach with $\mathbf{D}_1 \approx 0.58 J_1$. Not all of these expectations could be met within the complete approach but several features of the experimental data could be reproduced. Using the complete approach results in the best fit between theory and experiment in the low-energy regime for an even broader range of the BRILLOUIN zone so far. A reduction of the **D** components to our expected values of $0.1 - 0.2$ is also possible. The dominant value of $\mathbf{D}_1 \approx 0.48 J_1$ is still larger than estimated but states a 20 % reduction compared to our previous fit results. In contrast, the other components $D_0^y = 0.1 J_0$ and $D_2^z = -0.09 J_2$ assume values which meet our expectations. All modes display an individual down-bending behavior, but it turns out that the hybridization between the one- and two-particle states is not sufficient to describe the experimentally observed down-bending in a satisfying way.

5.4 Chapter summary

To conclude this chapter we sum up the results for the analysis of the alternating NNN coupling J_2 within the magnetic structure of the quantum antiferromagnet BCPO. The origin of this effect lies in the crystallographical inequivalent copper ions which describe the magnetic structure of BCPO. This spinisotropic effect induces a hybridization of one- and two-particle states, i.e. quasiparticle decay/fusion processes, due to its odd parity. Taking into account these processes we analyzed their influence on the one-particle dispersion. Because of the hybridization between the one- and two-particle HILBERT spaces we expected to receive an improved description of the experimental data with smaller **D** values compared to the previous analysis in chapter 4. In this context we used two different approaches. Firstly, we introduced the direct approach with is based on the spinisotropic analysis of BCPO, see sect. 4.1. After computing the renormalized spinisotropic dispersion we included the anisotropic couplings of BCPO within the bilinear ansatz explained in sect. 4.2.2. As a result, the renormalized anisotropic dispersions show several promising features in comparison with the experiment. These contain a

minimal reduction of the dominant component $\mathbf{D}_1 \approx 0.58J_1$, compared to $\mathbf{D}_1 \approx 0.6J_1$, and first indications of the experimentally observed down-bending behavior.
Secondly, as a more complex method we established the complete approach. Its starting point is given by the model of BCPO derived in chapter 4, which includes anisotropic couplings up to bilinear operator level in a mean-field approach. The decay and fusion processes stemming from the finite variation of the J_2 coupling are transformed into the basis of the bilinear model in order to analyze their effects on the one-particle dispersions. The results of this ansatz represent our current best agreement between theory and experiment. We were able to reduce the component $\mathbf{D}_1 \approx 0.48J_1$ furthermore and to set the components $\mathbf{D}_0 \approx 0.1J_0$ and $\mathbf{D}_2 \approx -0.1J_2$, which are consistent with our expection of $10 - 20\,\%$ of the isotropic couplings. The existing down-bending behavior can also be explained partially.
We performed the first explicit description of the J_2 variation in the crystal structure of BCPO in the literature receiving promising results. However, this is just one of the different effects in BCPO which induce SQPD. We strongly assume to improve our results by taking into account the decay and fusion processes which stem from the anisotropic couplings in BCPO directly. In the following chapter we discuss this issue in detail.

6 Description of the quantum antiferromagnet $BiCu_2PO_6$ on trilinear operator level with spin anisotropic effects

In the former chapter we discussed the effects of SQPD induced by a variation of the isotropic NNN coupling J_2 on the one-particle dispersions in the magnetic structure of BCPO. As a result we achieved an improved description of the experimental data in the low-energy regime using anisotropic couplings with values up to 48 % compared to the isotropic couplings with constant J_2. Compared to our results for BCPO without the effects of SQPD this represents a reduction of 20 % for the anisotropic couplings. The fact that the excitation modes of BCPO are not degenerated, but split, see sect. 1.4, shows clearly that DM interactions are present. Consequently, we also have to consider their contributions towards SQPD. The DM interactions themselves have odd parity and therefore provide transition processes between the one- and two-particle HILBERT space. We have the strong presumption that adding these effects to our calculations leads to a further improvement in understanding the observed down-bending behavior of the low-energy modes. A similiar analysis has been realized by PLUMB *et al.* [39] and HWANG and KIM [64] using diagrammatic perturbation theory and the quadratic bond operator theory. By means of their theoretical work it was possible to reduce the values of the anisotropic couplings from 60 % compared to the isotropic coupling strengths down to 30%. Additionally, the broadening of the spectral function inside the two-particle continuum can be described at a satisfactory level. Despite these achieved improvements, the prominent down-bending behavior of the low-energy modes could not be reproduced, neither qualitatively nor quantitatively.

Following our confirmation and refinement of the results from PLUMB *et al.* [70], see sect. 4.3, we take the effects of SQPD, which are induced by the DM interactions, into account on the basis of our previous established model of BCPO, see chapter 4. With this approach we provide a comprehensive description for the quantum antiferromag-

net BCPO and expect to receive clear explainations for all its experimentally observed features in the excitation spectrum.

6.1 Analysis of the anisotropic DM couplings

Our detailed symmetry analysis in sect. 4.2.1 revealed that the four components D_0^y, D_1^x, D_1^y and D_2^x out of the five existing $\mathbf{D}$ components in BCPO have odd parity, see table 4.1. Figure 6.1 displays the possible orientation of all $\mathbf{D}$ vectors in the spin model of BCPO consistent with the rules of Moriya [74].

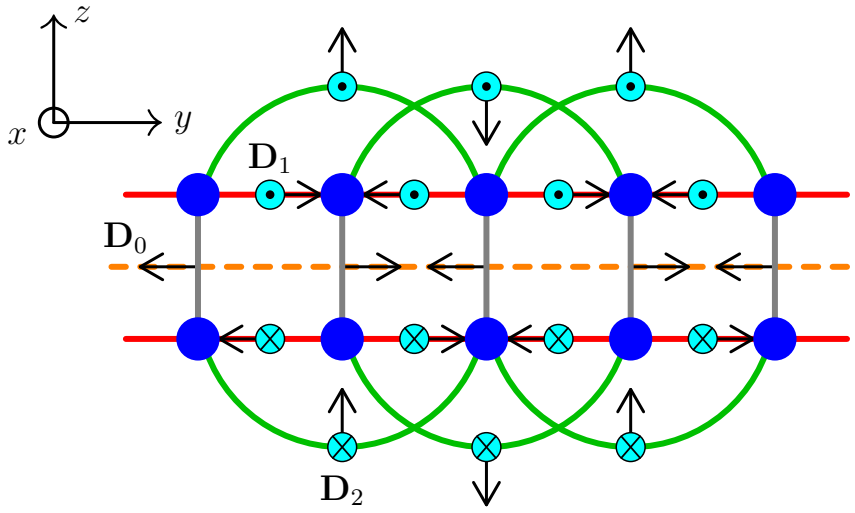

Figure 6.1: Orientation of the $\mathbf{D}$ vectors in the spin model of BCPO, see also figure 4.3. Note, that only a single spin ladder without the interladder coupling J' is depicted. The short arrows display the orientation of the $\mathbf{D}$ vectors in $\mathbf{D}_{ij} \cdot (\mathbf{S}_i \times \mathbf{S}_j)$, see eq. (4.2.11), whereas the spins on site i and j are ordered by ascending y respectively z coordinate. The length of the vectors is not to scale. The orange dashed line charactertizes the center line of the spin ladder. $\mathbf{D}$ components holding odd parity with respect to a reflection at this symmetry axis generate operator terms containing an odd number of single triplon operators.

To take the effects of the odd components D_0^y, D_1^x, D_1^y and D_2^x for our SQPD analysis into account we follow the complete approach, as outlined in sect. 5.1. For the first step we write down the observables which characterize the odd $\mathbf{D}$ components

$$\mathcal{H}^{D_0^y} = D_0^y \sum_i (-1)^i \left(S_i^{z,\mathrm{R}} S_i^{x,\mathrm{L}} - S_i^{x,\mathrm{R}} S_i^{z,\mathrm{L}} \right) \tag{6.1.1a}$$

$$\mathcal{H}^{D_1^x} = D_1^x \sum_i \left(S_i^{y,\mathrm{L}} S_{i+1}^{z,\mathrm{L}} - S_i^{z,\mathrm{L}} S_{i+1}^{y,\mathrm{L}} - S_i^{y,\mathrm{R}} S_{i+1}^{z,\mathrm{R}} + S_i^{z,\mathrm{R}} S_{i+1}^{y,\mathrm{R}} \right) \tag{6.1.1b}$$

$$\mathcal{H}^{D_1^y} = D_1^y \sum_i (-1)^i \left(S_i^{z,\mathrm{L}} S_{i+1}^{x,\mathrm{L}} - S_i^{x,\mathrm{L}} S_{i+1}^{z,\mathrm{L}} - S_i^{z,\mathrm{R}} S_{i+1}^{x,\mathrm{R}} + S_i^{x,\mathrm{R}} S_{i+1}^{z,\mathrm{R}} \right) \tag{6.1.1c}$$

$$\mathcal{H}^{D_2^x} = D_2^x \sum_i \left(S_i^{y,\mathrm{L}} S_{i+2}^{z,\mathrm{L}} - S_i^{z,\mathrm{L}} S_{i+2}^{y,\mathrm{L}} - S_i^{y,\mathrm{R}} S_{i+2}^{z,\mathrm{R}} + S_i^{z,\mathrm{R}} S_{i+2}^{y,\mathrm{R}} \right) \tag{6.1.1d}$$

and occur in the Hamiltonian $\mathcal{H}$, see eq. (4.2.11). Note, that the spins at site i and j are arranged according to ascending y coordinate[1], see also sect. 4.2.1. Since the components D_0^y and D_1^y alternate along the spin ladder in y-direction, see table 4.1, a factor of $(-1)^i$ has to be considered in eqs. (6.1.1a) and (6.1.1c). As the next steps in our analysis we have to apply a deepCUT in order to map the operator part of eqs. (6.1.1) onto operator terms including an odd number of single triplon operators[2]. Considering only operator terms up to trilinear level results in

$$\begin{aligned}
&t^{y,\dagger}_{i+\delta_1}, && t^{x,\dagger}_{i+\delta_1} t^{x,\dagger}_{i+\delta_2} t^{y}_{i+\delta_3}, && t^{x,\dagger}_{i+\delta_1} t^{y,\dagger}_{i+\delta_2} t^{x}_{i+\delta_3}, && t^{y,\dagger}_{i+\delta_1} t^{y,\dagger}_{i+\delta_2} t^{y}_{i+\delta_3}, \\
&t^{y,\dagger}_{i+\delta_1} t^{z,\dagger}_{i+\delta_2} t^{z}_{i+\delta_3}, && t^{z,\dagger}_{i+\delta_1} t^{z,\dagger}_{i+\delta_2} t^{y}_{i+\delta_3}, && t^{x,\dagger}_{i+\delta_1} t^{x,\dagger}_{i+\delta_2} t^{y,\dagger}_{i+\delta_3}, && t^{y,\dagger}_{i+\delta_1} t^{z,\dagger}_{i+\delta_2} t^{z,\dagger}_{i+\delta_3}, \\
&t^{y,\dagger}_{i+\delta_1} t^{y,\dagger}_{i+\delta_2} t^{y,\dagger}_{i+\delta_3} && + \text{h.c.}
\end{aligned} \tag{6.1.2}$$

for the observables from eqs. (6.1.1a) and (6.1.1c) and in

$$\begin{aligned}
&t^{x,\dagger}_{i+\delta_1}, && t^{x,\dagger}_{i+\delta_1} t^{y,\dagger}_{i+\delta_2} t^{y}_{i+\delta_3}, && t^{y,\dagger}_{i+\delta_1} t^{y,\dagger}_{i+\delta_2} t^{x}_{i+\delta_3}, && t^{z,\dagger}_{i+\delta_1} t^{z,\dagger}_{i+\delta_2} t^{x}_{i+\delta_3}, \\
&t^{x,\dagger}_{i+\delta_1} t^{z,\dagger}_{i+\delta_2} t^{z}_{i+\delta_3}, && t^{x,\dagger}_{i+\delta_1} t^{x,\dagger}_{i+\delta_2} t^{x}_{i+\delta_3}, && t^{x,\dagger}_{i+\delta_1} t^{y,\dagger}_{i+\delta_2} t^{y,\dagger}_{i+\delta_3}, && t^{x,\dagger}_{i+\delta_1} t^{z,\dagger}_{i+\delta_2} t^{z,\dagger}_{i+\delta_3}, \\
&t^{x,\dagger}_{i+\delta_1} t^{x,\dagger}_{i+\delta_2} t^{x,\dagger}_{i+\delta_3} && + \text{h.c.}
\end{aligned} \tag{6.1.3}$$

for the observables from eqs. (6.1.1b) and (6.1.1d) with the relative distances δ_1, δ_2, δ_3. The spin observables stemming from the components D_0^y and D_1^y (D_1^x and D_2^x) have both a spin orientation in y-direction (x-direction). As a consequence, the deepCUT maps both observables onto the same type of triplon operator terms but with different prefactors. Note, we only concentrate on terms with up to three single triplon operators since we expect these to have the main influence on the effects of SQPD, see also sect. 3.2. This means that we neglect all terms with five or more single triplon operators. In contrast to the spin isotropic observable for the alternating NNN coupling J_2, see sect. 5.1 and especially eq. (5.1.3), all the observables of the odd **D** components also generate linear terms, i.e. a single triplon creation/annihilation operator. The reason for this is that the observables in eqs. (6.1.1) have a concrete spin orientation, i.e. they have a total spin of S=1 just like a single triplon operator. As a single triplon operator does not describe a transition between the one- and two-particle HILBERT space, it has no direct influence on the effects of SQPD[3]. Therefore we do not take the linear operator terms into account in our calculations.

[1] For the rung component D_0^y the spin operators are sorted by ascending z coordinate.

[2] The applied deepCUT was performed up to order 10 in the Hamiltonian, i.e. up to order 9 for observables [94]. Since the spin ladder structure is invariant under the reflection symmetry S_{xy}, see figure 4.3 and sect. 4.2.1, this means that for observables processes with a maximum distance of 2×9 rungs in real space are taken into account.

[3] It is possible to include the effects of the linear operator term by applying a constant shift in all triplon operators but we neglect this aspect.

The next step is to apply a two-dimensional FOURIER transform to all trilinear operator terms, which stem from the deepCUT. For the observables of the components D_0^y and D_1^y this leads to the same expressions as in eqs. (5.3.11) and (5.3.12) because the observable of the J_2 variation holds also an alternating sign. By contrast, the decay/fusion terms stemming from the uniform observables D_1^x and D_2^x have the FOURIER transform

$$\left(\mathcal{H}^{D_1^x}+\mathcal{H}^{D_2^x}\right)_{\text{decay}}=(D_1^x+D_2^x)\sum_{\alpha',\beta',\gamma'}\sum_{k,q}\sum_{l,p}\sum_{\delta_1,\delta_2,\delta_3}\frac{\alpha_{\delta_1,\delta_2,\delta_3}^{\alpha',\beta',\gamma'}}{\sqrt{N_kN_l}}\mathrm{e}^{\mathrm{i}(\delta_2-\delta_1)q}\mathrm{e}^{\mathrm{i}(\delta_3-\delta_2)k}t_{q,p}^{\alpha',\dagger}t_{k-q,l-p}^{\beta',\dagger}t_{k,l}^{\gamma'} \tag{6.1.4}$$

with the flavor combinations $(\alpha',\beta',\gamma')\in\{(x,y,y),(y,y,x),(z,z,x),(x,z,z),(x,x,x)\}$. The variable $\alpha_{\delta_1,\delta_2,\delta_3}^{\alpha',\beta',\gamma'}\in\mathbb{C}$ denotes the prefactor of the corresponding triplon operator term in real space, which is determined by the applied deepCUT. The FOURIER transform of the remaining trilinear operator terms reads

$$\left(\mathcal{H}^{D_1^x}+\mathcal{H}^{D_2^x}\right)_{\text{fluc}}=(D_1^x+D_2^x)\sum_{\alpha',\beta',\gamma'}\sum_{k,q}\sum_{l,p}\sum_{\delta_1,\delta_2,\delta_3}\frac{\beta_{\delta_1,\delta_2,\delta_3}^{\alpha',\beta',\gamma'}}{\sqrt{N_kN_l}}\mathrm{e}^{\mathrm{i}(\delta_2-\delta_1)q}\mathrm{e}^{\mathrm{i}(\delta_2-\delta_3)k}t_{q,p}^{\alpha',\dagger}t_{-k-q,-l-p}^{\beta',\dagger}t_{k,l}^{\gamma',\dagger} \tag{6.1.5}$$

with the flavor combinations $(\alpha',\beta',\gamma')\in\{(x,y,y),(x,z,z),(x,x,x)\}$ and $\beta_{\delta_1,\delta_2,\delta_3}^{\alpha',\beta',\gamma'}\in\mathbb{C}$ being the prefactor in real space. Note, that in contrast to the FOURIER transform of an alternating quantity, see eqs. (5.3.11) and (5.3.12), no shift of π is present in the momentum of the second creation operator. Following the next step for the complete approach we have to transform all trilinear terms in momentum space into the same basis as the Hamiltonians $\widetilde{\mathcal{H}}_{\text{BCPO},z}^{\text{eff}}$ and $\widetilde{\mathcal{H}}_{\text{BCPO},bu}^{\text{eff}}$, see eqs. (4.2.20) and (4.2.32). After normal-ordering the transformed trilinear terms the following operator terms emerge

$$\begin{array}{lll}
\tilde{t}_{q,p}^{b,\dagger}\tilde{t}_{k-q,l-p}^{b,\dagger}\tilde{t}_{k,l}^{b}, & \tilde{t}_{q,p}^{b,\dagger}\tilde{t}_{k-q,l-p}^{u,\dagger}\tilde{t}_{k,l}^{b}, & \tilde{t}_{q,p}^{u,\dagger}\tilde{t}_{k-q,l-p}^{u,\dagger}\tilde{t}_{k,l}^{b},\\
\tilde{t}_{q,p}^{z,\dagger}\tilde{t}_{k-q,l-p}^{z,\dagger}\tilde{t}_{k,l}^{b}, & \tilde{t}_{q,p}^{b,\dagger}\tilde{t}_{k-q,l-p}^{b,\dagger}\tilde{t}_{k,l}^{u}, & \tilde{t}_{q,p}^{b,\dagger}\tilde{t}_{k-q,l-p}^{u,\dagger}\tilde{t}_{k,l}^{u},\\
\tilde{t}_{q,p}^{u,\dagger}\tilde{t}_{k-q,l-p}^{u,\dagger}\tilde{t}_{k,l}^{u}, & \tilde{t}_{q,p}^{z,\dagger}\tilde{t}_{k-q,l-p}^{z,\dagger}\tilde{t}_{k,l}^{u}, & \tilde{t}_{q,p}^{z,\dagger}\tilde{t}_{k-q,l-p}^{b,\dagger}\tilde{t}_{k,l}^{z},\\
\tilde{t}_{q,p}^{z,\dagger}\tilde{t}_{k-q,l-p}^{u,\dagger}\tilde{t}_{k,l}^{z}, & \tilde{t}_{0,0}^{b,\dagger}, & \tilde{t}_{0,0}^{u,\dagger}\\
\tilde{t}_{q,p}^{z,\dagger}\tilde{t}_{-k-q,-l-p}^{z,\dagger}\tilde{t}_{k,l}^{b,\dagger}, & \tilde{t}_{q,p}^{z,\dagger}\tilde{t}_{-k-q,-l-p}^{z,\dagger}\tilde{t}_{k,l}^{u,\dagger}, & \tilde{t}_{q,p}^{b,\dagger}\tilde{t}_{-k-q,-p}^{b,\dagger}\tilde{t}_{k,l}^{b,\dagger},\\
\tilde{t}_{q,p}^{b,\dagger}\tilde{t}_{-k-q,l-p}^{b,\dagger}\tilde{t}_{k,l}^{u,\dagger}, & \tilde{t}_{q,p}^{b,\dagger}\tilde{t}_{-k-q,-l-p}^{u,\dagger}\tilde{t}_{k,l}^{u,\dagger}, & \tilde{t}_{q,p}^{u,\dagger}\tilde{t}_{-k-q,-l-p}^{u,\dagger}\tilde{t}_{k,l}^{u,\dagger},
\end{array} \tag{6.1.6}$$

supplemented by the Hermitian conjugated part of each non-Hermitian operator term. By analogy with the complete approach for the alternating NNN coupling J_2 linear operator terms at a fixed momentum pair $(k=0,l=0)$ occur after normal-ordering, see sect. 5.3. Since the original spin observables, see eqs. (6.1.1), hold a specific spin orientation, the linear contributions $\tilde{t}_{0,0}^{b,\dagger}$ and $\tilde{t}_{0,0}^{u,\dagger}$ do not vanish in general. But as explained in the fifth step of the complete approach, see sect. 5.3, we neglect their

effects as well as the effects of the operator terms consisting of three creation/annihilation operators. Thus, we keep the following operator terms

$$\begin{aligned}
&\tilde{t}^{b,\dagger}_{q,p}\tilde{t}^{b,\dagger}_{k-q,l-p}\tilde{t}^{b}_{k,l}, \quad \tilde{t}^{b,\dagger}_{q,p}\tilde{t}^{u,\dagger}_{k-q,l-p}\tilde{t}^{b}_{k,l}, \quad \tilde{t}^{u,\dagger}_{q,p}\tilde{t}^{u,\dagger}_{k-q,l-p}\tilde{t}^{b}_{k,l}, \quad \tilde{t}^{z,\dagger}_{q,p}\tilde{t}^{z,\dagger}_{k-q,l-p}\tilde{t}^{b}_{k,l},\\
&\tilde{t}^{b,\dagger}_{q,p}\tilde{t}^{b,\dagger}_{k-q,l-p}\tilde{t}^{u}_{k,l}, \quad \tilde{t}^{b,\dagger}_{q,p}\tilde{t}^{u,\dagger}_{k-q,l-p}\tilde{t}^{u}_{k,l}, \quad \tilde{t}^{u,\dagger}_{q,p}\tilde{t}^{u,\dagger}_{k-q,l-p}\tilde{t}^{u}_{k,l}, \quad \tilde{t}^{z,\dagger}_{q,p}\tilde{t}^{z,\dagger}_{k-q,l-p}\tilde{t}^{u}_{k,l},\\
&\tilde{t}^{z,\dagger}_{q,p}\tilde{t}^{b,\dagger}_{k-q,l-p}\tilde{t}^{z}_{k,l}, \quad \tilde{t}^{z,\dagger}_{q,p}\tilde{t}^{u,\dagger}_{k-q,l-p}\tilde{t}^{z}_{k,l},
\end{aligned} \tag{6.1.7}$$

for our further calculations. As we are only interested in the properties of the z and the b mode in order to describe the low-energy regime, we focus on the trilinear operator terms which affect these. The remaining operator terms in (6.1.7) reveal that the b mode can decay in four different ways. A single triplon with flavor b and momentum (k,l) can decay into two particles with the flavors $(b,b)\,/\,(b,u)\,/\,(u,u)\,/\,(z,z)$ and the momenta (q,p) and $(k-q,l-p)$. This means that the one-particle dispersion $\widetilde{\omega}_b(k,l)$ couples to the four two-particle continua

$$\widetilde{\omega}_{2,bb}(k,l,q,p) = \widetilde{\omega}_b(q,p) + \widetilde{\omega}_b(k-q,l-p) \tag{6.1.8a}$$

$$\widetilde{\omega}_{2,bu}(k,l,q,p) = \widetilde{\omega}_b(q,p) + \widetilde{\omega}_u(k-q,l-p) \tag{6.1.8b}$$

$$\widetilde{\omega}_{2,uu}(k,l,q,p) = \widetilde{\omega}_u(q,p) + \widetilde{\omega}_u(k-q,l-p) \tag{6.1.8c}$$

$$\widetilde{\omega}_{2,zz}(k,l,q,p) = \widetilde{\omega}_z(q,p) + \widetilde{\omega}_z(k-q,l-p) \tag{6.1.8d}$$

with the total momentum (k,l) and the relative momentum (q,p) using the one-particle dispersions $\widetilde{\omega}_b(k,l)$, $\widetilde{\omega}_u(k,l)$ and $\widetilde{\omega}_z(k,l)$, which we derived in eqs. (4.2.21) and (4.2.30). Concerning the possible decay channels of a single particle with z flavor and fixed momentum (k,l) the listed operator terms in (6.1.7) reveal that it can decay in two different ways. Namely, the one-particle dispersion $\widetilde{\omega}_z(k,l)$ couples to the two different two-particle-continua

$$\widetilde{\omega}_{2,zb}(k,l,q,p) = \widetilde{\omega}_z(q,p) + \widetilde{\omega}_b(k-q,l-p) \tag{6.1.9a}$$

$$\widetilde{\omega}_{2,zu}(k,l,q,p) = \widetilde{\omega}_z(q,p) + \widetilde{\omega}_u(k-q,l-p)\,. \tag{6.1.9b}$$

As the last step of the complete approach we can now add the trilinear terms in eq. (6.1.7) to the Hamiltonians $\widetilde{\mathcal{H}}^{\text{eff}}_{\text{BCPO},z}$ and $\widetilde{\mathcal{H}}^{\text{eff}}_{\text{BCPO},bu}$, see eqs. (4.2.20) and (4.2.32). Again, we leave out the explicit expression of the prefactors of the trilinear operator terms in eq. (6.1.7) since they are given by long formulae which are evaluated numerically anyway. For this composed Hamiltonian we follow the last step of the complete approach, i.e. we perform a Lanczos tridiagonalization with a maximum number of two quasiparticles and calculate the renormalized dispersions $\widetilde{\omega}_{z,r}(k)$ and $\widetilde{\omega}_{b,r}(k)$ for our trilinear anisotropic model of BCPO as explained in sects. 2.3.1, 2.3.2 and 2.3.3.

In order to search for the values of the **D** components which provide the best match between our theoretical results and the experimental data in a systematic manner, we analyze the effects of each odd **D** component on the renormalized dispersion $\widetilde{\omega}_{b,r}(k)$ separately[4].

As pointed out in sect. 4.2.2, the x and y mode are coupled by finite values of the **D** component D_2^z and the matrix entry Γ_1^{xy}. If these components are equal to zero, the bilinear anisotropic Hamiltonian $\mathcal{H}_{\mathrm{BCPO},xy}^{\mathrm{eff}}$, see eq. (4.2.22), is solved by two separate bosonic BOGOLIUBOV transformations reading

$$t_{k,l}^{\alpha,\dagger} = \cosh\left(\vartheta_{k,l}^{\alpha}\right)\tilde{t}_{k,l}^{\alpha,\dagger} + \sinh\left(\vartheta_{k,l}^{\alpha}\right)\tilde{t}_{-k,-l}^{\alpha} \tag{6.1.10a}$$

$$t_{-k,-l}^{\alpha} = \cosh\left(\vartheta_{k,l}^{\alpha}\right)\tilde{t}_{-k,-l}^{\alpha} + \sinh\left(\vartheta_{k,l}^{\alpha}\right)\tilde{t}_{k,l}^{\alpha,\dagger} \tag{6.1.10b}$$

with $\alpha \in \{x, y\}$[5]. We also set the isotropic interladder coupling J' to zero so that we concentrate on one-dimensional models in the following. Thus, the solution of the complete bilinear anisotropic Hamiltonian $\mathcal{H}_{\mathrm{BCPO},xy}^{\mathrm{eff}} + \mathcal{H}_{\mathrm{BCPO},z}^{\mathrm{eff}}$, see eqs. (4.2.22) and (4.2.16), is given by

$$\sum_{k,\alpha} \underbrace{\sqrt{\left(\omega_0(k)\right)^2 + 2\omega_0(k)\left(\Gamma_0^{\alpha\alpha}(k) + \Gamma_1^{\alpha\alpha}(k) + \Gamma_2^{\alpha\alpha}(k)\right)}}_{=\widetilde{\omega}_1^{\alpha}(k)} \tilde{t}_k^{\alpha,\dagger}\tilde{t}_k^{\alpha} \tag{6.1.11}$$

with $\alpha \in \{x, y, z\}$ and the abbreviations

$$\Gamma_0^{\alpha\alpha}(k) = -2\Gamma_0^{\alpha\alpha}a^2(k) \tag{6.1.12a}$$

$$\Gamma_1^{\alpha\alpha}(k) = 4\Gamma_1^{\alpha\alpha}a^2(k)\cos(k) \tag{6.1.12b}$$

$$\Gamma_2^{\alpha\alpha}(k) = 4\Gamma_2^{\alpha\alpha}a^2(k)\cos(2k)\,. \tag{6.1.12c}$$

As a consequence, it is possible to analyze the effects of the anisotropic couplings on all modes independently of each other. At a later stage of this thesis, we find out that is it crucial to choose a finite value for the components D_2^z and Γ_1^{xy} in order to fit our theoretically calculated dispersions to the experimental data. This means that the original x and y modes are coupled and mapped onto the b and u mode, see sect. 4.2.2. Since the solutions for the x and y mode are identical up to a shift of π, see again sect. 4.2.2, it is sufficient to analyze only the x mode or only the y mode in detail even for

[4] As described in sect. 4.2.3 we only present the effects of the anisotropic couplings on $\widetilde{\omega}_b(k)$ because during our analysis it turned out that the dispersion $\widetilde{\omega}_z(k)$ cannot be fitted in a satisfying way. The effects on the dispersion $\widetilde{\omega}_u(k)$, see eq. (4.2.30), are not relevant for our analysis since we want to describe the low-energy regime.

[5] See eqs. (4.2.38) and (4.2.39) for the used abbreviations.

the decoupled cases. As the x mode contributes to the b mode at the same momentum k, see sect. 4.2.2, we choose the x mode and analyze its renormalized dispersion $\widetilde{\omega}_{x,r}(k)$ in detail in the following.

6.1.1 Analysis of the components D_0^y and D_1^y

In this subsection we analyze the effects of the anisotropic couplings D_0^y and D_1^y on the isotropic dispersion $\omega_0(k)$ of a single spin ladder, see sect. 4.1.1, in detail. All other anisotropic couplings are set to zero. As a finite value of the components D_0^y and D_1^y do not induce a coupling between the x and y mode, the modes can be treated separately and we focus on the effects on the x mode, see sect. 6.1. The deepCUT maps the observables of the components D_0^y and D_1^y, see eqs. (6.1.1a) and (6.1.1c), onto the same operator terms, see eq. (6.1.2). Applying a bosonic BOGOLIUBOV transformation for each flavor separately on these trilinear operator terms reveals that a single triplon with flavor x and momentum k can only decay into two triplons with flavors x and y holding the momenta q and $k-q+\pi$. This means that the components D_0^y and D_1^y induce a hybridization of the one-triplon states with flavor x and momentum k and the two-triplon states with the flavors (x,y) and total momentum $k+\pi$. As a consequence, the limiting values for the LANCZOS coefficients $a_\infty(k)$ and $b_\infty(k)$, see Appendix A, are determined by the lower and upper boundary of the two-particle continuum

$$\widetilde{\omega}_{2,xy}(k+\pi,q) = \widetilde{\omega}_1^x(q) + \widetilde{\omega}_1^y(k-q+\pi) \tag{6.1.13}$$

at a total momentum of $k+\pi$. For the Hamiltonian[6]

$$\widetilde{\mathcal{H}}_{\mathrm{BCPO},x}^{\mathrm{decay},D_0^y+D_1^y} = \sum_{k,\alpha} \widetilde{\omega}_1^\alpha(k)\, \tilde{t}_k^{\alpha,\dagger}\tilde{t}_k^\alpha + \sum_{k,q}\left(\widetilde{\Gamma}^{xyx}(k,q)\, \tilde{t}_q^{x,\dagger}\tilde{t}_{k-q+\pi}^{y,\dagger}\tilde{t}_k^x + \mathrm{h.c.}\right) \tag{6.1.14}$$

we perform a LANCZOS tridiagonalization[7] and calculate the renormalized dispersion $\widetilde{\omega}_{x,r}(k)$, see sects. 2.3.1, 2.3.2 and 2.3.3, which we want to analyze in detail for different values of D_0^y and D_1^y. The results are depicted in figure 6.2 and discussed in the following. Note, that the two-particle continuum $\widetilde{\omega}_{2,xy}(k+\pi,q)$ is also affected by D_0^y and D_1^y. For a better overview concerning the renormalized dispersion $\widetilde{\omega}_{x,r}(k)$ we display only the lower boundary of the two-particle continuum $\widetilde{\omega}_{2,xy}(k+\pi,q)$, see eq. (6.1.13), for the case $D_0^y = D_1^y = 0$ in figure 6.2 as an orientation. In our studies we distinguish between the effects inside and outside of the two-particle continuum.

[6] The variable $\widetilde{\Gamma}^{xyx}(k,q) \in \mathbb{C}$ is the prefactor of the corresponding operator term in the basis of the separate BOGOLIUBOV transformations for the x and y mode.

[7] The initial state is a one-triplon state with flavor x and momentum k.

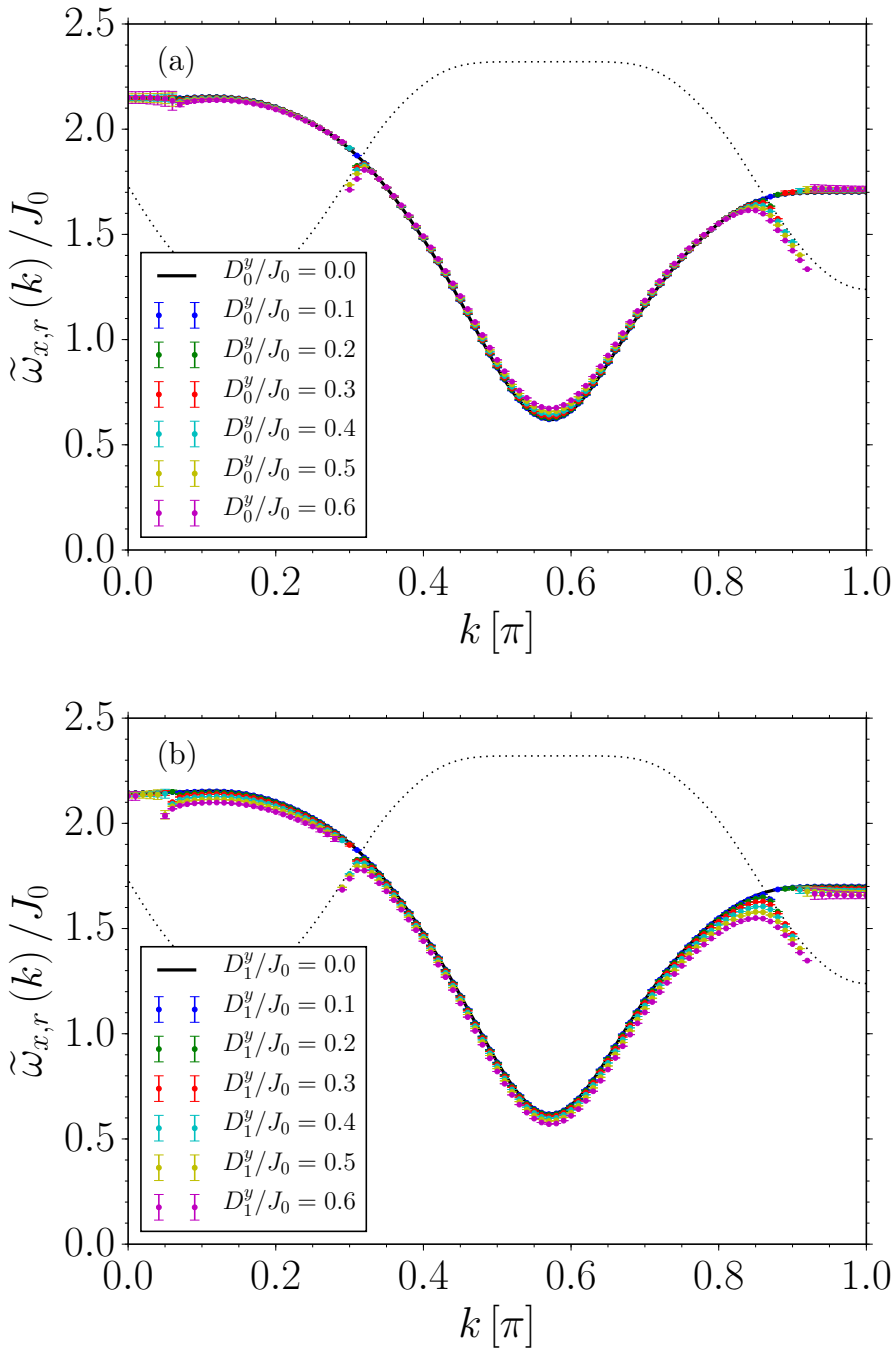

Figure 6.2: (a) Illustration of the renormalized dispersion $\widetilde{\omega}_{x,r}(k)$ as a function of the component D_0^y. All other $\mathbf{D}$ components are set to zero. As thresholds to identify quasiparticle peaks in the corresponding spectral functions, see sect. 3.4.1, we set a maximum relative HWHM of $\left(\gamma(k)/\Delta\widetilde{\omega}_{2,xy}(k+\pi)\right)_{\max} = 0.05$ and a minimal spectral weight of $(1/s)_{\min} = 0.005$. (b) Illustration of the renormalized dispersion $\widetilde{\omega}_{x,r}(k)$ as a function of the component D_1^y. All other $\mathbf{D}$ components are set to zero. As thresholds to identify quasiparticle peaks in the corresponding spectral functions, we set a maximum relative HWHM of $\left(\gamma(k)/\Delta\widetilde{\omega}_{2,xy}(k+\pi)\right)_{\max} = 0.01$ and a minimal spectral weight of $(1/s)_{\min} = 0.001$. For the parameters of the isolated frustrated spin ladder we use the values $x = 1.2$ and $y = 0.9$ in both panels. The dotted line in both panels is the lower boundary of the two-particle continuum $\widetilde{\omega}_{2,xy}(k+\pi, q)$, see eq. (6.1.13), for the case $D_0^y = D_1^y = 0$.

Panel (a) of figure 6.2 illustrates the effects of D_0^y on the x mode.

Inside the two-particle continuum, $D_0^y \neq 0$

Inside the two-particle continuum between $k = 0\pi$ and $k \approx 0.3\pi$ an increase of D_0^y provides shifts to lower energies, but which are difficult to notice. The corresponding HWHMs are also hardly to observe meaning that in the corresponding spectral functions the quasiparticle peaks are sharp and their position does not differ much from $\omega_0(k)$. Inside the two-particle continuum between $k \approx 0.9\pi$ and $k = \pi$ the dispersion is shifted to higher energies. The HWHMs are also small.

Outside the two-particle continuum, $D_0^y \neq 0$

Near the lower boundary of the corresponding two-particle continuum $\widetilde{\omega}_{2,xy}(k+\pi, q)$ at $k \approx 0.3\pi$ and $k \approx 0.9\pi$ we see a down-bending behavior of the renormalized one-particle dispersion $\widetilde{\omega}_{x,r}(k)$, which becomes more pronounced for larger values of D_0^y. Outside the two-particle continuum an increase of D_0^y results in a slight shift to higher energies. In total, the component D_0^y has only slight effects on the x mode and the lifetime of a triplon with flavor x is not affected so strongly that it becomes impossible to identify it as a quasiparticle.

Panel (b) of figure 6.2 shows the effects of D_1^y on the x mode.

Inside the two-particle continuum, $D_1^y \neq 0$

Inside the two-particle continuum, i.e. in the approximate intervals $k \in [0\pi, 0.3\pi]$ and $k \in [0.9\pi, \pi]$, the dispersion is only slightly reduced and the HWHM of each quasiparticle peak in the corresponding spectral function is small. So it is possible to identify them clearly. Increasing the value for D_1^y makes these effects more pronounced.

Outside the two-particle continuum, $D_1^y \neq 0$

Near the lower boundary of the two-particle continuum at $k \approx 0.3\pi$ and $k \approx 0.9\pi$ the renormalized dispersion $\widetilde{\omega}_{x,r}(k)$ shows a clearly visible down-bending behavior, which correlates positively with D_1^y. Outside the two-particle continuum the dispersion is lowered.

On the whole, neither D_1^y nor D_0^y have a strong impact on the x mode. An increasing value of D_1^y leads to an energy reduction in the complete BRILLOUIN zone. Furthermore, the lifetime of a triplon with flavor x is sufficiently large to identify it as a quasiparticle.

6.1.2 Analysis of the components D_1^x and D_2^x

In this subsection we discuss the effects of the anisotropic couplings D_1^x and D_2^x on the isotropic dispersion $\omega_0(k)$ of a single spin ladder, see sect. 4.1.1, in detail. The other anisotropic couplings are set to zero. Since the components D_1^x and D_2^x do not cause a coupling between the x and y mode, we can treat the modes separately and focus on the effects on the x mode, see sect. 6.1. Applying a deepCUT to the observables of the components D_1^x and D_2^x, see eqs. (6.1.1b) and (6.1.1d), results in the same operator

terms which are listed in eq. (6.1.3). Applying a bosonic BOGOLIUBOV transformation for each flavor separately on these trilinear operator terms reveals that there are three different decay channels for the x mode. A single triplon with flavor x and momentum k can decay into two triplons with the flavor combinations $(y,y)\,/\,(z,z)\,/\,(x,x)$ holding the momenta $(q, k-q)$. As the behavior of the sign of the components D_1^x and D_2^x is uniform, see table 4.1, the components D_1^x and D_2^x induce a hybridization of the one-triplon states with flavor x and momentum k and the two-triplon states with the flavor combinations (y,y), (z,z) and (x,x) with the same total momentum k. Consequently, the limiting values for the LANCZOS coefficients $a_\infty(k)$ and $b_\infty(k)$, see Appendix A, are fixed by the lower and upper boudary of the three two-particle continua

$$\widetilde{\omega}_{2,yy}(k,q) = \widetilde{\omega}_1^y(q) + \widetilde{\omega}_1^y(k-q) \tag{6.1.15a}$$

$$\widetilde{\omega}_{2,zz}(k,q) = \widetilde{\omega}_1^z(q) + \widetilde{\omega}_1^z(k-q) \tag{6.1.15b}$$

$$\widetilde{\omega}_{2,xx}(k,q) = \widetilde{\omega}_1^x(q) + \widetilde{\omega}_1^x(k-q) \tag{6.1.15c}$$

at total momentum k each. For a better understanding, we combine the three mentioned two-particle continua to one two-particle continuum which we name $\widetilde{\omega}_{2,x}(k,q)$. For the Hamiltonian[8]

$$\begin{aligned}\widetilde{\mathcal{H}}_{\mathrm{BCPO},x}^{\mathrm{decay},D_1^x+D_2^x} = &\sum_{k,\alpha}\widetilde{\omega}_1^\alpha(k)\,\tilde{t}_k^{\alpha,\dagger}\tilde{t}_k^\alpha + \sum_{k,q}\left(\widetilde{\Gamma}^{yyx}(k,q)\,\tilde{t}_q^{y,\dagger}\tilde{t}_{k-q}^{y,\dagger}\tilde{t}_k^x + \mathrm{h.c.}\right) + \\ &\sum_{k,q}\left(\widetilde{\Gamma}^{zzx}(k,q)\,\tilde{t}_q^{z,\dagger}\tilde{t}_{k-q}^{z,\dagger}\tilde{t}_k^x + \widetilde{\Gamma}^{xxx}(k,q)\,\tilde{t}_q^{x,\dagger}\tilde{t}_{k-q}^{x,\dagger}\tilde{t}_k^x + \mathrm{h.c.}\right)\end{aligned}^{9} \tag{6.1.16}$$

we perform a LANCZOS tridiagonalization[10] and calculate the renormalized dispersion $\widetilde{\omega}_{x,r}(k)$, see sects. 2.3.1, 2.3.2 and 2.3.3, which we want to analyze in detail for different values of D_1^x and D_2^x. The results are presented in figure 6.3 and discussed in the following. As well as in sect. 6.1.1, we display only the lower boundary of the two-particle continuum $\widetilde{\omega}_{2,x}(k,q)$ for the case $D_1^x = D_2^x = 0$ in figure 6.3 as an orientation to ensure a better overview of the renormalized dispersion $\widetilde{\omega}_{x,r}(k)$.

[8] The variables $\{\widetilde{\Gamma}^{yyx}(k,q), \widetilde{\Gamma}^{zzx}(k,q), \widetilde{\Gamma}^{xxx}(k,q)\} \in \mathbb{C}$ are the prefactors of the corresponding operator terms in the basis of the separate BOGOLIUBOV transformations for the modes x, y and z.

[10] The initial state is again a one-triplon state with flavor x and momentum k.

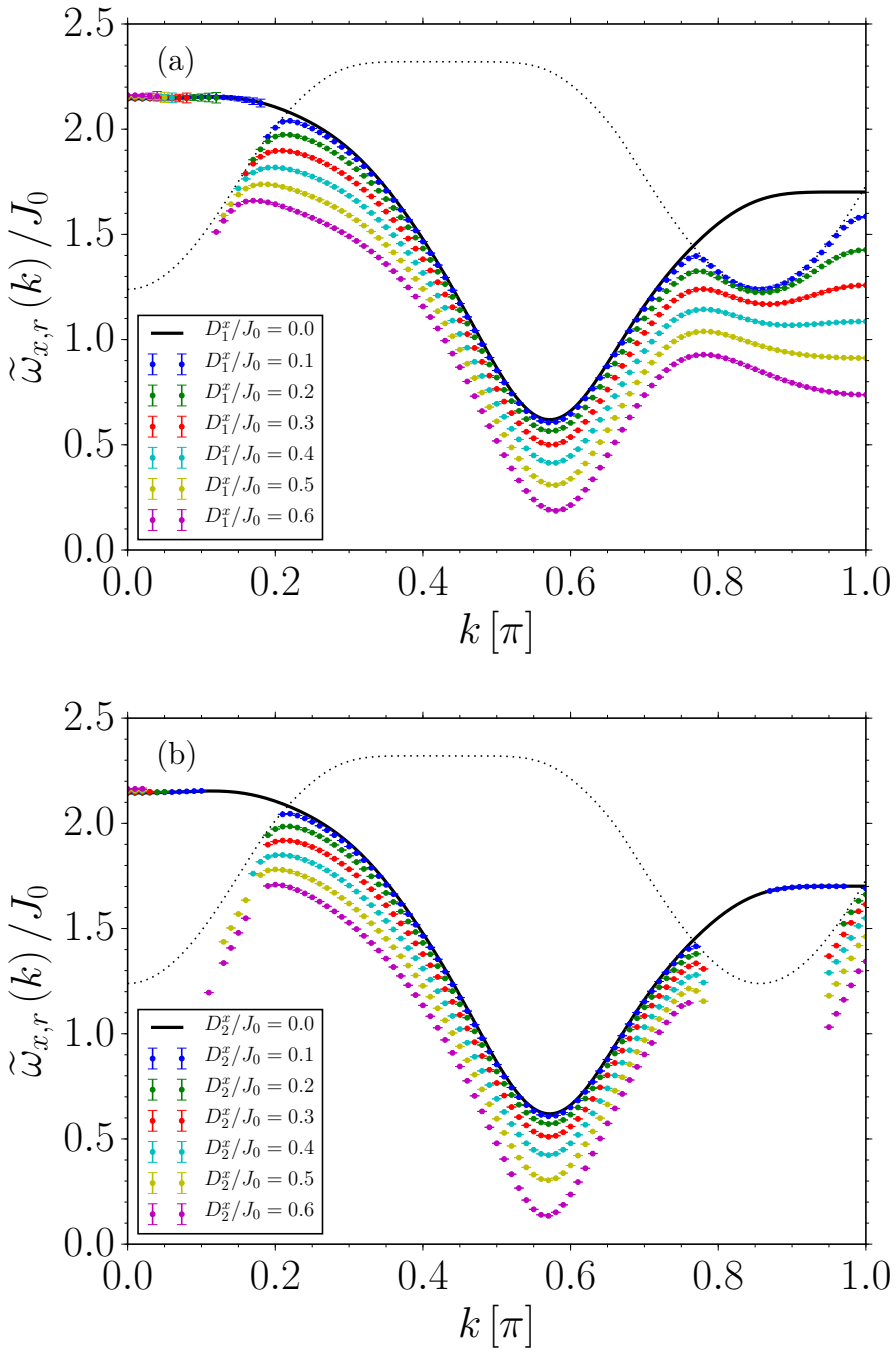

Figure 6.3: (a) Illustration of the renormalized dispersion $\widetilde{\omega}_{x,r}(k)$ as a function of the component D_1^x. All other $\mathbf{D}$ components are set to zero. As thresholds to identify quasiparticle peaks in the corresponding spectral functions, see sect. 3.4.1, we set a maximum relative HWHM of $(\gamma(k)/\Delta\widetilde{\omega}_{2,x}(k))_{\max} = 0.01$ and a minimal spectral weight of $(1/s)_{\min} = 0.001$. (b) Illustration of the renormalized dispersion $\widetilde{\omega}_{x,r}(k)$ as a function of the component D_2^x. All remaining $\mathbf{D}$ components are set to zero. As thresholds to identify quasiparticle peaks, we set a maximum relative HWHM of $(\gamma(k)/\Delta\widetilde{\omega}_{2,x}(k))_{\max} = 0.001$ and a minimal spectral weight of $(1/s)_{\min} = 0.001$. For the parameters of the isolated frustrated spin ladder we use the values $x = 1.2$ and $y = 0.9$ in both panels. The dotted line in both panels is the lower boundary of the two-particle continuum $\widetilde{\omega}_{2,x}(k,q)$ for the case $D_1^x = D_2^x = 0$.

Panel (a) of figure 6.3 depicts the effects of D_1^x on the x mode.

Inside the two-particle continuum, $D_1^x \neq 0$

Inside the two-particle continuum $\widetilde{\omega}_{2,x}(k,q)$ between $k = 0\pi$ and $k \approx 0.2\pi$ an increase of D_1^x shows only hardly noticeable shifts of the dispersion to higher energies. The corresponding HWHMs are also small and difficult to spot. In contrast to the results in section 6.1.1, the HWHMs of the quasiparticle peaks in the corresponding spectral functions become larger than the chosen threshold of $(\gamma(k)/\Delta\widetilde{\omega}_{2,x}(k)) = 0.01$ with increasing D_1^x. This means that the lifetime of the triplon is not sufficient long enough to consider it as a quasiparticle.

Outside the two-particle continuum, $D_1^x \neq 0$

Outside and near the border of the two-particle continuum at $k \approx 0.8\pi$ the one-particle dispersion is shifted to lower energies significantly. Especially the prominent down-bending behavior near the lower boundary of the two-particle continuum at $k \approx 0.8\pi$ is an important aspect to mention. The level repulsion between the relevant one-particle and two-particle HILBERT spaces is so strong that the one-particle dispersion is pushed below the two-particle continuum[11].

Overall, the component D_1^x has a strong influence on the x mode and induces such a strong level repulsion between the corresponding one- and two-particle HILBERT spaces so that the renormalized dispersion $\widetilde{\omega}_{x,r}(k)$ is pushed below the two-particle continuum.

The effects of the component D_2^x on the x mode are shown in panel (b) in figure 6.3.

Inside the two-particle continuum, $D_2^x \neq 0$

Inside the two-particle continuum $\widetilde{\omega}_{2,x}(k,q)$ between $k = 0\pi$ and $k \approx 0.1\pi$ no significantly visible effects on the renormalized dispersion $\widetilde{\omega}_{x,r}(k)$ exist. Inside the two-particle continuum from $k \approx 0.8\pi$ to $k = \pi$ we observe that an increasing value of D_2^x ensures that the one-particle dispersion of a triplon with flavor x vanishes. However, around $k = \pi$ the level repulsion between the corresponding one- and two-particle HILBERT spaces is so strong that the one-particle dispersion is pushed below the lower boundary of the two-particle continuum.

Outside the two-particle continuum, $D_2^x \neq 0$

Near the lower boundary of the two-particle continuum $\widetilde{\omega}_{2,x}(k,q)$ at $k \approx 0.1\pi$ a clear down-bending behavior can be observed which grows upon increasing D_2^x. Outside the two-particle continuum from $k \approx 0.1\pi$ to $k \approx 0.8\pi$ the renormalized dispersion $\widetilde{\omega}_{x,r}(k)$ is shifted significantly to lower energies. Near the lower boundary of $\widetilde{\omega}_{2,x}(k,q)$ at $k \approx 0.8\pi$ only a slight down-bending can be identified and the renormalized dispersion terminates

[11] In regards to the experimental data of BCPO, see e.g. figure 4.1, this point is essential since the data are characterized by a prominent down-bending behavior of the two lower modes as mentioned before.

abruptly when entering the two-particle continuum because it is strongly damped.
In total, the component D_2^x has a strong influence on the x mode and ensures that its one-particle dispersion is reduced strongly outside the two-particle continuum. Inside the two-particle continuum an increasing value of D_2^x leads to the scenario that the x mode vanishes.

6.1.3 Analysis of the combination of the components D_1^x and D_1^y

In this subsection we analyze the effects of finite values of the anisotropic couplings D_1^x and D_1^y on the isotropic dispersion $\omega_0(k)$ of a single spin ladder, see sect. 4.1.1. The remaining anisotropic couplings are set to zero. In this case the matrix element Γ_1^{xy} holds a non-zero value, see eq. (2.4.84), and provides a coupling between the x and y mode, see sect. 4.2.2. So we have to analyze the effects of the combination of D_1^x and D_1^y on the b mode, see sect. 6.1 for further details[12]. The results are presented in figure 6.4 and discussed in the following. By analogy with the results in sects. 6.2 and 6.3, we display only the lower boundary of the two-particle continuum $\widetilde{\omega}_{2,b}(k,q)$ for the case $D_1^x = 0.1J_0$ and $D_1^y = 0.2J_0$ respectively $D_1^x = 0.2J_0$ and $D_1^y = 0.1J_0$ in order to provide a detailed overview of the renormalized one-particle dispersion $\widetilde{\omega}_{b,r}(k)$.

At first, we analyze the effects of the component D_1^x with a constant value of $D_1^y = 0.2J_0$ on the b mode, which are displayed in panel (a) in figure 6.4.

Inside the two-particle continuum, $D_1^x \neq 0$ and $D_1^y = \text{const.}$

Inside the two-particle continuum $\widetilde{\omega}_{2,b}(k,q)$ at $k \approx 0\pi$ even small values of D_1^x lead to the scenario that no quasiparticle energies can be identified and the renormalized one-particle dispersion $\widetilde{\omega}_{b,r}(k)$ vanishes. With an increasing value of D_1^x the level repulsion between the one- and the multiple corresponding two-particle states becomes strong enough to push the one-particle dispersion below the two-particle continuum, see the case $D_1^x = 0.6J_0$. In the interval $k \in [0.8\pi, \pi]$, we can observe the same situation to a greater extent.

Outside the two-particle continuum, $D_1^x \neq 0$ and $D_1^y = \text{const.}$

Outside the two-particle continuum a clear lowering of the renormalized one-particle dispersion $\widetilde{\omega}_{b,r}(k)$ is visible. In contrast to the results of the previous subsections 6.1.1 and 6.1.2, this lowering effect varies in the BRILLOUIN zone. In the interval $k \in [0.5\pi, \pi]$ the energy reduction is significantly stronger than in the interval $k \in [0\pi, 0.5\pi]$. These insights are consistent with our results concerning the effects of D_1^x, see sect. 6.1.2 and panel (a) in figure 6.3.

[12] Note, that we also set the interladder coupling J' to zero, so that the calculations explained in sect. 6.1 are reduced to a one-dimensional problem, i.e. the second momentum has be discarded in all steps.

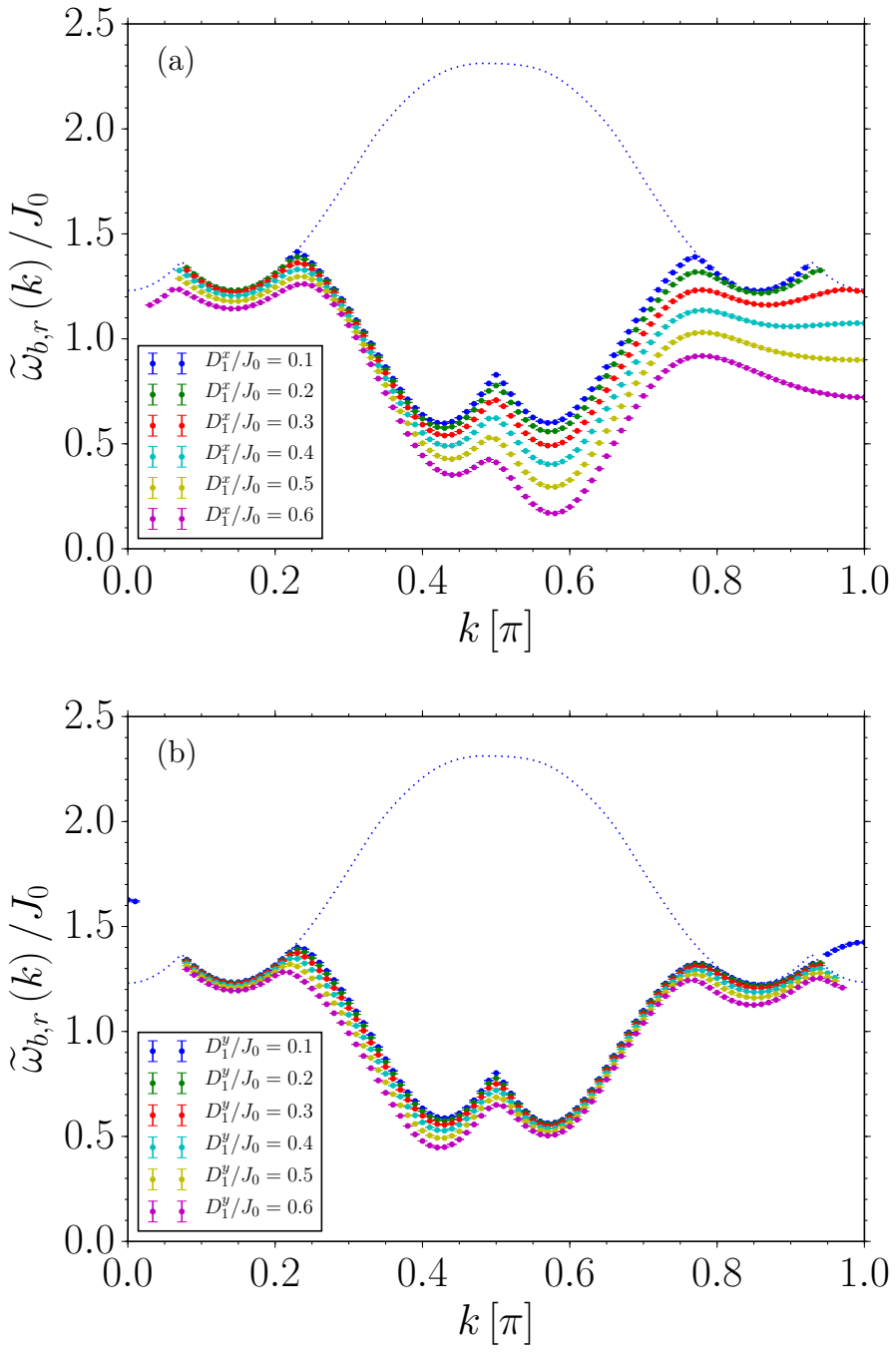

Figure 6.4: (a) Illustration of the renormalized dispersion $\widetilde{\omega}_{b,r}(k)$ as a function of the component D_1^x with a fixed value of $D_1^y = 0.2J_0$. All other $\mathbf{D}$ components are equal to zero. As thresholds to identify quasiparticle peaks in the corresponding spectral functions, see sect. 3.4.1, we set a maximum relative HWHM of $(\gamma(k)/\Delta\widetilde{\omega}_{2,b}(k))_{\max} = 0.001$ and a minimal spectral weight of $(1/s)_{\min} = 0.001$. (b) Illustration of the renormalized dispersion $\widetilde{\omega}_{b,r}(k)$ as a function of the component D_1^y with a fixed value of $D_1^x = 0.2J_0$. All remaining $\mathbf{D}$ components are set to be zero. As thresholds to identify quasiparticle peaks, we set a maximum relative HWHM of $(\gamma(k)/\Delta\widetilde{\omega}_{2,b}(k))_{\max} = 0.001$ and a minimal spectral weight of $(1/s)_{\min} = 0.001$. For the parameters of the isolated frustrated spin ladder we use the values $x = 1.2$ and $y = 0.9$ in both panels. The dotted line in both panels is the lower boundary of the two-particle continuum $\widetilde{\omega}_{2,b}(k,q)$ for the case $D_1^x = 0.1J_0$ and $D_1^y = 0.2J_0$ respectively $D_1^x = 0.2J_0$ and $D_1^y = 0.1J_0$.

Finally, we discuss the influence of the component D_1^y with a constant value of $D_1^x = 0.2J_0$ on the b mode, see panel (b) in figure 6.4.

Inside the two-particle continuum, $D_1^y \neq 0$ and $D_1^x = \text{const.}$

Inside the two-particle continuum $\widetilde{\omega}_{2,b}(k,q)$ at $k \approx 0\pi$ already small values of D_1^y have the effect that no quasiparticle energies can be located because the corresponding resonances are smeared out too strongly. By analogy with the coupling D_1^x, an increasing value of the component D_1^y generates a level repulsion between the one- and the multiple corresponding two-particle states which is strong enough to push the one-particle states energetically below the two-particle continuum. In the interval $k \in [0.8\pi, \pi]$ we receive the same results.

Outside the two-particle continuum, $D_1^y \neq 0$ and $D_1^x = \text{const.}$

Outside the two-particle continuum only small effects can be observed. Increasing the value of D_1^y provides a slight reduction of the renormalized one-particle dispersion $\widetilde{\omega}_{b,r}(k)$. Furthermore, the concrete characteristic of this lowering effect varies in the BRILLOUIN zone. In the interval $k \in [0\pi, 0.5\pi]$ the energy reduction is slightly stronger than in the interval $k \in [0.5, \pi]$. These findings are consistent with out results concerning the effects of D_1^y, see sect. 6.1.1 and panel (b) of figure 6.2. Compared to the asymmetric energy reduction to the point $k = 0.5\pi$ induced by a variation of the component D_1^x, the impact of a comparably large value for D_1^y is significantly smaller and the asymmetry is reversed.

6.2 Results for the trilinear anisotropic Hamiltonian of BCPO

The main issue for the trilinear anisotropic description of the quantum antiferromagnet BCPO is to take the effects of SQPD into account, which are induced by the majority of the allowed **D** components, see eqs. (6.1.1). With this comprehensively extended model of BCPO we determine the values of all allowed **D** components, see table 4.1, which provide the best fit for the experimentally measured data of the dispersions. As discussed thoroughly in sect. 4.2.3, we expect the consideration of SQPD to provide a great improvement of the results compared to the bilinear anisotropic model of BCPO, see chapter 4.

The detailed studies of the effects of each odd **D** component on the calculated one-particle dispersion $\widetilde{\omega}_x(k)$ or $\widetilde{\omega}_b(k)$ in sects. 6.1.1, 6.1.2 and 6.1.3 are the basis for fitting the experimental dispersion data. The main results are listed in table 6.1 as a reminder.
Using the knowledge of the effects of each **D** component on the bilinear operator level, see table 4.3, and on the trilinear operator level, see table 6.1, we can search for the values of the **D** components which lead to the best match between our calculated

D_{ij}^{α}	$\widetilde{\omega}_x(k)$ or $\widetilde{\omega}_b(k)$	effects inside continuum	effects outside continuum
D_0^y	$\widetilde{\omega}_x(k)$	slight shifts	slight increase
D_1^x	$\widetilde{\omega}_x(k)$	slight shifts	strong down-bending behavior
D_1^y	$\widetilde{\omega}_x(k)$	slight reduction	strong lowering
D_1^x and $D_1^y = \text{const.}$	$\widetilde{\omega}_b(k)$	vanishing behavior	asymmetric lowering about $k = \frac{\pi}{2}$ $\rightarrow$ stronger lowering at $k > \frac{\pi}{2}$ and strong down-bending behavior
D_1^y and $D_1^x = \text{const.}$	$\widetilde{\omega}_b(k)$	vanishing behavior	asymmetric lowering about $k = \frac{\pi}{2}$ $\rightarrow$ stronger lowering at $k < \frac{\pi}{2}$
D_2^x	$\widetilde{\omega}_x(k)$	slight shifts	strong lowering

Table 6.1: SQPD effects of an increase of the various odd **D**-components on the one-particle dispersion $\widetilde{\omega}_x(k)$ or $\widetilde{\omega}_b(k)$, see eqs. (6.1.11) and (4.2.30). Note, that the component D_2^z has even parity, see table 4.1, and therefore does not contribute to SQPD.

dispersions and the experimentally received data in a systematic manner. Again, we take over the results for the isotropic approach, see sect. 4.1, meaning that we keep the parameters $x = 1.2$, $y = 0.9$ and $J'/J_0 = 0.16$ fixed and adjust only the values of the **D** components and the global energy scale J_0.
In the following we discuss several issues concerning our best fit, which is shown in figures 6.5 and 6.6, and compare the results to the ones of the bilinear anisotropic model, see figure 4.4.

(i) The good agreement between the two lowest-lying modes 1 and 2 and the calculated dispersions $\widetilde{\omega}_{b,r}(k)$ and $\widetilde{\omega}_b(k+\pi)$ in the bilinear model, see figure 4.4, could not be reproduced by taking into account the effects of SQPD stemming from anisotropic couplings. The asymmetry of $\widetilde{\omega}_{b,r}(k)$ around $k = 0.5\,\text{r.l.u.}$ is created by choosing $\widetilde{D}_1^x \neq \widetilde{D}_1^y \neq 0$, see sect. 6.1.3. Our analysis in this section reveals that this asymmetric effect around $k = 0.5\,\text{r.l.u.}$ including the effects of SQPD does not match the observed behavior of mode 1 and mode 2 simultaneously, in contrast to the bilinear anisotropic model, see figure 4.4. Therefore, it is only possible to describe mode 1 or mode 2 in a satisfying way within our trilinear anisotropic model of BCPO[13]. Following the results of our bilinear anisotropic model of BCPO we decided to choose $\widetilde{D}_1^y$ to be slightly larger than $\widetilde{D}_1^x$ in order to create the asymmetric behavior of the renormalized dispersions around $k = 0.5\,\text{r.l.u.}$. We stress that we achieved a clear reduction of the two dominant components $\widetilde{D}_1^x = 0.25$ and $\widetilde{D}_1^y = 0.38$ compared to the previous results $\widetilde{D}_1^x = 0.48$ and $\widetilde{D}_1^y = 0.61$, see figure 4.4. This states a reduction of $\approx 50\,\%$ and $\approx 40\,\%$.

[13]Again, it is possible to swap $\widetilde{\omega}_{b,r}(k)$ and $\widetilde{\omega}_{b,r}(k+\pi)$ by simply exchanging the values of $\widetilde{D}_1^x$ and $\widetilde{D}_1^y$.

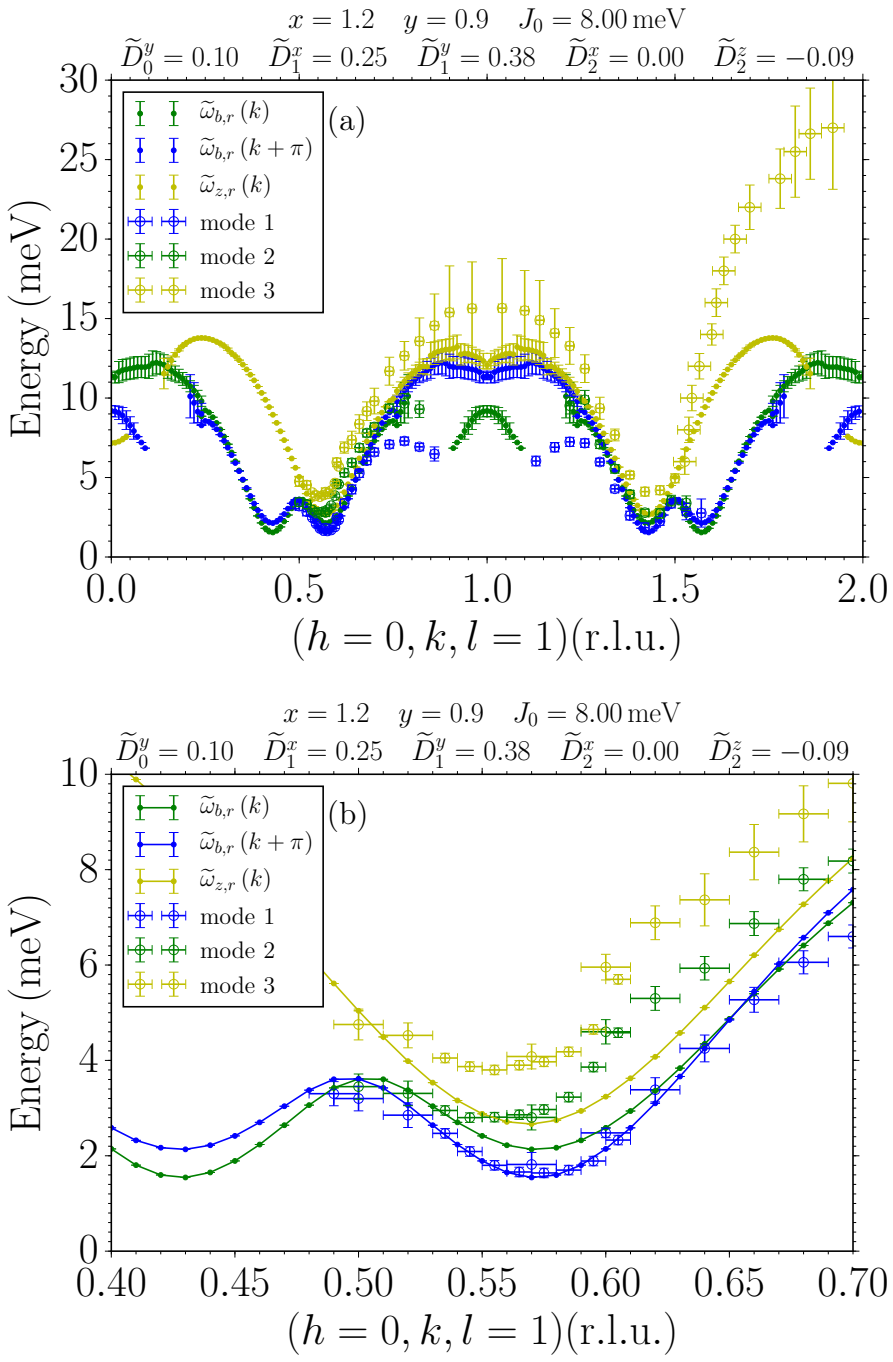

Figure 6.5: (a) Fitted theoretical dispersions, which stem from the z, x and y mode for the fixed parameters $x = 1.2$, $y = 0.9$ and $J'/J_0 = 0.16$. Their error bars depict the corresponding HWHM, see eq. (2.3.72). As thresholds to identify quasiparticle peaks in the corresponding spectral functions, see sect. 3.4.1, we set a maximum relative HWHM of $\left(\gamma(k)/\Delta\widetilde{\omega}_2(k)\right)_{\max} = 0.05$ and a minimal spectral weight of $\left(1/s\right)_{\min} = 0.001$. The fitted parameters are J_0, $\widetilde{D}_0^y$, $\widetilde{D}_1^x$, $\widetilde{D}_1^y$, $\widetilde{D}_2^x$ and $\widetilde{D}_2^z$. Their values are listed in the panel itself. (b) Zoom of panel (a) into the vicinity of the left minimum.

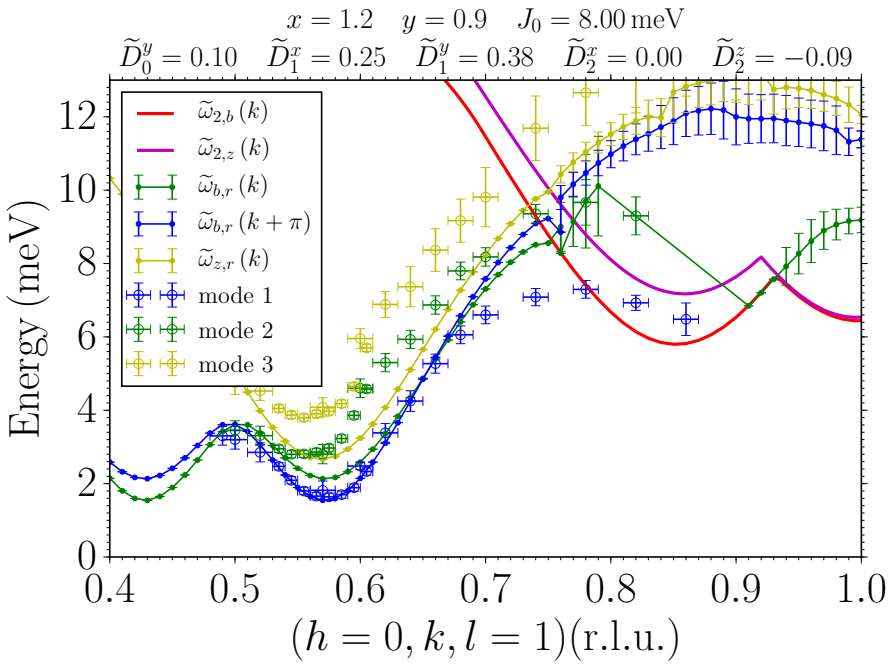

Figure 6.6: Zoom of panel (a) of figure 6.5 into the range where mode 1 and 2 show the prominent down-bending behavior. Additionally, the lower boundaries of the two-particle continua $\widetilde{\omega}_{2,b}(k)$ and $\widetilde{\omega}_{2,z}(k)$ are depicted by solid lines.

As a consequence, our result for $\widetilde{D}_1^x$ can be considered as a realistic value[14] whereas $\widetilde{D}_1^y = 0.38$ is still larger than expected. With this we want to emphasize that our established trilinear anisotropic model for the quantum antiferromagnet BCPO represents a more realistic model as its corresponding **D** components assume more reasonable values compared to previous discussed models.
Still, the components $\widetilde{D}_1^x$ and $\widetilde{D}_1^y$ present by far the largest values of all possible **D** components. Their combination has a strong impact on the shape of the calculated renormalized dispersion $\widetilde{\omega}_{b,r}(k)$, see table 6.1. We also stress that our results in figure 6.5 describe an improved description of the lowest-lying mode 1 in the interval $k = 0.5 - 0.7$ r.l.u. compared to the results of the bilinear model in figure 4.4.
Another positive aspect to comment on is the received value of $\widetilde{D}_0^y = 0.1$, which meets our expectations. Table 6.1 reveals that the component $\widetilde{D}_0^y$ affects the renormalized dispersions only slightly, but it is important to achieve the good match in the low-energy regime. As discussed in detail in passage (i) in sect. 5.3, D_0^y compensates the dominant effect of the quadratic component Γ_1^{xy} resulting from $\widetilde{D}_1^x$ and $\widetilde{D}_1^y$.

(ib) In the previous part (i) we mainly concentrated on the good agreement between

[14] As a reminder, our expectation concerning the value of the anisotropic couplings is $10 - 20\,\%$ of the corresponding isotropic couplings.

mode 1 and our results for $\widetilde{\omega}_{b,r}(k+\pi)$. A similiar satisfying agreement between mode 2 and our results for $\widetilde{\omega}_{b}(k)$ is not possible to achieve. This aspect was also discernible in figure 5.4 and discussed in part (ib) in sect. 5.3 in detail. Since the statements given there also hold for the trilinear anisotropic model, we ask the reader to reconsider this part.

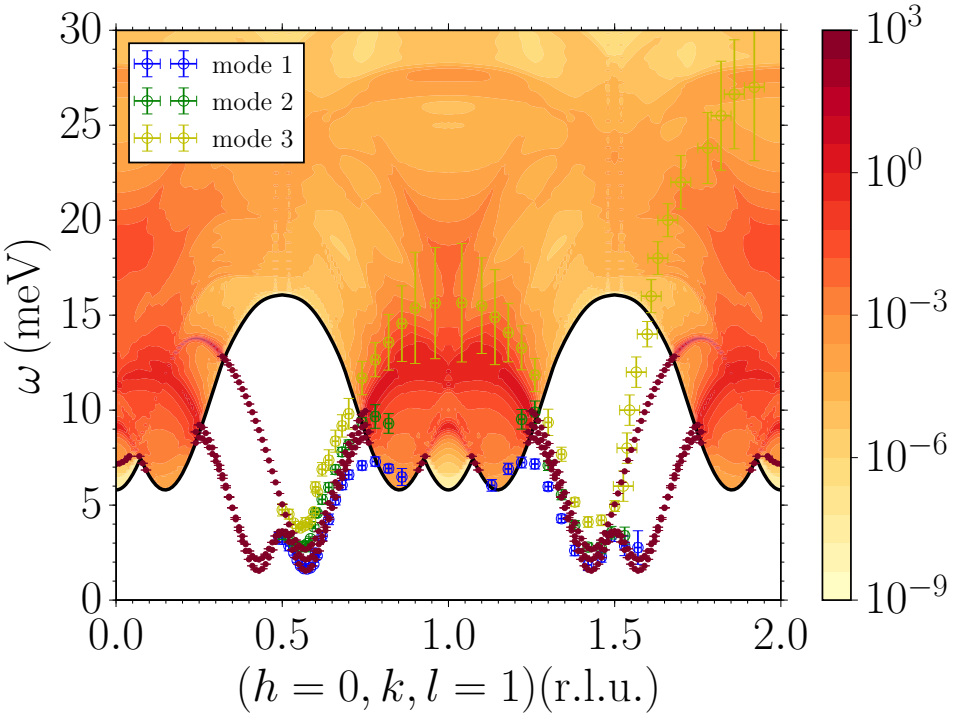

Figure 6.7: Logarithmic color map of the computed spectral function $A(k,\omega)$ for the fitted renormalized one-particle dispersions $\widetilde{\omega}_{b,r}(k)$, $\widetilde{\omega}_{b,r}(k+\pi)$ and $\widetilde{\omega}_{z,r}(k)$ with the parameters shown in figure 6.5. The black solid line represents the lowest border of the two-particle continua $\widetilde{\omega}_{2,b}(k)$, $\widetilde{\omega}_{2,b}(k+\pi)$ and $\widetilde{\omega}_{2,z}(k)$. Outside the corresponding two-particle continua the one-particle dispersions are depicted with error bars equal to zero implying triplon excitations with infinite lifetime.

(ii) As the only exception the component $\widetilde{D}_2^z$ holds even parity, see table 4.1, and therefore cannot give rise to the phenomenon of SQPD in BCPO. It just has an influence on the bilinear anisotropic model, which serves as a starting point for our more comprehensive trilinear anisotropic model. Its absolute value increases from $\widetilde{D}_2^z = -0.02$ for the bilinear model up to $\widetilde{D}_2^z = -0.09$ for the trilinear anisotropic model. This is still small compared to value of the dominant components $\widetilde{D}_1^x$ and $\widetilde{D}_1^y$ but meets our expectations. The effects and importance of $\widetilde{D}_2^z$, which were discussed in detail in passage (ii) in sect. 5.3, also hold for our received results in this section. Therefore we refer to this previous point of this thesis.

(iii) Our calculations and studies of the trilinear anisotropic model of BCPO reveal that even this comprehensive model is not able to provide a satisfying match between

the calculated renormalized dispersion $\widetilde{\omega}_{z,r}(k)$ and the experimentally received mode 3. Compared to $\widetilde{\omega}_z(k)$ in the bilinear model the renormalized dispersion $\widetilde{\omega}_{z,r}(k)$ is shifted to lower energies in general but still does not suit the data of mode 3 in the minimum area. Around $k = 1\,\text{r.l.u.}$ our results can still be considered as acceptable since the experimental data overlap with $\widetilde{\omega}_{z,r}(k)$ within the displayed error ranges[15]. In this interval we see that the HWHM becomes larger from 0.23 meV to 0.82 meV which goes well with the experimental observations. The missing explanations concerning the measured resonances at high energies remain. For the sake of completeness, we point out again that it is possible to obtain a better description of mode 3 with our results for $\widetilde{\omega}_{z,r}(k)$ but this would mean a declined fit of the two lowest modes 1 and 2.

(iv) Discussing the results of the bilinear model in sect. 4.2.3 we formulated the presumption that a hybridization between the one- and two-triplon states is responsible for the dominant down-bending behavior of the two lowest-lying modes in the experiment. In our extended trilinear anisotropic model of BCPO we take this aspect into account and can identify several effects. In figure 6.6 we can see a clear down-bending behavior of $\widetilde{\omega}_{b,r}(k)$ at $k \approx 0.75\,\text{r.l.u.}$ where it approaches the lower boundary of the two-particle continuum $\widetilde{\omega}_{2,b}(k)$. The one-particle dispersion tries to avoid an overlap with the two-particle continuum, see the third scenario of SQPD in sect. 2.3, and is pushed below it. After entering the two-particle continuum the lifetime of the triplons becomes finite, represented by the displayed error bars of $\widetilde{\omega}_{b,r}(k)$. At $k \approx 0.75\,\text{r.l.u.}$ it is still possible to identify quasiparticle energies inside the two-particle continuum, i.e. the relative HWHM of the quasiparticle peaks in the corresponding spectral functions is smaller than our chosen threshold of $\left(\gamma(k)/\Delta\widetilde{\omega}_2(k)\right)_{\max} = 0.05$. In the interval $k \approx 0.8 - 0.9\,\text{r.l.u.}$ no quasiparticle energies can be determined. This means that the lifetime of the triplons is so short that they cannot be considered as quasiparticles anymore. Although the exact shape of the measured data cannot be reproduced this behavior, i.e. the down-bending of $\widetilde{\omega}_{b,r}(k)$, the finite lifetime of the triplons and their disappearance, goes with the experimental data in general.
In the interval $k = 0.9 - 1\,\text{r.l.u.}$ we can determine quasiparticle energies again. This is not in agreement with the experiment but we stress that our chosen criteria to identify quasiparticle peaks could be adapted such that the theoretical data points in this interval are not displayed in figure 6.6. Another crucial aspect concerning this issue refers to the experimental side. In INS experiments the DSF is measured, see sect. 1.2, which is identical to the spectral function in the case of zero temperature, see sect. 2.3.1. Just like in our theoretical calculations, see sect. 3.4.1, it is crucial to decide

[15] As a reminder, our denoted error bars represent the HWHM of the corresponding peaks in the spectral function, see sect. 2.3.3.

whether a peak in the measured data of the DSF is sharp enough to be considered as a quasiparticle peak or not. In order to do so, one has to introduce certain criteria which solve this issue. Changing these criteria leads different results for the quasiparticle energies. Therefore, it is possible that the experiment holds more data, which can also be interpreted as quasiparticle energies, as shown.
The down-bending behavior of mode 1 cannot be reproduced at all. We tried hard but could not find a parameter combination which provides more satisfying results concerning the down-bending behavior while keeping the good agreement in the low-energy regime. Beyond the considered hybridization effects taking into account two-particle interactions in addition could ensure an improved fit especially concerning the observed down-bending behavior. As discussed in our toy model two-particle interactions can give rise to bound states and lower the two-particle states energetically, see sect. 3.3. In combination with the hybridization effects discussed here this can result in an increased level repulsion which finally leads to a further energetical reduction of the one-particle dispersions and hence to a prominent down-bending.
To the best of our knowledge no theoretical description of BCPO including two-particle interactions exists in the literature. We address this issue in detail in chapter 7.

(v) With regard to the resonances of mode 3 in the high energy regime at $\approx 27\,\mathrm{meV}$, the trilinear anisotropic model of BCPO is not able to explain these. We tried hard but could not find a parameter combination which provides a good agreement between theory and experiment in this energy range. Panel (a) of figure 6.5 reveals that the renormalized dispersion $\widetilde{\omega}_{z,r}(k)$ shows a clear down-bending behavior at $k \approx 0.3\,\mathrm{r.l.u.}$. In this range the dispersion approaches the lower boundary of the corresponding two-particle continuum $\widetilde{\omega}_{2,z}(k,q)$[16] and tries to avoid an overlap with it, see the third scenario of SQPD in sect. 2.3. Compared to the results of the bilinear model, see figure 4.4, the quasiparticle energies of a triplon with flavor z are noticeably reduced in this part of the Brillouin zone. The spectral function $A(k,\omega)$, see figure 6.7, also shows that no significant amount of spectral weight is present near the experimentally measured resonances around $\approx 27\,\mathrm{meV}$. Finally, we conclude that our presumption of the bilinear model, see aspect (v) in sect. 4.2.3, that including states with a higher number of triplons and a hybridization with one-triplon states helps explaining the resonances a high energies, did not turn out to be true.

6.3 Chapter summary

In this chapter we analyzed the effects of SQPD, which stem from anisotropic couplings, in the magnetic strucuture of BCPO starting from its bilinear anisotropic model, which

[16] For reasons of clarity, the lower boundaries of the two-particle continua $\widetilde{\omega}_{2,b}(k,q)$ and $\widetilde{\omega}_{2,z}(k,q)$ are not displayed in figure 6.5.

we established in chapter 4. The symmetry analysis of the spin ladder structure of BCPO revealed that four out of five allowed anisotropic couplings hold odd parity. Consequently, these four **D** components induce a hybridization between the one- and two-particle states, i.e. quasiparticle decay/fusion processes. We discussed the influence of each **D** component on the one-particle dispersion separately. We found that the component $\mathbf{D}_1$ still has the greatest impact. Due to the considered hybridization effects we expected to provide an improved description of the experimental data with smaller **D** values compared to our starting point, i.e. the bilinear anisotropic model. Our results reveal several improvements concerning the match between our calculated renormalized dispersions and the experimental data. These comprise a significant reduction of the dominant component $\mathbf{D}_1 \approx 0.38 J_1$, compared to $\mathbf{D}_1 \approx 0.6 J_1$, and a better approximation of the slope of the energetically lowest-lying mode. The component $\mathbf{D}_1 \approx 0.38 J_1$ still has to be considered as remarkably large, but our results for the components $\mathbf{D}_0 \approx 0.1 J_0$ and $\mathbf{D}_2 \approx -0.1 J_2$ are in line with our expection of $10 - 20\,\%$ of the isotropic couplings. A major point of criticism concerning our results is the insufficient description of the characteristic down-bending behavior of the two lowest modes. The included level repulsion turned out to be too weak for this purpose. In order to solve this issue we use the results of our toy model, see chapter 3. Thereby, we demonstrated that taking into account two-particle interactions can solve this issue. These interactions can give rise to bound states and provide a shift of the two-particle states in energy. In combination with the already discussed hybridization effects this can result in an increased level repulsion and finally in a further lowering of the one-particle modes. We strongly assume that we can improve our current results, especially the description of the down-bending, by extending our current model of BCPO with the effects of two-particle interactions. We address this issue in the following chapter in detail.

Our results are similiar to the results from Hwang and Kim [64]. In their calculations they considered bilinear operator terms and two-particle interactions using the BOT on a mean-field level[17]. In addition, decay/fusion processes are included via the Green's function formalism on an one-loop level. Their best fitting parameters read: $x = y = 1$, $J_0 = 10\,\mathrm{meV}$, $J' = 2\,\mathrm{meV}$ and $D_1^x = D_1^y = 0.3 J_1$. Our results go roughly with these parameters, i.e. they differ up to $25\,\%$. Thus, our CUT based results can be interpreted as a confirmation of the BOT based results. In contrast to Hwang and Kim, our current results do not respect two-particle interactions at all. Therefore, we see further potential for improvement in our results concerning the match between theory and experiment by including the effects of two-particle interactions explicitly.

[17] Note, performing a mean-field decoupling of two-particle interactions precludes that bound states occur.

7 Description of the quantum antiferromagnet $BiCu_2PO_6$ on quadrilinear operator level

In the previous chapter we discussed the influence of SQPD, induced by the DM interaction, on the excitation spectrum of BCPO. Thereby, we concentrated only on processes which describe a transition between the one- and two-triplon HILBERT space. Concerning the characteristic down-bending of BCPOs excitation spectrum these processes had hardly any effect. Therefore, we extend our model for BCPO in a further step by considering two-triplon interactions. In our toy model we showed that attractive two-particle interactions can lead to an additional lowering effect of the one-particle energies, see sect. 3.3. In addition, bound states can occur. We presume that adding two-triplon interactions to our model of BCPO provides a better match between theory and experiment by choosing even smaller values for the fitted $\mathbf{D}$ components[1]. PLUMB *et. al.* and HWANG *et. al.* already included two-triplon interactions in their studies [39, 64] but not in a comprehensive range. In their calculations the two-triplon interactions were treated by a mean-field decoupling so that it was not possible to receive bound states. In our studies we will consider the existing two-triplon interactions in BCPO explicitly by using the complete approach, see sect. 5.1. By this, it is possible to observe bound states and to obtain a further lowering of the one-triplon dispersions.

7.1 Bound states in the isotropic spin ladder

In order to include the two-triplon interactions in BCPO, it is reasonable to neglect all anisotropies in the first place and analyze their influence on the isotropic spin ladder. Therefore, we first consider the Hamiltonian $\mathcal{H}_{\text{ladder}}$, see eqs. (4.1.1). In addition to the analysis performed in sect. 4.1.1, we also respect the existence of two triplons in the isotropic spin ladder. Then, the deepCUT provides the effective two-triplon interactions

[1] Previous studies on spin ladder models *without* spin anisotropic effects showed that considering two-triplon interactions leads to the existence of bound states and that spectral weight is shifted to lower energies [148, 149].

of the type

$$\mathcal{H}_{\text{quad},1} = \sum_i \sum_{\delta_1,\delta_2,\delta_3,\delta_4} \sum_{\alpha,\beta} \alpha^{\alpha,\alpha,\beta,\beta}_{\delta_1,\delta_2,\delta_3,\delta_4} t^{\alpha,\dagger}_{i+\delta_1} t^{\alpha,\dagger}_{i+\delta_2} t^{\beta}_{i+\delta_3} t^{\beta}_{i+\delta_4} \tag{7.1.1}$$

and

$$\mathcal{H}_{\text{quad},2} = \sum_i \sum_{\delta_1,\delta_2,\delta_3,\delta_4} \sum_{\alpha\neq\beta} \alpha^{\alpha,\beta,\alpha,\beta}_{\delta_1,\delta_2,\delta_3,\delta_4} t^{\alpha,\dagger}_{i+\delta_1} t^{\beta,\dagger}_{i+\delta_2} t^{\alpha}_{i+\delta_3} t^{\beta}_{i+\delta_4} \tag{7.1.2}$$

with the spin components $\alpha, \beta \in \{x, y, z\}$, the relative distances $\delta_1, \delta_2, \delta_3, \delta_4$ in real space and the corresponding prefactors $\{\alpha^{\alpha,\alpha,\beta,\beta}_{\delta_1,\delta_2,\delta_3,\delta_4}, \alpha^{\alpha,\beta,\alpha,\beta}_{\delta_1,\delta_2,\delta_3,\delta_4}\} \in \mathbb{R}$. The FOURIER transform of eqs. (7.1.1) and (7.1.2) yields

$$\mathcal{H}_{\text{quad,1D}} = \frac{1}{N} \sum_{k,q,q'} \alpha^{\alpha',\beta',\gamma',\delta'}(k,q,q')\, t^{\alpha',\dagger}_{q'} t^{\beta',\dagger}_{k-q'} t^{\gamma'}_{q} t^{\delta'}_{k-q} \tag{7.1.3}$$

with the general flavors $(\alpha', \beta', \gamma', \delta')$ assuming the occuring flavor combinations. The prefactor

$$\alpha^{\alpha',\beta',\gamma',\delta'}(k,q,q') = \sum_{\delta_1,\delta_2,\delta_3,\delta_4} \alpha^{\alpha',\beta',\gamma',\delta'}_{\delta_1,\delta_2,\delta_3,\delta_4} \mathrm{e}^{\mathrm{i}(\delta_2-\delta_1)q'} \mathrm{e}^{\mathrm{i}(\delta_3-\delta_4)q} \mathrm{e}^{\mathrm{i}(\delta_4-\delta_2)k} \tag{7.1.4}$$

adds up the prefactors $\alpha^{\alpha',\beta',\gamma',\delta'}_{\delta_1,\delta_2,\delta_3,\delta_4}$ of the two-triplon interactions from eqs. (7.1.1) and (7.1.2). Combining the effective Hamiltonian $\mathcal{H}^{\text{eff}}_{\text{ladder}}$, see eq. (4.1.2), with the discussed two-triplon interactions gives rise to the appearance of bound states. By analogy with our toy model, see sect. 3.4.2, we choose the two-particle state

$$|k,\alpha\rangle\,|1,\beta\rangle = \frac{1}{\sqrt{N}} \sum_{i=0}^{N-1} \mathrm{e}^{\mathrm{i}k\left(r_i+\frac{1}{2}\right)} t^{\alpha,\dagger}_i t^{\beta,\dagger}_{i+1} |0\rangle \tag{7.1.5}$$

as the initial state for our calculations. Note, that this state takes different triplon flavors into account in contrast to $|k,1\rangle$ in eq. (3.4.28). In the isotropic case, where the total spin $\mathbf{S}_{\text{tot}}$ is a good quantum number, two triplons can form two-triplon states with a total spin of S=0, 1, 2 [150]. For our concerns we concentrate only on the S=0 and S=1 bound states. The S=2 two-particle state describes an anti-bound state which is located above the two-particle continuum. Such a state is of no interest for BCPO where we focus on the low-energy regime.

7.1.1 S=0 and S=1 bound states

Due to the SU(2) symmetry of the considered Hamiltonian $\mathcal{H}_{\text{ladder}}$, see eq. (4.1.1), it is possible to focus only on one single $S^z_{\text{tot}} = m$ value for a fixed total spin S. For our calculations we choose $m = 0$. In real space the S=0 two-particle state, see eq. (7.1.5),

yields

$$|k,1\rangle_{m=0}^{\mathrm{S}=0} = \frac{1}{\sqrt{3N}} \sum_{i=0}^{N-1} \mathrm{e}^{\mathrm{i}k\left(r_i+\frac{1}{2}\right)} \left(t_i^{x,\dagger} t_{i+1}^{x,\dagger} - t_i^{z,\dagger} t_{i+1}^{z,\dagger} + t_i^{y,\dagger} t_{i+1}^{y,\dagger} \right) |0\rangle \,. \tag{7.1.6}$$

For a detailed derivation we refer to Refs. [123, 150]. The FOURIER transform of eq. (7.1.6) results in

$$|k,1\rangle_{m=0}^{\mathrm{S}=0} = \frac{1}{\sqrt{3N}} \sum_{q} \cos\left(\frac{k}{2} - q\right) \left(t_q^{x,\dagger} t_{k-q}^{x,\dagger} - t_q^{z,\dagger} t_{k-q}^{z,\dagger} + t_q^{y,\dagger} t_{k-q}^{y,\dagger} \right) |0\rangle \,, \tag{7.1.7}$$

which serves as our initial state for the LANCZOS calculations in momentum space. For a total spin of S=1 the two-particle state in real space reads

$$|k,1\rangle_{m=0}^{\mathrm{S}=1} = \frac{\mathrm{i}}{\sqrt{2N}} \sum_{i=0}^{N-1} \mathrm{e}^{\mathrm{i}k\left(r_i+\frac{1}{2}\right)} \left(t_i^{y,\dagger} t_{i+1}^{x,\dagger} - t_i^{x,\dagger} t_{i+1}^{y,\dagger} \right) |0\rangle \tag{7.1.8}$$

yielding

$$|k,1\rangle_{m=0}^{\mathrm{S}=1} = -\sqrt{\frac{2}{N}} \sum_{q} \sin\left(\frac{k}{2} - q\right) t_q^{x,\dagger} t_{k-q}^{y,\dagger} |0\rangle \tag{7.1.9}$$

in momentum space. In figure 7.1 the dispersions of the S=0 and S=1 two-particle bound state are presented.

On average, we note a stronger attraction for the S=0 two-particle bound state compared to the S=1 state except in the region around $k \approx 0$. There the situation is the opposite. Our results are in qualitative accordance with previous results on spin ladders [148,149]. The exciting aspect of the results in figure 7.1 is that in BCPO the S=0 and S=1 two-particle states are mixed by the DM interactions. The down-bending of the two lowest modes reminds strongly of the S=0 bound state. Thus, extending our model of BCPO by two-particle interactions represents a promising approach.

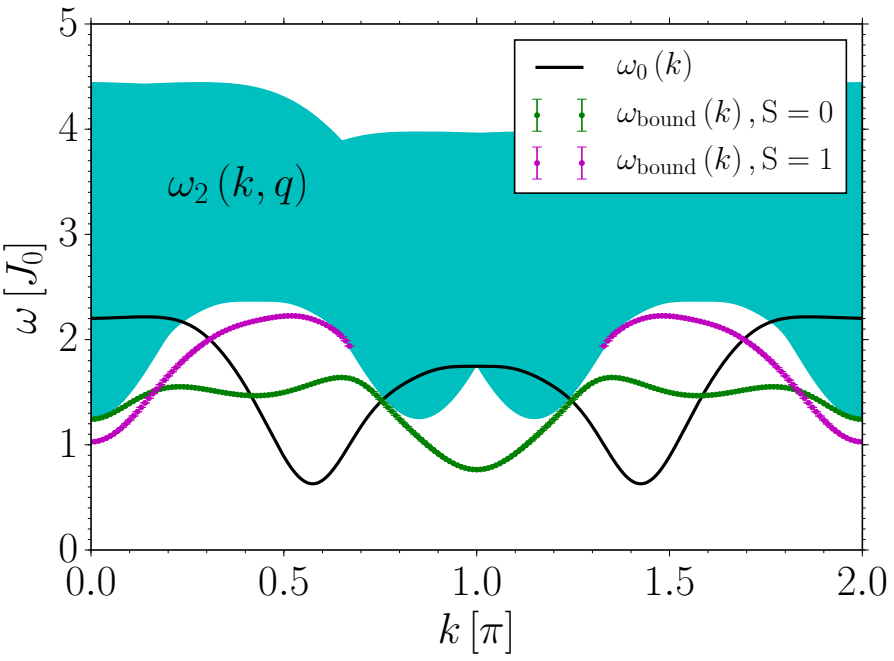

Figure 7.1: Dispersions of the two-particle bound state $\omega_{\text{bound}}(k)$ with a total spin of S=0 and S=1 for the isotropic spin ladder. The coupling ratios are x=1.2 and $y = 0.9$. For the calculations a discretization of $N = 800$ in k-space was chosen and 200 LANCZOS steps have been performed. The energy ω is discretized in steps of $0.001 J_0$ and up to $n_{\text{Lanczos,max}} = 25$ for S=0 and up to $n_{\text{Lanczos,max}} = 30$ for S=1 LANCZOS coefficients were used in order to solve the DYSON equation, see eq. (2.3.66).

7.2 Results for the quadrilinear anisotropic Hamiltonian of BCPO

In order to take two-particle interactions into account for our trilinear anisotropic model of BCPO, see chapter 6, we again follow the steps of the complete approach as explained in sect. 5.3. The first steps have already been performed in sect. 7.1 partially. As the magnetic structure of BCPO is two-dimensional, we have to modify the FOURIER transform of the two-particle interactions, see eq. (7.1.3), to read

$$\mathcal{H}_{\text{quad,2D}} = \frac{1}{N_k N_l} \sum_{k,q,q'} \sum_{l,p,p'} \alpha^{\alpha',\beta',\gamma',\delta'}(k,q,q')\, t^{\alpha',\dagger}_{q',p'} t^{\beta',\dagger}_{k-q',l-p'} t^{\gamma'}_{q,p} t^{\delta'}_{k-q,l-p}. \tag{7.2.10}$$

This expression describes transitions between two-particle states, which hold total momentum (k,l) and relative momentum (q,p), and different two-particle states with the same total momentum (k,l) and relative momentum (q',p')[2]. The next step is to transform all these quadrilinear operator terms in momentum space into the same BOGOLI-

[2]Of course the case $q = q'$, $p = p'$ is also possible and describes a self-interaction of the corresponding two-particle state.

UBOV basis as the Hamiltonians $\widetilde{\mathcal{H}}^{\text{eff}}_{\text{BCPO},z}$ and $\widetilde{\mathcal{H}}^{\text{eff}}_{\text{BCPO},bu}$, see eqs. (4.2.20) and (4.2.32). Subsequent normal-ordering would give rise to quadrilinear operator terms which do not conserve the number of particles and bilinear operator terms. The former are neglected anyway in the complete approach as it considers only interactions in the one- and two-particle HILBERT space and transitions between them. Concerning the bilinear operator terms of the type $\tilde{t}^{\dagger}\tilde{t}$ would not be neglected directly within the complete approach. However, to hold the calculation effort low we also neglect these bilinear operator terms. This means that we only keep the terms of the type $\tilde{t}^{\dagger}\tilde{t}^{\dagger}\tilde{t}\tilde{t}$ for our further calculations. Thus, the operator terms of the type $\tilde{t}^{\dagger}_{q',p'}\tilde{t}^{\dagger}_{k-q',l-p'}\tilde{t}_{q,p}\tilde{t}_{k-q,l-p}$ with the flavor combinations

$$\begin{aligned}
&\tilde{t}^{b,\dagger}\tilde{t}^{b,\dagger}\tilde{t}^{b}\tilde{t}^{b}, \quad \tilde{t}^{b,\dagger}\tilde{t}^{u,\dagger}\tilde{t}^{b}\tilde{t}^{u}, \quad \tilde{t}^{u,\dagger}\tilde{t}^{u,\dagger}\tilde{t}^{u}\tilde{t}^{u}, \quad \tilde{t}^{z,\dagger}\tilde{t}^{z,\dagger}\tilde{t}^{z}\tilde{t}^{z}, \quad \tilde{t}^{b,\dagger}\tilde{t}^{b,\dagger}\tilde{t}^{b}\tilde{t}^{u}, \\
&\tilde{t}^{b,\dagger}\tilde{t}^{b,\dagger}\tilde{t}^{u}\tilde{t}^{u}, \quad \tilde{t}^{z,\dagger}\tilde{t}^{z,\dagger}\tilde{t}^{b}\tilde{t}^{b}, \quad \tilde{t}^{b,\dagger}\tilde{t}^{u,\dagger}\tilde{t}^{u}\tilde{t}^{u}, \quad \tilde{t}^{z,\dagger}\tilde{t}^{z,\dagger}\tilde{t}^{b}\tilde{t}^{u}, \quad \tilde{t}^{z,\dagger}\tilde{t}^{z,\dagger}\tilde{t}^{u}\tilde{t}^{u}, \\
&\tilde{t}^{z,\dagger}\tilde{t}^{b,\dagger}\tilde{t}^{z}\tilde{t}^{b}, \quad \tilde{t}^{z,\dagger}\tilde{t}^{b,\dagger}\tilde{t}^{z}\tilde{t}^{u}, \quad \tilde{t}^{z,\dagger}\tilde{t}^{u,\dagger}\tilde{t}^{z}\tilde{t}^{u},
\end{aligned} \tag{7.2.11}$$

emerge including the Hermitian conjugated part of each non-Hermitian operator term. These two-particle interactions describe transitions between all occuring two-particle HILBERT spaces as pointed out in sect. 6.1. As the final step of the complete approach we add the quadrilinear terms in eq. (7.2.11) to our trilinear anisotropic model of BCPO, see sect. 6.1, and receive the renormalized dispersions $\widetilde{\omega}_{z,r,\text{qu}}(k)$ and $\widetilde{\omega}_{b,r,\text{qu}}(k)$. Again, we forego the explicit expressions of the prefactors of the quadrilinear operator terms in eq. (7.2.11) since they are given by extremely cumbersome formulae which are evaluated numerically anyway. This calculation step turned out to be very challenging. After developing and implementing different algorithms this numerical evaluation appears only to be possible for a maximal discretization of $N_k = 40$. In section 7.3 we go into detail and explain why higher discretizations are not possible for the currently available computational resources.
However, even with small discretizations reasonable results can be received and the effects of two-particle interactions in BCPO can be analyzed. Before discussing the final results of the renormalized dispersions $\widetilde{\omega}_{z,r,\text{qu}}(k)$ and $\widetilde{\omega}_{b,r,\text{qu}}(k)$ we have to discuss the convergence behavior of the corresponding LANCZOS coefficients.

As pointed out in sect. 3.4.1 it is essential to identify the number of LANCZOS steps $n_{\text{Lanczos,max}}$ at which the coefficients reach their limiting values sufficiently well. Coarse discretizations can lead to the scenario that this convergence behavior does not exist due to finite size effects [129]. Figure 7.2 demonstrates this issue.
Even the LANCZOS coefficients with the maximal possible discretization of $N_k = 40$ including two-particle interactions do not show convergence at all. Considering the

first five to ten coefficients we can already identify deviations between the different discretizations.

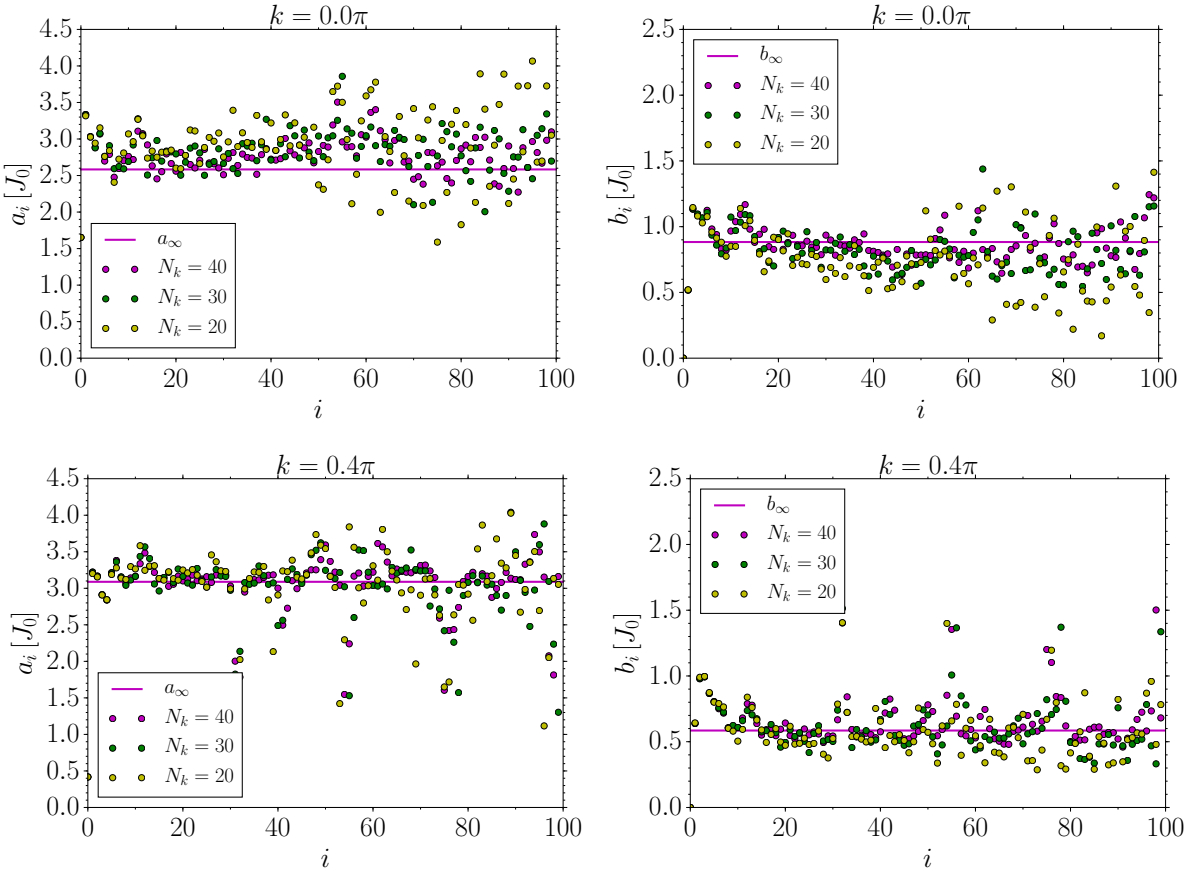

Figure 7.2: Convergence behavior of the LANCZOS coefficients for different k-values and different discretizations N_k including two-particle interactions in BCPO. The used parameters are identical to the best fitting parameters of the trilinear anisotropic model, see figure 6.5. As an initial state for the LANCZOS tridiagonalization a single particle with the flavor b was chosen. The index i represents the number of the LANCZOS coefficients.

In order to determine a reasonable value for $n_{\text{Lanczos,max}}$, which we need for the calculations of the spectral functions and renormalized dispersions, we align ourselves to the convergence behavior of the LANCZOS coefficients *without* the two-particle interactions, i.e. the trilinear anisotropic model of BCPO, see chapter 6. Figure 7.3 illustrates the results.

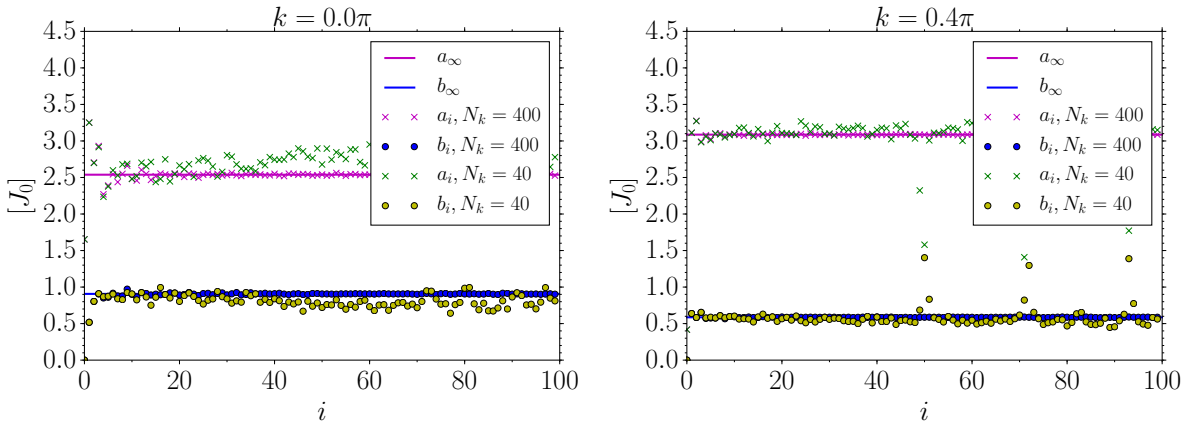

Figure 7.3: Convergence behavior of the LANCZOS coefficients for different k-values and different discretizations N_k *without* two-particle interactions BCPO, i.e. for the trilinear anisotropic model, see chapter 6. The used parameters are identical to its best fitting parameters, see figure 6.5. As an initial state for the LANCZOS tridiagonalization a single particle with the flavor b was chosen. The index i represents the number of the LANCZOS coefficients.

For the discretization $N_k = 400$ the coefficients converge clearly towards their limiting values. For the coefficients belonging to the notably coarser discretization $N_k = 40$ we can identify deviations from the results for $N_k = 400$ beginning at the tenth coefficient approximately. We compared spectral functions of the trilinear anisotropic model with $N_k = 400$ and $n_{\text{Lanczos,max}} = 40$ to results with $N_k = 40$ and $n_{\text{Lanczos,max}} = 10$ in order to find out whether the latter results contain all physical meaningful features or not[3]. Besides more numerical artefacts occuring in the results for $N_k = 40$ and $n_{\text{Lanczos,max}} = 10$ the spectral functions are similar to the ones with the parameters $N_k = 400$ and $n_{\text{Lanczos,max}} = 40$. Thus, it is reasonable to set $n_{\text{Lanczos,max}} = 10$ for the LANCZOS coefficients for the calculations *with* two-particle interactions as well despite the missing convergence behavior.

With this knowledge basis, we extend our current model of the quantum antiferromagnet BCPO by the effects of two-particle interactions. Thus, we provide the first explicit description of BCPO including two-particle interactions in the literature giving rise to the phenomenon of bound states. The prefactors of the quadrilinear operator terms in eq. (7.2.11) do not depend on the $\mathbf{D}$ components explicitly. They are only influenced by the $\mathbf{D}$ components via the transformation matrix $K^{-1}_{k,l}$ and the parameter $\vartheta^z_{k,l}$, see eqs. (4.2.27) and (4.2.19). Therefore, it is not necessary to perform a complete new analysis concerning the effects of each $\mathbf{D}$ component on the renormalized dispersions $\widetilde{\omega}_{z,r,\text{qu}}(k)$

[3]These results are not shown in this thesis.

and $\widetilde{\omega}_{b,r,\mathrm{qu}}(k)$. It is reasonable to begin our fitting process by starting with the results of the trilinear anisotropic model, see figure 6.5. Next, we vary the **D** components and the energy scale J_0 in a systematic manner step by step in order to approach the best match between theory and the experimental data of BCPO[4]. We can use the effects of the anisotropic couplings on the trilinear anisotropic model, see table 6.1, as an orientation. As the bilinear anisotropic description of BCPO serves as a starting point, we take over the fixed parameters $x = 1.2$, $y = 0.9$ and $J'/J_0 = 0.16$, see sect. 4.1.2.
In the following, we discuss several aspects concerning our best fits, see figures 7.4, 7.5 and 7.6, and compare these with the results of the trilinear anisotropic model, see figures 6.5 and 6.6. We do this by plotting the results of the trilinear anisotropic model $\widetilde{\omega}_{z,r,\mathrm{tri}}(k)$ and $\widetilde{\omega}_{b,r,\mathrm{tri}}(k)$ in addition to the results including two-particle interactions. To maintain a good overview in the plots we decided to illustrate the modes in separate figures.

(i) As in the trilinear anisotropic model of BCPO, we assign the solutions of $\widetilde{\omega}_{b,r,\mathrm{qu}}(k+\pi)$ to the measured mode 1, see figure 7.4. In addition, the missing good agreement between the two lowest-lying modes 1 and 2 and our calculated solutions for $\widetilde{\omega}_{b,r,\mathrm{qu}}(k)$ and $\widetilde{\omega}_{b,r,\mathrm{qu}}(k+\pi)$ remains like in the previous model, see also figure 7.6 for the solutions for $\widetilde{\omega}_{b,r,\mathrm{qu}}(k)$. One striking feature of our results including two-particle interactions is that the fitting parameters are nearly identical to the ones we received for the trilinear anisotropic model[5]. Especially the dominant values of the components $\widetilde{D}_1^x = 0.25$ and $\widetilde{D}_1^y = 0.38$ stay unaltered. This aspect is reflected in the fact that $\widetilde{\omega}_{b,r,\mathrm{tri}}(k+\pi)$ and $\widetilde{\omega}_{b,r,\mathrm{qu}}(k+\pi)$ do not display large deviations due to the two-particle interactions in the low-energy regime, which we want to describe as well as possible[6]. This means that the two-particle interactions do not have a great impact in the low-energy regime and cannot lead to a further reduction of the dominant components $\widetilde{D}_1^x$ and $\widetilde{D}_1^y$.

(ii) As already mentioned, the only difference between the results *with* and *without* the effects of two-particle interactions lies in the value of the anisotropic coupling $\widetilde{D}_2^z$. Starting with $\widetilde{D}_2^z = -0.02$ for the bilinear anisotropic model its absolute value increases up to $\widetilde{D}_2^z = -0.06$ for the quadrilinear model of BCPO. Compared to the results of the trilinear anisotropic model holding $\widetilde{D}_2^z = -0.09$ its value decreased again.

[4]Note, that with the maximally possible discretization $N_k = 40$ the majority of experimental data points is not addressed in our calculations. One has to keep this aspect in mind while discussing our results in the following.

[5]Only the value of the component $\widetilde{D}_2^z$ differs slightly. We address this point in part (ii) in detail.

[6]Therefore, we refer to part (i) in sect. 6.2 for further details concerning the effects of the components $\widetilde{D}_1^x$, $\widetilde{D}_1^y$ and $\widetilde{D}_0^y$.

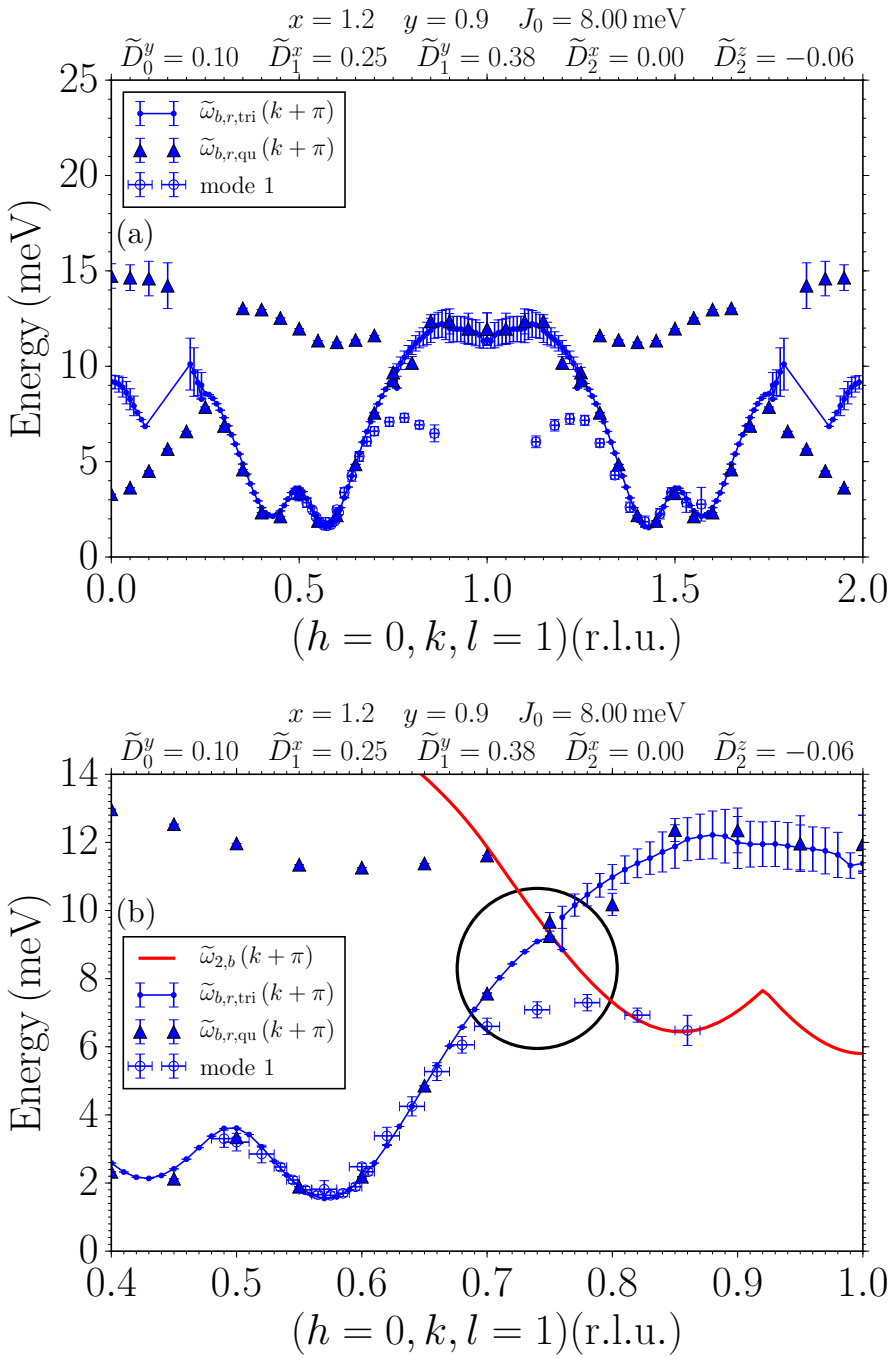

Figure 7.4: (a) Fitted theoretical dispersion $\widetilde{\omega}_{b,r,\mathrm{qu}}(k+\pi)$ for the fixed parameters $x = 1.2$, $y = 0.9$ and $J'/J_0 = 0.16$ including two-particle interactions (filled triangles). Their displayed error bars depict the corresponding HWHM, see eq. (2.3.72). As thresholds to identify quasiparticle peaks in the corresponding spectral functions, see sect. 3.4.1, we set a maximum relative HWHM of $(\gamma(k)/\Delta\widetilde{\omega}_2(k))_{\max} = 0.05$ and a minimal spectral weight of $(1/s)_{\min} = 0.01$. The fitted parameters are J_0, $\widetilde{D}_0^y$, $\widetilde{D}_1^x$, $\widetilde{D}_1^y$, $\widetilde{D}_2^x$ and $\widetilde{D}_2^z$. Their values are listed in the panel itself. The data $\widetilde{\omega}_{b,r,\mathrm{tri}}(k+\pi)$ illustrate the results of the trilinear anisotropic model, see figure 6.5, with the parameter $\widetilde{D}_2^z = -0.09$ being different compared to the listed parameters. (b) Zoom of panel (a) into the range where mode 1 shows the prominent down-bending behavior, marked by a circle. Additionally, the lower boundary of the two-particle continuum $\widetilde{\omega}_{2,b}(k+\pi)$ is depicted by a solid line.

Note, that the component $\widetilde{D}_2^z$ is mainly responsible for fitting the position of the minimum. It is the only **D** component which contributes in linear order, see table 4.3. As a consequence, even small deviations in its value show visible effects in the renormalized dispersions. Furthermore, we want to stress that our results including two-particle interactions have to be considered with caution since we can only perform calculations with a maximum discretization of $N_k = 40$. Therefore, we have significantly less points of reference when comparing our theoretical results including two-particle interactions with the experimental data. Keeping this in mind, the small difference between the component $\widetilde{D}_2^z$ of the results *with* and *without* two-particle interactions should not be considered as of great importance.

(iii) The unsatisfying match between our solutions of the z mode and the measured mode 3 from the trilinear anisotropic model, see part (iii) in sect. 6.2, remains for the quadrilinear model. Comparing our results for the renormalized dispersion of the z mode *with* and *without* the effects of two-particle interactions, see figure 7.5, no significant differences can be identified. Only in the interval $k \approx 0 - 0.3\,\text{r.l.u.}$ a further shift to lower energies for $\widetilde{\omega}_{z,r,\text{qu}}(k)$ is visible. In this range the dispersion approaches the two-particle continuum. As explained in sect. 3.3, the considered two-particle interactions ensure an increased level repulsion, which leads to this further lowering of the z mode. In the minimum area, see figure 7.5b), the consideration of two-particle interactions does not show any visible effects. Concerning the resonances of mode 3 at high energies we refer to part (v) in the following.

(iv) Including the effects of the hybridization between the one- and two-particle states in chapter 6 for our model of BCPO revealed that these cannot reproduce the characteristic down-bending behavior in the excitation spectrum. Focusing on the interval $k \approx 0.75 - 0.85\,\text{r.l.u.}$ in figure 7.4 we notice that $\widetilde{\omega}_{b,r,\text{qu}}(k+\pi)$ is not as well in agreement with the experimental data as $\widetilde{\omega}_{b,r,\text{tri}}(k+\pi)$. In figure 7.4b) we can identify a weak down-bending effect near the lower boundary of the two-particle continuum $\widetilde{\omega}_{2,b}(k+\pi)$. After entering the continuum the lifetime of the corresponding triplons becomes finite but it is long enough, i.e. the corresponding HWHM is small enough, to be considered as a quasiparticle furthermore. However, including the effects of two-particle interactions provides striking features in our results. We find solutions for $\widetilde{\omega}_{b,r,\text{qu}}(k+\pi)$ which are energetically located above the minimum area at $\approx 12\,\text{meV}$. In figure 7.6 the solutions of $\widetilde{\omega}_{b,r,\text{qu}}(k)$ and $\widetilde{\omega}_{b,r,\text{qu}}(k+\pi)$ are illustrated in a scatter plot. The solutions which lie outside the respective two-particle continuum, i.e. which correspond to sharp resonances in the spectral function, are colored with regard to their spectral weight. The solutions at $\approx 12\,\text{meV}$ hold a spectral weight of $0.01 - 0.1$.

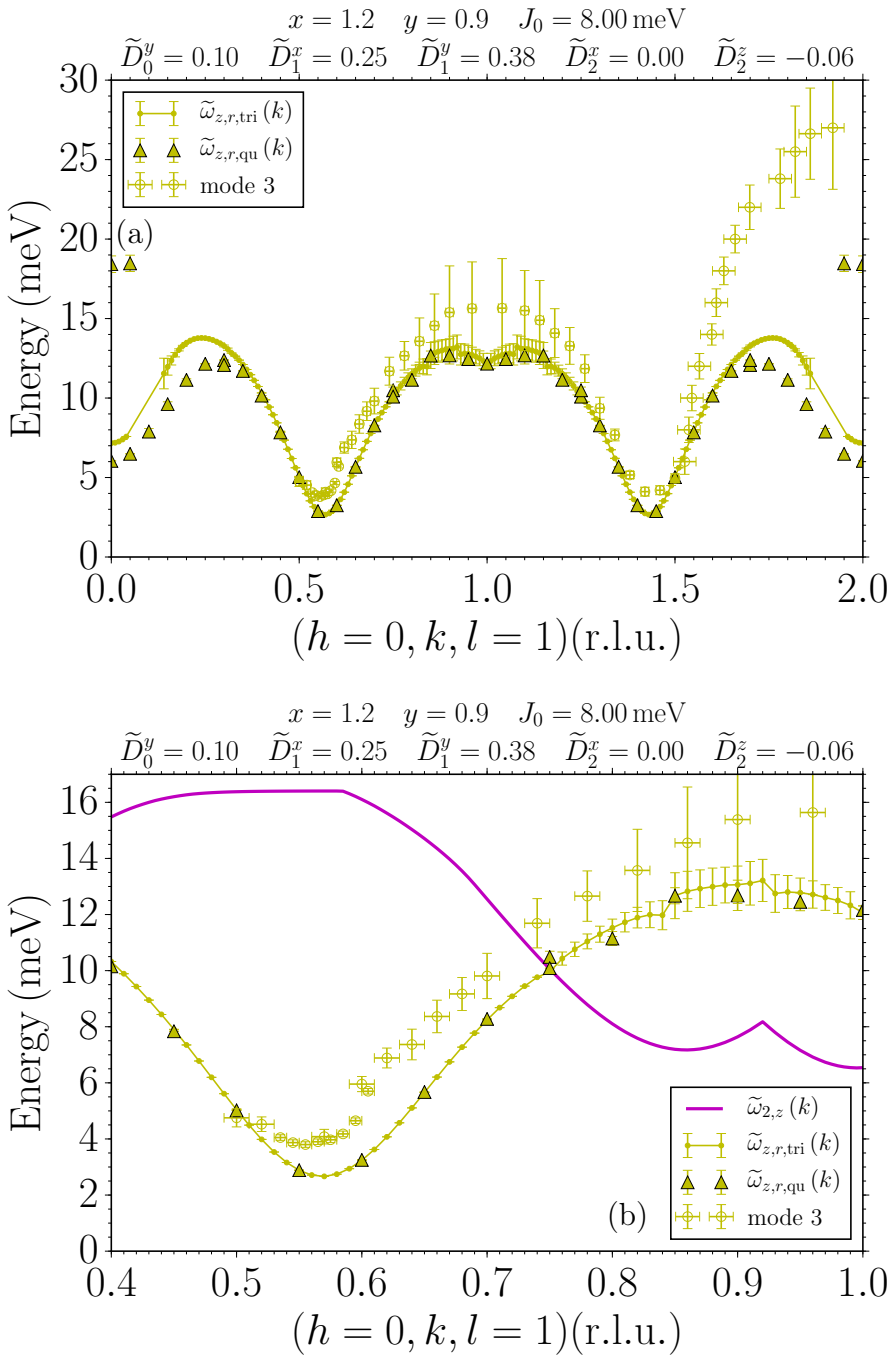

Figure 7.5: (a) Fitted theoretical dispersion $\widetilde{\omega}_{z,r,\mathrm{qu}}(k)$ for the fixed parameters $x = 1.2$, $y = 0.9$ and $J'/J_0 = 0.16$ including two-particle interactions (filled triangles). Their displayed error bars depict the corresponding HWHM, see eq. (2.3.72). As thresholds to identify quasiparticle peaks in the corresponding spectral functions, see sect. 3.4.1, we set a maximum relative HWHM of $(\gamma(k)/\Delta\widetilde{\omega}_2(k))_{\max} = 0.05$ and a minimal spectral weight of $(1/s)_{\min} = 0.01$. The fitted parameters are J_0, $\widetilde{D}_0^y$, $\widetilde{D}_1^x$, $\widetilde{D}_1^y$, $\widetilde{D}_2^x$ and $\widetilde{D}_2^z$. Their values are listed in the panel itself. The data $\widetilde{\omega}_{z,r,\mathrm{tri}}(k)$ illustrate the results of the trilinear anisotropic model, see figure 6.5, with the parameter $\widetilde{D}_2^z = -0.09$ being different compared to the listed parameters. (b) Zoom of panel (a) into the minimum area. Additionally, the lower boundary of the two-particle continuum $\widetilde{\omega}_{2,z}(k + \pi)$ is depicted by a solid line.

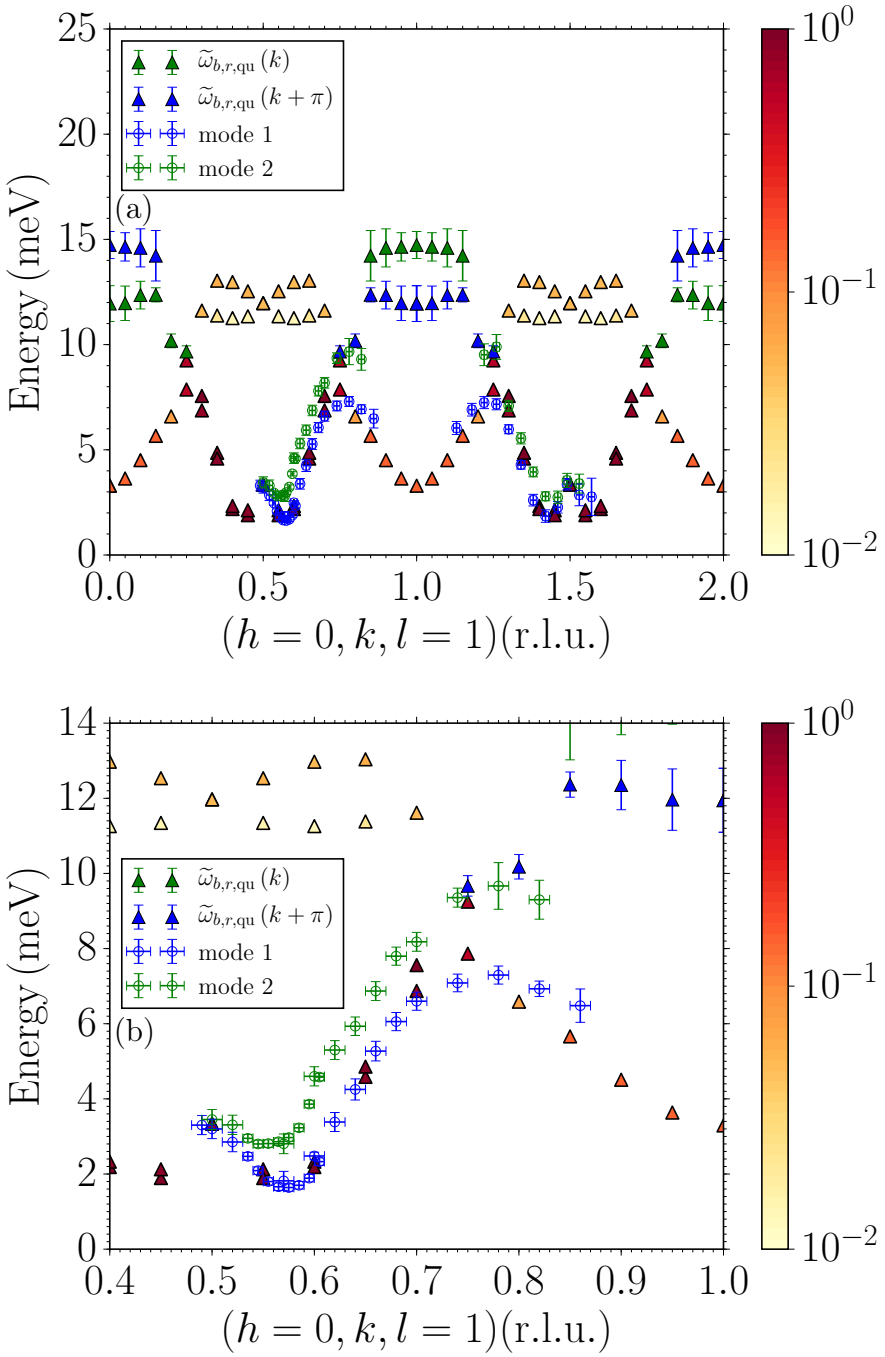

Figure 7.6: (a) Solutions of the two lowest modes $\widetilde{\omega}_{b,r,\mathrm{qu}}(k)$ and $\widetilde{\omega}_{b,r,\mathrm{qu}}(k+\pi)$ stemming from the x and y mode using the fitting parameters shown in figure 7.4. The data points outside the corresponding two-particle continuum are colored according to their spectral weight. (b) Zoom of panel (a) into the range where the experimental modes 1 and 2 show the characteristic down-bending behavior.

The solutions in the energy range below 10 meV possess a greater spectral weight of $0.1-1$. Comparing the results of the S= 0 and S= 1 two-particle bound states of the isotropic spin ladder, see figure 7.1, to the results shown in figure 7.6 we can identify

clear connections between them. As already mentioned in sect. 7.1, in the isotropic case the total spin $\mathbf{S}_{\mathrm{tot}}$ is a conserved quantity. Therefore, the corresponding S=0 and S=1 bound states are clearly separated in their calculations and do not mix. Since the DM interactions break the conservation of the total spin $\mathbf{S}_{\mathrm{tot}}$, a mixing of the original S=0 and S=1 bound states occurs and we can observe signatures of both in our results, see figures 7.4 and 7.6. The solutions of $\widetilde{\omega}_{b,r,\mathrm{qu}}(k)$ and $\widetilde{\omega}_{b,r,\mathrm{qu}}(k+\pi)$ around $\approx 12\,\mathrm{meV}$ stem from the S=1 bound state. The S= 0 bound state of the isotropic spin ladder is also reflected in the solutions of the quadrilinear model of BCPO. The significant down-bending behavior of our results in the interval $k \approx 0.75 - 1\,\mathrm{r.l.u.}$ in figure 7.6 recalls the dispersion of the S=0 bound state in figure 7.1. As discussed within our toy model in sect. 3.4.3 considering two-particle interactions and the hybridization between one- and two-particle states simultaneously leads to the scenario that the original one-particle dispersion $\omega_0(k)$ and the two-particle bound states $\omega_{\mathrm{bound}}(k)$ of the isotropic spin ladder are separated at anti-crossing points. So, we can conclude that the prominent down-bending behavior of our results in figure 7.6 is related to the original S=0 bound state of the isotropic spin ladder, see figure 7.1. The solutions inside the two-particle continuum in figure 7.6, which are not colored according to their spectral weight, are not in line with the shown experimental data at first sight. To analyze this aspect in more detail we compare the experimental intensity results with our results for the DSF $S(\vec{Q},\omega)$, see figures 7.7 and 7.8. To reproduce the spectral broadening of the experimental data within our calculations, see sect. 2.3.1, we shift the energy ω into the complex plane by a small real factor $\delta > 0$, see also sect. 2.3.2. This proceeding has the effect that the peaks in the spectral function $A(k,\omega)$, which are located outside of the two-particle continuum, are no longer sharp delta-functions but LORENTZ distributions with a finite HWHM, see sect. 2.3.1. We choose the parameter δ to be equal to the energy resolution of the experiment[7], which is $\delta = 0.25\,\mathrm{meV}$. Furthermore, we perform the continued fraction for determining the spectral function $A(k,\omega)$, see sect. 2.3.1, up to a depth of 100 coefficients, whereas the first ten LANCZOS coefficients, as discussed before in this section, are used. The remaining 90 coefficients are set to the limiting values $a_\infty(k)$ and $b_\infty(k)$, which are determined by the corresponding band edges, see also Appendix A. With this approach we simulate the usage of the square-root terminator and receive smooth results for the spectral function $A(k,\omega)$ in the energy ω. As we use single particle states with the flavors z and b for our LANCZOS calculations with a weight of 1 regardless of the corresponding momentum k, we rate our results for the spectral function $A(k,\omega)$ with the static structure factor $|a(k)|^2$, see eq. (4.1.6). By this, we take into account the deepCUT results for a single spin operator, see Refs. [123] and [151] for further details.

[7] We received this information by private communication with the researchers from Ref. [39].

Thus, within our made approximations the relation

$$S(k,\omega) = |a(k)|^2 A(k,\omega) \tag{7.2.12}$$

holds[8]. The results for $S(k,\omega)$ are depicted and compared to the experimental measurements in figures 7.7 and 7.8. Despite the coarse discretization $N_k = 40$, our results for

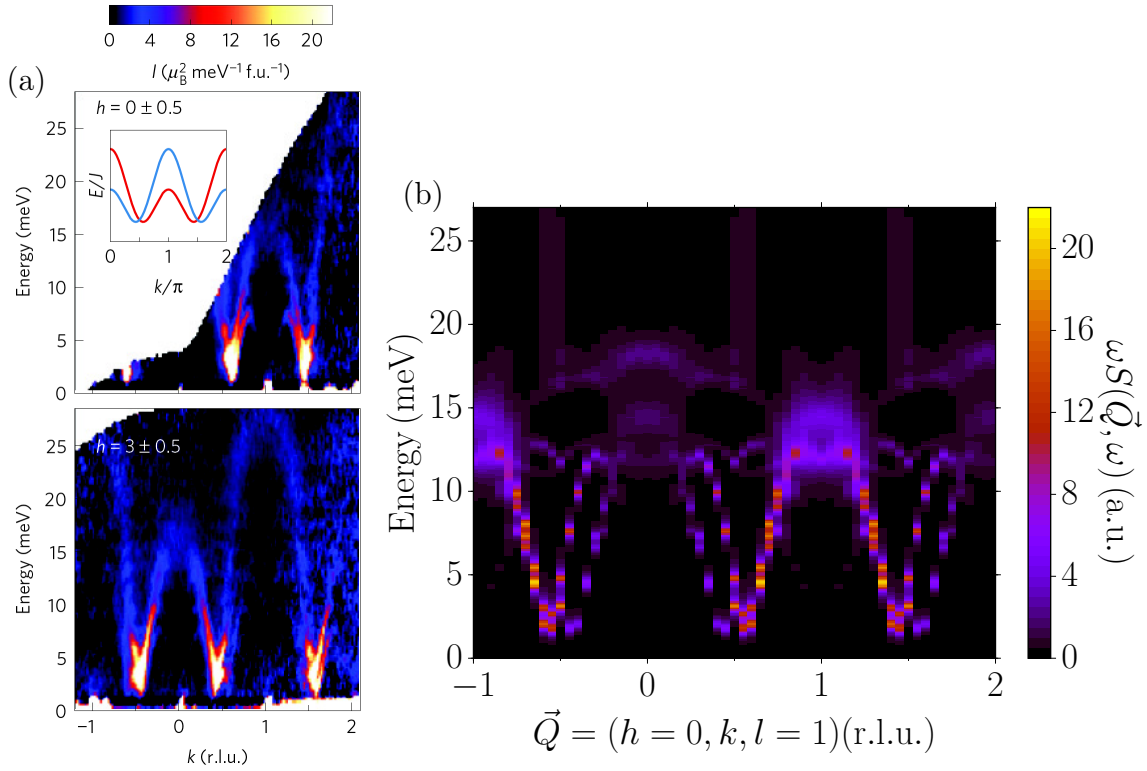

Figure 7.7: (a) Intensity results of the excitation spectrum of BCPO, received by INS experiments. The illustrations are taken from Ref. [39]. (b) Theoretically determined DSF $S(\vec{Q},\omega)$ multiplied by the energy ω in arbitrary units (a.u.). The results consider only the influence of the deepCUT calculations on the corresponding single particle states which were chosen for the Lanczos tridiagonalization. The effects of the Bogoliubov transformations for the original x, y and z mode, see sect. 4.2.2, are left out.

the DSF, see figures 7.7 and 7.8, show a good agreement with the experimental results within the energy range up to 15 meV. As expected, the intensity near the minimum area around $k \approx 0.5$ r.l.u. is larger than inside the continuum at $k \approx 1$ r.l.u., where we can reproduce the smeared out data in a satisfying manner. The enlarged display of the results, see figure 7.8, reveals the signature of the previous discussed orginal S= 0 bound state in the DSF clearly, which is in line with the down-bending behavior of the experimental data.

[8]Within a more comprehensive approach it would also be necessary to take into account the influence of the applied Bogoliubov transformations on the original x, y and z mode, see sect. 4.2.2.

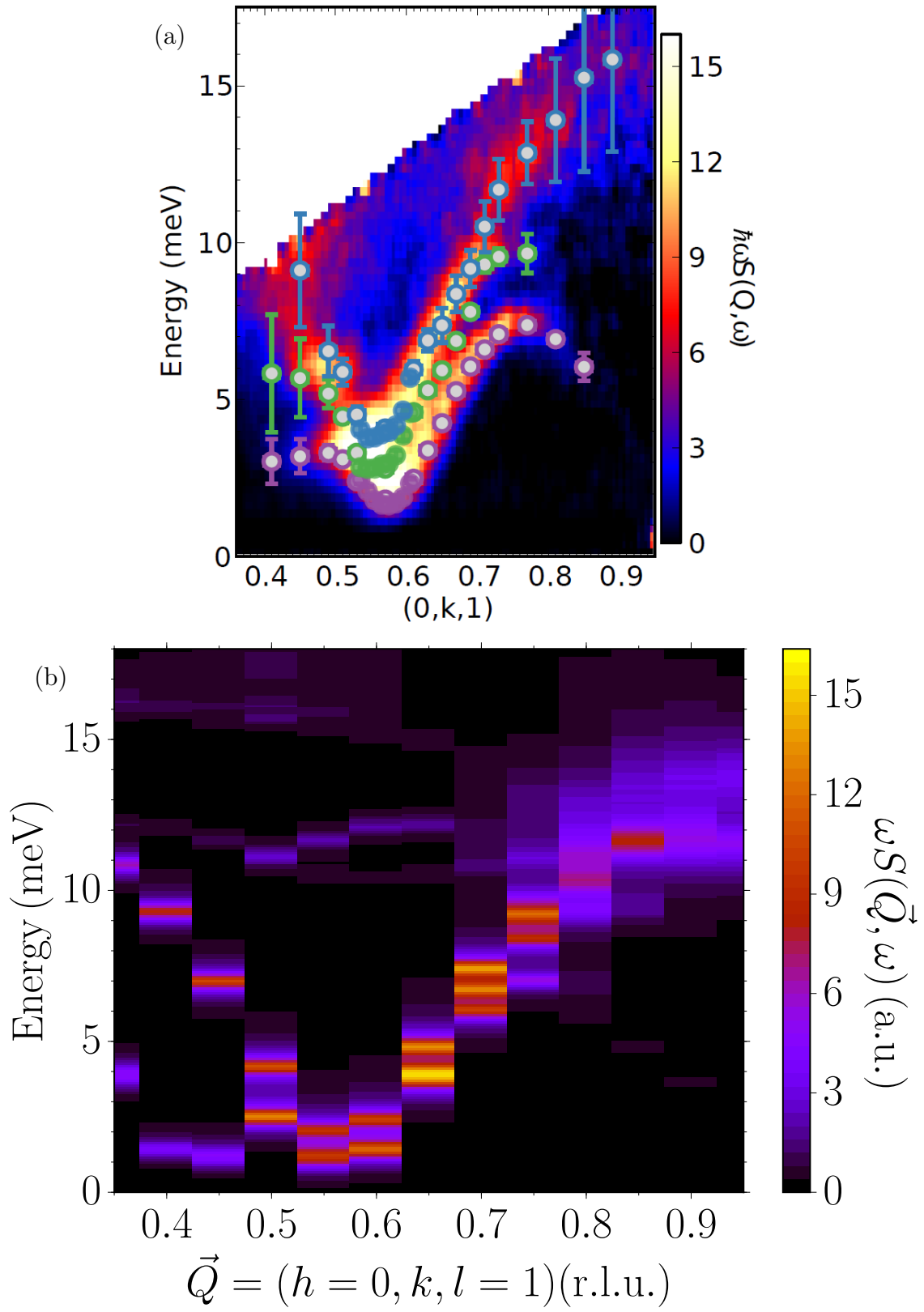

Figure 7.8: (a) Experimental results for the DSF, received by INS measurements in arbitrary units, in the low energy regime. The illustration is taken from Ref. [152] with permission from the author. (b) Theoretical results for the DSF $S(\vec{Q}, \omega)$ multiplied by the energy ω in arbitrary units (a.u.) in the low energy regime. Note, that the color scaling differs compared to the results shown in figure 7.7.

Once more we want to discuss our findings concerning the occuring bound state of BCPO in the energy range of $\approx$ 12 meV. As mentioned previously, there is no experimental evidence concerning a bound state in BCPO up to this point. The interesting aspect concerning this issue is that the performed experiments could not detect our claimed bound state at all since no experimental data have been received in this energy regime, see figure 7.8. This means that the existence of our claimed bound state in BCPO cannot be completely excluded by the current experimental findings. Therefore, we call for further measurements considering especially the energy regime of $\approx$ 12 meV, see also sect. 8.2.
With these findings we provide the first detailed explanation concerning the characteristic down-bending behavior in the excitation spectrum of BCPO, which stems from the S=0 two-particle bound state of the isotropic spin ladder. Furthermore, we claim the existence of a two-particle bound state in the energy regime of $\approx$ 12 meV, which derives from the S=1 two-particle bound state of the isotropic spin ladder.

(v) The unsolved issue concerning the resonances of mode 3 in the high energy regime at $\approx$ 27 meV remains even for the quadrilinear model of BCPO. Within this comprehensive model we could not find a parameter combination for the fitted **D** values which provides a good agreement between theory and experiment in this energy range. Even without our applied criterion of a maximum relative HWHM, see sect. 3.4.1 and figure 7.5 for the concrete value in this case, our numerical results for $\widetilde{\omega}_{z,r,\mathrm{qu}}(k)$ do not reveal any solutions at energies around $\approx$ 27 meV. Finally, this means that even adding the effects of two-particle interactions to the trilinear anisotropic model of BCPO, see chapter 6, does not lead to an explanation for the observed resonances in the high energy regime. One possible reason to clarify the origin of these resonances could be that they stem from particles states which include more than two particles. This presumption describes an issue for further research work, see sect. 8.2.

7.3 Technical challenges

As briefly mentioned in the previous section 7.2, computing the prefactors of the quadrilinear operator terms listed in eq. (7.2.11) turned out to be very demanding concerning the computational effort. As a first approach to estimate this computational effort we determine the required memory for **only storing** the numerical value of the prefactors. The required memory mr is given by the formula

$$mr\,(N_k, N_l) = 13 \cdot N_k^3 \cdot N_l^2 \cdot 16\,\mathrm{Byte} \tag{7.3.13}$$

and depends on the discretizations N_k and N_l, see sect. 5.3. The factor of 13 describes the number of different quadrilinear operator terms concerning the occuring flavor combi-

nations, see eq. (7.2.11). Since the magnetic structure of BCPO is two-dimensional, see sect. 1.4, and the total momentum of the two-particle interaction terms in eq. (7.2.11) is fixed, there are six independent momentum components present. The components k, q and q', see eq. (7.2.10), correspond to the direction along the spin ladder in y-direction, see figure 1.3. Their discretization is given by N_k. The momenta l, p and p', see eq. (7.2.10), belong to the direction perpendicular to the spin ladder in z-direction, see figure 1.3. Their discretization is given by N_l. As the experimental data are received for a fixed value of $l = 1\,\text{r.l.u.}$, we just have to store the prefactors which belong to a quadrilinear operator term with this fixed value of l. Concerning the remaining momentum components we have to compute all possible $N_k^3 \cdot N_l^2$ combinations. As discussed in sect. 5.3, we set $N_l = N_k/5$. To ensure that N_l is always an integer number we set

$$N_l = \text{floor}\,(N_k/5) \tag{7.3.14}$$

so that $mr\,(N_k, N_l)$, see eq. (7.3.13), depends only on the discretization N_k. The prefactors of the quadrilinear operator terms, see eq. (7.2.11), are composed of the prefactor $\alpha^{\alpha',\beta',\gamma',\delta'}\,(k, q, q')$, the entries of the transformation matrix $K_{k,l}^{-1}$ and the parameter $\vartheta_{k,l}^z$, see eqs. (7.1.4), (4.2.27) and (4.2.19). Since the components of the transformation matrix $K_{k,l}^{-1}$ can assume complex values, see sect. 4.2.2, the prefactors of the quadrilinear terms in eq. (7.2.11) can assume complex values as well. Therefore, we need to request 16 Byte memory[9] for each of the possible $N_k^3 N_l^2$ combinations. Figure 7.9 shows the required memory $mr\,(N_k)$ on a logarithmic scale and the current maximal available RAM of the LiDO3 cluster (1 TB) and of the cl1 cluster (256 GB)[10].
Figure 7.9 reveals clearly that on LiDO3 (cl1) a maximal discretization of $N_{k,\text{max,LiDO3}} \approx 170$ ($N_{k,\text{max,cl1}} \approx 130$) is possible. These discretization values are considerably smaller than the used discretization of $N_k = 400$ for the trilinear anisotropic model, see sect. 6.2, which ensured the convergence of the Lanczos coefficients.

[9] The memory requirement for a variable of the data type complex<double> in C++ is 16 Byte.
[10] The calculations have been performed in September/October 2020.

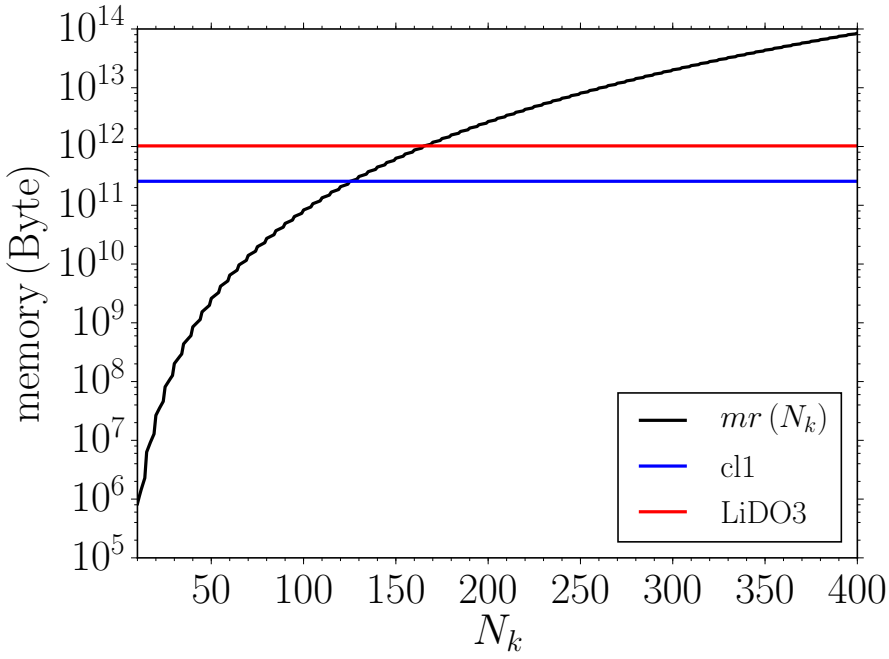

Figure 7.9: Logarithmic illustration of the required memory $mr\,(N_k)$ for **only storing** the numerical values of the prefactors of the quadrilinear operator terms in eq. (7.2.11). The current maximal available RAM of LiDO3 (1 TB) and cl1 (256 GB) are also shown.

As numerical computations need a very large amount of dynamic memory in addition to the final required storage memory, it is obvious that the maximal possible discretizations of $N_{k,\mathrm{max,LiDO3}} \approx 170$ and $N_{k,\mathrm{max,cl1}} \approx 130$ cannot not be realized. The true maximal possible discretization $N_{k,\mathrm{max,true}}$ is much smaller. To determine its value we run our calculations for different values of N_k and analyze the total utilized memory[11]. Figure 7.10 shows the results of this analysis. Note, that the jump in figure 7.10 occurs because of eq. (7.3.14). Determining the power law of the data points via a log-log-plot, see figure 7.10b), we receive that the complete utilized memory for our calculations grows with N_k^6. Extrapolating our data points with this power law reveals that on LiDO3 (cl1) a maximal discretization of $N_{k,\mathrm{max,true}} = 54$ ($N_{k,\mathrm{max,true}} = 42$) is possible.

Besides the needed memory for numerical computations the run time has to be considered as well. Therefore, we also analyzed the run time of our calculations for different values of N_k. The results are illustrated in figure 7.11.
The log-log-plot of our data points, see figure 7.11b) reveals that the run time for our computations grows with $N_k^{8.4}$. The maximal run time for calculations on LiDO3 and cl1 is 1 week, i.e. 168 hours. Extrapolating our data points with our run

[11] At the time of this analysis this was only possible on LiDO3. All computations were performed on an Intel Xeon CPU (E5 4640v4, 2.1 GHz.). The number of used cores was equal to N_k.

time power law of $N_k^{8.4}$ yields that a maximal discretization of $N_{k,\mathrm{max,true}} = 52$ is feasible.

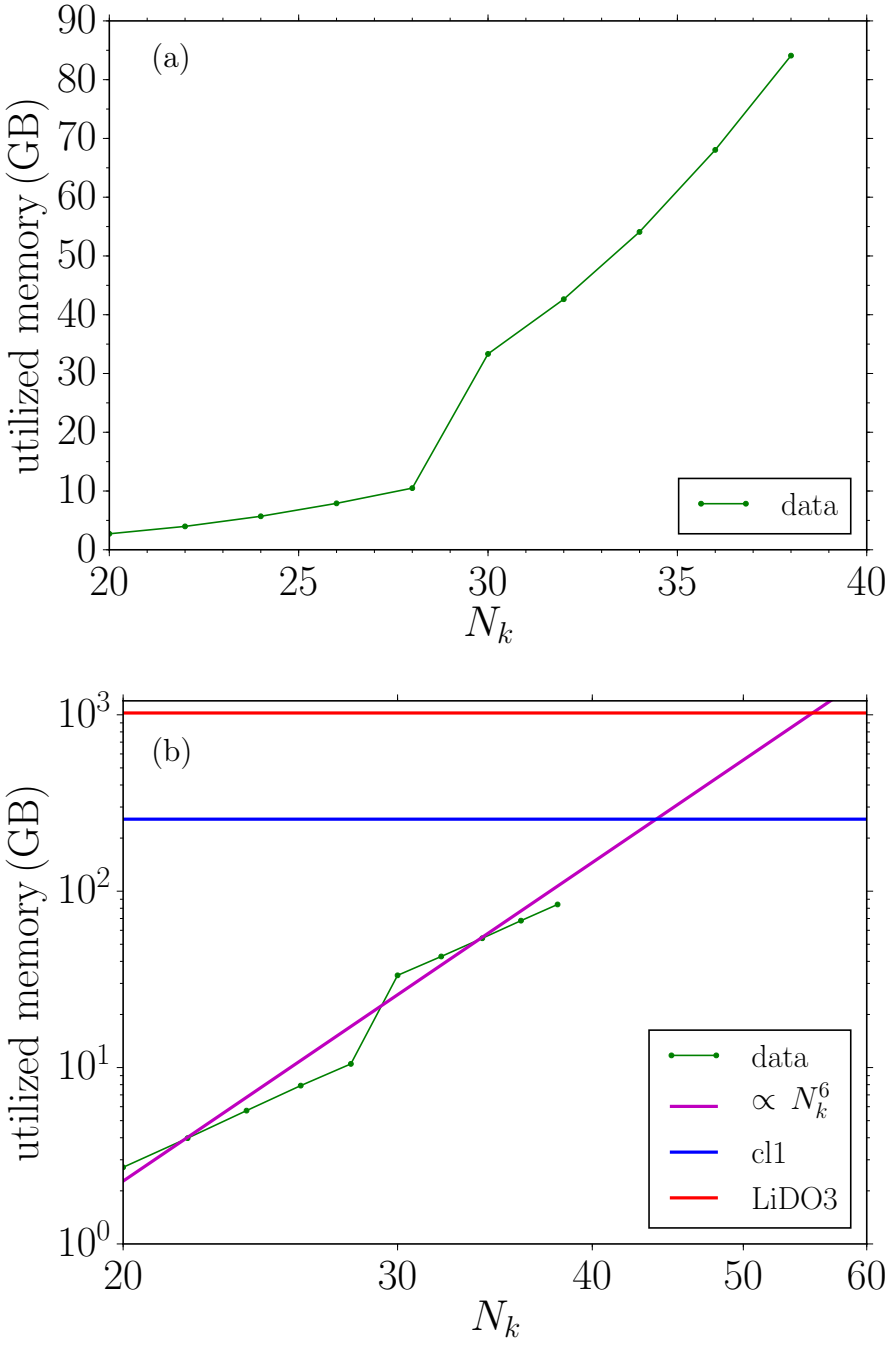

Figure 7.10: (a) Total utilized memory of the computations for determining the prefactors of the quadrilinear operator terms, see eq. (7.2.11), as a function of the discretization N_k. The calculations were performed on LiDO3. (b) Logarithmic illustration of panel (a). The power law of the data points is N_k^6 and also depicted in the panel as well as the current maximal available RAM of LiDO3 (1 TB) and cl1 (256 GB).

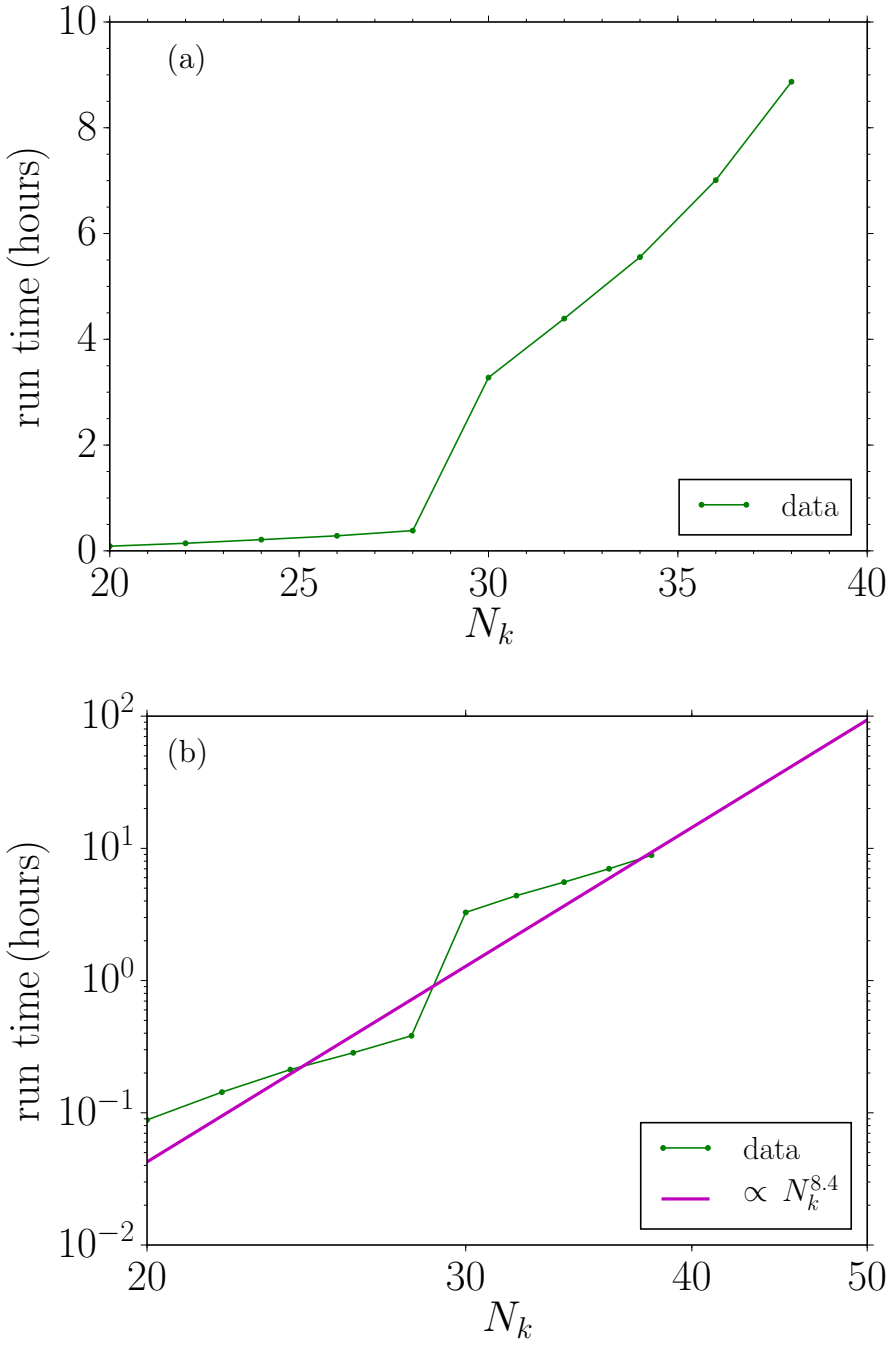

Figure 7.11: (a) Run time of the computations for determining the prefactors of the quadrilinear operator terms, see eq. (7.2.11), as a function of the discretization N_k. The calculations were performed on LiDO3. (b) Logarithmic illustration of panel (a). The power law of the data points is $N_k^{8.4}$ and also depicted in the panel.

Combining the limiting values concerning the maximal RAM and run time for computations on LiDO3 (cl1) we realize that the true maximal possible discretization is $N_{k,\mathrm{max,true}} = 54$ ($N_{k,\mathrm{max,true}} = 42$). We decided to perform all ongoing calculations on

our internal cluster cl1 since it is significantly less engaged than the university wide available cluster LiDO3. As we established the relation $N_l = N_k/5$ in sect. 5.3, we set $N_k = 40$ to be our maximal possible discretization for calculations concerning our quadrilinear model of BCPO.

7.4 Chapter summary

In this chapter we extended our trilinear anisotropic model of BCPO, which we established in chapter 6, by the inclusion of two-particle interactions. In doing so, we provide the first description of BCPO which considers two-particle interactions explicitly. Starting this project we found out that the anisotropic couplings in BCPO ensure a mixing of the S=0 and S=1 two-particle bound state of the isotropic spin ladder. Therefore, we assumed that their properties are reflected in our results for BCPO and that we can provide a more detailed understanding of its excitation spectrum. Our results for BCPO reveal that including two-particle interactions does not lead to visible effects in the low-energy regime. Therefore, the values of the anisotropic couplings did not change significantly compared to our results for the trilinear anisotropic model. The value of the dominant component $\mathbf{D}_1 \approx 0.38 J_1$ still has to be considered remarkable large, whereas our results for $\mathbf{D}_0 \approx 0.1 J_0$ and $\mathbf{D}_2 \approx -0.06 J_2$ are in line with our expectations of $10 - 20\,\%$ of the isotropic couplings. The unsolved issue of the characteristic down-bending of the two lowest modes could be solved within our quadrilinear model of BCPO. Our results reproduce this striking feature of the excitation spectrum on a qualitative and quantitative level. Furthermore, we identified the S=0 two-particle bound state of the isotropic spin ladder to be the mechanism behind this characteristic of BCPO. We stress that our results represent the first in the literature including this important aspect. The S=1 two-particle bound state of the isotropic spin ladder leads to the fact that we receive a clear signature mark of a two-particle bound state in the excitation spectrum of BCPO, which could not be found in the experimental data due to missing resolution in this energy regime. Thus, we suggest further measurements to confirm the current experimental data of BCPO focusing especially on indications of a two-particle bound state in the energy regime of $\approx 12\,\mathrm{meV}$. Despite these highly satisfying results, the issue concerning the existing resonances in the high-energy regime still remains unsolved. Possible approaches will be discussed in sect. 8.2. The computational effort of our quadrilinear model of BCPO turned out to be significantly greater than for our previous models. We also discussed the limits of our calculations with respect to the current available computational resources in detail.

8 Summary & Outlook

8.1 Summary

In this thesis we established a microscopic model for the quantum antiferromagnet $BiCu_2PO_6$ (BCPO) which reproduces the characteristic properties of its one-particle dispersions[1] by using realistic coupling values. More specifically, we found out what mechanisms in the magnetic structure of BCPO are responsible for the decay processes which occur in its excitation spectrum. We also clarified the reasons for the prominent down-bending of the two energetically lowest-lying modes before they cease to exist.

Before dealing with this complex issue we analyzed a simple one-dimensional bosonic model with hopping elements with regard to the influence of different effects on the one-particle dispersion. We included pair creation terms, hybridization effects between the one- and two-particle HILBERT space, i.e. decay/fusion processes, and two-particle interactions step by step. Already with this toy model we were able to observe and to understand the different types of decay processes.

As a first approach for a microscopic model of BCPO we solved the isotropic case of BCPO, i.e. an isotropic frustrated spin ladder, using a directly evaluated continuous unitary transformation (deepCUT). By coupling multiple frustrated spin ladders via a weak interladder coupling $|J'/J_0| \ll 1$ within a mean-field approach we received a two-dimensional isotropic model for BCPO. With this we determined the best matching values concerning the coupling ratios $x = J_1/J_0 = 1.2$ and $y = J_2/J_1 = 0.9$ with a fixed relative value for the interladder coupling $J'/J_0 = 0.16$ as assumed in previous studies [39, 70]. By means of a comprehensive symmetry analysis of BCPO we included the Dzyaloshinskii-Moriya interaction (DM interaction) to the two-dimensional isotropic model by a perturbative treatment of the anisotropic couplings within a mean-field approach up to bilinear operator level. Our results cannot describe the different kinds of decay processes but can reproduce the low-energy regime using remarkably large anisotropic couplings $\mathbf{D}_1 \approx 0.6J_1$.

We used this bilinear anistropic model as the basis for analyzing the effects of quasiparticle decay at zero temperature in BCPO. Thereto, we focused on effects in its magnetic structure holding odd parity, which give rise to transition processes between the one-

[1] The excitation modes are not degenerated, but split. This means that anisotropic interactions are present in BCPO lifting the degeneracy of the excitation modes.

and two-particle HILBERT space, i.e. decay processes. First, we focused on a variation in the next-nearest-neighbor coupling, which can originate from the two crystallographically inequivalent copper ions Cu_A and Cu_B. With this spin isotropic effect we received the best fitting values for the anisotropic couplings: $\mathbf{D}_1 \approx 0.48J_1$, $\mathbf{D}_0 \approx 0.1J_0$ and $\mathbf{D}_2 \approx -0.1J_2$. While the value of $\mathbf{D}_1$ is still remarkable large, our results for $\mathbf{D}_0$ and $\mathbf{D}_2$ are in accordance with our expectations. Unfortunately, it was not possible to reproduce the spontaneous quasiparticle decay (SQPD) characteristics of the experimental data of BCPO within this trilinear isotropic model.

Besides the variation in the the next-nearest-neighbor coupling, we extended our bilinear anisotropic model of BCPO by the effects of SQPD which stem from the anisotropic couplings themselves. After a detailed analysis concerning the effects of each $\mathbf{D}$ component on the one-particle dispersions we received the best fitting parameters: $\mathbf{D}_1 \approx 0.38J_1$, $\mathbf{D}_0 \approx 0.1J_0$ and $\mathbf{D}_2 \approx -0.1J_2$. Our results represent a reduction of up to $\approx 40\,\%$ compared to the bilinear anisotropic model and are comparable to the results from HWANG and KIM [64]. With this trilinear anisotropic model of BCPO it is possible to reproduce the low-energy regime but it still cannot describe the occuring decay characteristics, e.g. the down-bending behavior of the two lowest modes.

As a final extension we included two-particle interactions to our trilinear anisotropic model. Within the limits of the current available computational ressources we determined the best fitting values for the anisotropic couplings: $\mathbf{D}_1 \approx 0.38J_1$, $\mathbf{D}_0 \approx 0.1J_0$ and $\mathbf{D}_2 \approx -0.06J_2$. We found out that the low-energy regime is only hardly effected by the included two-particle interactions which is why the results are almost identical to the ones without two-particle interactions. However, within this quadrilinear model of BCPO it is possible to explain the experimentally observed down-bending behavior of the two lowest-lying modes. The mechanism behind this feature is the S=0 two-particle bound state of the isotropic case of BCPO, which is mixed with the S=1 two-particle state by the DM interaction. This means that the observed down-bending behavior of the two lowest modes is not a down-bending in the sense of an effect stemming from the hybridization between the one- and two-particle HILBERT space and level repulsion between the corresponding energy levels. It is a signature of the S= 0 two-particle bound state of the isotropic case of BCPO and can only be identified when two-particle interactions are considered explicitly. In addition, our quadrilinear model yields a clear two-particle bound state for BCPO above the low-energy regime, which could not be found in experiments so far. It stems from the S=1 two-particle bound state of the isotropic case. Further experimental investigations concerning this specific question are called for.

In this way, we established the first comprehensive model of the quantum antiferromagnet BCPO which is able to reproduce the different types of decay processes in its

excitation spectrum. Unfortunately, its occuring resonances at high energies remain unexplained.

8.2 Outlook

This thesis shows that successive extensions of a microscopic model for a complex compound lead to the point that more and more of its properties can be explained. There are several possibilities for extending our model of BCPO.

One enhancement on theoretical side is related to the number of considered particles. We strongly assume that augmenting our model of BCPO by including more than two particles can provide an explanation for the present resonances in the high-energy regime.

Another option to improve our results is to combine the decay processes which stem from the variation of the next-nearest-neighbor coupling with the ones which originate from the DM interactions, i.e. a combination of the models from chapter 5 and 6. On top of that one could also take the two-particle interactions, see chapter 7, into account to receive an even more comprehensive model of BCPO.

Furthermore, it is possible to extend our model by including the effects of SQPD and two-particle interactions stemming from the symmetric anisotropic interactions, see sect. 2.4.2. As they have a great influence on the one-particle dispersions on bilinear operator level, it is reasonable to assume identical observations on trilinear and quadrilinear operator level. On the technical side these enhancements require the further development and implementation of efficient algorithms in order to transform multi-particle interactions into the basis of the bilinear anisotropic model. Concerning the determination of the fitting parameters, i.e. the values of the anisotropic couplings, introducing a different systematic approach, based on a numerical multi-dimensional determination of the best parameters, can lead to better fits between theory and experiment. With this we mean that this fitting process could be automated.

On experimental side, further inelastic neutron scattering (INS) measurements on BCPO in order to confirm and refine the previous results are preferable. In particular, we suggest measurements with a sufficiently high resolution in the energy regime of $\approx 12\,\mathrm{meV}$ to enable the possibility of locating our claimed S=1 two-particle bound state in BCPO.

Appendix

A Lanczos tridiagonalization

To compute the retarded Green's function of the form

$$G^{\mathrm{ret}}(k,\omega) = \langle u_0| \frac{1}{\omega - \bar{H}(k)} |u_0\rangle \tag{A.1}$$

the Lanczos tridiagonalization can be used. This algorithm sets up an orthogonal basis $|u_i\rangle$, in which the Hamiltonian $\bar{H}$ has the form

$$\bar{H}(k) = \begin{pmatrix} a_0(k) & b_1(k) & 0 & 0 & \cdots \\ b_1(k) & a_1(k) & b_2(k) & 0 & \cdots \\ 0 & b_2(k) & a_3(k) & b_3(k) & \cdots \\ \vdots & \vdots & \vdots & \vdots & \ddots \end{pmatrix} \tag{A.2}$$

with the real Lanczos coefficients $a_i(k)$ and $b_i(k)$.
These coefficients and the orthogonal basis $|u_i\rangle$ can be calculated via the recursion scheme

$$|u_0\rangle \tag{A.3a}$$
$$|u_1\rangle = (H(k) - a_0(k))|u_0\rangle \tag{A.3b}$$
$$|u_2\rangle = (H(k) - a_1(k))|u_1\rangle - b_1^2(k)|u_0\rangle \tag{A.3c}$$
$$|u_3\rangle = (H(k) - a_2(k))|u_2\rangle - b_2^2(k)|u_1\rangle \tag{A.3d}$$
$$... \tag{A.3e}$$

with the Lanczos coefficients reading

$$a_i(k) = \frac{\langle u_i| H(k) |u_i\rangle}{\langle u_i|u_i\rangle} \quad \text{for } i = 0,1,2,... \tag{A.4a}$$
$$b_i^2(k) = \frac{\langle u_i|u_i\rangle}{\langle u_{i-1}|u_{i-1}\rangle} \quad \text{for } i = 1,2,3,... \tag{A.4b}$$
$$b_0(k) = 0. \tag{A.4c}$$

For our issues the start state $|u_0\rangle$ is a one-particle state with fixed momentum k.
Thus, the retarded GREEN'S function can be expressed by a continued fraction

$$G^{\mathrm{ret}}(k,\omega) = \cfrac{1}{\omega - a_0(k) - \cfrac{b_1^2(k)}{\omega - a_1(k) - \cfrac{b_2^2(k)}{\omega - a_2(k) - \cdots}}}, \tag{A.5}$$

which has to be terminated at a specific iteration level n_{LANCZOS}.
In the case of decay processes from one particle into two the limiting values of the LANCZOS coefficients are determined by the lower band edge of the concerning two-particle continuum $\omega_{2,\min}(k)$ and the upper band edge $\omega_{2,\max}(k)$. The coefficients $a_\infty(k) \coloneqq \lim_{i\to\infty} a_i(k)$ and $b_\infty(k) \coloneqq \lim_{i\to\infty} b_i(k)$ fulfill the relations

$$\omega_{2,\min}(k) = a_\infty(k) - 2b_\infty(k) \tag{A.6a}$$

$$\omega_{2,\max}(k) = a_\infty(k) + 2b_\infty(k). \tag{A.6b}$$

Numerically only a finite number of LANCZOS tridiagonalization steps can be performed. To simulate infinite large systems in the thermodynamic limit one has to terminate the algorithm. It is reasonable to truncate at the iteration step where the LANCZOS coefficients fulfill the relations (A.6) up to negligible deviations.
There are different types of terminators to reconstruct GREEN'S functions from incomplete continued fractions. The simplest way of termination is the square-root terminator $T(k,\omega)$, which is given by

$$T(k,\omega) = \frac{1}{2b_\infty^2(k)}\left(\omega - a_\infty(k) - \sqrt{R(k,\omega)}\right) \qquad \text{for } \omega \geq \omega_{2,\max}(k) \tag{A.7a}$$

$$T(k,\omega) = \frac{1}{2b_\infty^2(k)}\left(\omega - a_\infty(k) - \mathrm{i}\sqrt{-R(k,\omega)}\right) \qquad \text{for } \omega_{2,\min} \leq \omega \leq \omega_{2,\max}(k) \tag{A.7b}$$

$$T(k,\omega) = \frac{1}{2b_\infty^2(k)}\left(\omega - a_\infty(k) + \sqrt{R(k,\omega)}\right) \qquad \text{for } \omega \leq \omega_{2,\min}(k) \tag{A.7c}$$

with the radicand

$$R(k,\omega) = (\omega - a_\infty(k))^2 - 4b_\infty^2(k). \tag{A.8}$$

It is evident that the square-root terminator has an imaginary part only inside the two-particle continuum.

B Parameters of the toy model

Here the parameters for the toy model, presented in chapter 3, are listed.
The values of the hopping elements were calculated by a deepCUT using the 1n-generator in the one-particle space. The underlying model is a frustrated isotropic spin S=1/2 HEISENBERG ladder with rung coupling J_0, nearest-neighbor coupling J_1 and next-nearest-neighbor coupling J_2. The rung coupling J_0 is determined to be the global energy scale. The used coupling ratios are given by $x = \frac{J_1}{J_0} = 1.2$ and $y = \frac{J_2}{J_1} = 0.9$.

d	t_d
0	1.549938420848804
1	0.1794088852461154
2	0.2623695437552867
3	-0.1048611048320241
4	-0.08017242688698614
5	0.04837581228692146
6	0.005231194502012992
7	-0.01735217860096988
8	5.623129910602866e-05
9	0.006964869432389426
10	-0.003188537391764854
11	-0.002018711432624706
12	0.002147797713125333
13	0.0002306605843470841

Table B.1: Values of the hopping elements t_d, which have been used for the toy model. Note that only the values for the distances $d \geq 0$ are listed because the model is symmetric around the rungs. This symmetry implies the relation $t_d = t_{-d}$.

The used values of v_δ, which present the amplitude of the decay terms, are from the same deepCUT calculation as the prefactors t_d. We chose a single spin operator $S_i^{\alpha,\mathrm{R}}$, transformed it by the deepCUT and set the prefactors of the linear terms $t_{i+\delta}^{\alpha}/t_{i+\delta}^{\alpha,\dagger}$ to be the values of v_δ. These values were already produced for previous calculations and do not simulate any physically realistic decay amplitudes. They serve only for an example.

δ	v_δ
0	-0.3874491109155713
1	0.05165001704799924
2	0.08095884805094124
3	-0.03713614889687351
4	-0.0219291397751164
5	0.01719462494862808
6	0.004727305201296136
7	-0.01024208259455439
8	0.001628782296091526
9	0.00497492501969249
10	-0.002315960919757644
11	-0.001621270078823474
12	0.001835116321222724

Table B.2: Values of the decay amplitude v_δ, which have been used for the toy model. Note that only the values for the distances $\delta \geq 0$ are listed because the model is symmetric around the rungs. This symmetry implies the relation $v_\delta = v_{-\delta}$.

C Brent's method

Computing the roots of a given function numerically is possible with different kinds of methods or algorithms. In this thesis we used Brent's method to address this issue. This method is a numerical one which calculates the roots of a continuous function on an iterative basis [153]. It combines the bisection method, the secant method and inverse quadratic interpolation.
The starting point is finding the roots $f(x) = 0$ of a continuous function $f(x)$, which is defined on an intervall $[a_0, b_0] \to \mathbb{R}$, while the signs of the values $f(a_0)$ and $f(b_0)$ differ. That means the function $f(x)$ has a root in the intervall $[a_0, b_0]$.

In principle, Brent's method represents a modification of the Dekker method, which combines the bisection method and the secant method. The Dekker method starts with the intervall $[a_0, b_0]$, as described before, and calculates two values in each iteration step. First the value

$$s = b_k - \frac{b_k - b_{k-1}}{f(b_k) - f(b_{k-1})} f(b_k) \tag{C.1}$$

is determined with the secant method and second the value

$$m = \frac{a_k + b_k}{2} \tag{C.2}$$

using the bisection method is calculated. Hereby the variable b_k describes the current iteration value and a_k describes the other point of the intervall so that the sign of the values $f(a_k)$ and $f(b_k)$ differ. Additionally the relation $|f(b_k)| \leq |f(a_k)|$ holds,

meaning that b_k represents a better approximation for the root than a_k. In the first iteration step $b_{k-1} = a_0$ holds.
If the relation $m < s < b_k$ ist valid, the new iteration value is set to $b_{k+1} = s$, otherwise the result of the bisection method $b_{k+1} = m$ is chosen. For the new iteration value a_{k+1} is has to be ensured that $f(a_{k+1})$ and $f(b_{k+1})$ have different signs. If the values $f(a_k)$ and $f(b_{k+1})$ show up different sign, then $a_{k+1} = a_k$ holds. If this is not the case, the signs of the values $f(b_{k+1})$ and $f(b_k)$ have to be different so that $a_{k+1} = b_k$ is set. As a last step the next iteration values a_{k+1} and b_{k+1} have to be arranged such that $|f(b_{k+1})| \leq |f(a_{k+1})|$ is fulfilled.

It is possible that the DEKKER method converges more slowly than the bisection method itself since the intervall $[b_k, b_{k-1}]$ can become arbitrarily small. The key point of BRENT'S method is a modification of the DEKKER method to avoid this case. Therefore this method uses inverse quadratic interpolation so that its convergence is not slower than the convergence of the bisection method. Furthermore the value of b_k always has to change by a certain tolerance value to avoid slow convergence. This tolerance value depends on the machine accuracy ϵ and the requested precision t of the result.
For our calculations we used a machine accuracy of $\epsilon = 10^{-14}$ and a precision of $t = 10^{-8}$, which implies that the calculated roots of the function $f(x)$ are exact up to 10^{-8}. For further details we refer to Ref. [153].

D Symmetry analysis of $\mathbf{D}_1$

We choose the vector $\mathbf{D}_1$ concerning the NN bonds, see figure 4.3, as an example to demonstrated the symmetry analysis in detail. The symmetry analyses of the vectors $\mathbf{D}_0$ and $\mathbf{D}_2$ are similiar and presented in detail in the Appendix of Ref. [89].

By applying the rotation RS_y we map the bonds of the vectors $\mathbf{D}_{1,LU}$ and $\mathbf{D}_{1,LO}$, respectively, to the bonds to which the vectors $\mathbf{D}_{1,RO}$ and $\mathbf{D}_{1,RU}$ belong. It is not necessary to rearrange the spin operators according to our notation after the rotation because the spin operators stay in the same order with regard to the y-coordinate. In this way, we obtain the following relations

$$\mathbf{D}_{1,RO} = \mathrm{RS}_y(\mathbf{D}_{1,LU}) \tag{D.1a}$$

$$\mathbf{D}_{1,RU} = \mathrm{RS}_y(\mathbf{D}_{1,LO}) \tag{D.1b}$$

$$\mathbf{D}_{1,LU} = \mathrm{RS}_y(\mathbf{D}_{1,RO}) \tag{D.1c}$$

$$\mathbf{D}_{1,LO} = \mathrm{RS}_y(\mathbf{D}_{1,RU}). \tag{D.1d}$$

Second, we consider the rotation R_x and obtain

$$\mathbf{D}_{1,RO} = -\mathrm{R}_x\left(\mathbf{D}_{1,LU}\right) \tag{D.2a}$$
$$\mathbf{D}_{1,RU} = -\mathrm{R}_x\left(\mathbf{D}_{1,LO}\right) \tag{D.2b}$$
$$\mathbf{D}_{1,LU} = -\mathrm{R}_x\left(\mathbf{D}_{1,RO}\right) \tag{D.2c}$$
$$\mathbf{D}_{1,LO} = -\mathrm{R}_x\left(\mathbf{D}_{1,RU}\right). \tag{D.2d}$$

After the rotation R_x the spin operators have to be swapped to comply with our convention. Thus an additional minus sign appears in eqs. (D.2a)-(D.2d).
Next, the reflection S_{xy} is applied yielding

$$\mathbf{D}_{1,RU} = -\mathrm{S}_{xy}\left(\mathbf{D}_{1,LU}\right) \tag{D.3a}$$
$$\mathbf{D}_{1,RO} = -\mathrm{S}_{xy}\left(\mathbf{D}_{1,LO}\right) \tag{D.3b}$$
$$\mathbf{D}_{1,LO} = -\mathrm{S}_{xy}\left(\mathbf{D}_{1,RO}\right) \tag{D.3c}$$
$$\mathbf{D}_{1,LU} = -\mathrm{S}_{xy}\left(\mathbf{D}_{1,RU}\right). \tag{D.3d}$$

The additional minus sign occurs due to the pseudovector properties of the spin operators. Now we derive the relations between the vectors $\mathbf{D}_1$ which arise from applying the reflection S_{xz}

$$\mathbf{D}_{1,LO} = \mathrm{S}_{xz}\left(\mathbf{D}_{1,LU}\right) \tag{D.4a}$$
$$\mathbf{D}_{1,LU} = \mathrm{S}_{xz}\left(\mathbf{D}_{1,LO}\right) \tag{D.4b}$$
$$\mathbf{D}_{1,RU} = \mathrm{S}_{xz}\left(\mathbf{D}_{1,RO}\right) \tag{D.4c}$$
$$\mathbf{D}_{1,RO} = \mathrm{S}_{xz}\left(\mathbf{D}_{1,RU}\right). \tag{D.4d}$$

In this case the minus signs resulting from the pseudovector properties and the rearrangement of the spin operators compensate.
Finally, we employ the reflection SS_{yz} to receive the following relations

$$\mathbf{D}_{1,LO} = -\mathrm{SS}_{yz}\left(\mathbf{D}_{1,LU}\right) \tag{D.5a}$$
$$\mathbf{D}_{1,LU} = -\mathrm{SS}_{yz}\left(\mathbf{D}_{1,LO}\right) \tag{D.5b}$$
$$\mathbf{D}_{1,RU} = -\mathrm{SS}_{yz}\left(\mathbf{D}_{1,RO}\right) \tag{D.5c}$$
$$\mathbf{D}_{1,RO} = -\mathrm{SS}_{yz}\left(\mathbf{D}_{1,RU}\right). \tag{D.5d}$$

Here the minus sign occurs because of the pseudovector properties of the spin operators. With the above relations we are now able to derive the parity and the behavior of the

sign along the legs of the ladder of the vector $\mathbf{D}_1$. We start from the ansatz

$$\mathbf{D}_{1,LU} = c_x \mathbf{e}_x + c_y \mathbf{e}_y + c_z \mathbf{e}_z, \tag{D.6}$$

which means that $\mathbf{D}_{1,LU}$ is an arbitrary combination of the unit vectors $\mathbf{e}_x$, $\mathbf{e}_y$ and $\mathbf{e}_z$ with constant real coefficients c_x, c_y and c_z. Using this ansatz for eq. (D.4a) we obtain

$$\mathbf{D}_{1,LO} = c_x \mathbf{e}_x - c_y \mathbf{e}_y + c_z \mathbf{e}_z. \tag{D.7}$$

Additionally, we insert the ansatz in eq. (D.5a) and obtain

$$\mathbf{D}_{1,LO} = c_x \mathbf{e}_x - c_y \mathbf{e}_y - c_z \mathbf{e}_z. \tag{D.8}$$

To fulfill eqs. (D.7) and (D.8), the z-component has to vanish, i.e. $c_z = 0$ holds. Using eqs. (D.3a) and (D.1a), respectively, we obtain

$$\mathbf{D}_{1,RU} = -c_x \mathbf{e}_x - c_y \mathbf{e}_y \tag{D.9a}$$

$$\mathbf{D}_{1,RO} = -c_x \mathbf{e}_x + c_y \mathbf{e}_y. \tag{D.9b}$$

In conclusion, we see that the sign of the x-component does not change along the legs, i.e. the signs of the x-component of the vectors $\mathbf{D}_{1,LO}$ and $\mathbf{D}_{1,LU}$ are the same as the signs of the x-component of the vectors $\mathbf{D}_{1,RO}$ and $\mathbf{D}_{1,RU}$.
In contrast, the y-component alternates along the legs, i.e. the signs of the y-component of the vectors $\mathbf{D}_{1,LO}$ and $\mathbf{D}_{1,LU}$ differ and so do the signs of the vectors $\mathbf{D}_{1,RO}$ and $\mathbf{D}_{1,RU}$. To determine the parity of $\mathbf{D}_1$ we compare the sign of each components of $\mathbf{D}_{1,LO}$ with the one of $\mathbf{D}_{1,RO}$ and $\mathbf{D}_{1,LU}$ with $\mathbf{D}_{1,RU}$. As a result we find that the components on the left leg have a different sign than the components on the right leg. Hence, the parity of $\mathbf{D}_1$ is odd.

E deepCUT results for the isotropic spin ladder

The dispersion of the frustrated isotropic spin ladder is calculated by the deepCUT method, see sect. 2.1, yielding

$$\omega_0(k) = \sum_{\delta=0}^{13} \omega_\delta \cos(\delta k). \tag{E.1}$$

The coefficients ω_δ are given in table E.1. With the same deepCUT a single spin operator $S_i^{\alpha,\mathrm{L/R}}$ is transformed to the effective spin operator

$$S_{i,\mathrm{eff}}^{\alpha,\mathrm{L}} = -S_{i,\mathrm{eff}}^{\alpha,\mathrm{R}} = \sum_{\delta=-12}^{12} a_{|\delta|} \left(t_{i+\delta}^{\alpha,\dagger} + t_{i+\delta}^{\alpha} \right) + \text{bilinear and higher terms}, \tag{E.2}$$

with the amplitudes a_δ, which are also given in table E.1. The spin operators are labeled with the indices L and R referring to the left and right spin of a single dimer in the spin ladder.

δ	ω_δ	a_δ
0	1.5499384208488	0.3874491109155713
1	0.358817770492231	-0.05165001704799924
2	0.524739087510573	-0.08095884805094124
3	-0.209722209664048	0.03713614889687351
4	-0.160344853773972	0.0219291397751164
5	0.0967516245738429	-0.01719462494862808
6	0.010462389004026	-0.004727305201296136
7	-0.0347043572019398	0.01024208259455439
8	0.000112462598212057	-0.001628782296091526
9	0.0139297388647789	-0.00497492501969249
10	-0.00637707478352971	0.002315960919757644
11	-0.00403742286524941	0.001621270078823474
12	0.00429559542625067	-0.001835116321222724
13	0.000461321168694168	

Table E.1: The coefficients ω_δ in order to describe the dispersion of the frustrated isotropic spin ladder as well as the prefactors a_δ to transform a single spin operator are determined by using a deepCUT calculation for the ratios $x = J_1/J_0 = 1.2$ and $y = J_2/J_1 = 0.9$.

List of Figures

List of Tables

Bibliography

[1] P. Drude. Zur Elektronentheorie der Metalle. *Annalen der Physik*, **306**:566, 1900.

[2] P. Drude. Zur Elektronentheorie der Metalle; II. Teil. Galvanomagnetische und thermomagnetische Effecte. *Annalen der Physik*, **308**:369, 1900.

[3] N. W. Ashcroft and N. D. Mermin. *Solid State Physics*. Holt, Rinehart and Winston, 1976.

[4] J. J. Sakurai. *Modern Quantum Mechanics*. Benjamin/Cummings, 1985.

[5] D. J. Griffiths. *Introduction to Quantum Mechanics*. Prentice-Hall, 1995.

[6] L. E. Ballentine. *Quantum Mechanics - A Modern Development*. World Scientific, 2015.

[7] D. C. Mattis. *The Theory of Magnetism I*. Springer-Verlag Berlin Heidelberg, 1981.

[8] K. Yosida. *Theory of Magnetism*. Springer, 1996.

[9] E. Ising. Beitrag zur Theorie des Ferromagnetismus. *Zeitschrift für Physik*, **31**:253, 1925.

[10] W. Pauli. Über den Einfluß der Geschwindigkeitsabhängigkeit der Elektronenmasse auf den Zeemaneffekt. *Zeitschrift für Physik*, **31**:373, 1925.

[11] W. Pauli. Exclusion principle and quantum mechanis. *Nobel Lecture*, 1946.

[12] W. Gerlach and O. Stern. Der experimentelle Nachweis der Richtungsquantelung im Magnetfeld. *Zeitschrift für Physik*, **9**:349, 1922.

[13] G. Uhlenbeck and S. Goudsmit. Ersetzung der Hypothese vom unmechanischen Zwang durch eine Forderung bezüglich des inneren Verhaltens jedes einzelnen Elektrons. *Die Naturwissenschaften*, **13**:953, 1925.

[14] R. Moessner and A. P. Ramirez. Geometrical frustration. *Physics Today*, **59**:24, 2006.

[15] G. H. Wannier. Antiferromagnetism. The Triangular Ising Net. *Phys. Rev.*, **79**:357, 1950.

[16] G. H. Wannier. Antiferromagnetism. The Triangular Ising Net. *Phys. Rev. B*, **7**:5017, 1973.

[17] H. T. Diep, editor. *Frustrated Spin Systems*. World Scientific, 2004.

[18] C. Lacroix, P. Mendels, and F. Mila. *Introduction to Frustrated Magnetism*. Springer, 2011.

[19] A. P. Ramirez. Strongly Geometrically Frustrated Magnets. *Annu. Rev. Mater. Sci.*, **24**:453, 1994.

[20] J. Vannimenus and G. Toulouse. Theory of the frustration effect. II. Ising spins on a square lattice. *J. Phys. C: Solid State Phys.*, **10**:L537, 1977.

[21] J. Villain. Spin glass with non-random interactions. *J. Phys. C: Solid State Phys.*, **10**:1717, 1977.

[22] A. Auerbach. *Interacting Electrons and Quantum Magnetism*. Springer, 1994.

[23] K. Kano and S. Naya. Antiferromagnetism. The Kagomé Ising Net. *Prog. Theor. Phys.*, **10**:158, 1953.

[24] P. Azaria, H. T. Diep, and H. Giacomini. Coexistence of Order and Disorder and Reentrance in an Exactly Solvable Model. *Phys. Rev. Lett.*, **59**:1629, 1987.

[25] M. Debauche, H. T. Diep, P. Azaria, and H. Giacomini. Exact phase diagram of a generalized Kagomé Ising lattice: Reentrance and disorder lines. *Phys. Rev. B*, **44**:2369, 1991.

[26] B. D. Gaulin. Geometrically-frustrated magnetism on triangular and tetrahedral lattices. *Hyperfine Interactions*, **85**:159, 1994.

[27] J. E. Greedan. Geometrically frustrated magnetic materials. *J. Mater. Chem.*, **11**:37, 2001.

[28] R. Moessner. Unconventional magnets in external magnetic fields. *J. Phys.: Conf. Ser.*, **145**:012001, 2009.

[29] C. Castelnovo, R. Moessner, and S. L. Sondhi. Spin Ice, Fractionalization, ans Topological Order. *Annu. Rev. Condens. Mater. Phys.*, **3**:35, 2012.

[30] S. T. Bramwell and M. J. P. Gingras. Spin Ice State in Frustrated Magnetic Pyrochlore Materials. *Science*, **294**:1495, 2001.

[31] A. A. Zvyagin. New physics in frustrated magnets: Spin ices, monopoles, etc. (Review Article). *Low Temp. Phys.*, **39**:901, 2013.

[32] G. L. Squires. *Introduction to the theory of thermal neutron scattering*. Cambridge University Press, 1978.

[33] S. W. Lovesey. *Theory of neutron scattering from condensed matter, Volume 1*. Clarendon Press, Oxford, 1984.

[34] S. W. Lovesey. *Theory of neutron scattering from condensed matter, Volume 2*. Clarendon Press, Oxford, 1984.

[35] S. Sachdev. *Quantum phase transitions*. Cambridge University Press, 2011.

[36] P. Coleman. *Introduction into Many-Body Physics*. Cambridge University Press, 2015.

[37] M. B. Stone, I. A. Zaliznyak, T. Hong, C. L. Broholm, and D. H. Reich. Quasiparticle breakdown in a quantum spin liquid. *Nature*, **440**:187, 2006.

[38] T. Hong, Y. Qiu, M. Matsumoto, D. A. Tennant, K. Coester, K. P. Schmidt, F. F. Awwadi, M. M. Turnbull, H. Agrawal, and A. L. Chernyshev. Field induced spontaneous quasiparticle decay and renormalization of quasiparticle dispersion in a quantum antiferromagnet. *Nat Commun*, **8**:15148, 2017.

[39] K. W. Plumb, K. Hwang, Y. Qiu, L. W. Harriger, G. E. Granroth, A. I. Kolesnikov, G. J. Shu, F. C. Chou, C. Ruegg, Y. B. Kim, and Y.-J. Kim. Quasiparticle-continuum level repulsion in a quantum magnet. *Nat Phys*, **12**, 2015.

[40] M. E. Zhitomirsky and A. L. Chernyshev. *Colloquium*: Spontaneous magnon decays. *Rev. Mod. Phys.*, **85**:219, 2013.

[41] M. E. Zhitomirsky. Decay of quasiparticles in quantum spin liquids. *Phys. Rev. B*, **73**73:100404, 2006.

[42] B. Fauseweh, J. Stolze, and G. S. Uhrig. Finite-temperature line shapes of hard-core bosons in quantum magnets: A diagrammatic approach tested in one dimension. *Phys. Rev. B*, **90**:024428, 2014.

[43] L. P. Pitaevskii. Properties of the spectrum of elementary excitations near the disintegration threshold of the excitations. *Sov. Phys. JETP*, **36**:830, 1959.

[44] A. D. B. Woods and R. A. Cowley. Structure and excitations of liquid helium. *Rep. Prog. Phys.*, **36**:1135, 1972.

[45] A. J. Smith, A. Cowley, A. D. B. Woods, W. G. Stirling, and P. Martel. Roton-roton interactions and excitations in superfluid helium at large wavevectors. *J. Phys. C: Solid State Phys.*, **10**:543, 1977.

[46] B. Fåk and J. Bossy. Temperature Dependence of $S(Q, E)$ in Liquid ^{4}He Beyond the Roton. *Journal of Low Temperature Physics*, **112**:1, 1998.

[47] T. Masuda, A. Zheludev, H. Manaka, L.-P. Regnault, J.-H. Chung, and Y. Qiu. Dynamics of Composite Haldane Spin Chains in IPA-$CuCl_3$. *Phys. Rev. Lett.*, **96**:047210, 2006.

[48] T. Fischer, S. Duffe, and G. S. Uhrig. Microscopic model for Bose-Einstein condensation and quasiparticle decay. *EPL*, **96**:47001, 2011.

[49] J. Oh, M. D. Le, J. Jeong, J.-h. Lee, H. Woo, W.-Y. Song, T. G. Perring, W. J. L. Buyers, S.-W. Cheong, and J.-G. Park. Magnon Breakdown in a Two Dimensional Triangular Lattice Heisenberg Antiferromagnet of Multiferroic $LuMnO_3$. *Phys. Rev. Lett.*, **111**:257202, 2013.

[50] J. Ma, Y. Kamiya, T. Hong, H. B. Cao, G. Ehlers, W. Tian, C. D. Batista, Z. L. Dun, H. D. Zhou, and M. Matsuda. Static and Dynamical Properties of the Spin-1/2 Equilateral Triangular-Lattice Antiferromagnet $Ba_3CoSb_2O_9$. *Phys. Rev. Lett.*, **166**:087201, 2016.

[51] Y. Kohama, S. Wang, A. Uchida, K. Prsa, S. Zvyagin, Y. Skourski, R. D. McDonald, L. Balicas, H. M. Ronnow, C. Rüegg, and M. Jaime. Anisotropic Cascade of Field-Induced Phase Transitions in the Frustrated Spin-Ladder System $BiCu_2PO_6$. *Phys. Rev. Lett.*, **109**:167204, 2012.

[52] H. Nagasawa, T. Kawamata, K. Naruse, M. Ohno, Y. Matsuoka, H. Sudo, Y. Hagiya, M. Fujita, T. Sasaki, and Y. Koike. Thermal Conductivity in the Frustrated Two-Leg Spin- Ladder System $BiCu_2PO_6$. *J. Phys.: Conf. Ser.*, **568**:42012, 2014.

[53] B. Koteswararao, S. Salunke, A. V. Mahajan, I. Dasgupta, and J. Bobroff. Spin-gap behavior in the two-leg spin-ladder $BiCu_2PO_6$. *Phys. Rev. B*, **76**:52402, 2007.

[54] B. Koteswararao, A. V. Mahajan, L. K. Alexander, and J. Bobroff. Doping effects in the coupled, two-leg spin ladder $BiCu_2PO_6$. *Journal of Physics: Condensed Matter*, **22**:35601, 2010.

[55] O. Mentré, E. M. Ketatni, M. Colmont, M. Huvé, F. Abraham, and V. Petricek. Structural Features of the Modulated BiCu2(P1-xVx)O6 Solid Solution; 4-D Treatment of x = 0.87 Compound and Magnetic Spin-Gap to Gapless Transition in New Cu2+ Two-Leg Ladder Systems. *Journal of the American Chemical Society*, **128**:10857, 2006.

[56] T. Sugimoto, M. Mori, T. Tohyama, and S. Maekawa. Effects of frustration on magnetic excitations in a two-leg spin-ladder system. *Phys. Rev. B*, **87**:155143, 2013.

[57] T. Sugimoto, M. Mori, T. Tohyama, and S. Maekawa. Lifshitz Transition Induced by Magnetic Field in Frustrated Two-Leg-Spin-Ladder. *JPS Conf. Proc.*, **8**:034005, 2015.

[58] T. Sugimoto, M. Mori, T. Tohyama, and S. Maekawa. Magnetization plateaus by reconstructed quasispinons in a frustrated two-leg spin ladder under a magnetic field. *Phys. Rev. B*, **92**:125114, 2015.

[59] A. Lavarélo, G. Roux, and N. Laflorencie. Melting of a frustration-induced dimer crystal and incommensurability in the J_1-J_2 two-leg ladder. *Phys. Rev. B*, **84**:144407, 2011.

[60] A. Tsirlin, I. Rousochatzakis, D. Kasinathan, O. Janson, R. Nath, F. Weickert, C. Geibel, A. Läuchli, and H. Rosner. Bridging frustrated-spin-chain and spin-ladder physics: Quasi-one-dimensional magnetism of $BiCu_2PO_6$. *Phys. Rev. B*, **82**:144426, 2010.

[61] F. Casola, T. Shiroka, S. Wang, K. Conder, E. Pomjakushina, J. Mesot, and H.-R. Ott. Direct Observation of Impurity-Induced Magnetism in a Spin-$\frac{1}{2}$ Antiferromagnetic Heisenberg Two-Leg Spin Ladder. *Phys. Rev. Lett.*, **105**:67203, 2010.

[62] L. K. Alexander, J. Bobroff, A. V. Mahajan, B. Koteswararao, N. Laflorencie, and F. Alet. Impurity effects in coupled-ladder $BiCu_2PO_6$ studied by NMR and quantum Monte Carlo simulations. *Phys. Rev. B*, **81**:54438, 2010.

[63] O. Mentré, E. Janod, P. Rabu, M. Hennion, F. Leclercq-Hugeux, J. Kang, C. Lee, M.-H. Whangbo, and S. Petit. Incommensurate spin correlation driven by frustration in $BiCu_2PO_6$. *Phys. Rev. B*, **80**:180413, 2009.

[64] K. Hwang and Y. B. Kim. Theory of triplon dynamics in the quantum magnet $BiCu_2PO_6$. *Phys. Rev. B*, **93**:235130, 2016.

[65] S. Wang, E. Pomjakushina, T. Shiroka, G. Deng, N. Nikseresht, Ch. Rüegg, H. M. Rønnow, and K. Conder. Crystal growth and characterization of the dilutable frustrated spin-ladder compound $Bi(Cu_{1-x}Zn_x)_2PO_6$. *Journal of Crystal Growth*, **313**:51, 2010.

[66] Y. Kohama, K. Mochidzuki, T. Terashima, A. Miyata, A. DeMuer, T. Klein, C. Marcenat, Z. L. Dun, H. Zhou, G. Li, L. Balicas, N. Abe, Y. H. Matsuda, S. Takeyama, A. Matsuo, and K. Kindo. Entropy of the quantum soliton lattice and multiple magnetization steps in $BiCu_2PO_6$. *Phys. Rev. B*, **90**:60408, 2014.

[67] F. Casola, T. Shiroka, A. Feiguin, S. Wang, M. S. Grbić, M. Horvatić, S. Krämer, S. Mukhopadhyay, K. Conder, C. Berthier, H.-R. Ott, H. M. Rønnow, Ch. Rüegg, and J. Mesot. Field-Induced Quantum Soliton Lattice in a Frustrated Two-Leg Spin-1/2 Ladder. *Phys. Rev. Lett.*, **110**:187201, 2013.

[68] J. Bobroff, N. Laflorencie, L. K. Alexander, A. V. Mahajan, B. Koteswararao, and P. Mendels. Impurity-Induced Magnetic Order in Low-Dimensional Spin-Gapped Materials. *Phys. Rev. Lett.*, **103**:47201, 2009.

[69] K. W. Plumb, Z. Yamani, M. Matsuda, G. J. Shu, B. Koteswararao, F. C. Chou, and Y.-J. Kim. Incommensurate dynamic correlations in the quasi-two-dimensional spin liquid $BiCu_2PO_6$. *Phys. Rev. B*, **88**:24402, 2013.

[70] K. W. Plumb, K. Hwang, Y. Qiu, L. W. Harriger, G. E. Granroth, G. J. Shu, F. C. Chou, C. Rüegg, Y. B. Kim, and Y.-J. Kim. Giant Anisotropic Interactions in the Copper Based Quantum Magnet $BiCu_2PO_6$. *arXiv:1408.2528v1*, 2014.

[71] M. Malki, L. Müller, and G. S. Uhrig. Absence of localized edge modes in spite of a non-trivial Zak phase in $BiCu_2PO_6$. *Phys. Rev. Research*, **1**:033197, 2019.

[72] Kai P. Schmidt and Götz S. Uhrig. Excitations in One-Dimensional $S = \frac{1}{2}$ Quantum Antiferromagnets. *Phys. Rev. Lett.*, **90**:227204, 2003.

[73] T. Moriya. New Mechanism of Anisotropic Superexchange Interaction. *Phys. Rev. Lett.*, **4**:228, 1960.

[74] T. Moriya. Anisotropic Superexchange Interaction and Weak Ferromagnetism. *Phys. Rev.*, **120**:91, 1960.

[75] H. Bethe. Zur Theorie der Metalle. *Zeitschrift für Physik*, **71**:205, 1931.

[76] W. Heisenberg. Zur Theorie des Ferromagnetismus. *Zeitschrift für Physik*, **49**:619, 1928.

[77] J. Hubbard. Electron correlations in narrow bands. *The Royal Society*, **276**:238, 1963.

[78] L. Onsager. Crystal Statistics. I. A Two-Dimensional Model with an Order-Disorder Transition. *Phys. Rev.*, **65**:117, 1944.

[79] N. N. Bogoljubov. On a new method in the theory of superconductivity. *Nuovo Cimento*, **7**:794, 1958.

[80] J. G. Valatin. Comments on the theory of superconductivity. *Nuovo Cimento*, **7**:843, 1958.

[81] D. Bohm and D. Pines. A Collective Description of Electron Interactions. I. Magnetic Interactions. *Phys. Rev.*, **82**:625, 1951.

[82] D. Pines and D. Bohm. A Collective Description of Electron Interactions: II. Collective vs Individual Particle Aspects of the Interactions. *Phys. Rev.*, **85**:338, 1952.

[83] D. Bohm and D. Pines. A Collective Description of Electron Interactions: III. Coulomb Interactions in a Degenerate Electron Gas. *Phys. Rev.*, **92**:609, 1953.

[84] U. Schollwöck. The density-matrix renormalization group. *Rev. Mod. Phys.*, **77**:259, 2005.

[85] H. Yokoyama and H. Shiba. Variational Monte-Carlo Studies of Hubbard Model. I. *Journal of the Physical Society of Japan*, **56**:1490, 1986.

[86] H. Yokoyama and H. Shiba. Variational Monte-Carlo Studies of Hubbard Model. II. *Journal of the Physical Society of Japan*, **56**:3582, 1987.

[87] H. Yokoyama and H. Shiba. Variational Monte-Carlo Studies of Superconductivity in Strongly Correlated Electron Systems. *Journal of the Physical Society of Japan*, **57**:2482, 1988.

[88] R. R. dos Santos. Introduction to Quantum Monte Carlo Simulations for Fermionic Systems. *Brazilian Journal of Physics*, **33**:36, 2002.

[89] L. Splinter, N. A. Drescher, H. Krull, and G. S. Uhrig. Minimal model for the frustrated spin ladder system $BiCu_2PO_6$. *Phys. Rev. B*, **94**:155115, 2016.

[90] R. D. Mattuck. *A Guide to Feynman Diagrams in the Many-Body Problem*. Dover Publications, Inc., New York, 1992.

[91] C. Knetter and G. S. Uhrig. Perturbation theory by flow equations: dimerized and frustrated S=1/2 chain. *Eur. Phys. J. B*, **13**:209, 2000.

[92] C. Knetter, K. P. Schmidt, and G. S. Uhrig. The structure of operators in effective particle-conserving models. *J. Phys. A.: Math. Gen.*, **36**:7889, 2003.

[93] T. Fischer, S. Duffe, and G. S. Uhrig. Adapted continuous unitary transformation to treat systems with quasi-particles of finite lifetime. *New Journal of Physics*, **12**:33048, 2010.

[94] H. Krull, N. Drescher, and G. S. Uhrig. Enhanced perturbative continuous unitary transformations. *Phys. Rev. B*, **86**:125113, 2012.

[95] F. Wegner. Flow-equations for Hamiltonians. *Annalen der Physik*, **506**:77, 1994.

[96] S. D. Glazek and K. G. Wilson. Renormalization of Hamiltonians. *Phys. Rev. D*, **48**:5863, 1993.

[97] S. D. Glazek and K. G. Wilson. Perturbative renormalization group for Hamiltonians. *Phys. Rev. D*, **49**:4214, 1994.

[98] S. Dusuel and G. S. Uhrig. The quartic oscillator: a non-perturbative study by continous unitary transformations. *J. Phys. A.: Math. Gen.*, **37**:9275, 2004.

[99] H. Y. Yang and K. P. Schmidt. Effective models for gapped phases of strongly correlated quantum lattice models. *EPL*, **97**:17004, 2011.

[100] G. Uhrig, K. Schmidt, and M. Grüninger. Unifying Magnons and Triplons in Stripe-Ordered Cuprate Superconductors. *Phys. Rev. Lett.*, **93**:267003, 2004.

[101] K. P. Schmidt and G. S. Uhrig. Spectral Properties of Magnetic Excitations in Cuprate Two-Leg Ladder Systems. *Mod. Phys. Lett. B*, **19**:1179, 2005.

[102] S. Notbohm, P. Ribero, B. Lake, D. A. Tennant, K. P. Schmidt, G. S. Uhrig, C. Hess, R. Klingeler, G. Behr, B. Büchner, M. Reehuis, R. I. Bewley, C. D. Frost, P. Manuel, and R. S. Eccleston. One- and Two-Triplon Spectra of a Cuprate Ladder. *Phys. Rev. Lett.*, **98**:27403, 2007.

[103] B. Normand and Ch. Rüegg. Complete bond-operator theory of the two-chain spin ladder. *Phys. Rev. B*, **83**:054415, 2011.

[104] E. Dagotto and T. M. Rice. Surprises on the Way from One- to Two-Dimensional Quantum Magnets: The Ladder Materials. *Science*, **271**:618, 1996.

[105] J. Bardeen, L. N. Cooper, and J. R. Schrieffer. Theory of Superconductivity. *Phys. Rev.*, **108**, 1957.

[106] J. Bardeen, L. N. Cooper, and J. R. Schrieffer. Microscopic Theory of Superconductivity. *Phys. Rev.*, **106**:162, 1957.

[107] O. Maldonado. On the Bogoliubov transformation for quadratic boson observables. *Journal of Mathematical Physics*, **34**:5016, 1993.

[108] Y. Tikochinsky. Transformation brackets of generalized Bogolyubov-boson transformations. *Journal of Mathematical Physics*, **19**:270, 1978.

[109] C. Tsallis. Diagonalization methods for the general bilinear Hamiltonian of an assembly of bosons. *Journal of Mathematical Physics*, **19**:277, 1978.

[110] J.-P. Blaizot and G. Ripka. *Quantum Theory of Finite Systems*. The MIT Press, Cambridge, Massachusetts, 1986.

[111] R. Shindou, R. Matsumoto, S. Murakami, and J.-i. Ohe. Topological chiral magnonic egde mode in a magnonic crystal. *Phys. Rev. B*, **87**:174427, 2013.

[112] J. H. P. Colpa. Diagonalization Of The Quadratic Boson Hamiltonian. *Physica*, **93A**:327, 1978.

[113] Y. Kawaguchi and M. Ueda. Spinor Bose-Einstein condensates. *Phys. Rep.*, **520**:253, 2012.

[114] A. Kolezhuk and S. Sachdev. Magnon Decay in Gapped Quantum Spin Systems. *Phys. Rev. Lett.*, **96**:087203, 2006.

[115] H. Bruus and K. Flensberg. *Many-Body Quantum Theory in Condensed Matter Physics - An introduction*. Oxford University Press, 2004.

[116] R. Kubo. The fluctuation-dissipation theorem. *Rep. Prog. Phys.*, **29**:255, 1966.

[117] D. N. Zubarev. Double-Time Green Functions in Statistical Physics. *Soviet Physics Uspekhi*, **3**:320, 1960.

[118] V. S. Viswanath and G. Müller. *The Recursion Method - Application to Many-Body Dynamics*. Springer, 1994.

[119] C. Lanczos. An Iteration Method for the Solution of the Eigenvalue Problem of Linear Differential and Integral Operators. *Journal of Research of the National Bereau of Standards*, **45**:255, 1950.

[120] F. J. Dyson. The S Matrix in Quantum Electrodynamics. *Phys. Rev.*, **75**:1736, 1949.

[121] R. P. Kanwal and K. C. Liu. A Taylor expansion approach for solving integral equations. *International Journal of Mathematical Education in Science and Technology*, **20**:411, 2006.

[122] W. Nolting. *Grundkurs Theoretische Physik 7*. Springer Spektrum, 2015.

[123] T. Fischer. *Description of quasiparticle decay by continuous unitary transformations*. PhD thesis, Technische Universität Dortmund, 2011.

[124] I. Dzyloshinsky. A Thermodynamic Theory of "weak" Ferromagnetism of Antiferromagnetics. *Journal of Physics and Chemistry of Solids*, **4**:241, 1958.

[125] P. W. Anderson. New Approach to the Theory of Superexchange Interactions. *Phys. Rev.*, **115**, 1959.

[126] L. Shekhtman, O. Entin-Wohlman, and A. Aharony. Moriya's anisotropic superexchange interaction, frustration, and Dzyaloshinsky's weak ferromagnetism. *Phys. Rev. Lett.*, **69**:836, 1992.

[127] V. Fock. Konfigurationsraum und zweite Quantelung. *Zeitschrift für Physik*, **75**:622, 1932.

[128] D. G. Pettifor and D. L. Weaire. *The Recursion Method and Its Applications*. Springer, 1985.

[129] A. A. Zvyagin. *Finite size effects in correlated electron models*. Imperial College Press, 2005.

[130] V. S. Viswanath and G. Müller. Recursion method in quantum spin dynamics: The art of terminating a continued fraction. *Journal of Applied Physics*, **67**:5486, 1998.

[131] L. Van Hove. The Occurrence of Singularities in the Elastic Frequency Distribution of a Crystal. *Phys. Rev.*, **89**:1189, 1953.

[132] G. Czycholl. *Theoretische Festkörperphysik Band 1*. Springer Spektrum, 2016.

[133] M. G. Zacher, R. Eder, E. Arrigoni, and W. Hanke. Stripes in Doped Antiferromagnets: Single-Particle Spectral Weight. *Phys. Rev. Lett.*, **85**:2585, 2000.

[134] J. Lorenzana, G. Seibold, and R. Coldea. Sum rules and missing spectral weight in magnetic neutron scattering in the cuprates. *Phys. Rev. B*, **72**:224511, 2005.

[135] L. Coffey and D. Coffey. Quasiparticle spectral weight of cuprate oxide superconductors. *Phys. Rev. B*, **48**:4184, 1992.

[136] S. Sachdev and R.N. Bhatt. Bond-operator representation of quantum sspin: Meanfield theory of frustrated quantum Heisenberg antiferromagnets. *Phys. Rev. B*, **41**:9323, 1990.

[137] R. P. Feynman. *Statistical Mechanics*. Benjamin, Reading, Mass., 1972.

[138] J. Zak. Berry's Phase for Energy Bands in Solids. *Phys. Rev. Lett.*, **62**:2747, 1989.

[139] P. Delplace, D. Ullmo, and G. Montambaux. Zak phase and the existence of edge states in graphene. *Phys. Rev. B*, **84**:195452, 2011.

[140] L. Fidkowski, T. S. Jackson, and I. Klich. Model Characterization of Gapless Edge Modes of Topological Insulators Using Intermediate Brillouin-Zone Functions. *Phys. Rev. Lett.*, **107**:036601, 2011.

[141] R. S. K. Mong and V. Shivamoggi. Edge states and the bulk-boundary correspondence in Dirac Hamiltonians. *Phys. Rev. B*, **83**:125109, 2011.

[142] T. Fukui, K. Shiozaki, T. Fujiwara, and S. Fujimoto. Bulk-Edge Correspondence for Chern Topological Phases: A Viewpoint from a Generalized Index Theorem. *Journal of the Physical Society of Japan*, **81**:114602, 2012.

[143] A. M. Essin and V. Gurarie. Bulk-boundary correspondence of topological insulators from their respective Green's functions. *Phys. Rev. B*, **84**:125132, 2011.

[144] M. Wada, S. Murakami, F. Freimuth, and G. Bihlmayer. Localized edge states in two-dimensional topological insulators: Ultrathin Bi films. *Phys. Rev. B*, **83**:121310(R), 2011.

[145] S. Murakami. Two-dimensional topological insulators and their edge states. *J. Phys.: Conf. Ser.*, **302**:012019, 2011.

[146] B.-J. Yang, M. S. Bahramy, and N. Nagaosa. Topological protection of bound states against the hybridization. *Nat. Commun.*, **4**:1524, 2013.

[147] S. Gopalan, T. M. Rice, and M. Sigrist. Spin ladders with spin gaps: A description of a class of cuprates. *Phys. Rev. B*, **49**:8901, 1994.

[148] S. Trebst, H. Monien, C. J. Hamer, Z. Weihong, and R. R. P. Singh. Strong-Coupling Expansions for Multiparticle Excitations: Continuum and Bound States. *Phys. Rev. Lett.*, **85**:4373, 2000.

[149] C. Knetter, K. P. Schmidt, M. Grüninger, and G. S. Uhrig. Fractional and Integer Excitations in Quantum Antiferromagnetic Spin 1/2 Ladders. *Phys. Rev. Lett.*, **87**:167204, 2001.

[150] F. Schwabl. *Quantenmechanik*. Springer, 2007.

[151] N. Drescher. *Variational and Perturbative Extensions of Continuous Unitary Transformations for Low-Dimensional Spin Systems*. PhD thesis, Technische Universität Dortmund, 2014.

[152] K. Plumb. Novel Spin Excitations in the Frustrated Quantum Magnet $BiCu_2PO_6$. *APS March Meeting*, 2014.

[153] R. P. Brent. *Algorithms for Minimization Without Derivatives*. Dover Publications, Mineola, New York, 2002.

Danksagung

An dieser Stelle möchte ich mich zuerst aufrichtig bei meinem Doktorvater Prof. Dr. Götz S. Uhrig für die Vergabe des Forschungsthemas und die intensive Betreuung und Zusammenarbeit, besonders während der Corona-Pandemie, bedanken.

Prof. Dr. Kai Phillip Schmidt danke ich für die Übernahme der Rolle des Zweitgutachters.

Prof. Dr. Joachim Stolze danke ich für die fachlichen Ratschläge bezüglich meiner Doktorarbeit während des Sabbatsemesters meines Doktorvaters im Wintersemester 2018/19.

Dr. Nils A. Drescher und Dr. Holger Krull danke ich für die Einführung und Übernahme des verwendeten Programmcodes der deepCUT sowie für die Weitergabe der experimentellen Daten.

Bei Dr. Carsten Nase und Philipp Schering bedanken ich mich für die intensive Unterstützung in Bezug auf die Verwendung des oben genannten Codes bei der Clusterumstellung von cl1 von PBS auf slurm im November 2019.

Philip Bleicker und Philipp Schering danke ich für ihre Ratschläge in Programmierfragen.

Meinen Bürokollegen danke ich für die zahlreichen fachlichen und auch nicht-fachlichen Diskussionen. Außerdem möchte ich mich bei der gesamten Arbeitsgruppe für die Hilfsbereitschaft bedanken.

Meinen (ehemaligen) Kollegen Dr. Benedikt Fauseweh, Dr. Maik Malki und Gary Ferkinghoff danke ich für die Zusammenarbeit in verschiedenen Nebenprojekten.

Letztendlich möchte ich mich bei Dr. Benedikt Fauseweh und Philip Bleicker für das intensive Korrekturlesen dieser Arbeit bedanken.

Danksagung II

Eine zweite Danksagung? Wieso? Das werden Sie sich/Das wirst du dich sicher an dieser Stelle fragen. Im Laufe meiner Promotion ist mir klar geworden, dass nicht nur eine fachliche Unterstützung für eine erfolgreiche Promotion von essenzieller Bedeutung ist, sondern auch eine emotionale/menschliche Überstützung besonders während der Phasen in einer Promotion, in denen einfach nichts funktioniert. In meinen Augen ist diese Unterstützung der promovierenden Person, die auch nur ein Menschen ist (!), mindestens genauso wichtig wie die fachliche Unterstützung. Um diese klar voneinander zu trennen, gibt es diese zweite Danksagung. Die Reihenfolge hat keinerlei Bedeutung.

Liebste Maggi, unsere unzähligen Kaffeepausen und Treffen und der intensive Austausch über die Promotion haben mich an einigen Tagen getragen. Nach jedem Gespräch mit dir, egal ob digital, per Telefon, oder persönlich, war ich wieder sehr motiviert weiter an meiner Dissertation zu arbeiten. Du bist für mich ein sehr wertvoller Mensch!

Lieber Philip, deine unzähligen Sprachnachrichten, unsere Telefonate, unsere Gespräche und besonders unser intensiver Austausch während der Corona-Pandemie waren für mich jedes Mal sehr wertvoll. Du hast mir Kraft gegeben weiter zu machen und dass ich mich wieder an nicht-funktionierende Punkte dran gesetzt und mir auch mal Auszeiten von der Diss gegönnt habe. Ich bin dir unendlich dankbar dafür!

Lieber Philipp, ich bin dir dankbar für unsere Kaffee-/oder Eispausen im Sommer 2019. Vielen Dank, dass du dir auch nach der Masterarbeitszeit an unserem Lehrstuhl noch immer meine Klagen angehört hast und mir Rat und Mut gegeben hast.

Lieber Gary, ich danke dir dafür, dass du einer meiner allerbesten Bürokollegen warst! Ich bewundere wie hilfsbereit du bist und dabei nie deine Geduld und positive Art verloren hast. Vielen Dank für all die Stunden die wir gemeinsam im Büro gearbeitet haben und manchmal auch bis spät abends uns auch noch privat unterhalten oder rumgealbert haben. Auch die Zeit, in der wir nicht gearbeitet haben, war wichtig für meine Dissertation, da ich aus ihr neue Kraft schöpfen konnte.

Liebe Kira, liebe Jasmin, liebe Alina, ich bin unfassbar dankbar euch während meiner Promotion durch meine Gleichstellungsaktivitäten kennengelernt zu haben. Ihr seid alle drei richtige Powerfrauen! Jedes Gespräch mit euch hat mich motiviert weiterzumachen, egal ob in der Diss oder in der Gleichstellung. Vielen Dank für eure ganze Unterstützung und eure Gespräche. Ich wünsche euch bei euren Doktor-/Masterarbeiten Alles Gute!

Lieber Joachim, vielen Dank, dass du mir während der Corona-Pandemie immer mit Rat und Tat zur Seite gestanden hast! Deine ruhige Art hat auch mich bei jeder noch so stressigen Situation zur Ruhe gebracht.

Liebe Frau Boomhuis, vielen Dank für Ihre Unterstützung gegen Ende meiner Promotion. Sie haben mich bei jedem unserer Gespräche in meinen Plänen gestärkt und mir immer wieder neue Kraft gegeben. Danke!

Lieber Felix, ich fand es schön auch mit dir einige Jahre an der TU Dortmund verbracht zu haben. Vielen Dank für deine Besuche bei mir im Büro und die gemeinsamen Mensapausen. Auch neben der Uni warst du immer für mich da und hast mir zugehört. Du bist ein toller Bruder!

Liebe Mama, lieber Papa, vielen Dank, dass ihr mir das Physikstudium ermöglicht und auch immer an mich geglaubt habt! Danke, dass ihr mir immer zugehört und mich immer wieder im meinem Vorhaben bestärkt habt!

Liebster Heiko, mein geliebter Ehemann, ich kann nicht in Worte fassen was du für mich während meiner Promotion geleistet hast. Ich danke dir, dass du auch in den schweren Zeiten nicht von meiner Seite gewichen bist und einfach nur für mich da warst. Ich freue mich auf mein Leben mit dir nach der TU Dortmund.

Eine Promotion dauert mehrere Jahre. Deswegen passiert es, dass einen während der Promotion auch Menschen aus den verschiedensten Gründen verlassen. Dies war auch bei mir der Fall, aber ich bin dankbar dafür, dass sie mich zu Beginn begleitet haben. Zweien davon möchte ich ganz besonders danken und damit meine Dissertation auch wirklich abschließen. Ihr wisst, dass ihr gemeint seid: „Ich bin Batman!“ und
„Yabba Dabba Doo!“.